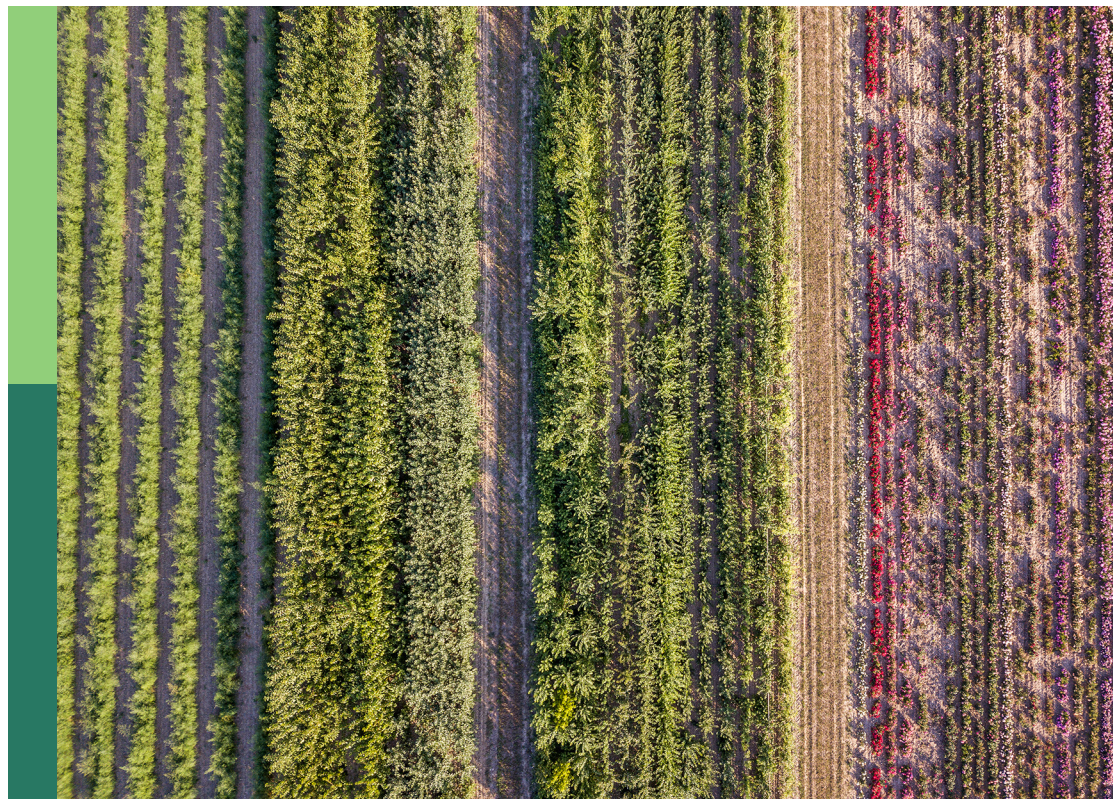# Rapid screening for organic pollutants analysis in food

Edited by
Xiuxiu Dong, Sujun Guan, Lin Luo, Xixia Liu,
Derek Hao and Yiming Zhang

Published in
Frontiers in Sustainable Food Systems

About Frontiers

Frontiers is more than just an open access publisher of scholarly articles: it is a pioneering approach to the world of academia, radically improving the way scholarly research is managed. The grand vision of Frontiers is a world where all people have an equal opportunity to seek, share and generate knowledge. Frontiers provides immediate and permanent online open access to all its publications, but this alone is not enough to realize our grand goals.

Frontiers journal series

The Frontiers journal series is a multi-tier and interdisciplinary set of open-access, online journals, promising a paradigm shift from the current review, selection and dissemination processes in academic publishing. All Frontiers journals are driven by researchers for researchers; therefore, they constitute a service to the scholarly community. At the same time, the *Frontiers journal series* operates on a revolutionary invention, the tiered publishing system, initially addressing specific communities of scholars, and gradually climbing up to broader public understanding, thus serving the interests of the lay society, too.

Dedication to quality

Each Frontiers article is a landmark of the highest quality, thanks to genuinely collaborative interactions between authors and review editors, who include some of the world's best academicians. Research must be certified by peers before entering a stream of knowledge that may eventually reach the public - and shape society; therefore, Frontiers only applies the most rigorous and unbiased reviews. Frontiers revolutionizes research publishing by freely delivering the most outstanding research, evaluated with no bias from both the academic and social point of view. By applying the most advanced information technologies, Frontiers is catapulting scholarly publishing into a new generation.

What are Frontiers Research Topics?

Frontiers Research Topics are very popular trademarks of the *Frontiers journals series*: they are collections of at least ten articles, all centered on a particular subject. With their unique mix of varied contributions from Original Research to Review Articles, Frontiers Research Topics unify the most influential researchers, the latest key findings and historical advances in a hot research area.

Find out more on how to host your own Frontiers Research Topic or contribute to one as an author by contacting the Frontiers editorial office: frontiersin.org/about/contact

Rapid screening for organic pollutants analysis in food

Table of contents

Check for updates

Editorial: Rapid screening for organic pollutants analysis in food

Xiuxiu Dong[1], Sujun Guan[2], Lin Luo[3], Xixia Liu[4]*, Derek Hao[5] and Yiming Zhang[6]*

[1]School of Agricultural Engineering, Jiangsu University, Zhenjiang, China, [2]Research Center for Space System Innovation, Tokyo University of Science, Chiba, Japan, [3]College of Food Science, South China Agricultural University, Guangzhou, China, [4]College of Life Science, Hubei Normal University, Huangshi, China, [5]School of Science, RMIT University, Melbourne, VIC, Australia, [6]College of Food and Health, Zhejiang A&F University, Hangzhou, China

Editorial on the Research Topic
Rapid screening for organic pollutants analysis in food

The global population is expected to reach at least 9 billion by the year 2050, requiring up to 70% more food and demanding food production systems and the food chain to become fully sustainable. Within this context, food safety must become an enabler of global food security (Fritsche, 2018). Food safety is closely related to people's health and the stability of the food market. Some of these hazards may include bacterial pathogens (*Salmonella*, *Escherichia coli*, etc.); physical contaminants, and adulterants (glass, metal, animal feces, etc.); naturally occurring toxicants (mycotoxins, alkaloids, lectins, etc.); agrochemical and veterinary drug residues, prions, and aflatoxins (Madilo et al., 2024). Hence, implementing reliable, effective, and rapid screening methods can ensure the accuracy of analytical results, improve the efficiency of analysis, and contribute to strengthening food safety supervision, thus promoting the sustainable development of the food system.

Lincomycin, a natural antibiotic, is widely used by animal and fishery husbandries to prevent infections and treat diseases. It endangers people's health when they eat food containing lincomycin residue, especially the frequent consumption of milk and chicken products containing lincomycin. Zhang et al. prepared lincomycin-imprinted silica nanoparticles according to boronate affinity-based template-immobilized surface imprinting. The prepared lincomycin-imprinted silica nanoparticles exhibited several significant results, such as good specificity, high binding capacity (19.45 mg/g), fast kinetics (6 min), and low binding pH (pH 5.0) toward lincomycin.

Pesticide is indispensable for modern agriculture. However, the improper and excessive use of pesticides results in residue in food and environment, which is a serious problem. First of all, sample pretreatment is an essential procedure in pesticide analysis, as the matrix effect can significantly influence the results. Huang et al. synthesized a covalent organic framework (COF) using 1,2,4,5-tetrakis-(4-formylphenyl)benzene and benzidine to mitigate the matrix effect in vegetable and fruit samples. This COF was then used to develop a solid-phase extraction method. In addition, the COF was used to create a magnetic COF (MCOF) for use in magnetic solid-phase extraction. The

reuse test demonstrated that the synthesized COF and MCOF can be reused up to 15 times. Chen et al. developed a simple and sensitive fluoroimmunoassay (FIA) based on a nanobody-alkaline phosphatase fusion protein (VHHjd8-ALP) and blue-emissive carbon dots (bCDs) for the rapid detection of fenitrothion. Compared with the p-nitrophenylphosphate-based one-step conventional indirect competitive enzyme-linked immunoassay (icELISA), the developed FIA showed an 11-fold sensitivity improvement. Furthermore, the analysis period of FIA only takes ~55 min, which was obviously faster than that of the conventional icELISA.

Malachite green, a triphenylmethane dye, is used in the aquaculture industry as a disinfectant and insect repellent due to its potent bactericidal and pesticidal properties. However, its use poses potential environmental and health risks. Wu et al. analyzed and designed two haptens using computer simulation. Serum data confirmed the feasibility of introducing an arm at the dimethylamine group. Subsequently, a highly selective monoclonal antibody strain was successfully prepared based on the hapten.

Ma et al. reported an effective electrochemical sensor for simultaneous detection of ascorbic acid and dopamine by using Co-modified MCM-41 as the electrocatalytic material. And this work has important implications for the construction of methods for detecting low-molecule organic pollutants in food.

Millet is one of the major coarse grain crops in China. Its geographical origin and Fusarium fungal contamination with ergosterol and deoxynivalenol have a direct impact on food quality. Six hundred millet samples were collected from 12 production areas in China, and traditional algorithms such as random forest and support vector machine were selected to compare with the deep learning models for the prediction of millet geographical origin and toxin content. Nie et al. firstly develops a deep learning model (wavelet transformation-attention mechanism long short-term memory, WT-ALSTM) by combining hyperspectral imaging to achieve the best prediction effect, the wavelet transformation algorithm effectively eliminates noise in the spectral data, while the attention mechanism module improves the interpretability of the prediction model by selecting spectral feature bands.

Rapid assessment and prevention of diseases caused by foodborne pathogens is one of the existing food safety regulatory issues faced by various countries, and it has received wide attention from all sectors of society. Dong et al. summarized the recent advances in foodborne pathogen detection using photoelectrochemical biosensors from photoactive material to sensing strategy.

Per- and polyfluoroalkyl substances (PFAS) are a group of persistent organic pollutants which pose significant risks to human health and the environment. Senovilla-Herrero et al. comprehensively examines the implications of new legislation concerning PFAS for food sustainability.

Phthalic acid esters (PAEs) are often added to plastics to enhance elasticity, transparency, durability and prolong service life as a kind of plasticizer. However, it is easy to be released into the environment and enter the human body from various potential sources. Zhang et al. introduced the recent advancements and trends in optical sensors for detection of PAEs represented by colorimetric sensors, fluorescence sensors and surface-enhanced Raman scattering platform.

This Research Topic will provide an overview of the present scenario on food safety and potential adaptation in response to the global food safety.

Author contributions

XD: Conceptualization, Investigation, Writing – original draft, Writing – review & editing. SG: Writing – review & editing. LL: Writing – review & editing. XL: Conceptualization, Writing – review & editing. DH: Writing – review & editing. YZ: Conceptualization, Writing – review & editing.

Acknowledgments

We acknowledge the authors, reviewers, and the editors for supporting us completing this important task.

Conflict of interest

The authors declare that the research was conducted in the absence of any commercial or financial relationships that could be construed as a potential conflict of interest.

Publisher's note

All claims expressed in this article are solely those of the authors and do not necessarily represent those of their affiliated organizations, or those of the publisher, the editors and the reviewers. Any product that may be evaluated in this article, or claim that may be made by its manufacturer, is not guaranteed or endorsed by the publisher.

References

Fritsche, J. (2018). Recent developments and digital perspectives in food safety and authenticity. *J. Agric. Food Chem.* 66, 7562–7567. doi: 10.1021/acs.jafc.8b00843

Madilo, F. K., Kunadu, A. P. H., and Tano-Debrah, K. (2024). Challenges with food safety adoption: a review. *J. Food Saf.* 44:e13099. doi: 10.1111/jfs.13099

High-capacity boronate affinity-based template-immobilized surface imprinted silica nanoparticles for rapid, selective, and efficient extraction and determination of lincomycin in milk and chicken

Yansong Zhang[1]*, Yihan Ding[2], Yidan Ma[2], Zixin Zhang[2], Yipei Wang[2], Daojin Li[2] and Shuangshou Wang[3]*

[1]School of Food and Drug, Luoyang Normal University, Luoyang, China, [2]Henan Key Laboratory of Function-Oriented Porous Materials, College of Chemistry and Chemical Engineering, Luoyang Normal University, Luoyang, China, [3]School of Chemistry and Chemical Engineering, Anhui University of Technology, Ma'anshan, China

Background: Lincomycin, a natural antibiotic, is widely used by animal and fishery husbandries to prevent infections and treat diseases. It endangers people's health when they eat foods containing lincomycin residue, especially the frequent consumption of milk and chicken products containing lincomycin. Hence, it is extremely important to evaluate the content of lincomycin in food samples. However, a direct analysis of lincomycin in milk and chicken is quite difficult because of its very low concentration level and the presence of undesirable matrix effects. Therefore, selective and efficient extraction of lincomycin from complex food samples prior to its quantification is required.

Results: In this study, lincomycin-imprinted silica nanoparticles were prepared according to boronate affinity-based template-immobilized surface imprinting. Silica nanoparticles and boronic acid ligands 3-fluoro-4-formylphenylboronic acid were used as supporting materials and functional monomers, respectively. The prepared lincomycin-imprinted silica nanoparticles exhibited several significant results, such as good specificity, high binding capacity (19.45 mg/g), fast kinetics (6 min), and low binding pH (pH 5.0) toward lincomycin. The reproducibility of lincomycin-imprinted silica nanoparticles was satisfactory. The lincomycin-imprinted silica nanoparticles could still be reused after seven adsorption−desorption cycles, which indicated high chemical stability. In addition, the recoveries of the proposed method for lincomycin at three spiked levels of analysis in milk and chicken were 93.3−103.3% and 90.0−100.0%, respectively.

Conclusion: The prepared lincomycin-imprinted silica nanoparticles are feasible for the recognition of target lincomycin with low concentrations in real food samples such as milk and chicken. Our approach makes sample pre-preparation simple, fast, selective, and efficient.

KEYWORDS

boronate affinity, lincomycin, template-immobilized surface imprinting, milk, chicken, silica nanoparticles

1. Introduction

Antimicrobial agents are widely used to prevent and treat diseases and promote growth in animal husbandry (Ding et al., 2021; Khafi et al., 2023). However, food safety issue by veterinary drug residues has become a worldwide public health concern. As a lincosamide antibiotic, lincomycin (Lin) is widely used in human and veterinary medicine due to its excellent antibacterial effect (Dasenaki and Thomaidis, 2015; Koike et al., 2021). Meanwhile, Lin is also used in association with other antimicrobial drugs to treat livestock infections caused by *Bacteroides fragilis*, as well as diseases of the respiratory tract in different animal species (Maddaleno et al., 2019). However, it also has an adverse impact on human products and life because of the irrational use of Lin. Antibiotic residues may lead to disturbances in ecological functions and promote the development and distribution of resistant genes, which pose a potential risk to the environment (Bengtsson-Palme and Larsson, 2016; Andrade et al., 2020). Among the most important effects of Lin getting released into the environment are the transfer of Lin-resistant genes (LRGs) and the alteration of the microbial community, such as the impact on food safety and human health due to crop plant uptake (Mehrtens et al., 2021). It affects people's health when they eat foods containing Lin residue, especially the frequent consumption of milk and chicken products containing Lin. The acceptable maximum residual level (MRL) of Lin in milk and chicken was set at 150 and 200 $\mu g\,kg^{-1}$ by the Codex Alimentarius Commission and the European Union, respectively (Du et al., 2019). Therefore, it is important to have in place an efficient way to evaluate the levels of Lin in animal-derived food samples such as milk and chicken.

Thus far, a variety of analytical methods have been used to evaluate Lin in different real samples including GC–MS (Tao et al., 2011), LC–MS (Khadim et al., 2023), LC–MS/MS (Fernandes-Cunha et al., 2015; Maddaleno et al., 2019; Du et al., 2021; Li et al., 2021), and immunoassay (Zhou et al., 2014; Cao et al., 2015). Although these methods have many advantages, especially good sensitivity and accuracy, most of them suffer from several drawbacks, such as costly instruments, complicated sample preparation, long time consumption, and poor storage stability. This compels the need for a simple, fast, and sensitive quantitative method that absorbs Lin in food samples. However, the low content of Lin and high content of complex interfering substances add to the difficulty and challenges in the direct determination of Lin in food samples using UV detection. Therefore, an efficient sample pre-preparation prior to detection becomes very necessary, including separation and enrichment of Lin in food samples.

Molecularly imprinted polymers (MIPs) have been used as efficient solid phase extraction (SPE) adsorbents on account of their high specificity, easy preparation, low cost, and good physicochemical stability (Vlatakis et al., 1993; Li et al., 2015; Hao et al., 2016). To the best of our knowledge, although there are several reports on the preparation of MIPs for Lin to date (Li et al., 2017; Zhang et al., 2019; Dong et al., 2020), the molecular imprinting used in these studies was performed through a one-pot process. In fact, such an imprinting methodology is bulk imprinting in essence because the thickness of the imprinted coating cannot be calibrated to the size of the template, which thereby greatly affects the imprinting effect. To address these issues, the template-immobilized surface imprinting approach (Li et al., 2015; Hao et al., 2016; Zhang et al., 2022) should be used to prepare imprinting coating on the surface of silica because it can

be adjusted to the size of the template effectively. This method of surface imprinting offers several advantages, including easy template removal, high binding capacity, and fast mass transfer. Recently, we used boronate affinity-based oriented surface imprinting to prepare chlorogenic acid-imprinted magnetic nanomaterials and catecholamine-imprinted magnetic nanomaterials, which were applied, respectively, for the selective recognition of chlorogenic acid in fruit juices and for trace analysis of catecholamine in human urine (Li et al., 2020; Li P. et al., 2022). However, the binding capacity of the above imprinted magnetic nanomaterials was relatively low. In addition, this kind of template-immobilized surface imprinting has not been used to develop MIPs for Lin for food safety in previous reports. The pesticide residue of Lin is one of the most important food safety concerns. In this study, a novel boronic acid ligand, FFPBA, has been used for the first time as a functional monomer, and its pKa value has also been measured for the first time. Although boronic acid functionalized magnetic nanoparticles (MNP) were developed for highly efficient capture of lincomycin (Zhang et al., 2023), the selective ability of the boronic acid functionalized magnetic nanoparticles for Lin was weak due to the absence of an imprinting site. To improve its selectivity and binding, boronate affinity-based imprinted nanoparticles specific to Lin were prepared.

In the template-immobilized surface imprinting strategy, template immobilization and removal are the key steps. Fortunately, Lin has a cis-diols structure; boronate affinity materials can covalently bind compounds with cis-diol at high pH values, and boronate esters can dissociate at relatively low pH values under mild ambient conditions (Liu et al., 2012; Qu et al., 2012; Li D. et al., 2022). In addition, 3-fluoro-4-formylphenylboronic acid (FFPBA) has been used for the first time as boronic acid ligands to immobilize and imprint Lin. Silica nanoparticles (SiO$_2$), due to their good biocompatibility, low toxicity, easy post-modification, high yield synthesis, and easy preparation, can be used successfully as solid substrates (He et al., 2010; Lin et al., 2012; Arabi et al., 2016). Therefore, high-density boronic acid ligands can be formed on the surface of SiO$_2$ by post-modification reactions. Furthermore, the imprinted coating is important for the binding properties of the imprinted materials. The poly (2-anilinoethanol) with a more hydrophilic domain can be used as a good imprinting coating.

In this study, we attempted to prepare novel Lin-imprinted silica nanoparticles (Lin-imprinted SiO$_2$@APTES@FFPBA) using a boronate affinity-based template-immobilized surface imprinting approach. As depicted in Figure 1, the imprinting process included three steps. First, Lin was immobilized onto FFPBA-functionalized SiO$_2$ (SiO$_2$@APTES@FFPBA) through boronate affinity interaction. Then, the 2-anilinoethanol was self-polymerized on the surface of SiO$_2$@APTES@FFPBA to form an imprinting coating with appropriate thickness. Generally, the thickness of the imprinting coating should be adjusted to 1/3 to 2/3 of the molecular size of the template in one of the three dimensions. Finally, the Lin template was removed by an acidic solution with SDS to form the MIPs with an imprinting cavity containing FFPBA. Because the obtained imprinting coating could cover excessive binding sites, non-specific adsorption could be effectively eliminated. The prepared Lin-imprinted SiO$_2$@APTES@FFPBA exhibited several significant advantages, such as good specificity, high binding capacity, fast kinetics, and low binding pH toward Lin. In addition, the recoveries of the proposed method for Lin at three spiked levels of analysis in milk and chicken were 95.3–102.7%
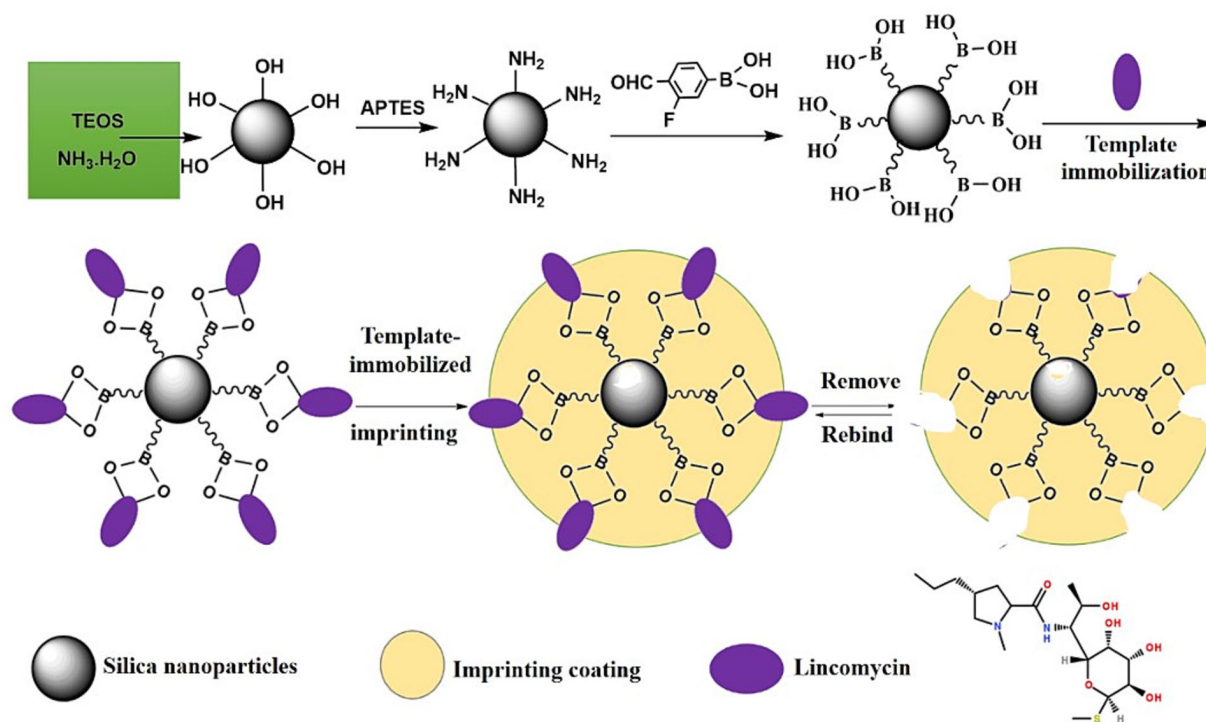
FIGURE 1
The formation mechanism of Lin-imprinted silica nanoparticles by boronate affinity-based template-immobilized surface imprinting.

and 96.8–104.5%, respectively, which indicated the successful detection of Lin in real samples.

2. Experimental materials and methods

2.1. Materials

Adenosine (A), deoxyadenosine (DA), guanosine (G), 2'-O-methylguanosine (Gm), dopamine (Dop), rutin (Rut), quercertin (Que), Baicalein (Bai), Vitamin b12, genistein (Gen), kaempferol (Kae), Lin, desonide (Des), 2-anilinoethanol, tetraethoxysilane (TEOS), (3-amino-propyl) triethoxysilane (APTES), ammonium persulfate (APS), FFPBA, Sodium cyanoborohydride, and anhydrous methanol were purchased from J&K Scientific Ltd. (Shanghai, China). All other reagents were of analytical grade or above and used without further treatment.

2.2. Instruments

Transmission electron microscopy (TEM) characterization was performed on a JEM-1010 system (JEOL, Tokyo, Japan). UV absorbance and the adsorption isotherm measurements were carried out using a U-3010 UV spectrophotometer equipped with a 1-cm cuvette (Kyoto, Japan). The X-ray photoelectron spectroscopy (XPS) was performed with an ESCALAB 250Xi X-ray photoelectron spectrometer (Thermo, USA) with Al Kα radiation (hv = 1486.6 eV). The instrument was calibrated against the C1s band at 284.8 eV. Powder

X-ray diffraction (XRD) analyses were carried out using a Bruker D8 Advance diffractometer with Cu Kα radiation, and the scanning angle ranged from 10° to 80° of 2θ.

2.3. Preparation of FFPBA-functionalized silica nanoparticles (SiO$_2$@APTES@FFPBA)

FFPBA-functionalized MNPs were prepared by the following three-step reaction (Figure 1): (1) synthesis of silica nanoparticles (SiO$_2$), (2) functionalization with APTES (SiO$_2$@APTES), and (3) functionalization of SiO$_2$@APTES using FFPBA by the Schiff base reaction (SiO$_2$@APTES@FFPBA). The bare SiO$_2$ was synthesized according to a modified previously reported method (Lin et al., 2014). Briefly, 6 mL of TEOS was gradually added to a mixture of 100 mL ethanol, 4 mL deionized water, and 3.2 mL aqueous solution of 25–28% ammonium. The mixture solutions were vigorously stirred at 30°C for 24 h. The resulting SiO$_2$ was rinsed with water and ethanol three times in sequence and then vacuum-dried at 40°C overnight. Then, 1.0 mL of APTES was added dropwise to 20 mL anhydrous methanol containing 120 mg SiO$_2$, and the SiO$_2$@APTES was obtained by stirring the mixture for 24 h. The resultant SiO$_2$@APTES was purified by three cycles of centrifugation, separation, and resuspension in ethanol by ultrasonication and dried at room temperature under vacuum for further use. The third step was to functionalize SiO$_2$@APTES with FFPBA. 100 mg of SiO$_2$@APTES was added to 150 mL anhydrous methanol containing 2.0 g FFPBA, and the obtained mixture was stirred for 12 h at 30°C. After that, sodium cyanoborohydride was added into the above solution (400 mg every 6 h) and kept for 24 h at 30°C. The

SiO$_2$@APTES@FFPBA was separated from the mixtures by a magnet and washed with water and ethanol in turn. The dried SiO$_2$@APTES@FFPBA was obtained using vacuum drying (40°C) and needed cold preservation.

2.4. Selectivity of SiO$_2$@APTES@FFPBA

The selectivity of SiO$_2$@APTES@FFPBA was evaluated using A, G, and Lin as cis-diol compounds with DA and Gm as non-cis-diol analogs. The cis-diol or non-cis-diol solution (1 mg/mL) was obtained after they were dissolved in 50 mM PBS (pH 7.0), respectively. SiO$_2$@APTES@FFPBA of 3 mg were dispersed into 1 mL above solution respectively, and the mixture was shaken at room temperature for 30 min. Then, the obtained targets-treated SiO$_2$@APTES@FFPBA were collected by magnetic force and rinsed with 500 μL PBS (pH 7.0) three times. After that, the target-treated SiO$_2$@APTES@FFPBA were eluted with an acetic acid solution for 1 h, and the obtained eluates containing targets were collected.

2.5. Preparation of Lin-imprinted SiO$_2$@ APTES@FFPBA

The Lin-imprinted SiO$_2$@APTES@FFPBA were prepared according to the boronate affinity-based template-immobilized surface imprinting approach. As depicted in Figure 1, Lin templates were first immobilized onto SiO$_2$@APTES@FFPBA. Specifically, 100 mg of SiO$_2$@APTES@FFPBA were dispersed into 20 mL phosphate buffer solution (pH 7.0) containing 20 mg Lin, and the obtained suspension was shaken at 25°C for 1 h. The obtained Lin-immobilized SiO$_2$@APTES@FFPBA were collected and washed with 50 mM phosphate buffer solution (pH 7.0). Then, 80 mg Lin-immobilized SiO$_2$@APTES@FFPBA were dispersed into 10 mL 2-anilinoethanol solution (100 mM in pH 7.0 PBS) and shaken at 25°C for 5 min. Subsequently, 10 mL APS solution of 50 mM was added into the above-obtained suspension. The mixture was rapidly sealed and shaken at 25°C for 30 min. The imprinted polymer layer was formed by the self-polymerization of 2-anilinoethanol. Finally, the Lin templates were removed using 100 mM acetic acid and then washed with water and ethanol. The same process was followed for the preparation of non-imprinted SiO$_2$@APTES@FFPBA, except it did not involve Lin templates.

2.6. Optimization of imprinting conditions

As key imprinting conditions, the concentration of 2-anilinoethanol and polymerization time were investigated by measuring the imprinting effect. The Lin solution of 1 mg/mL in 50 mM phosphate (pH 7.0) was applied as a template solution. An equivalent Lin-imprinted SiO$_2$@APTES@FFPBA was added to each centrifuge tube. Then, 500 μL of Lin template solution was added to a centrifuge tube with Lin-imprinted SiO$_2$@APTES@FFPBA and shaken for 1 h at 25°C. After the Lin-immobilized SiO$_2$@APTES@FFPBA was washed with phosphate buffer of pH 7.0 two to three times, an equivalent 10 mL of 2-anilinoethanol and APS solutions at different concentrations was added in sequence to obtain the concentration of

2-anilinoethanol at 20, 40, 60, 80, and 100 mM. Additionally, the process of polymerization was carried out for a duration of 5–60 min.

The imprinting factor (IF) was calculated by the ratio of Q_{MIPs} to Q_{NIPs}, which was used to evaluate the imprinting effect of Lin-immobilized SiO$_2$@APTES@FFPBA toward Lin. Q_{MIPs} and Q_{NIPs} (mg/g) represent the adsorption capacities of Lin-immobilized SiO$_2$@APTES@FFPBA and non-imprinted SiO$_2$@APTES@FFPBA for Lin.

2.7. Specificity of Lin-imprinted SiO$_2$@ APTES@FFPBA

The specificity of the Lin-immobilized SiO$_2$@APTES@FFPBA for Lin was evaluated using nine samples, including Lin, Dop, Rut, Que., Bai, VB12, Gen, Des, and Kae. First, an equivalent amount of Lin-imprinted SiO$_2$@APTES@FFPBA was added to each centrifugal tube of 1.5 mL. Each sample solution (1 mg/mL) of 500 μL was added to each centrifuge tube and shaken at 25°C for 1 h. After being washed with phosphate buffer three times, the Lin-immobilized SiO$_2$@APTES@FFPBA were eluted using 100 μL of acetic acid solution (pH 2.7) for 2 h. The eluent was measured with UV absorbance at maximum absorption wavelength. The measurement was repeated three times.

2.8. Determination of the pK_a value of FFPBA

The pK_a value of FFPBA was measured according to the previously reported method. UV absorption changes were measured by the titration of 0.1 mM solution of FFPBA in 100 mM phosphate buffer with 1 M sodium hydroxide. The wavelength of the spectrophotometer was set at 268 nm, and a pH meter was fixed in the solution to continuously record the pH of the solution.

2.9. Binding isotherm and Scatchard analysis

The dissociation constant (K_d) and maximum binding capacity (Q_{max}) were determined according to a previously reported method (Li et al., 2015). An equivalent quantity of Lin-immobilized SiO$_2$@ APTES@FFPBA (3 mg each) was mixed with 500 μL of Lin solutions at different concentrations (0.01, 0.02, 0.03, 0.04, 0.05, 0.06, 0.08, 0.10, and 0.12 mg/mL) in centrifuge tubes. Then, the obtained mixture solutions were shaken on a rotator for 1 h at room temperature. The Lin-imprinted SiO$_2$@APTES@FFPBA were collected, rinsed, and eluted with PBS (pH 7.0) and acetic acid solution, respectively. The obtained eluates were used to measure the Lin in the eluates. The K_d and Q_{max} were calculated based on the following Scatchard equation (Li et al., 2015):

$$\frac{Q_e}{C_s} = \frac{Q_{max}}{K_d} - \frac{Q_e}{K_d}$$

Q_e and C_s are the binding capacity and the free concentration of the Lin-imprinted SiO$_2$@APTES@FFPBA for Lin at equilibrium,

respectively. K_d and Qmax can be calculated from the slope and the intercept of the plots of Qe/Cs versus Qe.

2.10. Analysis of Lin in real milk and chicken samples

70 mL of milk was placed in a 100 mL centrifugal tube and shaken with ultrasound for 10 min to achieve a uniform milk sample (Li and Bie, 2017). To determine Lin in milk, 30 mg of Lin-imprinted SiO$_2$@APTES@FFPBA was added to 15 mL of the milk sample and shaken for 10 min at room temperature. The Lin-imprinted SiO$_2$@APTES@FFPBA, which absorbed the Lin, was eluted with acetic acid, and the eluent was collected and measured. To evaluate the recoveries of Lin in the milk sample, different amounts of Lin were mixed into milk to obtain milk solutions containing Lin at different concentrations (0.05, 0.15, and 0.30 μg/g). Then, an equivalent quantity of Lin-imprinted SiO$_2$@APTES@FFPBA was placed in the above-prepared 15 mL milk solution. After washing, Lin-imprinted SiO$_2$@APTES@FFPBA were eluted with 2 mL acetic acid solution (pH 2.7) each time for three times, and 6 mL of eluent was collected. The feasibility of pretreatment of Lin in milk by Lin-imprinted SiO$_2$@APTES@FFPBA was analyzed by HPLC-UV.

Chicken samples (20 g) were added to 80 mL acetonitrile and extracted by ultrasonics for 40 min (Li et al., 2017). Then, the extracted solutions were transferred into a 100 mL flask for evaporation and drying on a rotary evaporator. The final residue was dissolved in 20 mL PBS (100 mM in pH 7.0) to form chicken sample solutions containing Lin. Then, 20 mg of Lin-imprinted SiO$_2$@APTES@FFPBA was added to 5 mL of the chicken sample solutions and shaken for 10 min at room temperature. The Lin-imprinted SiO$_2$@APTES@FFPBA, which absorbed the Lin, was eluted with acetic acid, and the eluent was collected and measured by absorbance. To evaluate the recoveries of Lin in chicken samples, equivalent amounts of Lin-imprinted SiO$_2$@APTES@FFPBA were placed in the chicken sample solutions containing Lin at different concentrations (0.10, 0.20, and 0.40 μg/g). Lin-imprinted SiO$_2$@APTES@FFPBA after adsorption were collected and washed with pH 7.0 PBS. Next, Lin-imprinted SiO$_2$@APTES@FFPBA were eluted with 2 mL acetic acid solution (pH 2.7) each time for three times, and 6 mL of eluent was collected and analyzed by HPLC-UV.

3. Results and discussion

3.1. Characterization of Lin-imprinted SiO$_2$@APTES@FFPBA

Figure 2A represents the TEM images of Lin-imprinted SiO$_2$@APTES@FFPBA. It can be observed clearly that Lin-imprinted SiO$_2$@APTES@FFPBA exhibits approximately spherical morphologies and relatively narrow size distributions with a diameter of about 100 nm. This result indicated that the Lin-imprinted SiO$_2$@APTES@FFPBA had satisfactory dispersibility, which is highly advantageous for the selective recognition of Lin.

To verify the successful preparation of Lin-imprinted SiO$_2$@APTES@FFPBA, X-ray photoelectron survey spectrometry (XPS) of bare SiO$_2$ and Lin-imprinted SiO$_2$@APTES@FFPBA was investigated.

As shown in Figure 2B, the XPS spectrum exhibited an O 1 s peak at 531 eV and a Si 2p peak at 105 eV in bare SiO$_2$. While the XPS spectrum exhibited a C 1 s peak at 286 eV, O 1 s peak at 531 eV, Si 2p peak at 105 eV, N 1 s peak at 399 eV, and B 1 s peak at 191 eV in Lin-imprinted SiO$_2$@APTES@FFPBA. The peak at a binding energy of 191 eV could be assigned to B atoms in the form of Lin-imprinted SiO$_2$@APTES@FFPBA, which proved successful preparation of Lin-imprinted SiO$_2$@APTES@FFPBA. In addition, the crystalline nature of bare SiO$_2$ and Lin-imprinted SiO$_2$@APTES@FFPBA could be confirmed by XRD analysis. As depicted in Figure 2C, the relatively discernible strong diffraction peaks corresponding to SiO$_2$ (2θ = 24.2°) were observed in the curves of two samples, which highly corresponded to the crystalline planes of cubic spinel nanostructure of the silica nanoparticles. This result indicated that the structure of the carrier SiO$_2$ was not changed during the coating process of the imprinted layer.

3.2. Selectivity of SiO$_2$@FFPBA

The post-modification of SiO$_2$ with boronic acid is a key for boronate affinity-based template-immobilized surface imprinting. The post-modification of boronic acids can be confirmed by investigating the selectivity of the FFPBA-functionalized SiO$_2$ for cis-diols. A and G were tested as cis-diol-containing compounds, while DA and Gm were tested as non-cis-diol analogs. As seen in Figure 3, the boronic acid-modified SiO$_2$ (SiO$_2$@FFPBA) exhibited a higher binding amount for A or G than DA or Gm under neutral pH conditions (pH 7.0). Obviously, this result indicated that the SiO$_2$@FFPBA provided excellent selectivity. Because Lin contains one cis-diol, the SiO$_2$@FFPBA exhibited a relatively high binding capacity for Lin. Clearly, the boronic acid-functionalized SiO$_2$ exhibited selective binding to cis-diol-containing compounds. These results also confirmed the successful immobilization of boronic acid FFPBA onto the SiO$_2$.

3.3. Investigation of imprinting conditions

For the boronate affinity-based template-immobilized surface imprinting, the thickness of the imprinted coating on the surface of the SiO$_2$@FFPBA substrate is key for the binding properties of the imprinted materials. Generally, the thickness of the imprinted coating must be calibrated to a smaller size than the template. As we know, the thickness of the imprinted coating is closely related to the concentration of 2-anilinoethanol and polymerization time, and the influence of these two factors on the imprinting effect was systematically evaluated by IF. The thickness of the imprinting coating on SiO$_2$ is in direct proportion to the concentration of 2-anilinoethanol. The most appropriate 2-anilinoethanol concentration could be evaluated by the binding capacity of MIP and NIP prepared at different concentrations. As observed from Figure 4A, the most appropriate 2-anilinoethanol concentration was 60 mM, with an IF value reaching 7.11. In addition, the influence of polymerization time on the imprinting effect was also investigated. It can be observed from Figure 4B that the binding capacity of MIP for Lin gradually increased with time from 10 to 30 min, while the NIP gradually decreased. However, when the polymerization time was more than 30 min, the binding capacity of MIP for Lin decreased, and NIP remained nearly
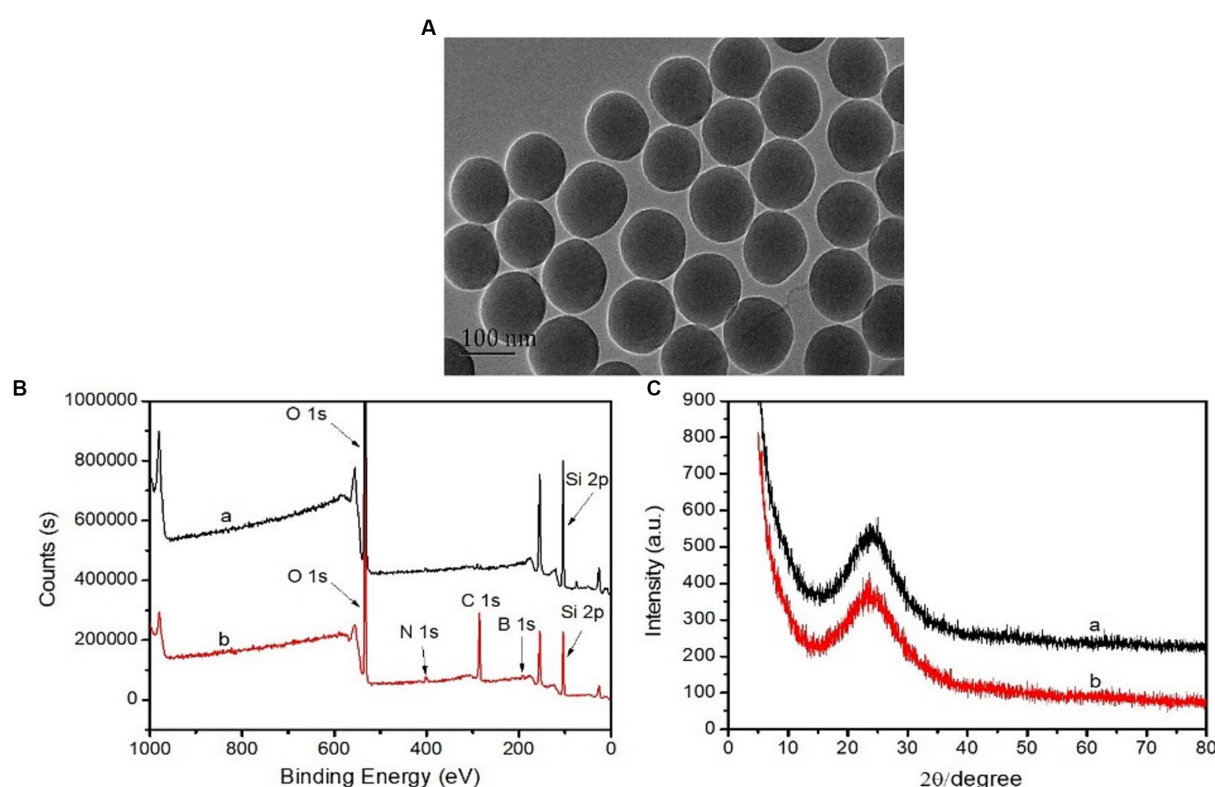
FIGURE 2
TEM images of Lin-imprinted SiO$_2$@APTES@FFPBA (A), XPS spectra (B), and XRD spectra (C) of bare SiO$_2$ (A) and Lin-imprinted SiO$_2$@APTES@FFPBA (B).
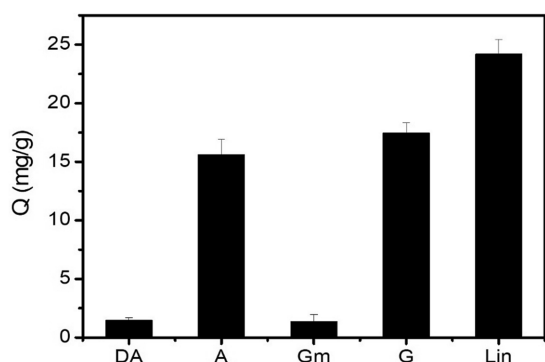
FIGURE 3
The binding amount of different analytes captured by boronic-acid modified SiO$_2$ (SiO$_2$@FFPBA). Binding buffer: 50 mM sodium phosphate buffer (pH 7.0); elution solution: 100 mM HAc (pH 2.7); samples: A, DA, Gm, G, and Lin dissolved in binding buffer (1 mg/mL).

a simple and effective method with the preferred optimized conditions reported here and only tune the polymerization time. If they do not work well, a *de novo* optimization should be carried out.

3.4. Specificity of Lin-imprinted SiO$_2$@ APTES@FFPBA

To evaluate the specificity of Lin-imprinted SiO$_2$@APTES@ FFPBA for Lin, several compounds, including Dop, Rut, Que., Bai, VB12, Gen, Des, and Kae, were selected as competitive compounds. As depicted in Figure 5, compared to the competitive compounds, Lin-imprinted SiO$_2$@APTES@FFPBA exhibited a higher binding capacity for Lin. In other words, Lin-imprinted SiO$_2$@APTES@FFPBA provided a higher affinity for Lin. Although Dop, Rut, Bai, and Que. contain cis-diols, Lin-imprinted SiO$_2$@APTES@FFPBA exhibited a relatively low binding capacity for these compounds. Therefore, the obtained Lin-imprinted SiO$_2$@APTES@FFPBA possessed excellent specificity toward Lin. This result implied that the boronate affinity-template immobilized surface imprinting strategy gained great success due to the thickness-controllable imprinting coating generated by the in-water self-polymerization of 2-anilinoethanol. Comparatively, the non-imprinted SiO$_2$@APTES@FFPBA (NIP) only exhibited a very slight affinity toward Lin and other competitive compounds, indicating that the imprinting coating contained only limited non-specific binding sites.
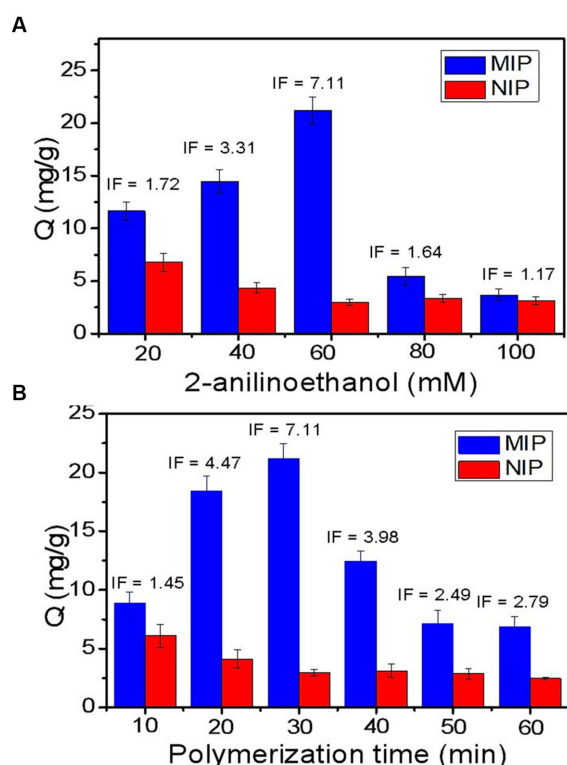
constant over time. Clearly, the changing trends of the IF were in good accordance with that of the binding amount of MIP. Thus, the optimal imprinting conditions for Lin was the self-polymerization of 60 mM 2-anilinoethanol for 30 min, which provided the best IF of 7.11. The high IF can be attributed to the fact that there were no boronic acid moieties outside of the imprinted cavities in the current imprinting method. For other antibiotic templates, the good choice is to employ
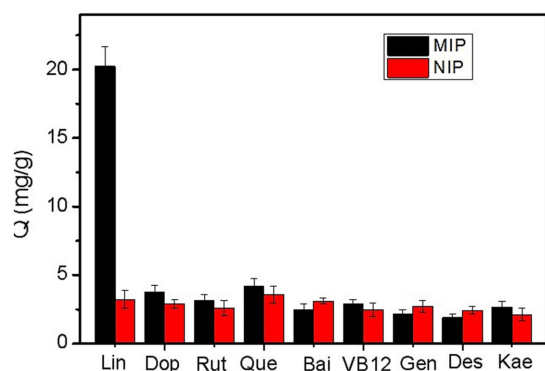
3.5. Binding pH

The binding pH is an important binding property that is positively related to the binding affinity of boronic acids toward cis-diols. The binding affinity and binding pH are determined by the structures of the boronic acid ligands and supporting materials (Lin-imprinted SiO₂@APTES@FFPBA). As shown in Figure 6A, the pK_a value of

FFPBA was measured to be approximately 5.8 due to the presence of electron-withdrawing groups in FFPBA. Clearly, these specific boronic acid ligands could work under low pH conditions of 6.0 (Figure 6B). In addition, the imprinted cavities in the Lin-imprinted SiO₂@APTES@FFPBA could lead to higher binding affinity, thereby providing lower binding pH. To confirm this, the effect of pH on the binding capacity of Lin-imprinted SiO₂@APTES@FFPBA and non-imprinted SiO₂@APTES@FFPBA was investigated. As depicted in Figure 6B, Lin-imprinted SiO₂@APTES@FFPBA exhibited a lower binding pH value (pH 5.0) as compared with SiO₂@APTES@FFPBA (pH 6.0), while non-imprinted MNPs provided very limited binding capacity for Lin. The binding pH shift was due to the imprinted cavities in the structure of Lin-imprinted SiO₂@APTES@FFPBA. Such a pH shift is beneficial because a lower binding pH value generally results from increased affinity toward cis-diol compounds. These results indicated that Lin-imprinted SiO₂@APTES@FFPBA can enlarge the range of pH when directly applied to real samples without requiring pH adjustment.

3.6. Binding equilibrium

In order to evaluate the binding equilibrium time of Lin-imprinted SiO₂@APTES@FFPBA toward Lin, the effect of the response time on binding capacity (Q) was investigated (Figure 7). As seen in Figure 7, Lin-imprinted SiO₂@APTES@FFPBA had a faster adsorption rate than non-imprinted MNPs within the first 6 min. When the response time exceeded 6 min, the adsorption rate quickly slowed down, and the binding reaction reached equilibrium at 6 min. This result implied that most of the binding sites had been occupied by Lin in such a situation. Clearly, such an equilibrium time of Lin-imprinted SiO₂@APTES@FFPBA for Lin was lower than that of other imprinted polymers (8–90 min) (Gu et al., 2010; Li et al., 2012, 2017, 2018a; He et al., 2014; Hao et al., 2016). This result indicated that the Lin-imprinted SiO₂@APTES@FFPBA for Lin showed good binding kinetics.

3.7. Determination of K_d and Q_{max}

As we know, the binding affinity of Lin-imprinted SiO₂@APTES@FFPBA can determine how low concentrations of Lin can be extracted by Lin-imprinted SiO₂@APTES@FFPBA. Therefore, the binding isotherm of the Lin-imprinted SiO₂@APTES@FFPBA toward Lin was investigated to evaluate its binding affinity. As shown in Figure 8A, the Lin-imprinted SiO₂@APTES@FFPBA exhibited much higher binding capacity toward Lin as compared with the non-imprinted SiO₂@APTES@FFPBA. According to the binding isotherm, a Scatchard plot was drawn (Figure 8B), which could provide Q_{max} and K_d values of Lin-imprinted SiO₂@APTES@FFPBA. These were (19.45 ± 1.44) mg/g and (3.65 ± 0.38) × 10⁻⁵ M, respectively. Clearly, Lin-imprinted SiO₂ exhibited much higher binding capacity than other imprinted nanomaterials (Gu et al., 2010; Li et al., 2018a,b,c,d). Such a high-binding capacity could result from the combination of SiO₂ with easy post-modification and FFPBA with low pK_a. Conversely, it also benefited from the high imprinting efficiency. The strong binding strength of the prepared Lin-imprinted SiO₂@APTES@FFPBA for Lin favors the extraction of Lin of trace concentrations.
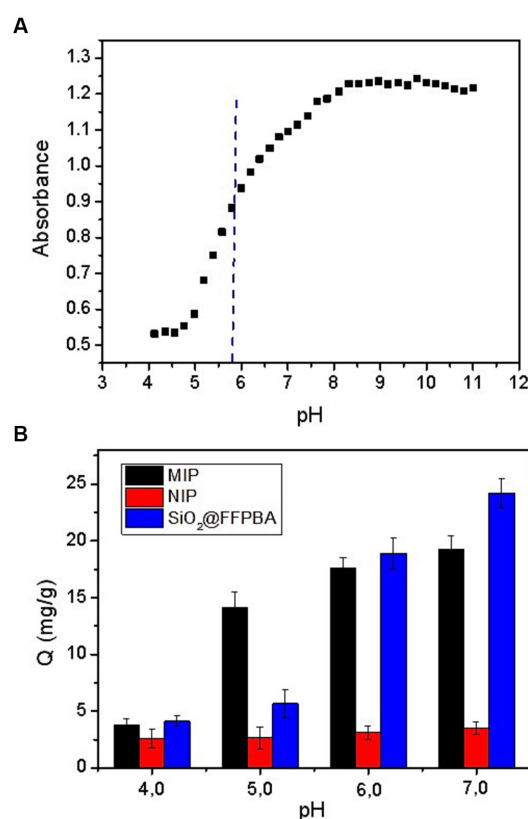
FIGURE 6
(A) The pH-dependence of the absorbance at 268 nm of FFPBA and **(B)** Target binding capability Q of Lin-imprinted SiO_2@APTES@FFPBA (MIP), non-imprinted SiO_2@APTES@FFPBA (NIP), and SiO_2@FFPBA at different pH values. Sample: 1 mg/mL Lin dissolved in 50 mM phosphate buffer (pH 4.0, 5.0, 6.0, and 7.0).

FIGURE 8
(A) Binding isotherms for binding of the Lin-imprinted SiO_2@APTES@FFPBA and non-imprinted SiO_2@APTES@FFPBA to Lin, and **(B)** Scatchard plots for the binding of the Lin-imprinted SiO_2@APTES@FFPBA to Lin.

FIGURE 7
Binding equilibrium of Lin-imprinted SiO_2@APTES@FFPBA and non-imprinted SiO_2@APTES@FFPBA. Sample: 1.0 mg/mL of Lin containing 50 mM phosphate, pH 7.0.

3.8. Reproducibility and reusability

The reproducibility of the obtained Lin-imprinted SiO_2@APTES@FFPBA was evaluated by using six batches of Lin-imprinted SiO_2@APTES@FFPBA prepared on different days, and the measurements

replicated three times in parallel. It can be observed from Figure 9A that each individually prepared Lin-imprinted SiO_2@APTES@FFPBA exhibited similar binding capacities for Lin (21.30, 18.89, 17.43, 18.16, 17.85, and 17.46) mg/g, respectively. These results indicated that the reproducibility of Lin-imprinted SiO_2@APTES@FFPBA was satisfactory because the boronate affinity-based template immobilized surface imprinting was beneficial.

One of the main advantages of MIPs over native antibodies is their ability to be reused. Thus, the reusability of Lin-imprinted SiO_2@APTES@FFPBA was investigated, and the adsorption–desorption cycle was repeated ten times using the same batch of Lin-imprinted SiO_2@APTES@FFPBA (Figure 9B). Even after six adsorption–desorption cycles, the adsorption capacity of Lin-imprinted SiO_2@APTES@FFPBA = changed very little. Clearly, Lin-imprinted SiO_2@APTES@FFPBA could still be reused after seven adsorption–desorption cycles. Thus, Lin-imprinted SiO_2@APTES@FFPBA possesses high chemical stability.

3.9. Determination of Lin in food samples

In order to investigate the performance of the prepared Lin-imprinted SiO_2@APTES@FFPBA in food samples, the selective separation and determination of Lin from milk and chicken samples by Lin-imprinted SiO_2@APTES@FFPBA was carried out. The obtained results are given in Table 1. Clearly, the content of Lin in chicken was evaluated to be 0.025 μg/g, and no Lin was found in the

FIGURE 9
Batch-to-batch reproducibility **(A)** and reusability **(B)** of Lin-imprinted SiO$_2$@APTES@FFPBA. Sample: 1 mg/mL of Lin containing 50 mM phosphate, pH 7.0.
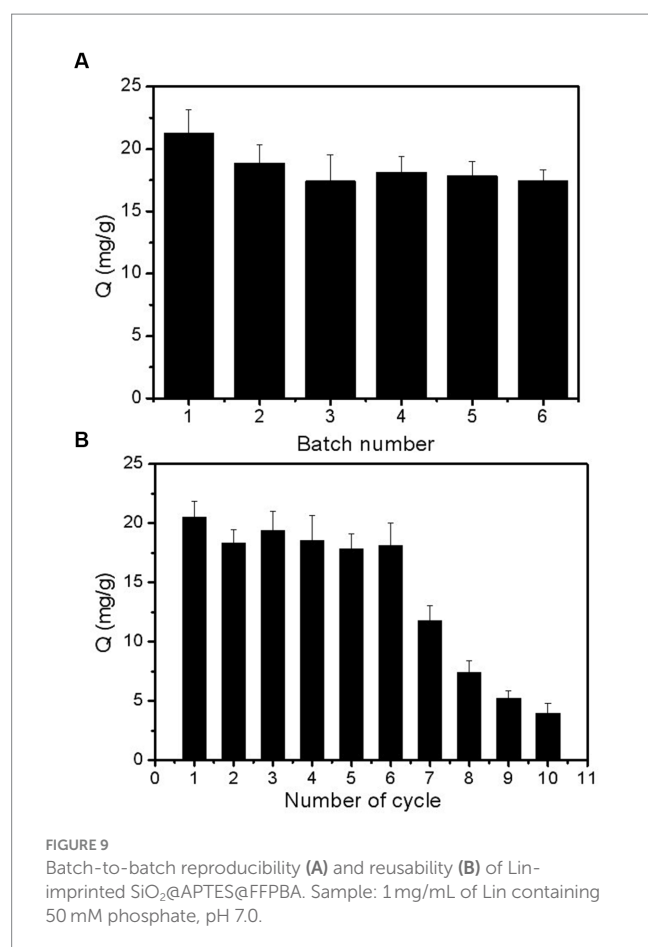
TABLE 1 Results of sample assay and recoveries for the determination of Lin ($n = 3$).

Samples	Spiked levels (μg/g)	Found (μg/g)	Recoveries (%)	RSD (%)
Milk	0.00	Not detected	--	--
	0.05	0.05	100.0	2.5
	0.15	0.14	93.3	4.6
	0.30	0.31	103.3	5.3
Chicken	0.00	0.03	--	5.5
	0.10	0.12	90.0	3.0
	0.20	0.23	100.0	3.7
	0.40	0.41	95.0	4.5

milk solution. In addition, to investigate the accuracy of the method by selective separation and determination of Lin in real food samples, the evaluation of Lin in milk and chicken was performed. The recoveries were investigated with three standard amounts of Lin added in milk and chicken solutions, and the spiked concentration was fixed at 0.05, 0.15, 0.30 μg/mL, and 0.10, 0.20, 0.40 μg/mL, respectively. By extraction and determination of Lin, the recoveries for milk and chicken solutions were shown in Table 1. The recoveries of Lin for milk and chicken solution were evaluated to be 93.3–103.3% and

90.0–100.0%, respectively. In addition, the RSD for milk and chicken solution ranged from 2.5–5.3% and 3.0–4.5%. The results indicated that the proposed method is accurate, sensitive, and selective for the determination of Lin in animal-derived food samples.

4. Conclusion

In this study, we used boronate affinity-based template-immobilized surface imprinting to prepare the boronate affinity-based Lin-imprinted SiO$_2$@APTES@FFPBA for the first time. The pKa value of FFPBA was first investigated. The use of boronic acid FFPBA in the MIPs provided several highly attractive features, including high specificity, high binding affinity, and low binding pH. Clearly, the prepared Lin-imprinted SiO$_2$@APTES@FFPBA are feasible for the recognition of target Lin with low concentrations in real food samples. We foresee rapid development and promising applications of this approach in the future.

Data availability statement

The raw data supporting the conclusions of this article will be made available by the authors, without undue reservation.

Author contributions

YZ: Data curation, Formal analysis, Investigation, Methodology, Writing – original draft. YD: Data curation, Methodology, Writing – original draft. YM: Conceptualization, Formal analysis, Project administration, Writing – review & editing. ZZ: Formal analysis, Validation, Writing – original draft. YW: Formal analysis, Validation, Writing – original draft. DL: Formal analysis, Project administration, Resources, Supervision, Validation, Writing – review & editing. SW: Formal analysis, Project administration, Resources, Supervision, Validation, Writing – review & editing.

Funding

Conflict of interest

The authors declare that the research was conducted in the absence of any commercial or financial relationships that could be construed as a potential conflict of interest.

Publisher's note

All claims expressed in this article are solely those of the authors and do not necessarily represent those of their affiliated organizations, or those of the publisher, the editors and the reviewers. Any product that may be evaluated in this article, or claim that may be made by its manufacturer, is not guaranteed or endorsed by the publisher.

References

Andrade, L., Kelly, M., Hynds, P., Weatherill, J., Majury, A., and O'Dwyer, J. (2020). Groundwater resources as a global reservoir for antimicrobial-resistant bacteria. *Water Res.* 170:115360. doi: 10.1016/j.watres.2019.115360

Arabi, M., Ghaedi, M., and Ostovan, A. (2016). Development of dummy molecularly imprinted based on functionalized silica nanoparticles for determination of acrylamide in processed food by matrix solid phase dispersion. *Food Chem.* 210, 78–84. doi: 10.1016/j.foodchem.2016.04.080

Bengtsson-Palme, J., and Larsson, D. G. (2016). Concentrations of antibiotics predicted to select for resistant bacteria: proposed limits for environmental regulation. *Environ. Int.* 86, 140–149. doi: 10.1016/j.envint.2015.10.015

Cao, S., Song, S., Liu, L., Kong, N., Kuang, H., and Xu, C. (2015). Comparison of an enzyme-linked immunosorbent assay with an Immunochromatographic assay for detection of Lincomycin in Milk and honey. *Immunol. Investig.* 44, 438–450. doi: 10.3109/08820139.2015.1021354

Dasenaki, M. E., and Thomaidis, N. S. (2015). Multi-residue determination of 115 veterinary drugs and pharmaceutical residues in milk powder, butter, fish tissue and eggs using liquid chromatography-tandem mass spectrometry. *Anal. Chim. Acta* 880, 103–121. doi: 10.1016/j.aca.2015.04.013

Ding, L., Zhao, Y., Li, H., Zhang, Q., Yang, W., Fu, B., et al. (2021). A highly selective ratiometric fluorescent probe for doxycycline based on the sensitization effect of bovine serum albumin. *J. Hazard. Mater.* 416:125759. doi: 10.1016/j.jhazmat.2021.125759

Dong, Z., Lu, J., Wu, Y., Meng, M., Yu, C., Sun, C., et al. (2020). Antifouling molecularly imprinted membranes for pretreatment of milk samples: selective separation and detection of lincomycin. *Food Chem.* 333:127477. doi: 10.1016/j.foodchem.2020.127477

Du, L., Li, G., Gong, W., Zhu, J., Liu, L., Zhu, L., et al. (2021). Establishment and validation of the LC-MS/MS method for the determination of lincomycin in human blood: application to an allergy case in forensic science. *J. Forensic Legal Med.* 77:102094. doi: 10.1016/j.jflm.2020.102094

Du, B., Wen, F., Zhang, Y., Zheng, N., Li, S., Li, F., et al. (2019). Presence of tetracyclines, quinolones, lincomycin and streptomycin in milk. *Food Control* 100, 171–175. doi: 10.1016/j.foodcont.2019.01.005

Fernandes-Cunha, G. M., Gouvea, D. R., de Fulgêncio, G. O., Rezende, C. M., da Silva, G. R., Bretas, J. M., et al. (2015). Development of a method to quantify clindamycin in vitreous humor of rabbits' eyes by UPLC-MS/MS: application to a comparative pharmacokinetic study and in vivo ocular biocompatibility evaluation. *J. Pharm. Biomed. Anal.* 102, 346–352. doi: 10.1016/j.jpba.2014.08.023

Gu, X. H., Xu, R., Yuan, G. L., Lu, H., Gu, B. R., and Xie, H. P. (2010). Preparation of chlorogenic acid surface-imprinted magnetic nanoparticles and their usage in separation of traditional Chinese medicine. *Anal. Chim. Acta* 675, 64–70. doi: 10.1016/j.aca.2010.06.033

Hao, Y., Gao, R., Liu, D., He, G., Tang, Y., and Guo, Z. (2016). A facile and general approach for preparation of glycoprotein-imprinted magnetic nanoparticles with synergistic selectivity. *Talanta* 153, 211–220. doi: 10.1016/j.talanta.2016.03.005

He, H., Fu, G., Wang, Y., Chai, Z., Jiang, Y., and Chen, Z. (2010). Imprinting of protein over silica nanoparticles via surface graft copolymerization using low monomer concentration. *Biosens. Bioelectron.* 26, 760–765. doi: 10.1016/j.bios.2010.06.043

He, H., Xiao, D., He, J., Li, H., He, H., Dai, H., et al. (2014). Preparation of a core-shell magnetic ion-imprinted polymer via a sol-gel process for selective extraction of cu(II) from herbal medicines. *Analyst* 139, 2459–2466. doi: 10.1039/c3an02096g

Khadim, A., Yaseen Jeelani, S. U., Khan, M. N., Kumari, S., Raza, A., Ali, A., et al. (2023). Targeted analysis of veterinary drugs in food samples by developing a high-resolution tandem mass spectral library. *J. Agric. Food Chem.* 71, 12839–12848. doi: 10.1021/acs.jafc.3c03715

Khafi, M., Javadi, A., and Mogaddam, M. R. A. (2023). Combination of three-phase extraction with deep eutectic solvent-based dispersive liquid–liquid microextraction for the extraction of some antibiotics from egg samples prior to HPLC-DAD. *Microchem. J.* 190:108652. doi: 10.1016/j.microc.2023.108652

Koike, H., Kanda, M., Hayashi, H., Matsushima, Y., Nakajima, T., Yoshikawa, S., et al. (2021). Monitoring of residual antibacterial agents in animal and fishery products in Tokyo from 2003 to 2019: application and verification of a screening strategy based on microbiological methods. *Food Addit. Contam. Part B Surveill.* 14, 66–73. doi: 10.1080/19393210.2021.1871973

Li, D., and Bie, Z. (2017). Branched polyethyleneimine-assisted boronic acid-functionalized magnetic nanoparticles for the selective enrichment of trace glycoproteins. *Analyst* 142, 4494–4502. doi: 10.1039/c7an01174a

Li, D., Bie, Z., Wang, F., and Guo, E. (2018a). Efficient synthesis of riboflavin-imprinted magnetic nanoparticles by boronate affinity-based surface imprinting for the selective recognition of riboflavin. *Analyst* 143, 4936–4943. doi: 10.1039/c8an01044g

Li, D., Chen, Y., and Liu, Z. (2015). Boronate affinity materials for separation and molecular recognition: structure, properties and applications. *Chem. Soc. Rev.* 44, 8097–8123. doi: 10.1039/c5cs00013k

Li, S., Liu, C., Yin, G., Zhang, Q., Luo, J., and Wu, N. (2017). Aptamer-molecularly imprinted sensor base on electrogenerated chemiluminescence energy transfer for detection of lincomycin. *Biosens. Bioelectron.* 91, 687–691. doi: 10.1016/j.bios.2017.01.038

Li, P., Pang, J., Xu, S., He, H., Ma, Y., and Liu, Z. (2022). A Glycoform-resolved dual-modal Ratiometric immunoassay improves the diagnostic precision for hepatocellular carcinoma. *Angewandte Chemie* 61:e202113528. doi: 10.1002/anie.202113528

Li, G., Shi, Z., and Li, D. (2020). Efficient synthesis of boronate affinity-based chlorogenic acid-imprinted magnetic nanomaterials for the selective recognition of chlorogenic acid in fruit juices. *New J. Chem.* 44, 11013–11021. doi: 10.1039/d0nj01716g

Li, D., Tang, N., Wang, Y., Zhang, Z., Ding, Y., and Tian, X. (2022). Efficient synthesis of boronate affinity-based catecholamine-imprinted magnetic nanomaterials for trace analysis of catecholamine in human urine. *New J. Chem.* 46, 16618–16626. doi: 10.1039/d2nj02552c

Li, D., Tu, T., and Wu, X. (2018c). Efficient preparation of template immobilization based boronate affinity surface-imprinted silica nanoparticles using poly (4-aminobenzyl alcohol) as an imprinting coating for glycoprotein recognition. *Anal. Methods* 10, 4419–4429. doi: 10.1039/C8AY00632F

Li, D., Tu, T., Yang, M., and Xu, C. (2018b). Efficient preparation of surface imprinted magnetic nanoparticles using poly (2-anilinoethanol) as imprinting coating for the selective recognition of glycoprotein. *Talanta* 184, 316–324. doi: 10.1016/j.talanta.2018.03.012

Li, H., Wang, H., Liu, Y., and Liu, Z. (2012). A benzoboroxole-functionalized monolithic column for the selective enrichment and separation of cis-diol containing biomolecules. *Chem. Commun.* 48, 4115–4117. doi: 10.1039/c2cc30230f

Li, D., Yuan, Q., Yang, W., Yang, M., Li, S., and Tu, T. (2018d). Efficient vitamin B12-imprinted boronate affinity magnetic nanoparticles for the specific capture of vitamin B12. *Anal. Biochem.* 561-562, 18–26. doi: 10.1016/j.ab.2018.09.009

Li, Y., Yue, X., Pan, Z., Liu, Y., Shen, M., Zhai, Y., et al. (2021). Development and validation of an LC-MS/MS method for quantifying nine antimicrobials in human serum and its application to study the exposure of Chinese pregnant women to antimicrobials. *J. Clin. Lab. Anal.* 35:e23658. doi: 10.1002/jcla.23658

Lin, Z., Sun, L., Liu, W., Xia, Z., Yang, H., and Chen, G. (2014). Synthesis of boronic acid-functionalized molecularly imprinted silica nanoparticles for glycoprotein recognition and enrichment. *J. Mater. Chem. B* 2, 637–643. doi: 10.1039/c3tb21520b

Lin, Z., Xia, Z., Zheng, J., Zheng, D., Zhang, L., Yang, H., et al. (2012). Synthesis of uniformly sized molecularly imprinted polymer-coated silica nanoparticles for selective recognition and enrichment of lysozyme. *J. Mater. Chem.* 22, 17914–17922. doi: 10.1039/c2jm32734a

Liu, L., Zhang, Y., Zhang, L., Yan, G., Yao, J., Yang, P., et al. (2012). Highly specific revelation of rat serum glycopeptidome by boronic acid-functionalized mesoporous silica. *Anal. Chim. Acta* 753, 64–72. doi: 10.1016/j.aca.2012.10.002

Maddaleno, A., Pokrant, E., Yanten, F., San Martin, B., and Cornejo, J. (2019). Implementation and validation of an analytical method for Lincomycin determination in feathers and edible tissues of broiler chickens by liquid chromatography tandem mass spectrometry. *J. Anal. Methods Chem.* 2019, 4569707–4569708. doi: 10.1155/2019/4569707

Mehrtens, A., Licha, T., and Burke, V. (2021). Occurrence, effects and behaviour of the antibiotic lincomycin in the agricultural and aquatic environment – A review. *Sci. Total Environ.* 778:146306. doi: 10.1016/j.scitotenv.2021.146306

Qu, Y., Liu, J., Yang, K., Liang, Z., Zhang, L., and Zhang, Y. (2012). Boronic acid functionalized core-shell polymer nanoparticles prepared by distillation precipitation polymerization for glycopeptide enrichment. *Chemistry* 18, 9056–9062. doi: 10.1002/chem.201103514

Tao, Y., Chen, D., Yu, G., Yu, H., Pan, Y., Wang, Y., et al. (2011). Simultaneous determination of lincomycin and spectinomycin residues in animal tissues by gas chromatography-nitrogen phosphorus detection and gas chromatography-mass spectrometry with accelerated solvent extraction. *Food Addit. Contam. Part A Chem. Anal. Control Expo. Risk Assess.* 28, 145–154. doi: 10.1080/19440049.2010.538440

Vlatakis, G., Andersson, L. I., Müller, R., and Mosbach, K. (1993). Drug assay using antibody mimics made by molecular imprinting. *Nature* 361, 645–647. doi: 10.1038/361645a0

Zhang, Y., Li, D., Li, Y., Niu, J., and Yuan, M. (2023). Branched polyethylenimine-assisted boronic acid functionalized magnetic nanoparticles for highly efficient capture of lincomycin and clindamycin. *Anal. Methods* 15:2657:2664. doi: 10.1039/d3ay00552f

Zhang, Y., Lu, Y., Zhong, J., Li, W., Wei, Q., and Wang, K. (2019). Molecularly imprinted polymer microspheres prepared via the two-step swelling polymerization for the separation of lincomycin. *J. Appl. Polym. Sci.* 136:47938. doi: 10.1002/app.47938

Zhang, Y., Tian, X., Zhang, Z., Tang, N., Ding, Y., Wang, Y., et al. (2022). Boronate affinity-based template-immobilization surface imprinted quantum dots as fluorescent nanosensors for selective and sensitive detection of myricetin. *Spectrochim. Acta A Mol. Biomol. Spectrosc.* 272:121023. doi: 10.1016/j.saa.2022.121023

Zhou, J., Zhu, K., Xu, F., Wang, W., Jiang, H., Wang, Z., et al. (2014). Development of a microsphere-based fluorescence immunochromatographic assay for monitoring lincomycin in milk, honey, beef, and swine urine. *J. Agric. Food Chem.* 62, 12061–12066. doi: 10.1021/jf5029416

Check for updates

A simple and sensitive fluoroimmunoassay based on the nanobody-alkaline phosphatase fusion protein for the rapid detection of fenitrothion

Zi-Jian Chen[1,2,3], Ai-Jun Huang[1,2,3], Xiu-Xiu Dong[4],
Yi-Feng Zhang[5], Lin Zhu[6], Lin Luo[5], Zhen-Lin Xu[5]* and
Hongwu Wang[1,2,3]*

[1]School of Food & Pharmaceutical Engineering, Zhaoqing University, Zhaoqing, China,
[2]Laboratory of Quality & Safety Risk Assessment for Agro-Products (Zhaoqing), Ministry of
Agriculture and Rural Affairs, Zhaoqing, China, [3]Guangdong Engineering Technology Research
Center of Food & Agricultural Product Safety Analysis and Testing, Zhaoqing, China, [4]Key
Laboratory of Modern Agricultural Equipment and Technology (Jiangsu University), Ministry of
Education, School of Agricultural Engineering, Jiangsu University, Zhenjiang, China, [5]Guangdong
Provincial Key Laboratory of Food Quality and Safety, South China Agricultural University,
Guangzhou, China, [6]Guangzhou Experimental Station, Chinese Academy of Tropical Agricultural
Sciences, Guangzhou, China

Immunoassay is a powerful tool for the rapid detection of small harmful organic molecules. In this study, a simple and sensitive fluoroimmunoassay (FIA) based on a nanobody-alkaline phosphatase fusion protein (VHHjd8-ALP) and blue-emissive carbon dots (bCDs) was developed for the rapid detection of fenitrothion. The bCDs were synthesized using the one-step hydrothermal method. Citric acid and urea were used as carbon and nitrogen sources, respectively. The synthesized bCDs were characterized by fluorescence spectrum, high-resolution transmission electron microscopy, x-ray photoelectron spectroscopy, and Fourier transform infrared spectroscopy. After one step of competitive immunoassay, the VHHjd8-ALP bound to the microplate and catalyzed the substrate p-nitrophenylphosphate (pNPP) into p-nitrophenol (pNP); the latter can quench the blue of bCDs due to an inner-filter effect. After condition optimization, an FIA calibration curve was finally created, which showed an IC_{50} value of 16.25 ng/mL and a limit of detection (LOD) of 0.19 ng/mL. Compared with the pNPP-based one-step conventional indirect competitive enzyme-linked immunoassay (icELISA), the developed FIA showed an 11-fold sensitivity improvement. Furthermore, the analysis period of FIA only takes approximately 55 min, which was obviously faster than that of the conventional icELISA. The recovery test showed recoveries from 81.8 to 119% with fruits and vegetable samples, which verified the practicability and accuracy of the developed FIA.

KEYWORDS

fluoroimmunoassay, fenitrothion, carbon dots, nanobody-alkaline phosphatase fusion protein, rapid detection

Introduction

Pesticide is indispensable for modern agriculture. However, the improper and excessive use of pesticides results in residues in foods and environments, which is a serious problem. Furthermore, consuming foods with high pesticide residue levels over the recommended levels can cause chronic poisoning and even cancer (Yang et al., 2018; Pedroso et al., 2022). Fenitrothion is a highly effective organophosphorus insecticide with a broad spectrum of activity. It is extensively utilized for controlling a wide range of pests and is also employed for the management of flies, mosquitoes, and other disease-carrying vectors, thereby contributing to the prevention of malaria and other public health issues (Gnanguenon et al., 2015; Abdel-Ghany et al., 2016). However, previous studies showed that the fenitrothion was harmful to human beings through the inhibition of the acetylcholinesterase activity (Faria et al., 2022). Moreover, fenitrothion exposure was associated with hepatic injury, renal injury, and reproductive toxicity (Galal et al., 2019; Li et al., 2023). As a consequence, the amount of fenitrothion residues in foods should be strictly monitored.

For the detection of fenitrothion, several methods have been reported in previous studies, including high-performance liquid chromatography (HPLC) (Ulusoy et al., 2020), gas chromatography–mass spectrometry (GC–MS/MS) (Kang et al., 2020), electrochemical sensor (Han et al., 2023), and fluorescent sensor (Delnavaz et al., 2023). However, fenitrothion is detected primarily through instrumental analysis, which is expensive, requires professional operators, and takes a long time. Therefore, it is necessary to develop a rapid, simple, sensitive, and low-cost method for the detection of fenitrothion.

Immunoassay is a powerful detection tool in analytical chemistry and exhibits broad applicability for accurately quantifying analytes present at extremely low concentrations (Wang et al., 2022), which shows advantages of sensitivity, rapid, high specificity, low cost, and easy-to-use. Conventional immunoassay depends on the output of the colorimetric signal, which limits the sensitivity for analysis. As an alternative, fluoroimmunoassay (FIA) is a promising and powerful detection tool owing to its advantages such as high sensitivity, non-destructive characteristics, real-time, fast response, and low cost (Yi et al., 2020). For the development of FIA, the fluorescent probe is the key element for signal amplification. As a novel fluorescent nanomaterial, carbon dots (CDs) show excellent features such as wide sources, cost-effectiveness, low toxicity, water-solubility, and easy synthesis (Luo et al., 2013; Lee et al., 2016; Zhu et al., 2019; Lin et al., 2021), which have garnered growing interest and are considered excellent candidates for the development of FIA.

In this study, an anti-fenitrothion nanobody-alkaline phosphatase fusion protein (VHHjd8-ALP) was employed to develop CDs-based FIA. As shown in Scheme 1, in the absence of fenitrothion, the VHHjd8-ALP binds on the microplate after a one-step competitive immunoassay. The substrate p-nitrophenylphosphate (pNPP) was catalyzed by VHHjd8-ALP into p-nitrophenol (pNP). Afterward, the blue-emissive CDs (bCDs) were added. In the presence of pNP, the fluorescent intensity of bCDs can be quenched through an inner-filter effect. The implementation of this sensitivity enhancement strategy does not require additional steps, making it a convenient, time-saving, and effective method for fenitrothion analysis. Moreover, the FIA being developed is undergoing meticulous optimization and will

be thoroughly validated using real samples to ensure its accuracy and practicality.

Materials and methods

Materials and reagents

Fenitrothion standard was purchased from Tanmo Technology Ltd. (Beijing, China). VHHjd8-ALP and coating antigen (Hapten-1-BSA) were prepared and stored in our laboratory (Chen et al., 2021; Liu et al., 2022). Tris(hydroxymethyl)aminomethane (Tris), Tween-20, citric acid, and sodium hydrogen citrate were purchased from Aladdin Chemical Technology Co., Ltd. (Shanghai, China). Urea was supplied by Heowns Biochemical Technology Co., Ltd. (Tianjin, China). The pNPP and dialysis bag (800 Da) were purchased from Yuanye Bio-Technology Co., Ltd. (Shanghai, China). For pretreatment purification, the primary secondary amine (PSA) was obtained from Biocomma Co., Ltd. (Shenzhen, China). The 96 microwell opaque plate and the ELISA plate were purchased from Jingan Biological Co., Ltd. (Shanghai, China).

Buffers

The following buffers and solutions were used in this study: Tris buffer (10 mM, pH 7.4); washing buffer (Tris buffer with 0.05% Tween-20); phosphate-buffered saline (PBS, 10 mM, pH 7.4); PBS with 0.05% Tween-20 (PBST); carbonate buffer (50 mM, pH 9.6); blocking buffer (5% skimmed milk in PBS); and ALP buffer (Tris, 5 mM, pH 9.6, with 2 mM $MgCl_2$).

Instruments

The morphology characterization of bCDs was performed in the Gene Pulser Xcell electroporator (Bio-Rad, Hercules, CA, United States). The Multiskan MK3 microplate reader was employed for the optical density (OD) value measurement (Thermo-Fisher, Waltham, MA, United States). SpectaMax i3x reader was used to measure fluorescence intensity (Molecular Devices, Sunnyvale, United States). Characterization of bCDs was performed using an FEI Talos F200X microscope (Thermo-Fisher, Hillsboro, OR, United States), a Nicolet IS10 FT-IR Spectrometer (Thermo-Fisher, Waltham, MA, United States), an FLS1000/FSS FL spectrometer (Edinburgh Instruments Ltd., Livingston, UK), and an ESCALAB 250XI electron spectrometer (Thermo Scientific, Waltham, MA, United States).

Preparation of rCDs

The synthesis of bCDs was referred to by Qu et al. (2016) using the hydrothermal method. A mixture of citric acid (1 g) and urea (2 g) was dissolved in N,N-dimethylformamide (10 mL) and then heated for 6 h at 160°C in a Teflon-lined autoclave. The obtained dark product was dialyzed by an 800 Da dialysis bag with deionized water to remove unreacted substances. The bCDs were finally obtained after dialysis and stored at 4°C until used.

Development of FIA

The Hapten-1-BSA was diluted in carbonate buffer (1 μg/mL) and added to an ELISA plate (100 μL/well) kept overnight at 37°C. After coating, the ELISA plate was washed twice with PBST. To block the uncoated sites, a blocking buffer was added (120 μL/well) and incubated for 3 h at 37°C and dried at 37°C for 1 h. A series of fenitrothion solutions (in Tris buffer) were added to the microplate (50 μL/well), followed by the addition of VHHjd8-ALP (in Tris buffer, 50 μL/well). After a 30-min incubation period, the wells were washed five times with a washing buffer. Subsequently, the pNPP substrate (in ALP buffer, 100 μL/well) was added and incubated at 37°C for 30 min, following which 50 μL of bCDs was introduced, and the mixture was then transferred to an opaque plate (100 μL/well). The fluorescence signal of bCDs was measured using an excitation wavelength of 370 nm and an emission wavelength of 470 nm.

Determination of samples

The GC–MS/MS was employed to verify the fenitrothion-free samples (tangerines, lettuces, and Chinese cabbages). The details are described in Supporting Information.

Results and discussion

Identification of bCDs

In a previous study, bifunctional VHHjd8-ALP was prepared for the one-step ELISA of fenitrothion, which was faster than the conventional icELISA. As a typical substrate, pNPP was widely employed for the response of ALP (Sun et al., 2018). However, the sensitivity of pNPP-based ELISA is limited by the strategy of OD value measurement. To overcome this shortcoming, this study synthesized and employed bCDs as a high-response signal probe for sensitivity improvement. Transmission electron microscopy (TEM) was used to characterize the obtained bCDs and revealed well-dispersed nanoparticles, exhibiting a spherical morphology with an interplanar spacing of 0.22 nm (Figure 1A). The size distribution histogram showed the average size of 2.7 nm for bCDs (Figure 1B). The small size of bCDs ensures their effective dispersion in an aqueous solution, enabling their utilization as fluorescent probes for uniform signal response. The optical performance of bCDs (including absorbance spectrum and fluorescence spectrum) was further characterized. As shown in Figure 1C, the UV absorption spectrum of bCDs showed several absorption peaks in the wavelength range of 300–750 nm, while the highest intensity was
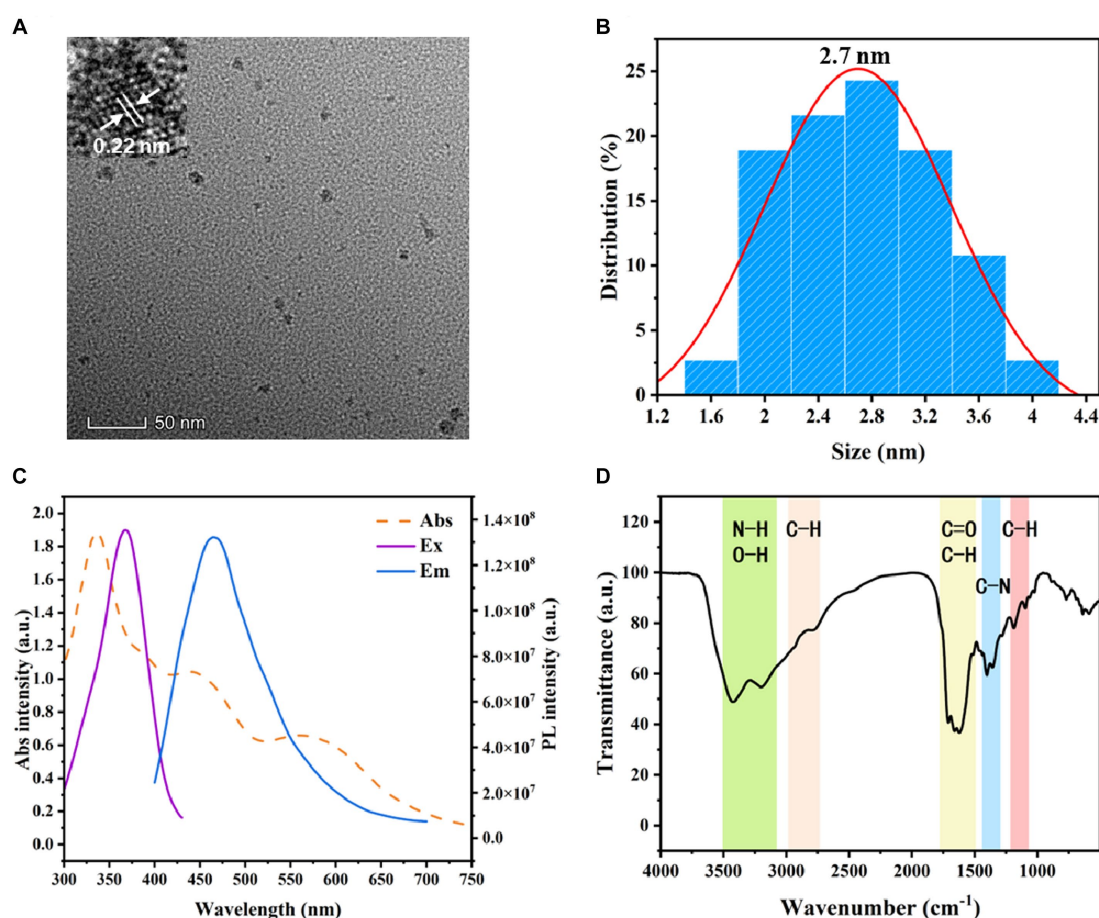
FIGURE 1
(A) TEM image of bCDs. (B) Particle size distribution of bCDs. (C) Absorbance spectrum, excitation, and emission spectrum of bCDs. (D) FT-IR spectrum of bCDs.
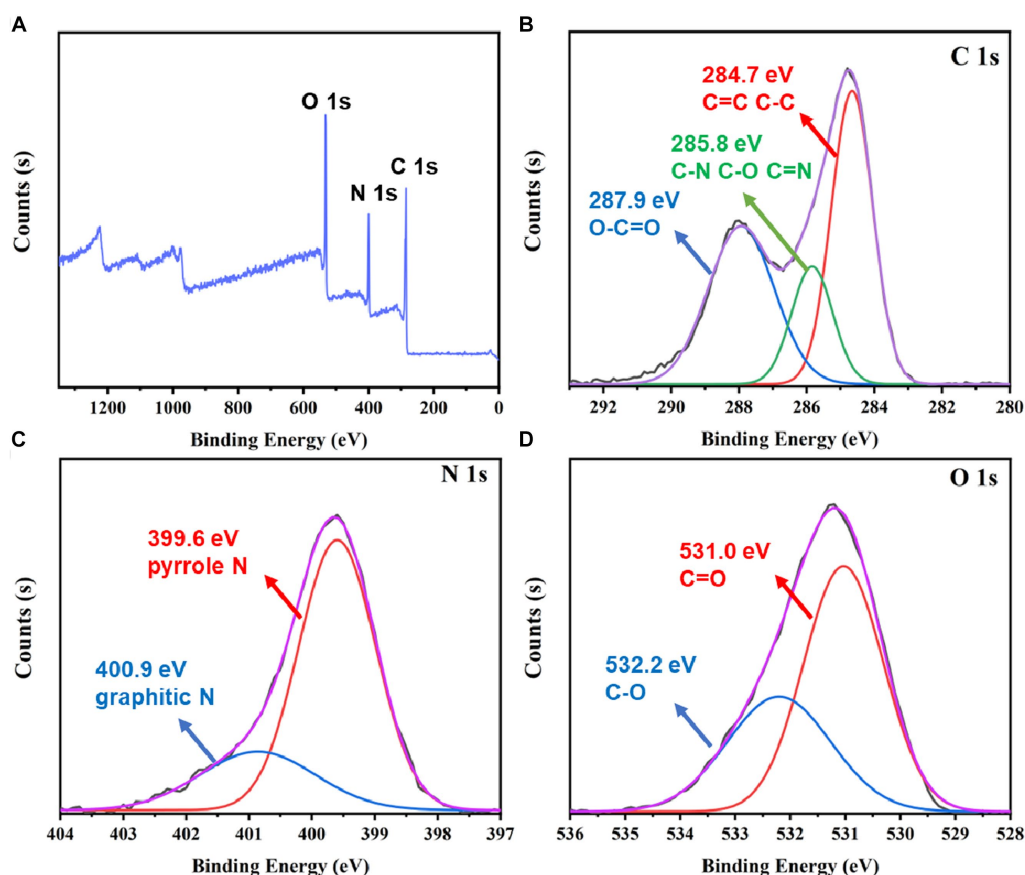
FIGURE 2
(A) Survey spectrum of XPS. (B–D) XPS spectrum of C 1 s, N 1 s, and O 1 s.

found at 338 nm. Moreover, the excitation spectrum (Ex) showed the strong peak at 370 nm, suggesting that the compound absorbs light most efficiently at this wavelength. Based on the optimized Ex, the emission spectrum was scanned and exhibited the peak centered at 470 nm.

Fourier transform infrared spectroscopy (FT-IR) was employed to analyze the functional groups of bCDs. As depicted in Figure 1D, the existence of wide bands within the range of 3,100–3,500 cm^{-1} confirmed the presence of stretching vibrations associated with O-H or N-H. This observation indicates the presence of -OH or-NH2 groups. These hydrophilic groups achieved good solubility of bCDs (Qu et al., 2016). A faint peak detected at 2800–3000 cm^{-1} signifies the stretching vibration of saturated C-H bonds (Holá et al., 2017). In the range of 580–1800 cm^{-1}, several absorption peaks were found. The FT-IR spectrum of the bCDs showed characteristic peaks at 1710 cm^{-1} and 1,660 cm^{-1}, indicating the presence of C=O double bond and C-H bond stretching vibrations, respectively (Zhang et al., 2020; Yu et al., 2022). Moreover, the FT-IR spectrum displayed peaks at 1620 cm^{-1} and 1,510 cm^{-1}, suggesting the presence of aromatic groups in bCDs (Zhang et al., 2020). An obvious peak at 1400 cm^{-1} suggested the presence of C-N stretching vibrations, indicating that the amide group exists in bCDs (Yu et al., 2022). The presence of a peak at 1360 cm^{-1} in the FT-IR spectrum was attributed to the bending vibration of the C-H group. The peaks in the range from 1,000 to 1,180 cm^{-1} indicated the C-O groups (Aladesuyi and Oluwafemi, 2023).

To further examine the chemical composition of bCDs, the XPS was employed. Figure 2A shows that the XPS survey spectrum exhibited three element peaks, namely, carbon (C 1 s), nitrogen (N 1 s), and oxygen (O 1 s). To further analyze the functional groups of bCDs, a high-resolution XPS spectrum was employed. Figure 2B shows that the C 1 s spectrum decomposed into three peaks. The peaks at 287.9 eV and 284.7 eV demonstrated the existence of O=C-O and C-C (or C=C). Moreover, the peak at 285.8 eV was attributed to the groups of C-N, C-O, or C=N (Zhang et al., 2020). The decomposition of N 1 s can be observed in Figure 2C, where it is divided into two distinct peaks at the binding energy of 399.6 eV and 400.9 eV. These peaks correspond to pyrrolic N and graphitic N, respectively (Huo et al., 2021; Wu et al., 2022). The binding energy of O 1 s (Figure 2D) can also be deconvoluted into two peaks at the binding energy of 531.0 eV and 532.2 eV, contributed by the bonds of C=O and C-O, respectively (Chen et al., 2020; Zhang et al., 2020). Based on the aforementioned findings, it can be inferred that the bCDs potentially possess a conjugation core consisting of the pyridine and graphitic groups. Additionally, the presence of hydrophilic groups, such as amino and hydroxyl groups on the surface, contributes to the high solubility of bCDs.
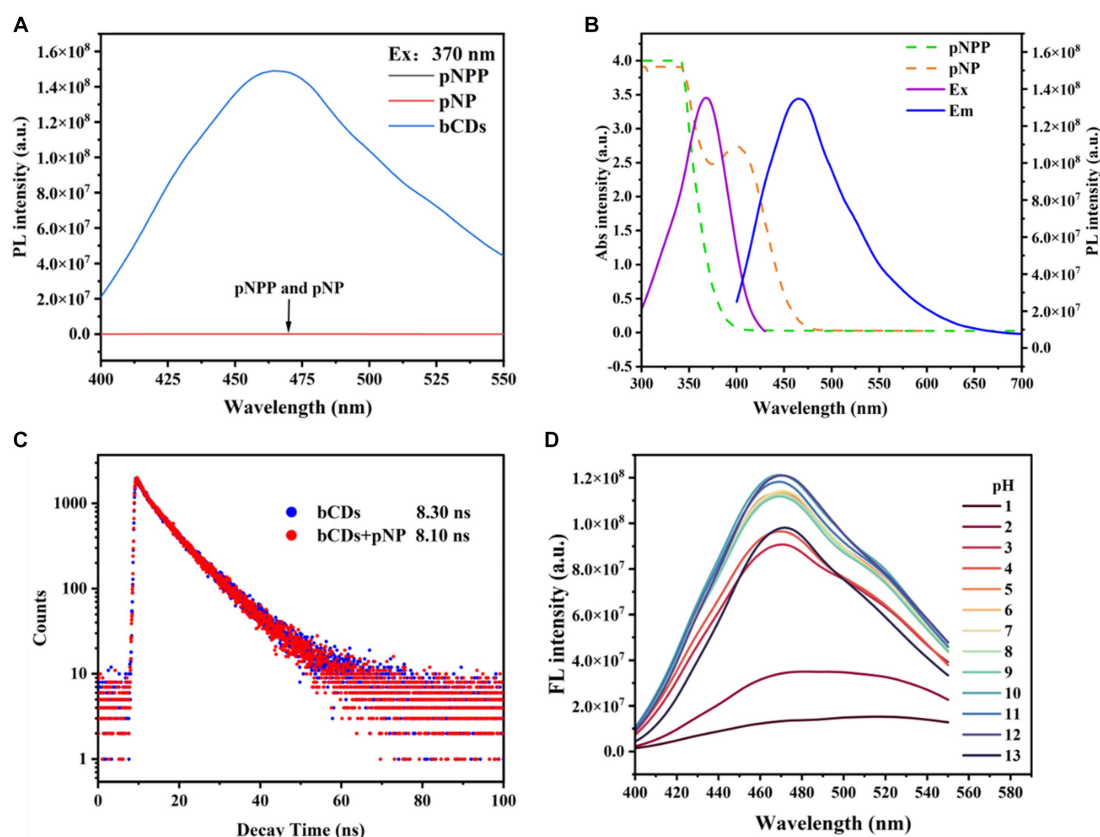
FIGURE 3
(A) Fluorescence influence of pNPP and pNP to bCDs. **(B)** Spectral overlapping of the fluorescence spectrum of bCDs and absorption spectrum of TMB and oxTMB. **(C)** Fluorescence lifetime of bCDs before and after mixing with pNP. **(D)** Optimized pH value for the fluorescent intensity of bCDs.

Construction of FIA

To verify the feasibility of FIA, several conditions were investigated. The fluorescence spectrum of pNP, pNPP, and bCDs were characterized. As shown in Figure 3A, only bCDs exhibited an obvious emission, and no fluorescence interference was observed for pNP and pNPP on bCDs, indicating the reliable signal output and good signal-to-noise ratio of FIA. To further investigate the quenching mechanism for bCDs, the UV spectrum of pNP and pNPP were measured and compared with the Ex and Em of bCDs. Figure 3B shows that no absorption peaks were observed for pNPP, while pNP showed an obvious absorption peak at 405 nm, which overlaps the Ex and Em peaks of bCDs. Moreover, the introduction of pNP did not affect the fluorescence lifetime of bCDs (Figure 3C). Therefore, the inner-filter effect might be the main reason for the fluorescence quenching of bCDs (Dong et al., 2019). Furthermore, the fluorescence of bCDs was examined across different pH values, revealing that bCDs demonstrated a strong fluorescence intensity within a wide pH range spanning from pH 5 to pH 13, demonstrating superior optics features and stability (Figure 3D). The pH value of ALP buffer was 9.6, which was suitable for the fluorescent response of bCDs. Therefore, bCDs were added without adjusting the pH value. All the above mentioned results indicated that the FIA system based on phosphate triggered to regulate the intensity of bCDs was feasible.

Development of FIA

Based on the mechanism of fluorescent regulation, the development of FIA was achieved by utilizing bCDs. In the absence of fenitrothion, the VHHjd8-ALP was bound to the microplate after a one-step competitive immune competition. Afterward, the pNPP was catalyzed into pNP through VHHjd8-ALP. Subsequently, the addition of bCDs resulted in the quenching of the fluorescence spectrum through the inner-filter effect, leading to a fluorescent response indicating the presence of fenitrothion (Scheme 1). To optimize the catalytic activity of VHHjd8-ALP for FIA, the pH value was adjusted and investigated using pNPP as the substrate. Figure 4A shows that the highest catalytic activity was observed with the pH value of 9.8, which was chosen as the optimized pH to develop FIA. Since the pH value for VHHjd8-ALP matched that of bCDs, no pH adjusting was performed after bCD addition, which was simple and convenient. Furthermore, the coating antigen concentration for the development of FIA was also investigated. Figure 4B demonstrates that the calibration curve attained optimal sensitivity, as evidenced by the limit of detection (LOD) of 0.77 ng/mL when the coating antigen concentration was set at 1 μg/mL. The calibration curve for FIA was successfully generated under the optimized conditions. The FIA analysis revealed an IC_{50} value of 16.25 ng/mL, with a limit of detection (LOD) of 0.07 ng/mL (Figure 5A).
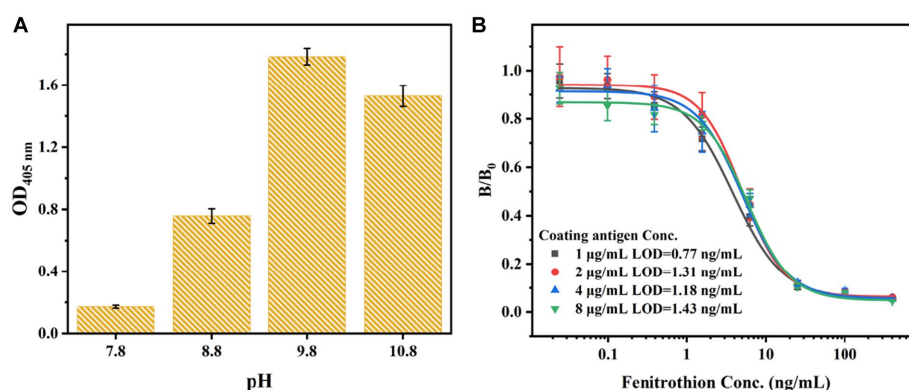
FIGURE 4
(A) pH optimization for the catalytic activity of VHHjd9-ALP. **(B)** Optimization of coating antigen concentration.
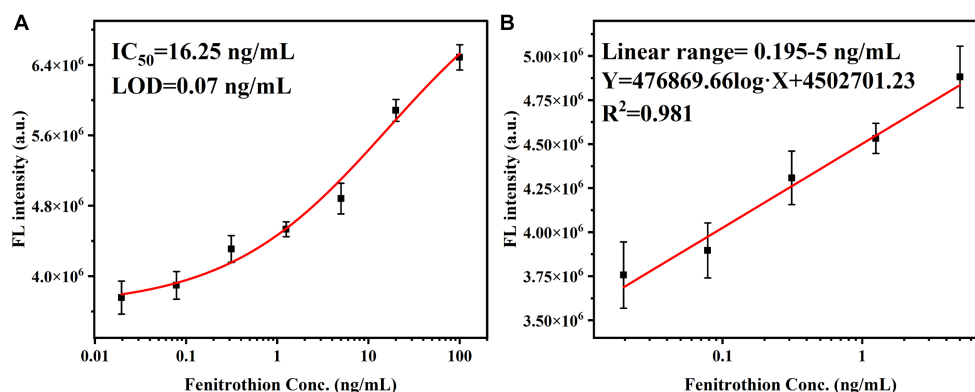
FIGURE 5
(A) Calibration curve and **(B)** linear range of FIA.

The fluorescent intensity exhibited a strong linear correlation with fenitrothion, with the concentration ranging from 0.195 ng/mL to 5 ng/mL, as evidenced by a high correlation coefficient of $R^2 = 0.981$ (Figure 5B). Compared with conventional pNPP-based one-step icELISA (Figure 4B), the developed FIA exhibited 11-fold improvement. Furthermore, the strategy of enhancing sensitivity necessitates no intricate methodologies, rendering it straightforward, convenient, and cost-effective.

Recovery test

Following the extraction and purification procedures, the extracting solutions were subsequently diluted using Tris buffer. Previous research has demonstrated that a 20-fold dilution effectively eliminates any matrix effect (Chen et al., 2022). To assess the accuracy of the developed FIA, a recovery test was conducted, and the results are summarized in Table 1. The recoveries achieved through FIA ranged from 81.8% to 119%, while those obtained through GC–MS/MS ranged from 86.5% to 116%. The coefficient of variances (CVs) for FIA ranged from 7% to 13.6%, and for GC–MS/MS, the CVs ranged from 4.3% to 11.6%. The results obtained from

FIA exhibited a high level of agreement with those obtained from GC–MS/MS, indicating the accuracy and practicality of the developed FIA method.

Conclusion

This study developed a simple FIA for sensitive detection of fenitrothion. The synthesized bCDs were used as a fluorescent probe for sensitivity improvement. After conducting a one-step competitive immunoassay, the VHHjd8-ALP fusion protein, upon binding to the microplate, catalyzed the conversion of pNPP into pNP; the latter can quench the intensity of bCDs through the inner-filter effect. After condition optimization, a high fluorescent response immunoassay was finally developed. Furthermore, in comparison to the conventional pNPP-based one-step icELISA, the developed FIA demonstrated a remarkable 11-fold enhancement. Furthermore, the approach to enhancing sensitivity does not require complex methodologies, making it simple, convenient, and economical. The recovery test served as confirmation that the developed FIA was both practical and accurate, establishing it as an exceptional method for rapidly and sensitively detecting fenitrothion in food samples.

TABLE 1 Recovery of fenitrothion from spiked food samples by proposed FIA (*n* = 3).

Sample	Spiked (ng/g)	FIA			GC–MS/MS		
		Measured Mean ± SD[a] (ng/g)	Recovery (%)	CV[b] (%)	Measured Mean ± SD (ng/g)	Recovery (%)	CV (%)
Chinese cabbage	2.0	1.6 ± 0.2	81.8	11.5	1.85 ± 0.2	92.5	10.8
	10.0	8.2 ± 0.8	82	9.8	10.34 ± 0.6	103.4	5.8
	50.0	57.8 ± 4.7	115.7	8.1	51.31 ± 3.2	102.6	6.2
Lettuce	2.0	2 ± 0.2	98.3	11.3	2.15 ± 0.2	107.5	9.3
	10.0	11.2 ± 1.4	112.3	12.6	9.47 ± 1	94.7	10.6
	50.0	56.6 ± 7.1	113.2	12.6	56.95 ± 3.9	113.9	6.9
Tangerine	2.0	1.9 ± 0.3	96.5	13.6	1.73 ± 0.2	86.5	11.6
	10.0	11.9 ± 0.8	119	7	11.6 ± 0.5	116	4.3
	50.0	53.8 ± 3.9	107.6	7.2	52.77 ± 3.2	105.6	6.1

[a]SD, standard deviation.
[b]CV, coefficient of variance, which was obtained from intra-assay.

SCHEME 1
Development of FIA.
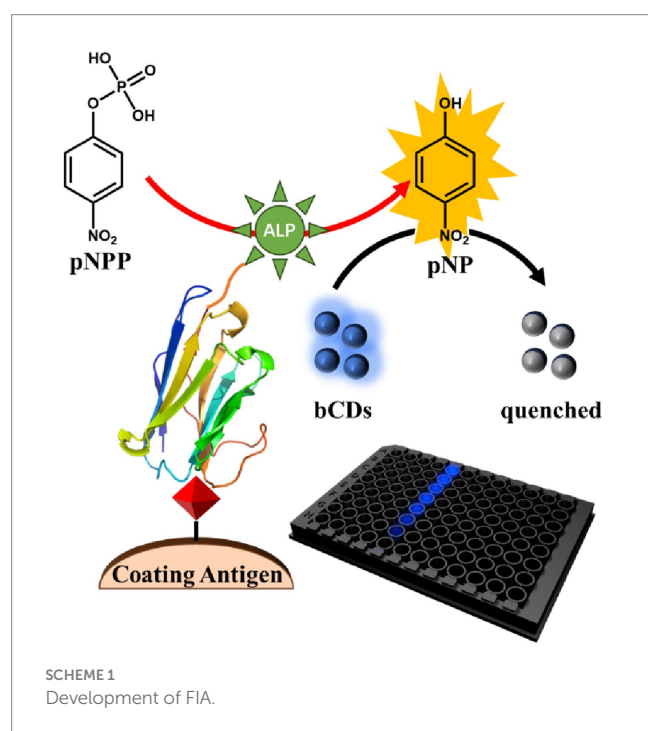
Z-LX: Conceptualization, Supervision, Writing – review & editing. HW: Conceptualization, Supervision, Writing – review & editing.

Funding

Conflict of interest

The authors declare that the research was conducted in the absence of any commercial or financial relationships that could be construed as a potential conflict of interest.

Publisher's note

Supplementary material

The Supplementary material for this article can be found online at: https://www.frontiersin.org/articles/10.3389/fsufs.2023.1320931/full#supplementary-material

Data availability statement

The original contributions presented in the study are included in the article/Supplementary material, further inquiries can be directed to the corresponding authors.

Author contributions

Z-JC: Data curation, Methodology, Writing – original draft. A-JH: Data curation, Methodology, Writing – original draft. X-XD: Methodology, Validation, Writing – review & editing. Y-FZ: Data curation, Methodology, Writing – original draft. LZ: Writing – review & editing, Supervision. LL: Writing – review & editing, Methodology.

References

Abdel-Ghany, R., Mohammed, E., Anis, S., and Barakat, W. (2016). Impact of exposure to Fenitrothion on vital organs in rats. *J. Toxicol.* 2016, 1–18. doi: 10.1155/2016/5609734

Aladesuyi, O. A., and Oluwafemi, O. S. (2023). Synthesis of N, S co-doped carbon quantum dots (N,S-CQDs) for sensitive and selective determination of mercury (Hg2+) in Oreochromis niloctus (Tilapia fish). *Inorg. Chem. Commun.* 153:110843. doi: 10.1016/j.inoche.2023.110843

Chen, Z. J., Huang, Z. C., Huang, S., Zhao, J. L., Sun, Y. M., Xu, Z. L., et al. (2021). Effect of proteins on the oxidase-like activity of CeO_2 nanozymes for immunoassays. *Analyst* 146, 864–873. doi: 10.1039/d0an01755h

Chen, Y. Q., Sun, X. B., Wang, X. Y., Pan, W., Yu, G. F., and Wang, J. P. (2020). Carbon dots with red emission for bioimaging of fungal cells and detecting Hg^{2+} and ziram in aqueous solution. *Spectrochim. Acta A* 233:118230. doi: 10.1016/j.saa.2020.118230

Chen, Z. J., Zhang, Y. F., Chen, J. L., Lin, Z. S., Wu, M. F., Shen, Y. D., et al. (2022). Production and characterization of biotinylated anti-fenitrothion nanobodies and development of sensitive fluoroimmunoassay. *J. Agric. Food Chem.* 70, 4102–4111. doi: 10.1021/acs.jafc.2c00826

Delnavaz, E., Amjadi, M., and Farajzadeh, M. A. (2023). Metal-organic framework with dual-loading of nickel/nitrogen-doped carbon dots and magnetic nanoparticles for fluorescence detection of fenitrothion in food samples. *J. Food Compos. Anal.* 115:104873. doi: 10.1016/j.jfca.2022.104873

Dong, B. L., Li, H. F., Mujtaba Mari, G., Yu, X. Z., Yu, W. B., Wen, K., et al. (2019). Fluorescence immunoassay based on the inner-filter effect of carbon dots for highly sensitive amantadine detection in foodstuffs. *Food Chem.* 294, 347–354. doi: 10.1016/j.foodchem.2019.05.082

Faria, M., Bellot, M., Bedrossiantz, J., Ramirez, J., Prats, E., Garcia-Reyero, N., et al. (2022). Environmental levels of carbaryl impair zebrafish larvae behaviour: the potential role of ADRA2B and HTR2B. *J. Hazard. Mater.* 431:128563. doi: 10.1016/j.jhazmat.2022.128563

Galal, A. A. A., Ramadan, R. A., Metwally, M. M. M., and El-Sheikh, S. M. A. (2019). Protective effect of N-acetylcysteine on fenitrothion-induced toxicity: the antioxidant status and metabolizing enzymes expression in rats. *Ecotoxicol. Environ. Saf.* 171, 502–510. doi: 10.1016/j.ecoenv.2019.01.004

Gnanguenon, V., Agossa, F. R., Badirou, K., Govoetchan, R., Anagonou, R., Oke-Agbo, F., et al. (2015). Malaria vectors resistance to insecticides in Benin: current trends and mechanisms involved. *Parasit. Vectors* 8:223. doi: 10.1186/s13071-015-0833-2

Han, J., Zhang, Y., Chen, Z., Zhang, A., and Shi, X. (2023). Synergistic effect of nitrogen and sulfur co-doped holey graphene for sensitive fenitrothion detection supported by DFT study. *Microchem. J.* 193:109218. doi: 10.1016/j.microc.2023.109218

Holá, K., Sudolská, M., Kalytchuk, S., Nachtigallová, D., Rogach, A. L., Otyepka, M., et al. (2017). Graphitic nitrogen triggers red fluorescence in carbon dots. *ACS Nano* 11, 12402–12410. doi: 10.1021/acsnano.7b06399

Huo, X., Shen, H., Liu, R., and Shao, J. (2021). Solvent effects on fluorescence properties of carbon dots: implications for multicolor imaging. *Acs Omega* 6, 26499–26508. doi: 10.1021/acsomega.1c03731

Kang, H. S., Kim, M., Kim, E. J., and Choe, W. (2020). Determination of 66 pesticide residues in livestock products using QuEChERS and GC–MS/MS. *Food Sci. Biotechnol.* 29, 1573–1586. doi: 10.1007/s10068-020-00798-4

Lee, C., Kwon, W., Beack, S., Lee, D., Park, Y., Kim, H., et al. (2016). Biodegradable nitrogen-doped carbon nanodots for non-invasive photoacoustic imaging and photothermal therapy. *Theranostics* 6, 2196–2208. doi: 10.7150/thno.16923

Li, W., Ma, L., Shi, Y., Wang, J., Yin, J., Wang, D., et al. (2023). Meiosis-mediated reproductive toxicity by fenitrothion in *Caenorhabditis elegans* from metabolomic perspective. *Ecotoxicol. Environ. Saf.* 253:114680. doi: 10.1016/j.ecoenv.2023.114680

Lin, X., Xiong, M., Zhang, J., He, C., Ma, X., Zhang, H., et al. (2021). Carbon dots based on natural resources: synthesis and applications in sensors. *Microchem. J.* 160:105604. doi: 10.1016/j.microc.2020.105604

Liu, M. L., Zeng, X., Deng, H., Wang, Y., Zhang, Y. F., Shen, Y. D., et al. (2022). Phosphate-triggered ratiometric multicolor immunosensor based on nanobody-alkaline phosphatase fusion protein for sensitive detection of fenitrothion. *Sensor. Actuat. B Chem.* 373:132734. doi: 10.1016/j.snb.2022.132734

Luo, P. G., Sahu, S., Yang, S., Sonkar, S. K., Wang, J., Wang, H., et al. (2013). Carbon "quantum" dots for optical bioimaging. *J. Mater. Chem. B* 1, 2116–2127. doi: 10.1039/c3tb00018d

Pedroso, T. M. A., Benvindo-Souza, M., de Araújo Nascimento, F., Woch, J., Dos Reis, F. G., de Melo, E., et al. (2022). Cancer and occupational exposure to pesticides: a bibliometric study of the past 10 years. *Environ. Sci. Pollut. Res.* 29, 17464–17475. doi: 10.1007/s11356-021-17031-2

Qu, S. N., Zhou, D., Li, D., Ji, W. Y., Jing, P. T., Han, D., et al. (2016). Toward efficient orange emissive carbon nanodots through conjugated sp2-domain controlling and surface charges engineering. *Adv. Mater.* 28, 3516–3521. doi: 10.1002/adma.201504891

Sun, J., Zhao, J., Bao, X., Wang, Q., and Yang, X. (2018). Alkaline phosphatase assay based on the chromogenic interaction of Diethanolamine with 4-aminophenol. *Anal. Chem.* 90, 6339–6345. doi: 10.1021/acs.analchem.8b01371

Ulusoy, H., Köseoğlu, K., Kabir, A., Ulusoy, S., and Locatelli, M. (2020). Fabric phase sorptive extraction followed by HPLC-PDA detection for the monitoring of pirimicarb and fenitrothion pesticide residues. *Microchim. Acta* 187:337. doi: 10.1007/s00604-020-04306-7

Wang, Y., Liu, X., Chen, C., Chen, Y., Li, Y., Ye, H., et al. (2022). Magnetic Nanorobots as maneuverable immunoassay probes for automated and efficient enzyme linked immunosorbent assay. *ACS Nano* 16, 180–191. doi: 10.1021/acsnano.1c05267

Wu, Z. L., Xiong, Z. K., Liu, R., He, C. S., Liu, Y., Pan, Z. C., et al. (2022). Pivotal roles of N-doped carbon shell and hollow structure in nanoreactor with spatial confined co species in peroxymonosulfate activation: obstructing metal leaching and enhancing catalytic stability. *J. Hazard. Mater.* 427:128204. doi: 10.1016/j.jhazmat.2021.128204

Yang, N., Wang, P., Xue, C. Y., Sun, J., Mao, H. P., and Oppong, P. K. (2018). A portable detection method for organophosphorus and carbamates pesticide residues based on multilayer paper chip. *J. Food Process Eng.* 41:e12867. doi: 10.1111/jfpe.12867

Yi, K. Y., Zhang, X. T., and Zhang, L. (2020). Eu^{3+}@metal–organic frameworks encapsulating carbon dots as ratiometric fluorescent probes for rapid recognition of anthrax spore biomarker. *Sci. Total Environ.* 743:140692. doi: 10.1016/j.scitotenv.2020.140692

Yu, M., Zhang, H., Liu, Y. N., Zhang, Y. L., Shang, M. H., Wang, L., et al. (2022). A colorimetric and fluorescent dual-readout probe based on red emission carbon dots for nitrite detection in meat products. *Food Chem.* 374:131768. doi: 10.1016/j.foodchem.2021.131768

Zhang, X. Q., Chen, C. Y., Peng, D. P., Zhou, Y. Z., Zhuang, J. L., Zhang, X. J., et al. (2020). pH-responsive carbon dots with red emission for real-time and visual detection of amines. *J. Mater. Chem. C* 8, 11563–11571. doi: 10.1039/d0tc02597f

Zhu, Z. J., Zhai, Y. L., Li, Z. H., Zhu, P. Y., Mao, S., Zhu, C. Z., et al. (2019). Red carbon dots: optical property regulations and applications. *Mater. Today* 30, 52–79. doi: 10.1016/j.mattod.2019.05.003

In light of the new legislation for per- and polyfluoroalkyl substances, can continued food sustainability be achieved?

Diana Senovilla-Herrero[1]*, Heather Moore[2], Matthew Service[2], Ray Thomas[3], Sarah Helyar[1], Lenka Mbadugha[4] and Katrina Campbell[1]*

[1]Institute for Global Food Security, School of Biological Sciences, Queen's University Belfast, Belfast, United Kingdom, [2]Agri-Food and Biosciences Institute, Belfast, United Kingdom, [3]Northern Ireland Environment Agency, Lisburn, United Kingdom, [4]School of Biological Sciences, University of Aberdeen, Aberdeen, United Kingdom

Per- and polyfluoroalkyl substances (PFAS) are a group of persistent organic pollutants which pose significant risks to human health and the environment. This article comprehensively examines the implications of new legislation concerning PFAS for food sustainability. The current legislative frameworks governing PFAS in food production and distribution are explored, highlighting the need for robust mitigation strategies to safeguard food safety and environmental integrity. It delves into the challenges posed by the legislation, raising questions about the balance between environmental protection and the sustainability of the food system. It provides a review of the state-of-the-art analytical methods for PFAS detection and quantification in water and food matrices. Their advantages and limitations are discussed, offering valuable insights for researchers in the field. In addition, a range of mitigation strategies to combat PFAS contamination in the food supply chain are explored. By collating current knowledge on PFAS contamination in sustainable food systems, this article aims to provide a comprehensive resource for researchers, policymakers, and practitioners striving to ensure the safety and sustainability of our global food supply. The integration of legislative insights, advanced analytical techniques, and practical mitigation approaches offers a holistic perspective on managing PFAS-related challenges in the context of sustainable food systems.

KEYWORDS

per- and polyfluoroalkyl substances, methods of detection, food safety, food policy and governance, sustainability

1 Introduction

So-called "forever chemicals" are pollutants of rising concern due to the thriving industry of plastic-associated substances. Highly persistent in the environment and human body due to the strength and stability of their unique chemistry, their extreme difficulty to degrade in the environment has led them to be a major outlet of contamination to date (HBM4EU, 2022; United Nations Environment Programme, 2023). Forever chemicals have been widely used since the 1940s in various industrial and consumer products including firefighting foams, cleaning agents, non-stick cookware, water-repellent clothing, additives in paints, and food

packaging, due to their resistance to heat, oil, and water (Buck et al., 2011; ECHA, 2022).

Per- and polyfluoroalkyl substances (PFAS) constitute part of these man-made chemicals of increasing global concern. They are technically defined as "any substance that contains at least one fully fluorinated methyl or methylene carbon atom (without any H/Cl/Br/I attached to it)" (OECD, 2021, p. 7). This means that any chemical with a minimum of one perfluorinated methyl ($-CF_3$) or methylene ($-CF_2-$) group is classified as a PFAS. This group of chemicals can be synthesized by two processes: electrochemical fluorination (ECF) or fluorotelomerisation (Evich et al., 2022), resulting in a large and complex class of thousands of compounds with highly diverse functional groups. Table 1 illustrates this collection with a comprehensive but not exhaustive summary of PFAS groups, their chemical structural characteristics, acronyms and examples. It is important to note that more of these groups are being produced each time one gets banned (Hammel et al., 2022).

PFAS have been classified as ubiquitous, persistent, bioaccumulative and toxic, posing a massive concern to regulators worldwide (Environment Agency, 2021). These highly persistent organic compounds can accumulate in the environment, particularly in water bodies, and subsequently in the tissues of aquatic organisms that enter the food chain (Houde et al., 2011). This bioaccumulation can pose significant health risks to both animals and humans who consume contaminated drinking water or food products, including potential links to cancer, hormone disruption, and immune system effects (Steenland et al., 2010). It is estimated that all biota on the planet, including humans, already has a PFAS body burden (Ingelido et al., 2018). Biomonitoring studies are currently underway globally to generate representative evidence of PFAS chemical exposure in the human population (EFSA CONTAM Panel et al., 2020; ATSDR, 2021).

An investigation conducted by the International Pollutants Elimination Network carried out in 17 countries across Asia, Africa, Europe, Latin America and the Caribbean found PFAS contents in 54% of sampled single-use food packaging and tableware (Straková et al., 2023). This highlights the global exposure of human population to PFAS from packaging and contaminated food. Similar findings have also been observed across a range of more site-specific studies. For example, PFAS pollution was reported to threaten water quality in North and Southeast Asia (Liu et al., 2021; Tang et al., 2023). A study on pregnant women in Shanghai, China, found all participants to contain PFAS in their blood at different concentrations (Tian et al., 2018). Further, PFAS were also found to be ubiquitous in infants in West Africa (Sørensen et al., 2023). The global threat posed by these pervasive chemicals is exacerbated by their association with multiple exposure pathways.

Two of the oldest and most commonly employed PFAS, perfluorooctane sulfonic acid (PFOS) and perfluorooctanoic acid (PFOA), have been listed in the annexes of the Stockholm Convention on Persistent Organic Pollutants (POPs) since 2009 and 2019, respectively (European Union Reference Laboratory for Halogenated POPs in Feed and Food, 2022). PFOS is listed under Annex B aiming for the restriction of production and use of chemicals, whereas PFOA is listed under Annex A which aims to eliminate production and uses completely (Stockholm Convention, 2019). Additionally, PFOS is on the List of Chemicals for Priority Action associated with the Convention for the Protection of the Marine Environment of the

North-East Atlantic (OSPAR). Several of PFOS precursors are also included in the OSPAR List of Substances of Possible Concern (OSPAR Commission, 2013). The recommendation by OSPAR is to take proactive steps in studying various PFAS in the marine environment and staying alert for new findings in their designated area, while focusing on evaluating eco-friendly alternatives to replace these substances.

In October 2020 the European Commission published a Chemicals Strategy for Sustainability Toward a Toxic-Free Environment aiming to implement tangible actions to increase the level of protection of public human health and the environment from hazardous chemicals (European Commission, 2020). The strategy sets the goal of transforming the EU industry via the production and consequent use of safe and sustainable chemicals. In doing so, the criteria for essential uses of certain substances will be redefined "to ensure that the most harmful chemicals are only allowed if their use is necessary for health, safety or is critical for the functioning of society and if there are no alternatives that are acceptable from the standpoint of environment and health" (European Commission, 2020, p. 10).

2 PFAS REACH restriction proposal

International efforts are being made to restrict the use of PFAS in order to reduce their release into the environment and subsequent transfer into the food chain. A restriction proposal under the Regulation for Registration, Evaluation, Authorization and Restriction of Chemicals (REACH) (European Parliament and Council of the European Union, 2006) was prepared and made available to the European Chemicals Agency (ECHA) at the beginning of 2023 by five EU authorities (Denmark, Germany, the Netherlands, Norway and Sweden). The restriction proposal, which is under consideration, would apply to any product containing PFAS, including food and food contact materials. The basis for this proposal is the concern in relation to the properties of PFAS chemicals, in particular their very high persistence and mobility within the environment, which could progressively lead to harmful exposure for biota and humans via soil, water, air and the pertinent food chains. Other properties of concern are their long-range transport potential, bioaccumulation, and endocrine activity and toxicity. Figure 1 shows the lifecycle of the emissions from PFAS from their origin at production sites to subsequent uses and product end-life disposal and waste recycling, including the exposure pathways to environmental and human health. PFAS also have been found in recycled bedding materials used in poultry farms, whereby these chemicals have subsequently made their way into the eggs and tissues of chickens entering the food market (Fernandes et al., 2023). Consequently, the presence of PFAS in products recovered from former waste could deeply affect safe and sustainable feed and food production in a circular economy approach.

3 European policy on PFAS in food, feed, and drinking water

According to the risk assessment carried out by the European Food Safety Authority (EFSA) on the human health risks associated with the presence of perfluoroalkyl contaminants in foodstuffs, the

TABLE 1 Overview of PFAS groups.

	Group	Name	Acronym	Chemical formula
PFASs	Perfluoroalkyl acids (PFAAs); including perfluoroalkylether acids (PFEAAs)	Perfluoroalkyl carboxylic acids	PFCAs	C_nF_{2n+1}-COOH
		Perfluoroalkane sulfonic acids	PFSAs	C_nF_{2n+1}-SO_3H
		Perfluoroalkyl phosphonic acids	PFPAs	C_nF_{2n+1}-PO_3H_2
		Perfluoroalkyl phosphinic acids	PFPIAs	$(C_nF_{2n+1})(C_mF_{2m+1})$-$PO_2H$
		Perfluoroalkylether carboxylic acids	PFECAs	e.g., $C_2F_5OC_2F_4OCF_2COOH$
		Perfluoroalkylether sulfonic acids	PFESAs	e.g., $C_6F_{13}OCF_2CF_2SO_3H$
		Perfluoroalkyl dicarboxylic acids	PFdiCAs	HOOC-C_nF_{2n}-COOH
		Perfluoroalkane disulfonic acids	PFdiSAs	HO_3S-C_nF_{2n}- SO_3H
		Perfluoroalkane sulfinic acids	PFSIAs	C_nF_{2n+1}-SO_2H
	Polyfluoroalkyl acids (PolyFAAs); including polyfluoroalkylether acids (PolyFEAAs)	Polyfluoroalkyl carboxylic acids	PFCAs	e.g., H-C_nF_{2n}-COOH, n > 1
		Perfluoroalkylether carboxylic acids	PFECAs	e.g., $CF_3OC_3F_6OCHFCF_2COOH$
		Perfluoroalkylether sulfonic acids	PFESAs	e.g., $ClC_6F_{12}OCF_2CF_2SO_3H$
	PFAA precursors	Fluorotelomer alcohols (n:1)	–	$C_nF_{2n+1}CH_2OH$
		Perfluoroalkanoyl fluorides	PACFs	$C_nF_{2n+1}COF$
		Perfluoroalkyl iodides	PFAIs	$C_nF_{2n+1}I$
		Perfluoroalkane sulfonyl fluorides	PASFs	$C_nF_{2n+1}SO_2F$
		Perfluoroalkylether non-polymers	–	e.g., $C_4F_9OC_2F_4OC_2F_4OCF_2$-$CH_2OH$
		Perfluoroalkylether side-chain fluorinated polymers*	–	–
		Perfluoroalkenes	–	C_nF_{2n}, n > 2
		Semifluorinated alkanes	SFAs	C_nF_{2n+1}-C_mH_{2m+1}
		Hydrofluorocarbons, Hydrofluoroethers, Hydrofluoroolefins, that have a perfluoroalkyl chain	HFCs HFEs HFOs	e.g., C_nF_{2n+1}-C_mH_{2m+1}, e.g., $C_nF_{2n+1}OC_mH_{2m+1}$, e.g., C_nF_{2n+1}-CH=CH_2
		Perfluoroalkyl ketones Semi-fluorinated ketones	–	e.g., $C_nF_{2n+1}C(O)C_mF_{2m+1}$, e.g., $C_nF_{2n+1}C(O)C_mH_{2m+1}$
		Perfluoroalkyl alcohols	–	$C_nF_{2n+1}OH$
	Other PFASs	Fluoropolymers*	FPs	
		Perfluoropolyethers*	PFPEs	e.g., $HOCH_2O$-$(C_mF_{2m}O)_n$-CH_2OH
		Side-chain fluorinated aromatics	–	e.g., C_nF_{2n+1}-aromatic rings
		Perfluoroalkanes	–	C_nF_{2n+2}
		Perfluoroalkyl-*tert*-amines	–	$(C_nF_{2n+1})_3N$
		Perfluoroalkylethers	–	e.g., $C_nF_{2n+1}OC_mF_{2m+1}$
		Others	–	–

Source: OECD (2021, p. 23). *Polymeric PFASs.

tolerable weekly intake for the sum of PFAS, represented by PFOS, PFOA, perfluorononanoic acid (PFNA) and perfluorohexane sulfonic acid (PFHxS), is 4.4 ng/kg body weight (EFSA CONTAM Panel et al., 2020). It is of concern that the exposure to these chemicals in certain parts of Europe exceeds this level (EFSA CONTAM Panel et al., 2020). Regulation (EU) 2023/915 sets separate maximum levels for PFOS, PFOA, PFNA, and PFHxS, and the sum of the four PFAS in animal and fish meat (European Commission and Directorate-General for Health and Food Safety, 2023). It has also been recommended to monitor other PFAS with different alkyl chains in a broad range of foodstuffs including fruits, vegetables, cereals, food for infants and young children, wine, beer and non-alcoholic drinks, among others (European Commission and Directorate-General for Health and Food Safety, 2022b). Table 2 showcases a list of over 20 PFAS compounds structurally similar to the identified significant PFOS, PFOA, PFNA, and PFHxS recommended for monitoring by the EU member states. In addition, arising PFAS substitutes need to be taken into account such as DONA, GenX, F-53B, Capstone A, and Capstone B (European

FIGURE 1
The lifecycle of PFAS emissions. Created partially with BioRender.com.
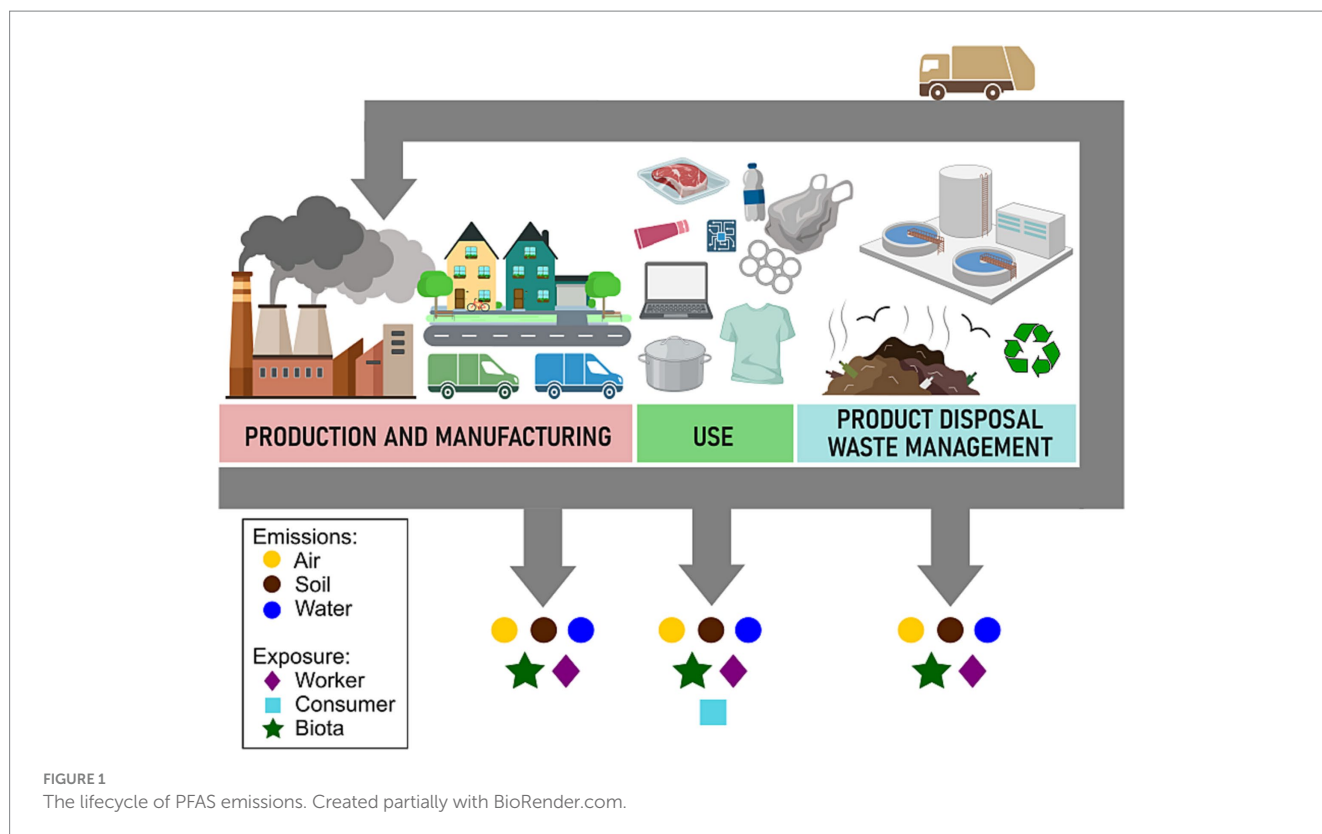
TABLE 2 PFAS compounds similar to PFOS, PFOA, PFNA, and PFHxS with high occurrence in food, drinking water and human serum.

Perfluoroalkyl substance	Acronym
Perfluorobutanoic acid	PFBA
Perfluoropentanoic acid	PFPeA
Perfluorohexanoic acid	PFHxA
Perfluoroheptanoic acid	PFHpA
Perfluorodecanoic acid	PFDA
Perfluoroundecanoic acid	PFUnDA
Perfluorododecanoic acid	PFDoDA
Perfluorotridecanoic acid	PFTrDA
Perfluorotetradecanoic acid	PFTeDA
Perfluorobutane sulfonic acid	PFBS
Perfluoropentanesulfonic acid	PFPS
Perfluoroheptane sulfonic acid	PFHpS
Perfluorononane sulfonic acid	PFNS
Perfluorodecane sulfonic acid	PFDS
Perfluoroundecane sulfonic acid	PFUnDS
Perfluorododecane sulfonic acid	PFDoDS
Perfluorotridecane sulfonic acid	PFTrDS
Perfluorooctane sulphonamide	FOSA

Source: European Commission and Directorate-General for Health and Food Safety (2022b).

Union Reference Laboratory for Halogenated POPs in Feed and Food, 2022).

The sampling and analytical methods for the official control of perfluoroalkyl substances in food are laid down in Regulation (EU) 2022/1428 (European Commission and Directorate-General for Health and Food Safety, 2022a). Target limits of quantification (LOQs) are displayed in Table 3 (European Commission and Directorate-General for Health and Food Safety, 2022b).

The maximum regulatory levels proposed by the European Commission are of concern as the contamination of food products of animal origin may be a result of bioaccumulation of existing PFAS levels in feed consumed by those animals (European Commission and Directorate-General for Health and Food Safety, 2022c). In January 2023, Danish organic eggs from large commercial farms around Denmark were found to be contaminated with PFAS as a result of contamination in fishmeal contained in chicken feed (DTU National Food Institute, 2023). Subsequent exposure to children is of high concern, as the consumption of only 2.5 organic eggs per week would exceed the tolerable weekly intake proposed by EFSA. Another concern is associated with the sensitivity of current methods of analysis of PFAS levels in feed. Therefore, it is difficult to establish the maximum PFAS levels in feed which would not lead to the exceedance of maximum levels in food. Although it has been acknowledged that present analytical methods require further development for setting these values, there are bigger challenges associated with the management of risks posed by feed. There exists a series of variables that have not been studied in detail which are linked to the uptake of PFAS in feed materials or products. Firstly, there may be some variation in PFAS levels in specific feed materials due to species, origin, season or production method. Secondly, variable amounts may be transferred from feed to food producing animals and their products. Thirdly, variable sensitivity of animals to PFAS and the duration of the contamination in their body. Finally, there is a lack of

TABLE 3 Targeted limits of quantification for the monitoring of the four main PFAS compounds in food.

Foodstuffs	Target LOQs (µg/kg)			
	PFOS	PFOA	PFNA	PFHxS
Fruits, vegetables, starchy roots and tubers, and food for infants and young children	0.002	0.001	0.001	0.004
Milk	0.010	0.010	0.020	0.040
Fish meat and meat of terrestrial animals	0.10	0.10	0.10	0.10
Eggs, crustaceans and mollusks	0.30	0.30	0.30	0.30
Edible offal of terrestrial animals and in fish oil	0.50	0.50	0.50	0.50

Source: European Commission and Directorate-General for Health and Food Safety (2022b).

specific knowledge of many of the PFAS substances. Until more scientific evidence is available on these issues, the solution is to reduce or eliminate the sources of contamination, so feed does not represent a danger to human, animal health or the environment.

PFAS contamination is ubiquitous and as such, it also affects drinking water to a large extent. Not only that, but water is also used and consumed in food production as well as manufacturing and home cooking. Directive (EU) 2020/2184 on the quality of water intended for human consumption set maximum levels for PFAS in drinking water, although these parametric values would not be enforced until the year 2026 (European Parliament and Council of the European Union, 2020). The maximum level for the sum of a subset of 20 PFAS of concern (see Table 2 excluding PFTeDA and FOSA) is 0.1 µg/L, whereas the limit for the totality of PFAS present is 0.5 µg/L. By 2024, the European Commission shall establish technical guidelines with respect to sampling frequency, detection limits and analytical methods. As mentioned above, there is an absence of regulatory levels in force in both feed and drinking water to date. Nonetheless, monitoring of perfluoroalkyl substances using reliable methods of analysis should be the focus of food business operators to ensure food safety in the years to come.

In low-income countries, the regulation and monitoring of contaminants in food may be limited when compared to more affluent states. Factors such as insufficient infrastructure, lack of resources or enforcement of standards, and competing priorities may contribute to challenges in adequately addressing PFAS contamination. In general, global standards for drinking water lack universal acceptance, and only in the USA and EU are water specifications considered mandatory (Whitehead, 2020). In the EU, there is a collective standard, but individual member states can add restrictions without weakening it. In the USA, local authorities can enhance the national standard. Elsewhere, guidelines are non-enforceable with varying targets, depending on local conditions. Water quality specifications differ widely between regions and countries, reflecting unique concerns and issues. In the case of PFAS, the USA proposed enforceable Maximum Contaminant Levels for six PFAS (US EPA,

2023), the EU updated safety standards under the revised Drinking Water Directive, and the UK follows a precautionary approach with no statutory standards but tiered guideline values (DWI, 2022). Contrary to this, certain parts of Asia are still in the early stages of PFAS awareness and regulation (Baluyot et al., 2021). International organizations, non-governmental organizations, and research institutions may play a role in supporting low-income countries in assessing and mitigating the impact of PFAS on food safety, taking into consideration that many Western guidelines may not be totally applicable across countries in the Middle East and Asia due to differences in diets, as well as the ways that food products and drinking water are sourced (Baluyot et al., 2021).

4 PFAS analytical methods

As has been made evident above, it is crucial to monitor and address PFAS contamination at all points in the PFAS emissions lifecycle, due to the widespread nature of these chemicals. The standard analytical methods, such as ISO 21675 (2019), US EPA 533 (2019), US EPA 537.1 (2020), US EPA Draft Method 1,633 (2021), ASTM D7979-19 or DIN 38407–42 (2011) (Winchell et al., 2021; Nahar et al., 2023; Ogunbiyi et al., 2023), used for PFAS testing are based on chromatographic techniques coupled with mass spectrometry (Getzinger and Ferguson, 2021; Ganesan et al., 2022). (Ultra) High performance liquid chromatography [(U)HPLC] coupled to low resolution, high resolution or tandem mass spectrometry (MS/MS) is the recommended method by the European Union Reference Laboratory for halogenated POPs in feed and food for PFAS analysis (European Union Reference Laboratory for Halogenated POPs in Feed and Food, 2022). The suggested instrumentation consists of a C18 LC column packed with solid phase particles, and a mass spectrometer capable of electrospray ionization in the negative ion mode. In regard to sample preparation, the sample material needs to be homogenized carefully to not introduce secondary contamination, followed by PFAS extraction, and subsequent (U)HPLC–MS analysis. No AOAC International official method for PFAS in foodstuff has been published yet, leading to disparities in result consistency across commercial testing laboratories covering PFOS, PFOA, PFNA, and PFHxS analysis (Delatour et al., 2023). However, at the time of writing, an AOAC integrated project was underway to define Standard Method Performance Requirements for PFAS in foods (AOAC International, 2022). Additionally, US EPA Method 1,633 is under draft for the determination of PFAS in aqueous, solid and tissue samples. The results of these projects would contribute to the development of analytical metrics for both screening and confirmatory methods.

The main challenges in mass spectrometry analysis arise due to the low target LOQs and the high sensitivity required to achieve those. Another challenging factor is the presence of several compounds with different properties and different sources of environmental contamination. Additional critical key issues linked with PFAS analysis are background contamination from other laboratory equipment or consumables (e.g., solvents, detergents, glassware, aluminum foil, lubricants, Decon 90, Teflon tubing used in (U) HPLC and sample extraction instrumentation, etc.), as well as quantification of the sum of linear and branched isomers as a result of the ECF synthesis of PFOS-related substances (European Union Reference Laboratory for Halogenated POPs in Feed and Food, 2022).

LC–MS and LC–MS/MS are targeted techniques which require analytical standards. As the list of chemical compounds classified as PFAS is in the thousands, the limited availability of reference standards, currently only available for a small subset, reduces the effectiveness of a targeted approach. Targeted techniques also measure only those substances for which the MS instrumentation has been calibrated and so fail to identify all PFAS substances present in the sample, therefore underestimating the full extent of PFAS contamination. Hence, it could be beneficial to make use of non-targeted methods (Strynar et al., 2023) such as non-target liquid chromatography-high resolution mass spectrometry, Adsorbable Organic Fluorine, Extractable Organic Fluorine, Total Oxidizable Precursor Assay (Göckener et al., 2023) or Total Organic Fluorine Assay. These methods quantify the presence of fluorine atoms within a sample. Nonetheless, although these chromatographic non-targeted methods can be used for water samples, food and feed samples represent a more challenging matrix. Another method that can be used for total PFAS detection are bioassays similar to the ones currently accepted for dioxins (Eichbaum et al., 2014; European Commission and Directorate-General for Health and Food Safety, 2017). Bioassays measure the biological responses of certain strains of bacteria or cell cultures via signal transduction pathways when exposed to chemicals (Tian et al., 2012). In this case, the bioassay does not determine concentrations of PFAS, but the effect of any bioactive PFAS which would, in turn, give a positive response. At present, bioassays are not a realistic possibility as regulations for food do not consider relative potency factors. Moreover, these methods are costly, limited in their transferability between laboratories and can often give false positives due to other contaminants being present in the sample.

While MS methods are highly sensitive and accurate, they are also time-consuming, expensive, and require specialized equipment and trained personnel. In contrast, biosensors such as lateral flow assays offer a promising alternative for PFAS detection as they are typically faster, cheaper, and easier to use than traditional methods, and they can be designed for on-site, real-time detection, which is crucial for effective environmental management and immediate response to contamination events (Huang et al., 2019). A non-exhaustive list of currently available sensor technologies for PFAS detection is displayed in Table 4. Recent efforts in biosensing applications are also focused on the use of binding proteins or protein bioreceptors for the detection of PFAS (Moro et al., 2020; Daems et al., 2021; Mann et al., 2022; Kowalska et al., 2023). The development of biosensors for PFAS detection, particularly in complex food matrices remains a challenge, as current efforts for end-product sensor development in the field focus heavily on water samples as their target analyte (Rodriguez et al., 2020; Garg et al., 2022).

5 Mitigation

PFAS remediation processes for contaminated drinking water are difficult and costly to implement (Brunn et al., 2023). Strategies should focus on regulating the use of PFAS in consumer products to minimize the appearance of these chemical substances at the contamination sources (Voulgaropoulos, 2022). Initial legislative steps toward this goal are already being taken via the implementation of maximum levels in drinking water and foodstuffs. Nonetheless, water purification treatments should be a priority until the effects of recent policies and

regulations begin to materialize. PFAS removal technologies for water systems consist of diverse approaches, such as granular activated carbon, reverse osmosis, nanofiltration or ion exchange resins (Voulgaropoulos, 2022; Brunn et al., 2023). All of these processes have limitations and are largely ineffective in removing PFAS from water. Granular activated carbon is ineffective for short-chain PFAS. Ion exchange resins, although more efficient, are more expensive as loading volumes are small and regeneration is restricted (US EPA, 2018). Reverse osmosis is energy-intensive and often not as effective. An alternative to purification is PFAS degradation. Advances in this field have increased as the extent of PFAS pollution becomes more apparent. Degradation of PFAS can occur as a result of defluorination or biotransformation caused by a number of microbial species and their enzymes. Examples of bacteria capable of microbial degradation are *Pseudomonads, Acidimicrobium* sp., and *Gordonia* sp. (Huang and Jaffé, 2019; Berhanu et al., 2023). An active sludge community in anaerobic conditions can also be used for PFAS biodegradation (Yu et al., 2022). Microbial degradation, although promising, still requires more work on identifying robust microorganisms and enzymes that can degrade PFAS in a targeted way (Berhanu et al., 2023). Thermal methods are another type of treatment processes used for the removal of PFAS (Winchell et al., 2022). These include microwave hydrothermal treatment, subcritical or supercritical treatment, electrical discharge plasma technology, or incineration, among others (Verma et al., 2023). These processes show good results at a laboratory scale but their applications in the real world still need to be investigated. Additional limitations are by-product formation, poor performance and high energy consumption (Verma et al., 2023). Oxidative and reductive processes can also be used as a mechanism for PFAS mitigation (Gar Alalm and Boffito, 2022). Electrochemical oxidation (Wang et al., 2022; Barisci and Suri, 2023; Mirabediny et al., 2023) as well as UV photolysis (Chen et al., 2022) are some of those methods which are gaining popular attention. Their efficiency depends on the chemical structure of the PFAS to be destructed. On top of that, nanomaterials are being explored for the elimination of PFAS (Saleh et al., 2019; Modiri-Gharehveran et al., 2023). Although all of these processes would serve a purpose of PFAS remediation, they could also have a detrimental effect on the environment, failing to restore the polluted sites to their original state (Buttle et al., 2023). Combinations of different techniques and further research will point us in the right direction for targeted PFAS degradation in complex matrices, being mindful of careful optimization and the formation of co-contaminants in the process.

One of the critical global environmental and public health challenges is the concentration of PFAS in wastewater biosolids, which is exacerbated by wastewater treatment plants aggregating these substances (Thompson et al., 2022). Crucially, treatment processes such as anaerobic digestion can transform PFAS precursors into more harmful terminal end compounds subject to regulation, which persist in biosolids applied to land (Lenka et al., 2021; O'Connor et al., 2022). This cycle poses a risk of PFAS accumulation in soil and crops, underscoring the need for advanced treatment methods and regulatory control to mitigate food chain contamination (Link et al., 2024). There are many understudied variables linked to PFAS uptake in feed materials and products such as the transfer of variable PFAS amounts from feed to animals and products; variation in PFAS feed levels due to species, origin, season, and production method; animal sensitivity and contamination duration; and limited knowledge of

TABLE 4 List of available sensor technologies for PFAS detection.

Method	Type of technology	Sample	Detection time (~sample preparation)	LOD	Specificity	Recovery rate	Complexity 1–3[1]	PFAS detected	References
Optical sensors									
Bioassay based on oligonucleotide modified gold (Au) nanoparticles (NPs)	Absorbance	River water	2 days (30 min)	10 pM	NS	103.4%	2	PFOS	Xia et al. (2011)
AuNPs	Colorimetric detection	Not tested in real world samples	10 min (−)	250 μM	Group selectivity for perfluorocarboxylic acids	–	2	PFOA	Takayose et al. (2012)
Molecularly imprinted polymer (MIP)–SiO$_2$ NPs	Fluorescence	River water	10–15 min (5 min)	11.14 nM	Selective over PFOA, PFHxA, PFHxS, Phenol, and SDBS	95.7–101%	2	PFOS	Feng et al. (2014)
Au-NPs	UV–vis absorbance	Tap water, river water	30 min (20 min)	10 μg/L	Not selective between perfluorinated compounds	85–115%	2	PFCs (CF$_2$ ≥ 7)	Niu et al. (2014)
Janus Green B (JGB)	Resonance light scattering (RLS)	Tap water, river water	5–10 min (15 min)	5.6 nM	Selective over 8 structural analogs	91–104%	3	PFOS	Cheng et al. (2016)
Surface plasmon resonance (SPR)-plastic optical fiber (POF)-MIP	Refractive index	Water	10–15 min (NS)	0.26 nM	Selective over a mixture sample containing 11 PFAS (C$_4$-C$_{11}$)	NS	3	PFOA	Cennamo et al. (2018a)
SPR-POF biosensor	Refractive index	Seawater	15 min (NS)	0.4–0.5 nM	NS	NS	3	PFOA PFOS	Cennamo et al. (2018b)
Nile blue A	Fluorescence	Tap water, river water	30 min (85 min)	3.2 nM	Selective over 8 structural analogs	94.2–103.4%	2	PFOS	Chen et al. (2018)
Smartphone app	Smartphone camera (RGB signal)	Tap water, groundwater	dual-LPE: 5 min (5 min) SPE: 3 h (30 min)	12 nM (dual-LPE) 1.2 nM (SPE)	Not selective over other anionic surfactants	60–85%	1	PFOA	Fang et al. (2018)
Covalent Organic Frameworks (COFs)-functionalized upconversion nanoparticles (UCNPs) (UCNPs@COFs)	Fluorescence	Tap water and food packaging materials	10 min (20–50 min)	0.15 pM	Selective over 6 structural analogs	103–108%	3	PFOS	Li et al. (2019)

(Continued)

TABLE 4 (Continued)

Method	Type of technology	Sample	Detection time (~sample preparation)	LOD	Specificity	Recovery rate	Complexity 1–3[1]	PFAS detected	References
Carbon quantum dots (CDs)	Fluorescence	Tap water, river water	30 min (30 min)	18.27 nM	Selective over 8 structural analogs	97.9–104.8%	2	PFOS	Chen et al. (2019)
Nitrogen doped carbon dots (N-CDs) with ethidium bromide	Fluorescence Second-order scattering (SOS)	Tap water, river water	30 min (85 min)	27.8 nM	Highly selective over 8 structural analogs	90.15–101.44%	2	PFOS	Chen et al. (2020)
ssDNA aptamer	Fluorescence	Wastewater	45 min (NS)	0.17 μM	Not selective over structurally similar PFAS (e.g., PFHxS, PFHpA)	NS	2	PFOA	Park et al. (2022)
Competitive molecular interaction in microfluidic chip	Smartphone camera (capillary flow velocity)	Effluent wastewater	5–30 min (0 min)	24.2 pM	Selective over SDS, Tween-20 and CTAB	NS	1	PFOA	Breshears et al. (2023)
Electrochemical sensors									
Fluorous membrane ion-selective electrodes (ISEs)	Potentiometry	Lake water	2 days (5 min)	0.86 nM	Minor interference with homologs differing in chain length, e.g., PFHxS, PFBS; $K^{pot}_{PFOS^-,PFHxS^-}$: -1.91 ± 0.01; $K^{pot}_{PFOS^-,PFBS^-}$: -3.19 ± 0.02	95.5 ± 2.8%	3	PFOS	Chen et al. (2013)
Inhibition biocatalysis of enzymatic biofuel cell	Voltammetry	Reservoir and River water	20 min (5 min)	1.6 nM	Selective over 4 structural analogs, and 2 other chemicals (SMNBS and SDS)	97.3–106.5%	2	PFOS	Zhang et al. (2014)
MIP modified TiO$_2$ nanotube arrays	Photo-electrochemistry	Tap water, river water, mountain water	3 h (5 min)	0.17 nM	Selective over 5 structural analogs	95.81–117.83%	2	PFOS	Tran et al. (2014)
MIP functionalized nanosheets	Electro-chemiluminescence	Tap water, river water	20 min (30–60 min)	24 pM	Selective over 10 structural analogs	96.9–103.8%	3	PFOA	Chen et al. (2015)
MIP on pencil lead	Potentiometry	Water	3 min (NS)	100 nM (PFOA)	Selective over anionic surfactants SDS and SDBS	NS	3	PFOA PFOS 6:2FTS	Fang et al. (2016)

(Continued)

TABLE 4 (Continued)

Method	Type of technology	Sample	Detection time (~sample preparation)	LOD	Specificity	Recovery rate	Complexity 1–3[1]	PFAS detected	References
MIP-coated gold electrode	Voltammetry	Drinking water	15 min (20 min)	0.04 nM	Small interference effect with DBSA, PFOA, PFHxA, PFHxS, HFBA and PFBS	82–110%	2	PFOS	Karimian et al. (2018)
Metal organic framework (MOF) capture probes	Impedance	Tap water, groundwater	8 h (NS)	1 pM	NS	NS	3	PFOS	Cheng et al. (2020)

[1]1, No training or facilities required; 2, Minimal training and facilities required; 3, Technical staff and facilities required.

PFAS substances. To ensure food safety and sustainability, it is crucial to reduce or eliminate PFAS sources in feed to protect human and animal health, as well as the broader environment, until more scientific evidence is available. Furthermore, in certain foodstuffs such as seafood, studies have reported that cooking methods such as boiling, frying and baking do not reduce the concentration of PFAS (Taylor et al., 2019; Chen et al., 2023). Surprisingly, in some cases, the cooking actually increased the concentration of the sum of PFAS in seafood, increasing the risks of dietary exposure of these chemicals.

Due to the large extent of PFAS occurrence in foodstuffs, combined with the low legislative maximum levels of detection, there is a possibility that PFAS contamination will be present in all tested foods as official standard analytical methods become more readily available. In this scenario, researchers and policymakers are faced with an uneasy question: Would the recommended course of action be to destroy all the contaminated food above regulatory PFAS limits? This solution would not be sustainable in a world where the population in need of food is estimated to grow exponentially. There needs to be a way to ensure sustainability in the current food system while dealing with and mitigating the PFAS problem. The use of PFAS-free feed sources would be a crucial step in this process. Further scientific evidence in relation to PFAS and feed would help to better understand PFAS behavior in the food chain and develop mitigation strategies accordingly. Additional measures would involve the implementation of strict control and monitoring of PFAS-containing products entering the food chain, regulatory oversight to enforce legislation on PFAS maximum levels, safe husbandry practices, providing education and awareness among stakeholders, and fostering collaboration between agriculture, food industry and regulatory bodies to adapt and implement the best mitigation strategies possible. Moreover, the challenge of PFAS contamination takes on a different dimension in low-income countries, as these regions often lack the infrastructure and resources to effectively monitor and manage such contaminants. The limited availability of advanced analytical methods for detecting PFAS compounds exacerbates the issue, potentially leading to higher exposure levels in local food supplies. Furthermore, the economic constraints and dependence on agricultural outputs make it difficult for these countries to discard contaminated foodstuffs, as doing so could aggravate food insecurity and economic hardships. In addition, the trend of high-income countries importing high-quality food from low-income countries presents a complex dilemma in the context of PFAS contamination. This practice could lead to a situation where low-income countries are incentivized to export their best produce, potentially leaving lower quality, and possibly more contaminated, foodstuffs for local consumption. This dynamic not only raises concerns about food safety and equity but also about the sustainability of food systems, as developing nations might face increased pressure to meet export demands while grappling with contamination issues. In these settings, sustainable approaches to the PFAS problem are not only crucial but also need to be tailored to local capacities and realities. This includes developing cost-effective methods for PFAS detection and remediation, strengthening regulatory frameworks, and enhancing local expertise and awareness about PFAS risks. International cooperation and support are vital to establish sustainable strategies for managing PFAS contamination, ensuring that measures taken do not compromise food security and livelihoods while safeguarding public health and the environment.

6 Conclusion

PFAS assessment and management requires holistic and cross-cutting approaches combined with novel analytical tools in a more dynamic legislative framework. There is still a need for the development of standardized reliable sensitive and cost-effective methods for the detection of sub-nanogram levels of PFAS in complex food matrixes (Garg et al., 2022). Both targeted and non-targeted screening procedures should be further evaluated in order to broaden the control and monitoring of the vast number of per- and polyfluoroalkyl substances in the environment. In addition, a greater understanding of the occurrence of these compounds is required and without highly sensitive inexpensive analytical tools this can only be performed in limited laboratories specializing in this area of work. The ultimate goal is to both minimize PFAS exposure and ensure a sustainable food supply. This requires a multi-faceted approach involving regulatory, industry, and consumer efforts.

Author contributions

DS-H: Writing – original draft, Writing – review & editing. HM: Writing – review & editing. MS: Writing – review & editing. RT: Writing – review & editing. SH: Writing – review & editing. LM: Writing – review & editing. KC: Writing – review & editing.

Conflict of interest

The authors declare that the research was conducted in the absence of any commercial or financial relationships that could be construed as a potential conflict of interest.

The author(s) declared that they were an editorial board member of Frontiers, at the time of submission. This had no impact on the peer review process and the final decision.

Publisher's note

All claims expressed in this article are solely those of the authors and do not necessarily represent those of their affiliated organizations, or those of the publisher, the editors and the reviewers. Any product that may be evaluated in this article, or claim that may be made by its manufacturer, is not guaranteed or endorsed by the publisher.

References

AOAC International. (2022). *New initiative: integrated standards and official methods development project for per- and Polyfluoroalkyl substances (PFAS) in foods*. Available at: https://www.aoac.org/news/new-initiative-integrated-standards-and-official-methods-development-project-for-per-and-polyfluoroalkyl-substances-pfas-in-foods/#:~:text=New%20Initiative%3A%20Integrated%20Standards%20and%20Official%20Methods%20Development,processed%20and%20packaged%20foods%20and%20raw%20agricultural%20commodities (Accessed August 9, 2023).

ATSDR (2021). *Toxicological profile for Perfluoroalkyls*. Atlanta: Department of Health and Human Services, Public Health Service.

Baluyot, J. C., Reyes, E. M., and Velarde, M. C. (2021). Per- and polyfluoroalkyl substances (PFAS) as contaminants of emerging concern in Asia's freshwater resources. *Environ. Res.* 197:111122. doi: 10.1016/j.envres.2021.111122

Barisci, S., and Suri, R. (2023). Degradation of emerging per- and polyfluoroalkyl substances (PFAS) using an electrochemical plug flow reactor. *J. Hazard. Mater.* 460:132419. doi: 10.1016/j.jhazmat.2023.132419

Berhanu, A., Mutanda, I., Taolin, J., Qaria, M. A., Yang, B., and Zhu, D. (2023). A review of microbial degradation of per- and polyfluoroalkyl substances (PFAS): biotransformation routes and enzymes. *Sci. Total Environ.* 859:160010. doi: 10.1016/j.scitotenv.2022.160010

Breshears, L. E., Mata-Robles, S., Tang, Y., Baker, J. C., Reynolds, K. A., and Yoon, J.-Y. (2023). Rapid, sensitive detection of PFOA with smartphone-based flow rate analysis utilizing competitive molecular interactions during capillary action. *J. Hazard. Mater.* 446:130699. doi: 10.1016/j.jhazmat.2022.130699

Brunn, H., Arnold, G., Körner, W., Rippen, G., Steinhäuser, K. G., and Valentin, I. (2023). PFAS: forever chemicals—persistent, bioaccumulative and mobile. Reviewing the status and the need for their phase out and remediation of contaminated sites. *Environ. Sci. Eur.* 35:20. doi: 10.1186/s12302-023-00721-8

Buck, R. C., Franklin, J., Berger, U., Conder, J. M., Cousins, I. T., De Voogt, P., et al. (2011). Perfluoroalkyl and polyfluoroalkyl substances in the environment: terminology, classification, and origins. *Integr. Environ. Assess. Manag.* 7, 513–541. doi: 10.1002/ieam.258

Buttle, E., Sharp, E. L., and Fisher, K. (2023). Managing ubiquitous 'forever chemicals': more-than-human possibilities for the problem of Pfas. *N. Z. Geogr.* 79, 97–106. doi: 10.1111/nzg.12365

Cennamo, N., D'agostino, G., Porto, G., Biasiolo, A., Perri, C., Arcadio, F., et al. (2018a). A molecularly imprinted polymer on a Plasmonic plastic optical Fiber to detect Perfluorinated compounds in water. *Sensors* 18:1836. doi: 10.3390/s18061836

Cennamo, N., Zeni, L., Tortora, P., Regonesi, M. E., Giusti, A., Staiano, M., et al. (2018b). A high sensitivity biosensor to detect the presence of perfluorinated compounds in environment. *Talanta* 178, 955–961. doi: 10.1016/j.talanta.2017.10.034

Chen, Q., Cheng, Z., Du, L., Zhu, P., and Tan, K. (2018). A sensitive three-signal assay for the determination of PFOS based on the interaction with Nile blue A. *Anal. Methods* 10, 3052–3058. doi: 10.1039/C8AY00938D

Chen, L. D., Lai, C.-Z., Granda, L. P., Fierke, M. A., Mandal, D., Stein, A., et al. (2013). Fluorous membrane ion-selective electrodes for Perfluorinated surfactants: trace-level detection and in situ monitoring of adsorption. *Anal. Chem.* 85, 7471–7477. doi: 10.1021/ac401424j

Chen, S., Li, A., Zhang, L., and Gong, J. (2015). Molecularly imprinted ultrathin graphitic carbon nitride nanosheets–based electrochemiluminescence sensing probe for sensitive detection of perfluorooctanoic acid. *Anal. Chim. Acta* 896, 68–77. doi: 10.1016/j.aca.2015.09.022

Chen, G., Liu, S., Shi, Q., Gan, J., Jin, B., Men, Y., et al. (2022). Hydrogen-polarized vacuum ultraviolet photolysis system for enhanced destruction of perfluoroalkyl substances. *J. Hazard. Mater. Lett.* 3:100072. doi: 10.1016/j.hazl.2022.100072

Chen, Z., Zhan, X., Zhang, J., Diao, J., Su, C., Sun, Q., et al. (2023). Bioaccumulation and risk mitigation of legacy and novel perfluoroalkyl substances in seafood: insights from trophic transfer and cooking method. *Environ. Int.* 177:108023. doi: 10.1016/j.envint.2023.108023

Chen, Q., Zhu, P., Xiong, J., Gao, L., and Tan, K. (2019). A sensitive and selective triple-channel optical assay based on red-emissive carbon dots for the determination of PFOS. *Microchem. J.* 145, 388–396. doi: 10.1016/j.microc.2018.11.003

Chen, Q., Zhu, P., Xiong, J., Gao, L., and Tan, K. (2020). A new dual-recognition strategy for hybrid ratiometric and ratiometric sensing perfluorooctane sulfonic acid based on high fluorescent carbon dots with ethidium bromide. *Spectrochim. Acta A Mol. Biomol. Spectrosc.* 224:117362. doi: 10.1016/j.saa.2019.117362

Cheng, Y. H., Barpaga, D., Soltis, J. A., Shutthanandan, V., Kargupta, R., Han, K. S., et al. (2020). Metal–organic framework-based microfluidic impedance sensor platform for ultrasensitive detection of Perfluorooctanesulfonate. *ACS Appl. Mater. Interfaces* 12, 10503–10514. doi: 10.1021/acsami.9b22445

Cheng, Z., Zhang, F., Chen, X., Du, L., Gao, C., and Tan, K. (2016). Highly sensitive and selective detection of perfluorooctane sulfonate based on the Janus green B resonance light scattering method. *Anal. Methods* 8, 8042–8048. doi: 10.1039/C6AY02739C

Daems, E., Moro, G., Berghmans, H., Moretto, L. M., Dewilde, S., Angelini, A., et al. (2021). Native mass spectrometry for the design and selection of protein bioreceptors for perfluorinated compounds. *Analyst* 146, 2065–2073. doi: 10.1039/D0AN02005B

Delatour, T., Theurillat, X., Mujahid, C., Eriksen, B. R., and Mottier, P. (2023). Determination of poly- and Perfluoroalkylated substances in food: how consistent are results across laboratories? *J. Agric. Food Chem.* 71, 4767–4768. doi: 10.1021/acs.jafc.3c01306

DTU National Food Institute (2023). *Indhold af PFAS i fiskemel og via indhold i økologisk foder i økologiske æg*. DTU Fødevareinstituttet. Available at: https://www.bing.com/ck/a?!&&p=295fb98868be87afJmltdHM9MTcwNTk2ODAwMCZpZ3VpZD0zZTcyNDg5Zi1lNWQyLTY2YTUtMmU0NC01YWYzZTRkNDY3ODAmaW5zaWQ9NTE4OA&ptn=3&ver=2&hsh=3&fclid=3e72489f-e5d2-66a5-2e44-5af3e4d46780&psq=PFAS-i-oekologiske-aeg-og-foder-Jan-2023%2520(2).pdf&u=a1aHR0cHM6Ly93d3d3cuZm9vZC5kdHUuZGsvLS9tZWRpYS9pbnN0aXR1dHRlci9mb2VkZXZhcmVpbnN0aXR1dHRldC9wdWJsaWthdGlvbmVyL3B1Ymxpa2F0aW9uZXJfMDIzL3BmYXMtaS1vZWtvbG9naXNrZS1hZWctb2ctZm9kZXItamFuLTIwMjMucGRmPxPWRhJmhhc2g9MzA4RjE0NDZGOUFFQzhFNjc0NkY4NDQ4MkRCRCY1Rjg0QjJGGRc2Ng&ntb=1

DWI (2022). *PFAS and forever chemicals*. Available at: https://www.dwi.gov.uk/pfas-and-forever-chemicals/#top (Accessed December 29, 2023).

ECHA (2022). *Proposal to ban 'forever chemicals' in firefighting foams throughout the Eu*. Available at: https://echa.europa.eu/-/proposal-to-ban-forever-chemicals-in-firefighting-foams-throughout-the-eu (Accessed December 28, 2022).

EFSA CONTAM PanelSchrenk, D., Bignami, M., Bodin, L., Chipman, J. K., Del Mazo, J., et al. (2020). Risk to human health related to the presence of perfluoroalkyl substances in food. *EFSA J.* 18:e06223. doi: 10.2903/j.efsa.2020.6223

Eichbaum, K., Brinkmann, M., Buchinger, S., Reifferscheid, G., Hecker, M., Giesy, J. P., et al. (2014). *In vitro* bioassays for detecting dioxin-like activity—application potentials and limits of detection, a review. *Sci. Total Environ.* 487, 37–48. doi: 10.1016/j.scitotenv.2014.03.057

Environment Agency (2021). *Poly- and perfluoroalkyl substances (PFAS): sources, pathways and environmental data*. Bristol: Environment Agency (*2021*).

European Commission (2020). *Chemicals strategy for sustainability towards a toxic-free environment*. Brussels. Publications Office of the European Union. Available at: https://eur-lex.europa.eu/LexUriServ/LexUriServ.do?uri=SWD:2020:0250:FIN:EN:PDF

European Commission and Directorate-General for Health and Food Safety (2017). *Commission regulation (Eu) 2017/644 of 5 April 2017 laying down methods of sampling and analysis for the control of levels of dioxins, dioxin-like Pcbs and non-dioxin-like Pcbs in certain foodstuffs and repealing regulation (Eu) no 589/2014*. Brussels: Official Journal of the European Union.

European Commission and Directorate-General for Health and Food Safety (2022a). *Commission implementing regulation (Eu) 2022/1428 of 24 august 2022 laying down methods of sampling and analysis for the control of perfluoroalkyl substances in certain foodstuffs*. Brussels: Official Journal of the European Union.

European Commission and Directorate-General for Health and Food Safety (2022b). *Commission recommendation (Eu) 2022/1431 of 24 august 2022 on the monitoring of perfluoroalkyl substances in food*. Brussels: Official Journal of the European Union.

European Commission and Directorate-General for Health and Food Safety (2022c). *Commission regulation (Eu) 2022/2388 of 7 December 2022 amending regulation (Ec) no 1881/2006 as regards maximum levels of perfluoroalkyl substances in certain foodstuffs*. Brussels: Official Journal of the European Union.

European Commission and Directorate-General for Health and Food Safety (2023). *Commission regulation (Eu) 2023/915 of 25 April 2023 on maximum levels for certain contaminants in food and repealing regulation (Ec) no 1881/2006*. Brussels: Official Journal of the European Union.

European Parliament and Council of the European Union (2006). *Regulation (Ec) no 1907/2006 of the European Parliament and of the council of 18 December 2006 concerning the registration, evaluation, authorisation and restriction of chemicals (Reach), establishing a European chemicals Agency, amending directive 1999/45/Ec and repealing council regulation (Eec) no 793/93 and commission regulation (Ec) no 1488/94 as well as council directive 76/769/Eec and commission directives 91/155/Eec, 93/67/Eec, 93/105/Ec and 2000/21/Ec*. Brussels: Official journal of the European Union.

European Parliament and Council of the European Union (2020). *Directive (Eu) 2020/2184 of the European Parliament and of the council of 16 December 2020 on the quality of water intended for human consumption*. Brussels: Official Journal of the European Union.

European Union Reference Laboratory for Halogenated POPs in Feed and Food (2022). *Guidance document on analytical parameters for the determination of per- and Polyfluoroalkyl substances (Pfas) in food and feed, version 1.2 of 11 May 2022*. EURL for halogenated POPs in Feed and Food c/o State Institute for Chemical and Veterinary Analysis Freiburg. Available at: https://eurl-pops.eu/user/pages/05.news/18.Guidance-Document-PFAS/Guidance%20Document%20on%20Analytical%20Parameters%20for%20the%20Determination%20of%20Per-%20and%20Polyfluoroalkyl%20Substances%20(PFAS)%20in%20Food%20and%20Feed%20V1.2%20(incl.%20Annex%20V1.0).pdf?g-64cde584

Evich, M. G., Davis, M. J. B., Mccord, J. P., Acrey, B., Awkerman, J. A., Knappe, D. R. U., et al. (2022). Per- and polyfluoroalkyl substances in the environment. *Science* 375:eabg9065. doi: 10.1126/science.abg9065

Fang, C., Chen, Z., Megharaj, M., and Naidu, R. (2016). Potentiometric detection of Afffs based on Mip. *Environ. Technol. Innov.* 5, 52–59. doi: 10.1016/j.eti.2015.12.003

Fang, C., Zhang, X., Dong, Z., Wang, L., Megharaj, M., and Naidu, R. (2018). Smartphone app-based/portable sensor for the detection of fluoro-surfactant PFOA. *Chemosphere* 191, 381–388. doi: 10.1016/j.chemosphere.2017.10.057

Feng, H., Wang, N., Tran, T. T., Yuan, L., Li, J., and Cai, Q. (2014). Surface molecular imprinting on dye–(Nh2)–SiO_2 Nps for specific recognition and direct fluorescent quantification of perfluorooctane sulfonate. *Sensors Actuators B Chem.* 195, 266–273. doi: 10.1016/j.snb.2014.01.036

Fernandes, A. R., Lake, I. R., Dowding, A., Rose, M., Jones, N. R., Smith, F., et al. (2023). The transfer of environmental contaminants (brominated and chlorinated dioxins and biphenyls, PBDEs, HBCDDs, PCNs and PFAS) from recycled materials used for bedding to the eggs and tissues of chickens. *Sci. Total Environ.* 892:164441. doi: 10.1016/j.scitotenv.2023.164441

Ganesan, S., Chawengkijwanich, C., Gopalakrishnan, M., and Janjaroen, D. (2022). Detection methods for sub-nanogram level of emerging pollutants – per and polyfluoroalkyl substances. *Food Chem. Toxicol.* 168:113377. doi: 10.1016/j.fct.2022.113377

Gar Alalm, M., and Boffito, D. C. (2022). Mechanisms and pathways of Pfas degradation by advanced oxidation and reduction processes: a critical review. *Chem. Eng. J.* 450:138352. doi: 10.1016/j.cej.2022.138352

Garg, S., Kumar, P., Greene, G., Mishra, V., Avisar, D., Sharma, R., et al. (2022). Nano-enabled sensing of per−/poly-fluoroalkyl substances (Pfas) from aqueous systems – a review. *J. Environ. Manag.* 308:114655. doi: 10.1016/j.jenvman.2022.114655

Getzinger, G. J., and Ferguson, P. L. (2021). High-throughput trace-level suspect screening for per- and Polyfluoroalkyl substances in environmental waters by peak-focusing online solid phase extraction and high-resolution mass spectrometry. *ACS ES T Water* 1, 1240–1251. doi: 10.1021/acsestwater.0c00309

Göckener, B., Fliedner, A., Weinfurtner, K., Rüdel, H., Badry, A., and Koschorreck, J. (2023). Tracking down unknown Pfas pollution – the direct top assay in spatial monitoring of surface waters in Germany. *Sci. Total Environ.* 898:165425. doi: 10.1016/j.scitotenv.2023.165425

Hammel, E., Webster, T. F., Gurney, R., and Heiger-Bernays, W. (2022). Implications of Pfas definitions using fluorinated pharmaceuticals. *iScience* 25:104020. doi: 10.1016/j.isci.2022.104020

HBM4EU (2022). *Substance report: per- and poly-fluoroalkyl substances (PFAS)*. HBM4EU. Available at: https://www.hbm4eu.eu/wpcontent/uploads/2022/07/PFAS_Substance-report.pdf

Houde, M., De Silva, A. O., Muir, D. C. G., and Letcher, R. J. (2011). Monitoring of perfluorinated compounds in aquatic biota: an updated review. *Environ. Sci. Technol.* 45, 7962–7973. doi: 10.1021/es104326w

Huang, S., and Jaffé, P. R. (2019). Defluorination of Perfluorooctanoic acid (PFOA) and Perfluorooctane sulfonate (PFOS) by *Acidimicrobium* sp. strain A6. *Environ. Sci. Technol.* 53, 11410–11419. doi: 10.1021/acs.est.9b04047

Huang, Y., Xu, T., Wang, W., Wen, Y., Li, K., Qian, L., et al. (2019). Lateral flow biosensors based on the use of micro- and nanomaterials: a review on recent developments. *Microchim. Acta* 187:70. doi: 10.1007/s00604-019-3822-x

Ingelido, A. M., Abballe, A., Gemma, S., Dellatte, E., Iacovella, N., De Angelis, G., et al. (2018). Biomonitoring of perfluorinated compounds in adults exposed to contaminated drinking water in the Veneto region, Italy. *Environ. Int.* 110, 149–159. doi: 10.1016/j.envint.2017.10.026

Karimian, N., Stortini, A. M., Moretto, L. M., Costantino, C., Bogialli, S., and Ugo, P. (2018). Electrochemosensor for trace analysis of Perfluorooctanesulfonate in water based on a molecularly imprinted poly (o-phenylenediamine) polymer. *ACS Sens.* 3, 1291–1298. doi: 10.1021/acssensors.8b00154

Kowalska, D., Sosnowska, A., Bulawska, N., Stępnik, M., Besselink, H., Behnisch, P., et al. (2023). How the structure of per- and Polyfluoroalkyl substances (Pfas) influences their binding potency to the peroxisome proliferator-activated and thyroid hormone receptors–an *in silico* screening study. *Molecules* 28:479. doi: 10.3390/molecules28020479

Lenka, S. P., Kah, M., and Padhye, L. P. (2021). A review of the occurrence, transformation, and removal of poly- and perfluoroalkyl substances (Pfas) in wastewater treatment plants. *Water Res.* 199:117187. doi: 10.1016/j.watres.2021.117187

Li, J., Zhang, C., Yin, M., Zhang, Z., Chen, Y., Deng, Q., et al. (2019). Surfactant-sensitized covalent organic frameworks-functionalized lanthanide-doped nanocrystals: an ultrasensitive sensing platform for Perfluorooctane sulfonate. *ACS Omega* 4, 15947–15955. doi: 10.1021/acsomega.9b01996

Link, G. W., Reeves, D. M., Cassidy, D. P., and Coffin, E. S. (2024). Per- and polyfluoroalkyl substances (PFAS) in final treated solids (biosolids) from 190 Michigan wastewater treatment plants. *J. Hazard. Mater.* 463:132734. doi: 10.1016/j.jhazmat.2023.132734

Liu, L., Qu, Y., Huang, J., and Weber, R. (2021). Per- and polyfluoroalkyl substances (PFASS) in Chinese drinking water: risk assessment and geographical distribution. *Environ. Sci. Eur.* 33:6. doi: 10.1186/s12302-020-00425-3

Mann, M. M., Tang, J. D., and Berger, B. W. (2022). Engineering human liver fatty acid binding protein for detection of poly- and perfluoroalkyl substances. *Biotechnol. Bioeng.* 119, 513–522. doi: 10.1002/bit.27981

Mirabedini, M., Sun, J., Yu, T. T., Åkermark, B., Das, B., and Kumar, N. (2023). Effective PFAS degradation by electrochemical oxidation methods-recent progress and requirement. *Chemosphere* 321:138109. doi: 10.1016/j.chemosphere.2023.138109

Modiri-Gharehveran, M., Choi, Y., Zenobio, J. E., and Lee, L. S. (2023). Perfluoroalkyl acid transformation and mitigation by nNiFe-activated carbon nanocomposites in

steady-state flow column studies. *J. Environ. Sci.* 127, 678–687. doi: 10.1016/j.jes.2022.06.040

Moro, G., Bottari, F., Liberi, S., Covaceuszach, S., Cassetta, A., Angelini, A., et al. (2020). Covalent immobilization of delipidated human serum albumin on poly (pyrrole-2-carboxylic) acid film for the impedimetric detection of perfluorooctanoic acid. *Bioelectrochemistry* 134:107540. doi: 10.1016/j.bioelechem.2020.107540

Nahar, K., Zulkarnain, N. A., and Niven, R. K. (2023). A review of analytical methods and Technologies for Monitoring per- and Polyfluoroalkyl Substances (PFAS) in water. *Water* 15:3577. doi: 10.3390/w15203577

Niu, H., Wang, S., Zhou, Z., Ma, Y., Ma, X., and Cai, Y. (2014). Sensitive colorimetric visualization of Perfluorinated compounds using poly (ethylene glycol) and Perfluorinated thiols modified gold nanoparticles. *Anal. Chem.* 86, 4170–4177. doi: 10.1021/ac403406d

O'connor, J., Bolan, N. S., Kumar, M., Nitai, A. S., Ahmed, M. B., Bolan, S. S., et al. (2022). Distribution, transformation and remediation of poly- and per-fluoroalkyl substances (PFAS) in wastewater sources. *Process Saf. Environ. Prot.* 164, 91–108. doi: 10.1016/j.psep.2022.06.002

OECD (2021). *Reconciling terminology of the universe of per- and Polyfluoroalkyl substances: Recommendations and practical guidance*. OECD Environment, Health and Safety Publications, Paris.

Ogunbiyi, O. D., Ajiboye, T. O., Omotola, E. O., Oladoye, P. O., Olanrewaju, C. A., and Quinete, N. (2023). Analytical approaches for screening of per- and poly fluoroalkyl substances in food items: a review of recent advances and improvements. *Environ. Pollut.* 329:121705. doi: 10.1016/j.envpol.2023.121705

OSPAR Commission (2013). *Ospar list of chemicals for priority action (revised 2013)*. OSPAR Convention for the Protection of the Marine Environment of the North-East Atlantic. Available at: https://view.officeapps.live.com/op/view.aspx?src=https%3A%2F%2Fospar-archive.s3.eu-west-1.amazonaws.com%2FDECRECS%2FAGREEMENTS%2F04-12e_agreement_list_of_chemicals_for_priority_action.doc%3FX-Amz-Content-Sha256%3DUNSIGNED-PAYLOAD%26X-Amz-Algorithm%3DAWS4-HMAC-SHA256%26X-Amz-Credential%3DAKIAJIACMW2T5USCSU5A%252F20240123%252Feu-west-1%252Fs3%252Faws4_request%26X-Amz-Date%3D20240123T155414Z%26X-Amz-SignedHeaders%3Dhost%26X-Amz-Expires%3D900%26X-Amz-Signature%3D95226355b85cfaad1ed08a8e79c9d1c34bc72f0cfe5f19ca2f1ae820af96c69f&wdOrigin=BROWSELINK

Park, J., Yang, K., Choi, Y., and Choe, J. (2022). Novel ssdna aptamer-based fluorescence sensor for perfluorooctanoic acid detection in water. *Environ. Int.* 158:107000. doi: 10.1016/j.envint.2021.107000

Rodriguez, K., Hwang, J., Esfahani, A., Sadmani, A., and Lee, W. (2020). Recent developments of Pfas-detecting sensors and future direction: a review. *Micromachines* 11:667. doi: 10.3390/mi11070667

Saleh, N. B., Khalid, A., Tian, Y., Ayres, C., Sabaraya, I. V., Pietari, J., et al. (2019). Removal of poly- and per-fluoroalkyl substances from aqueous systems by nano-enabled water treatment strategies. *Environ. Sci.* 5, 198–208. doi: 10.1039/C8EW00621K

Sørensen, M. M., Fisker, A. B., Dalgård, C., Jensen, K. J., Nielsen, F., Benn, C. S., et al. (2023). Predictors of serum- per- and polyfluoroalkyl substance (PFAS) concentrations among infants in Guinea-Bissau, West Africa. *Environ. Res.* 228:115784. doi: 10.1016/j.envres.2023.115784

Steenland, K., Fletcher, T., and Savitz, D. A. (2010). Epidemiologic evidence on the health effects of Perfluorooctanoic acid (PFOA). *Environ. Health Perspect.* 118, 1100–1108. doi: 10.1289/ehp.0901827

Stockholm Convention. (2019). *All pops listed in the stockholm convention*. Switzerland: Secretariat of the Stockholm Convention. Available at: https://chm.pops.int/TheConvention/Thepops/Listingofpops/tabid/2509/Default.aspx (Accessed January 5, 2023).

Straková, J., Broské, S., and Grechko, V. (2023). *Forever chemicals in single-use food packaging and tableware from 17 countries* IPEN. Available at: https://ipen.org/sites/default/files/documents/ipen-packaging-report-fin2.pdf

Strynar, M., Mccord, J., Newton, S., Washington, J., Barzen-Hanson, K., Trier, X., et al. (2023). Practical application guide for the discovery of novel Pfas in environmental samples using high resolution mass spectrometry. *J. Expo. Sci. Environ. Epidemiol.* 33, 575–588. doi: 10.1038/s41370-023-00578-2

Takayose, M., Akamatsu, K., Nawafune, H., Murashima, T., and Matsui, J. (2012). Colorimetric detection of Perfluorooctanoic acid (PFOA) utilizing polystyrene-modified gold nanoparticles. *Anal. Lett.* 45, 2856–2864. doi: 10.1080/00032719.2012.696225

Tang, Z. W., Shahul Hamid, F., Yusoff, I., and Chan, V. (2023). A review of PFAS research in Asia and occurrence of PFOA and PFOS in groundwater, surface water and coastal water in Asia. *Groundw. Sustain. Dev.* 22:100947. doi: 10.1016/j.gsd.2023.100947

Taylor, M. D., Nilsson, S., Bräunig, J., Bowles, K. C., Cole, V., Moltschaniwskyj, N. A., et al. (2019). Do conventional cooking methods alter concentrations of per- and polyfluoroalkyl substances (PFASs) in seafood? *Food Chem. Toxicol.* 127, 280–287. doi: 10.1016/j.fct.2019.03.032

Thompson, K. A., Mortazavian, S., Gonzalez, D. J., Bott, C., Hooper, J., Schaefer, C. E., et al. (2022). Poly- and Perfluoroalkyl substances in municipal wastewater treatment plants in the United States: seasonal patterns and Meta-analysis of long-term trends and average concentrations. *ACS ES T Water* 2, 690–700. doi: 10.1021/acsestwater.1c00377

Tian, W., Xie, H. Q., Fu, H., Pei, X., and Zhao, B. (2012). Immunoanalysis methods for the detection of dioxins and related chemicals. *Sensors* 12, 16710–16731. doi: 10.3390/s121216710

Tian, Y., Zhou, Y., Miao, M., Wang, Z., Yuan, W., Liu, X., et al. (2018). Determinants of plasma concentrations of perfluoroalkyl and polyfluoroalkyl substances in pregnant women from a birth cohort in Shanghai, China. *Environ. Int.* 119, 165–173. doi: 10.1016/j.envint.2018.06.015

Tran, T. T., Li, J., Feng, H., Cai, J., Yuan, L., Wang, N., et al. (2014). Molecularly imprinted polymer modified TiO2 nanotube arrays for photoelectrochemical determination of perfluorooctane sulfonate (PFOS). *Sensors Actuators B Chem.* 190, 745–751. doi: 10.1016/j.snb.2013.09.048

United Nations Environment Programme (2023). *Chemicals in plastics: a technical report*. Geneva. UNEP. Available at: https://www.unep.org/resources/report/chemicals-plastics-technical-report

US EPA. (2018). *Reducing PFAS in drinking water with treatment technologies*. Available at: https://www.epa.gov/sciencematters/reducing-pfas-drinking-water-treatment-technologies (Accessed December 29, 2023).

US EPA. (2023). *Proposed PFAS national primary drinking water regulation*. Available at: https://www.epa.gov/sdwa/and-polyfluoroalkyl-substances-pfas#:~:text=On%20May%204%2C%202023%2C%20epa,Da%20%28commonly (Accessed December 29, 2023).

Verma, S., Lee, T., Sahle-Demessie, E., Ateia, M., and Nadagouda, M. N. (2023). Recent advances on PFAS degradation via thermal and nonthermal methods. *Chem. Eng. J. Adv.* 13:100421, –100411. doi: 10.1016/j.ceja.2022.100421

Voulgaropoulos, A. (2022). Mitigation of Pfas in U.S. public water systems: future steps for ensuring safer drinking water. *Environ. Prog. Sustain. Energy* 41:e13800. doi: 10.1002/ep.13800

Wang, Y., Li, L., and Huang, Q. (2022). Electrooxidation of per- and polyfluoroalkyl substances in chloride-containing water on surface-fluorinated Ti4O7 anodes: mitigation and elimination of chlorate and perchlorate formation. *Chemosphere* 307:135877. doi: 10.1016/j.chemosphere.2022.135877

Whitehead, P. (2020). *What you are allowed to drink depends on where you live!* Available at: https://www.elgalabwater.com/blog/what-you-are-allowed-drink-depends-where-you-live (Accessed January 8, 2024).

Winchell, L. J., Ross, J. J., Brose, D. A., Pluth, T. B., Fonoll, X., Norton, J. W. Jr., et al. (2022). High-temperature technology survey and comparison among incineration, pyrolysis, and gasification systems for water resource recovery facilities. *Water Environ. Res.* 94:e10715. doi: 10.1002/wer.10715

Winchell, L. J., Wells, M. J. M., Ross, J. J., Fonoll, X., Norton, J. W., Kuplicki, S., et al. (2021). Analyses of per- and polyfluoroalkyl substances (PFAS) through the urban water cycle: toward achieving an integrated analytical workflow across aqueous, solid, and gaseous matrices in water and wastewater treatment. *Sci. Total Environ.* 774:145257. doi: 10.1016/j.scitotenv.2021.145257

Xia, W., Wan, Y.-J., Wang, X., Li, Y.-Y., Yang, W.-J., Wang, C.-X., et al. (2011). Sensitive bioassay for detection of Pparα potentially hazardous ligands with gold nanoparticle probe. *J. Hazard. Mater.* 192, 1148–1154. doi: 10.1016/j.jhazmat.2011.06.023

Yu, Y., Che, S., Ren, C., Jin, B., Tian, Z., Liu, J., et al. (2022). Microbial Defluorination of unsaturated per- and Polyfluorinated carboxylic acids under anaerobic and aerobic conditions: a structure specificity study. *Environ. Sci. Technol.* 56, 4894–4904. doi: 10.1021/acs.est.1c05509

Zhang, T., Zhao, H., Lei, A., and Quan, X. (2014). Electrochemical biosensor for detection of Perfluorooctane sulfonate based on inhibition biocatalysis of enzymatic fuel cell. *Electrochemistry* 82, 94–99. doi: 10.5796/electrochemistry.82.94

Recent advances in foodborne pathogen detection using photoelectrochemical biosensors: from photoactive material to sensing strategy

Xiuxiu Dong[1], Ao Huang[1], Lilong He[1], Chaoyang Cai[1] and Tianyan You[1,2]*

[1]Key Laboratory of Modern Agricultural Equipment and Technology (Jiangsu University), Ministry of Education, School of Agricultural Engineering, Jiangsu University, Zhenjiang, China, [2]College of Agricultural Equipment Engineering, Henan University of Science and Technology, Luoyang, China

Rapid assessment and prevention of diseases caused by foodborne pathogens is one of the existing food safety regulatory issues faced by various countries, and it has received wide attention from all sectors of society. When the content of foodborne pathogens in food is higher than the limit standard and spreads in a certain way, it can cause disease outbreaks, which seriously threaten human health or life safety. Developing a novel method to detect foodborne pathogens accurately and rapidly is significant. Because of the limitations of complex steps, time-consuming, low sensitivity or poor selectivity of commonly used methods, a photoelectrochemical (PEC) biosensor based on electrochemistry is developed. Its advantages include a low background signal, fast response and simple operation. It also has broad application prospects for sensing, which has attracted wide attention. However, an organized summary of the latest PEC biosensors for foodborne pathogen sensing has not been reported. Therefore, this review introduces the recent advances in foodborne pathogen detection using PEC biosensors as follows: (i) the construction of PEC biosensors, (ii) the research status of PEC biosensors for the detection of foodborne pathogens and (iii) the direction of future development in this field. Hopefully, the study will provide some insight into developing more mature bio-sensing strategies to meet the practical needs of foodborne pathogen surveillance.

KEYWORDS

foodborne pathogens, photoelectrochemical, biosensors, detection, food safety

1 Introduction

Foodborne pathogens are microorganisms that enter humans or animals via ingestion and cause infectious or toxic diseases (Schirone et al., 2019). Foodborne diseases are an ongoing and worldwide public health problem, seriously endangering human life. According to a report by the World Health Organization in June 2021, up to 600 million cases of foodborne diseases are reported every year. About one in 10 people get sick from eating contaminated food, and the situation of foodborne diseases is more severe in developing countries than in developed countries (Todd, 2020). Food safety has become a hot topic of common concern across the whole of society (Scharff et al., 2016). Although the government is highly concerned about

this issue, foodborne illnesses remain stubbornly high. The Centers for Disease Control and Prevention (CDC) estimates that one in six people in the United States are affected each year, and that up to 3,000 die from eating contaminated food (Scallan et al., 2011).

Common foodborne pathogens include *Listeria monocytogenes* (Taylor et al., 2019; Vongkamjan et al., 2017; Capita et al., 2019), *Staphylococcus aureus* (*S. aureus*) (Kümmel et al., 2016; Li et al., 2022; Argudín et al., 2012), *Vibrio parahaemolyticus* (Miles et al., 1997; Sun et al., 2016; Li LingZhi et al., 2019), *Salmonella* (Paniel and Noguer, 2019; Pye et al., 2023; Han et al., 2017) and *Escherichia coli* (*E. coli*) (Leng et al., 2022; Munekata et al., 2020; Lima et al., 2017) (Table 1). These pathogens have different tolerance to the external environment, and the foods they contaminate also differ (Guldimann and Johler, 2018). The prevention of foodborne diseases is mainly achieved by washing food, and keeping raw from cooked foods separate (Todd, 2020; Palomino-Camargo et al., 2018). Nevertheless, pathogenic bacteria can still enter processed foods at the packaging, transportation and marketing stages, making it challenging to eliminate contamination through these means. As a result, there is a need to focus on methods for rapid and early detection of pathogenic bacteria to significantly reduce the incidence of foodborne diseases.

Currently, traditional detection methods for foodborne pathogens include microbial and immunological detection (Liu et al., 2023; Xu et al., 2021). These methods can be used for the qualitative and quantitative detection of foodborne pathogens with reliable results. However, they are labor-intensive and time-consuming (Hao and Wang, 2016). In recent years, many optical biosensors have been used for the detection of foodborne pathogens (Xu et al., 2021, 2023), such as fluorescent (FL) biosensors (Liu et al., 2021), colorimetric (CL) biosensors (Zhu S. et al., 2021) and surface-enhanced Raman scatting (SERS) biosensors (Chen et al., 2017). FL biosensors are highly sensitive, but the instrument is very expensive (Liu et al., 2022). CL biosensors enable rapid detection, while their sensitivity is easily limited by color changes (Acunzo et al., 2022). SERS biosensors are simple to operate, but SERS probes are easily affected by the environment, resulting in signal fluctuations (Zhu et al., 2023). Compared with optical biosensors, electrochemical (EC) biosensors have the advantages of high sensitivity and low detection limits, and they have been increasingly used to detect foodborne pathogens (Wang J. et al., 2024; Yu et al., 2021; Wang B. et al., 2023). In particular, photoelectrochemical (PEC) biosensors developed based on EC biosensors have been widely explored in pathogen detection due to their advantages of high sensitivity, simple apparatus, quick detection and low cost (Ding et al., 2021; Zhang Z. et al., 2021). Some reviews have focused on the progress in PEC bio-sensing technologies and their applications for detecting various analyzes, such as metal ions, tumor markers, nucleic acids and antibiotics (Shi et al., 2022; Zhao et al., 2016; Bettazzi and Palchetti, 2018; Dong et al., 2022). Although PEC biosensors have been successfully used for the detection of foodborne pathogens (Wang X. et al., 2024; Ma et al., 2023; Yang G. et al., 2020; Yang H. et al., 2020; Jiang et al., 2024; Zhao et al., 2024; Chen et al., 2024), as far as is known, there has been no review of PEC biosensors for monitoring foodborne pathogens. Accordingly, this paper reviews the application of PEC biosensors in detecting foodborne pathogens. As shown in Figure 1, this review introduces the principle of the PEC biosensor. It summarizes the research progress of the PEC biosensor in the detection of foodborne pathogens in recent years, including the design of photoactive materials (such as improving the photoelectric conversion efficiency of photoactive materials and broadening the spectral absorption of photoactive materials) and optimization of sensing strategies (such as interface regulation, signal amplification and dual-signal output). Meanwhile, the development prospects and challenges of the PEC biosensor in detecting foodborne pathogens have been discussed in detail. Hopefully, this review provides broad applications and beneficial insights for scientists in diverse fields, including food safety monitoring, drug detection, medical diagnosis and environmental monitoring.

2 Brief overview of PEC biosensors

2.1 The principle of photocurrent generation

The PEC method is an emerging analytical technique based on EC, which interfaces with many disciplines, such as optics, electrochemistry, surface science and solid-state physics (Zhao et al., 2014; Sun et al., 2022; Zhao et al., 2015). It is generally believed that photoactive materials can absorb photons with sufficient energy to produce electron–hole pairs. The created carriers are then transferred to the electrodes, which generate an electrical signal in the electrolyte and convert energy through the redox reaction involved. These unique

TABLE 1 Common foodborne pathogens and their distribution in possible food category.

Foodborne pathogens	Species	Food category	References
Listeria monocytogenes	Gram-positive bacterium	Aquatic products, dairy products, fruit and vegetable products	Taylor et al. (2019), Vongkamjan et al. (2017), Capita et al. (2019)
S. aureus	Gram-positive bacterium	Dairy products, meat product, cereal product	Kümmel et al. (2016), Li et al. (2022), Argudín et al. (2012)
Vibrio parahaemolyticus	Gram-negative bacillus	Aquatic products, ready-to-eat seasoning	Miles et al. (1997), Sun et al. (2016), Li LingZhi et al. (2019)
Salmonella	Gram-negative enterobacterium	Dairy products, meat product, cereal product	Paniel and Noguer (2019), Pye et al. (2023), Han et al. (2017)
E. coli	Gram-negative brevibacterium	Meat product, fruit and vegetable products	Leng et al. (2022), Munekata et al. (2020), Lima et al. (2017)
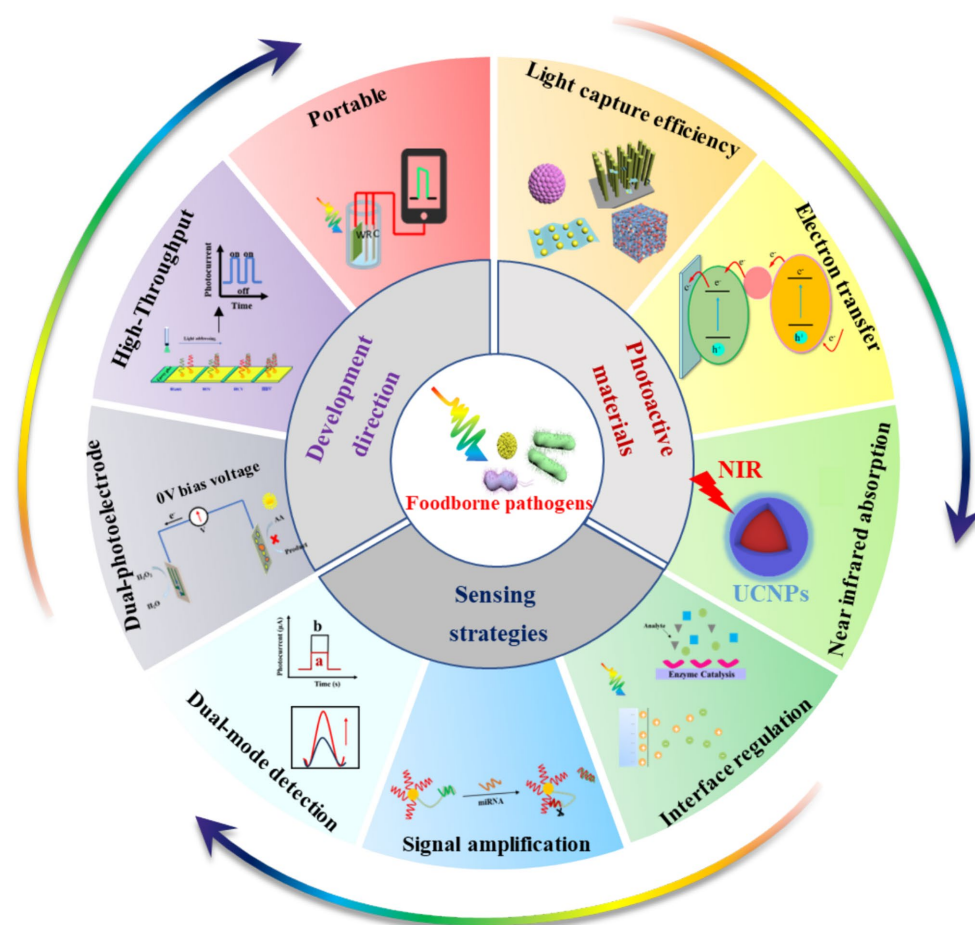
FIGURE 1
Summary and perspectives of PEC biosensors for monitoring foodborne pathogens.

properties of photochemistry have resulted in its widespread use in energy harvesting and environmental pollution mitigation (Lv et al., 2022; Dong et al., 2020).

Notably, the PEC sensor is an innovative and promising technology that integrates PEC processes and sensing. Its underlying principle is that when the surface of the photoactive materials (semiconductor materials, organic photoelectric materials, noble metals with various nanostructures, etc.) is irradiated such that the energy of the exciting light is greater than or equal to the band gap width of photoactive material, photo induced electron transfer reaction will occur in the photoactive material (Ge et al., 2019). The separation of electron–hole pairs occurs when electrons transition from the valence band (VB) to the conduction band (CB). This makes the excited photogenerated electrons unstable, and some will be transferred to the electrode surface or electrolyte. In contrast, others recombine the photogenerated holes of the VB. If the photogenerated electrons at the CB are transferred to the electrode surface, an anode photocurrent is generated. A cathode photocurrent is generated if the photogenerated electrons at the CB are transferred to the electrolyte and consumed by the electron acceptors in the electrolyte.

The generally accepted PEC mechanism consists of four successive steps: (i) the absorption of photons, (ii) the separation of electron–hole

pairs, (iii) the migration and recombination of electron–hole pairs and (iv) the utilization of electron–hole pairs. This process involves the generation of electrical signals at the interface and active participation in redox reactions (Sivula and van de Krol, 2016; Zang et al., 2017). The cumulative effect of these processes determines both the photoelectric conversion efficiency and the strength of the output signal (Figure 2A). When the concentration of the target changes, the electrical signal will change accordingly, so the target can be quantitatively detected through the change in the PEC signal. Current PEC sensors are basically amperometric biosensors (Wang et al., 2018). The presence of the analyte can cause a change in the photoactive material or electrolyte environment, which can affect one or more of the above processes. This results in a change in the PEC signal and facilitates the quantitative analysis process. Therefore, the detection signal can be processed by a variety of methods, which provide an effective way to detect different targets (Shu and Tang, 2019).

2.2 Composition and characteristics of the PEC biosensor

The PEC detection system is shown in Figure 2B. This system consists of three parts: an excitation light source, a test device
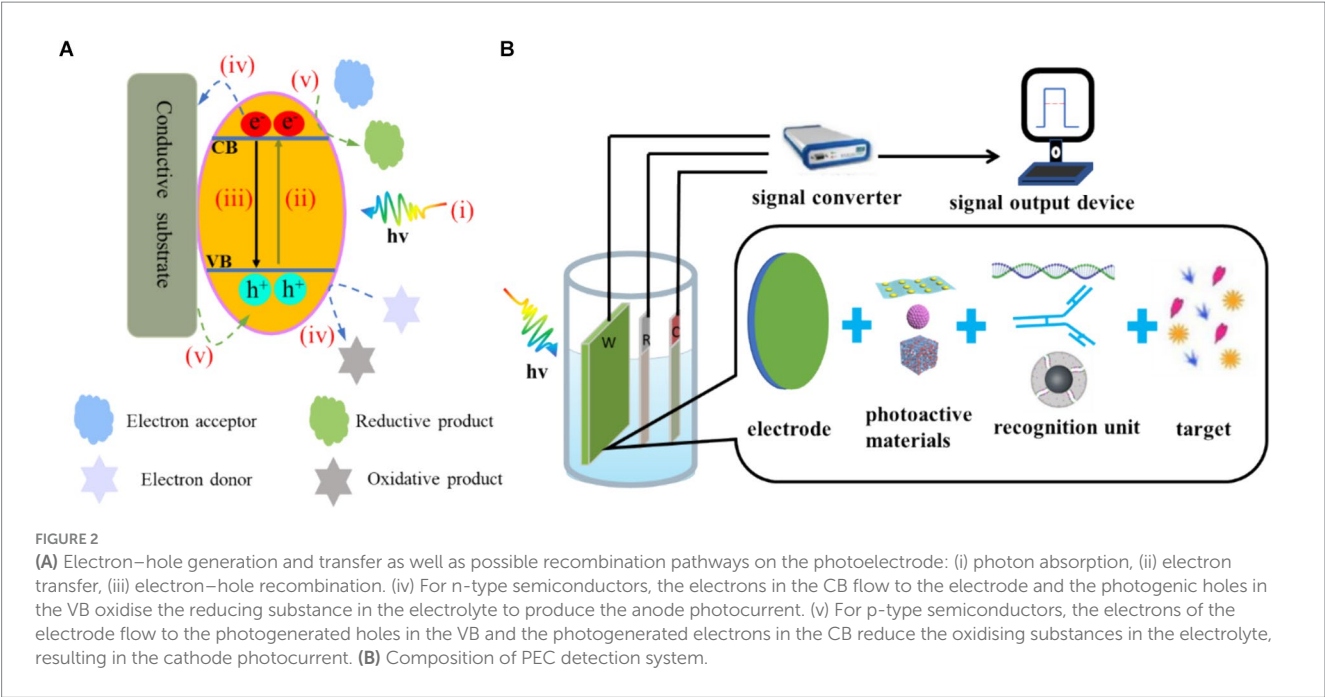
FIGURE 2
(A) Electron−hole generation and transfer as well as possible recombination pathways on the photoelectrode: (i) photon absorption, (ii) electron transfer, (iii) electron−hole recombination. (iv) For n-type semiconductors, the electrons in the CB flow to the electrode and the photogenic holes in the VB oxidise the reducing substance in the electrolyte to produce the anode photocurrent. (v) For p-type semiconductors, the electrons of the electrode flow to the photogenerated holes in the VB and the photogenerated electrons in the CB reduce the oxidising substances in the electrolyte, resulting in the cathode photocurrent. **(B)** Composition of PEC detection system.

TABLE 2 Characterization of PEC analytical properties based on different photoactive materials or signal amplification strategy for the determination of foodborne pathogens.

Foodborne pathogens	Photoactive materials	Signal amplification strategy	Linear range (CFU/mL)	LOD (CFU/mL)	Ref.
S. aureus	ZnS-Ag$_2$S	\	$1.0 \times 10^1 \sim 1.0 \times 10^6$	2	Yang et al. (2020)
S. aureus	ZnS/CdS/ITO	\	$1.0 \sim 4.0 \times 10^3$	1	Yang et al. (2019)
S. aureus	FePor-TPA	dual-mode detection	$1.0 \times 10^1 \sim 1.0 \times 10^8$	8.73	Zheng et al. (2023)
Vibrio parahaemolyticus	Bi$_2$WO$_6$ and Ag$_2$S	\	$3.2 \times 10^2 \sim 3.2 \times 10^8$	40	Hou et al. (2021)
Vibrio parahaemolyticus	Ho^{3+}/Yb^{3+}TiO$_2$ with CdSe QDs	\	$1.0 \times 10^2 \sim 1.0 \times 10^8$	25	Hao et al. (2019)
Salmonella	Au/Bi$_2$MoO$_6$/V$_2$CTx	\	$1.82 \times 10^2 \sim 1.82 \times 10^8$	26	Jiang et al. (2024)
E. coli O157:H7	CdS/ITO	MnO$_2$ acts as an interface regulator	$1.0 \times 10^1 \sim 5.0 \times 10^6$	3	Yang et al. (2020)
E. coli O157:H7	WO$_3$/Bi$_2$S$_3$	\	$1.5 \times 10^2 \sim 1.5 \times 10^8$	56	Zhao et al. (2024)
E. coli O157:H7	Au NPs/g-C$_3$N$_4$	\	$1.0 \times 10^2 \sim 1.0 \times 10^6$	30.5	Chen et al. (2024)

(three-electrode system and electrochemical workstation) and a signal output device (Shu and Tang, 2019). Compared with EC biosensors, PEC biosensors have two key elements: (i) photoactive materials (Dini et al., 2016; Yan et al., 2021) and (ii) bio-recognition elements (Mitsubayashi et al., 2022; Cesewski and Johnson, 2020). Photoactive materials have a photoelectric conversion effect. Bio-recognition elements include enzymes, antibodies and nucleic acids.

In PEC detection, light is used as the excitation source to excite the photoactive substance, and the electrical signal generated by photoexcitation is the detection signal. Because the excitation signal and detection signal of the PEC process belong to different energy forms, the background of the sensing signal is lower than that of the traditional electrochemical method, and the high signal-to-noise ratio is conducive to further reducing the detection limit (Jiang et al., 2021). Due to the uniqueness of the bio-recognition elements, a specific biological

reaction occurs with the target. The electrochemical workstation and signal output device are easy to integrate and miniaturise, so the technology has the numerous benefits of simple operation, fast response and portable equipment (Fu et al., 2020; Tao et al., 2023).

3 Construction of PEC biosensors for sensitive detection of foodborne pathogens

Establishing a rapid and sensitive PEC analytical method is one of the important means of ensuring global food safety and minimizing public health problems. Currently, most studies on the PEC detection of foodborne pathogens mainly focus on improving the performance of photoactive materials and optimizing sensing strategies, as shown in Table 2.
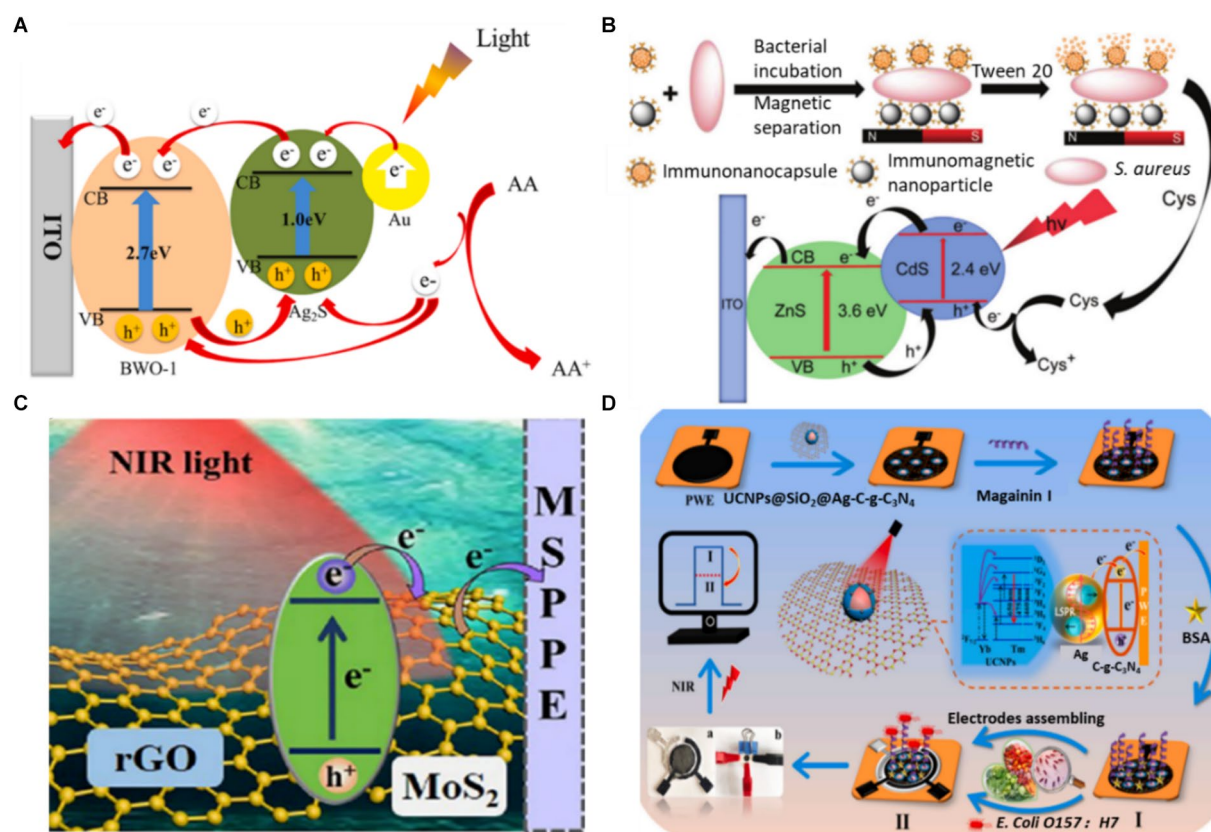
FIGURE 3
(A) Schematic diagram of photogenic electron transfer mechanism of aptamer sensor (Hou et al., 2021). **(B)** Illustration of the PEC detection of *S. aureus* (Yang H. et al., 2019). **(C)** Schematic of the PEC process on a GMS-modified electrode (Ge et al., 2022). **(D)** PEC response of UCNPs@SiO₂@ Ag/C-g-C₃N₄ under NIR light (980 nm) and the fabrication process of a PEC sensor for the detection of *E. coli* (Yin et al., 2022). Ascorbic acid (AA), cysteine (Cys), rGO-MoS₂ sheets (GMS), up-converting nanophosphors (UCNPs), bovine serum albumin (BSA).

3.1 Improving the performance of photoactive materials

The critical part of a PEC biosensor is the photoelectric conversion unit. Therefore, selecting the photoactive material is a key factor in the sensing performance of a PEC sensor. To date, different types of photoactive materials with distinct energy levels have been effectively utilized to develop PEC biosensors. For example, inorganic semiconductor materials (metal oxides and metal sulphides, etc.) (Wang et al., 2018; Zhu et al., 2019; Shu et al., 2018), organic small molecules, organic polymers and other common organic semiconductor materials (Zhu et al., 2015; Haddour et al., 2004; Zhou et al., 2019), graphite-phase carbon nitride, metal–organic frameworks, perovskites, quantum dots (QDs) and other new photoactive materials (Yang X. et al., 2019; Zhang G. et al., 2018; Li et al., 2019; Shi et al., 2018) have attracted extensive research interest due to both their optical and electrical-related properties. However, due to the shortcomings of a single photoactive material, such as a wide band gap, poor photon absorption ability or toxicity, it is challenging to meet the requirements for actual analysis and testing. Thus, it is necessary to improve the performance of photoactive materials to obtain high photoelectric conversion efficiency by speeding up electron transfer and broadening spectral absorption.

3.1.1 Improving the photoelectric conversion efficiency of photoactive materials

As mentioned above, to address these shortcomings of a single photoactive material, various strategies have been employed to improve the photoelectric conversion efficiency of individual semiconductors, such as doping heteroatoms or forming semiconductor heterojunctions (Sheng et al., 2020; Li et al., 2024). Element doping in the photoactive material effectively regulates the semiconductor energy band, reducing the band gap energy and inhibiting photogenerated electron–hole pair recombination (Raut et al., 2017). For example, Hou et al. (2021) combined rare earth-doped Bi₂WO₆ and Ag₂S as photoactive materials. The doped rare-earth ions in the Bi₂WO₆ matrix can effectively inhibit the recombination of photogenerated electron–hole pairs and improve the photocurrent response of Bi₂WO₆, thereby developing a PEC aptasensor for the detection of *Vibrio parahaemolyticus* (Figure 3A). The constructed PEC aptasensor exhibited excellent specificity, stability and reproducibility. By co-doping TiO₂ with Ho³⁺ and Yb³⁺, Hao et al. (2019) broadened the spectral response range of TiO₂ to the infrared region, improved the photocurrent response of TiO₂ and realized the sensitive detection of *Vibrio parahaemolyticus*. At the same time, building a heterostructure with two semiconductors is considered one of the most popular methods for obtaining photoelectrodes with the desired properties (Low et al., 2017). Band

structure and energy level matching are the main considerations in constructing semiconductor–semiconductor heterojunctions (Long et al., 2021). Zhao et al. (2024) modified Bi_2S_3 through continuous ion layer adsorption and reaction on the WO_3 electrode surface to form heterojunction, reduced electron–hole pair complexation and realized rapid detection of *E. coli*. Yang et al. (2019) synthesized ZnS/CdS heterojunction nanoparticles by electrodeposition on an ITO electrode in one pot, achieving the sensitive detection of *S. aureus*. The linear range of PEC detection for *S. aureus* is $1.0 \sim 4.0 \times 10^3$ CFU/mL under ideal circumstances. The detection of *S. aureus* in the milk and juice samples was effectively accomplished using the proposed method (Figure 3B). These results indicate that this is an effective strategy to enhance the photocurrent signal by element doping or forming a heterojunction. In addition, it is expected to further improve the performance of PEC biosensors by introducing new doping elements (such as lanthanide) (Arumugam et al., 2022) or constructing new heterojunctions (such as S-type heterojunctions) (Xiao et al., 2023).

3.1.2 Widening the optical absorption range of photoactive materials

Up to now, plenty of efforts have been devoted to investigating photosensitive materials. Most current PEC sensors are excited by ultraviolet–visible (UV–Vis) light (Chen et al., 2020), which hampers their future applications in bioanalysis (e.g., *in vivo* detection) due to the intrinsic limitation of short penetration of UV/Vis light. The efficient utilization of sunlight, especially wavelengths in the near-infrared (NIR) region, is particularly important for PEC biosensors, as NIR light accounts for the largest proportion of sunlight, at nearly 50% (Hsieh et al., 2020). In contrast to UV light, NIR light exhibits minimal phototoxicity and is highly compatible with living organisms. This advantageous biocompatibility makes NIR light an ideal choice for PEC biosensors that involve the detection of biological macromolecules (Lv et al., 2020). NIR PEC sensing materials have mainly been divided into direct NIR photoactive materials and indirect NIR photoactive materials (Yang et al., 2021). Direct NIR photoactive materials were constructed using narrow-bandgap photoactive materials, and indirect NIR photoactive materials were constructed using up-conversion nanomaterials.

The semiconductor bandgap directly affects the light efficiency of a photocatalysis reaction. A semiconductor with a wider bandgap can absorb higher-energy photons. As the semiconductor absorbs short wavelengths of light with high photonic energy, it can take advantage of only the smaller range of the solar spectrum concentrated in the UV region. Conversely, a semiconductor with a narrower bandgap can absorb lower-energy photons. Narrow-bandgap semiconductors absorb long wavelengths of light, thus utilising the solar spectrum from the Vis region to the NIR region (Feng et al., 2022). Therefore, controlling the narrow bandgap of semiconductors benefits the absorption of NIR light. Ge et al. (2022) reported an NIR-response PEC immunosensor for the 'on' analysis of *E. coli* O157:H7 under 980 nm light irradiation (as shown in Figure 3C). The form of narrow-band gap MoS_2 is regulated by rGO to promote carrier generation and migration. On the sensing platform, *E. coli* O157:H7 was detected in concentrations ranging from $5.0 \sim 5.0 \times 10^6$ CFU/mL, and the LOD was only 2.0 CFU/mL. Subsequently, this research group combined NIR-responsive materials with polar-flipping strategies in their follow-up work, expanding the scope of application of NIR-responsive PEC materials (Ge et al., 2023).

The construction of the indirect NIR PEC sensor is based on the inverse Stokes effect of the up-conversion material, which converts incident light with long wavelengths into emitted light with shorter wavelengths (Sakamoto et al., 2022). Due to its long luminous life, strong optical stability and large anti-Stokes displacement, the up-conversion material can be introduced from FL to the PEC sensing field as a light source converter (Wang G. et al., 2023). Combining it with appropriate PEC active materials can establish an indirect NIR PEC sensing platform. Yin et al. (2022) established an NIR PEC sensing platform for the ultra-sensitive detection of *E. coli* O157:H7 by assembling a flexible conducting paper electrode with core-shell up-converting nanophosphors (UCNPs)@SiO_2. As shown in Figure 3D, the presence of Ag nanoparticles significantly boosted the up-conversion luminescence of the UCNPs, promoting the separation and transport of photoelectrons through local surface plasmon resonance effects. The NIR PEC sensor successfully detected *E. coli* O157:H7 with a detection limit as low as 2.0 CFU/mL. It was effectively utilized to determine the presence of *E. coli* O157:H7 in contaminated pork, cabbage and milk samples. In the past two decades, the PEC analysis has received extensive attention and has made significant progress. However, research on NIR PEC sensing is still in its initial stage. Future research could focus on developing new NIR light-responsive materials and miniaturized photoelectrodes and further applying them to foodborne pathogen analysis.

3.2 Optimising the sensing strategy

In addition to preparing photoactive materials, the design of the sensing strategy is another key aspect that determines the performance of a constructed PEC sensor. At present, in the construction of various PEC biosensors, sensing strategies can be divided into three categories: (i) interface regulation, (ii) signal amplification strategy and (iii) signal output mode.

3.2.1 Interface regulation

The interface interaction in the PEC analysis was directly correlated with the performance of the PEC system. Precisely regulating the interface holds significant importance in achieving accurate detection, mainly through the control of the sensor recognition interface and the photoelectric conversion interface of the sensor (Kuang et al., 2017). For the recognition interface of a sensor, selecting a suitable immobilisation technique is crucial in the preparation of a sensor (Naresh and Lee, 2021). Bio-recognition elements in conventional PEC biosensors are mainly fixed to the electrode surface by attaching reagents. However, this approach may increase non-specific adsorption, leading to reduced sensitivity and limiting the ability to detect targets (Li et al., 2018). This adverse effect can be avoided by modifying the components (e.g., adding groups) or enhancing specific adsorption (e.g., designing photoactive materials with abundant active sites). Hao et al. (2019) detected *Vibrio parahaemolyticus* by sensitizing Ho^{3+}/Yb^{3+} TiO_2 with CdSe QDs. The antibody was immobilized by a coupling reaction between the -COOH group of the CdSe QDs and the -NH_2 group of the antibody of *Vibrio parahaemolyticus* (Figure 4A). Chemical bonds resulted in orderly and firm binding of the antibody. The detection limit of the constructed PEC immunosensor was as low as 25 CFU/mL, and the detection range was as wide as $1.0 \times 10^2 \sim 1.0 \times 10^8$ CFU/mL. Generally, the PEC sensing interface is
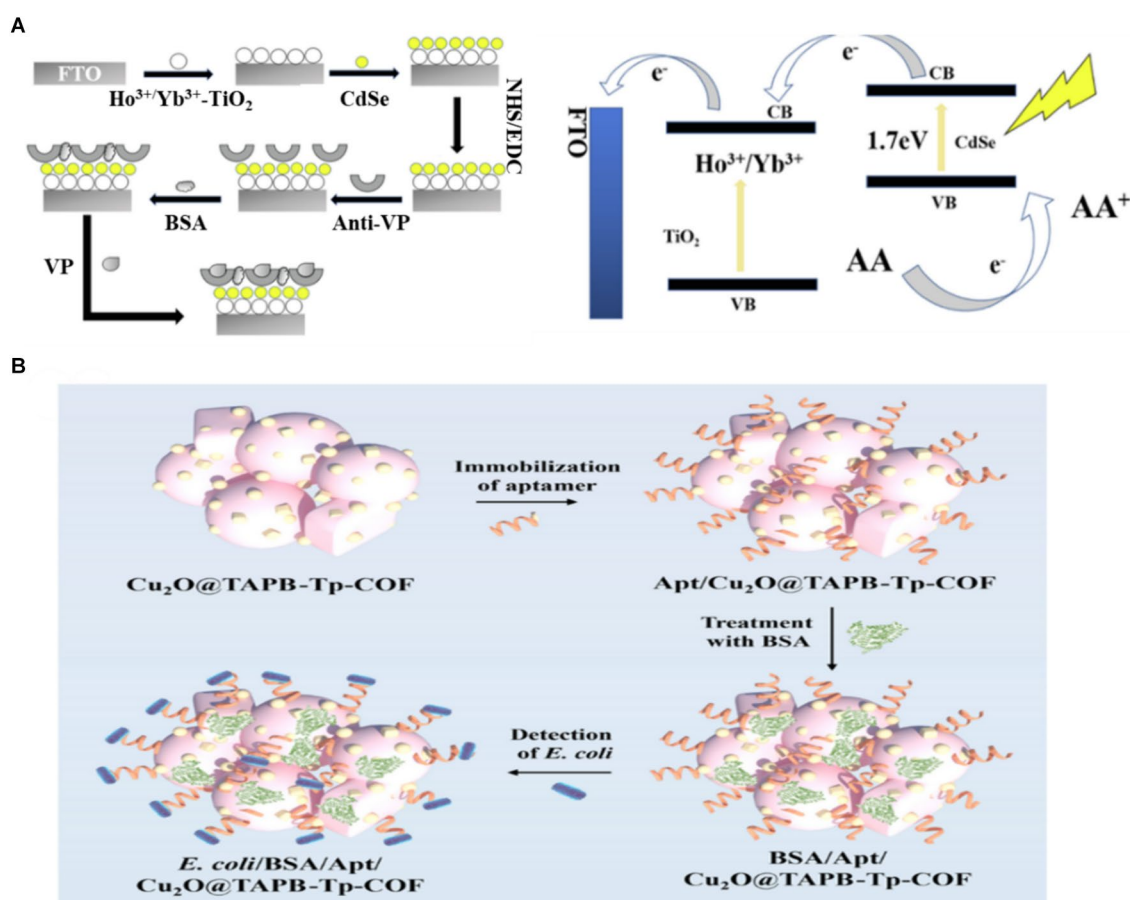
FIGURE 4
(A) Schematic illustration of the proposed PEC biosensor fabrication procedure and electron-transfer mechanism of CdSe QDs−sensitised Ho^{3+}/Yb^{3+}-TiO$_2$ PEC sensor in AA electrolyte (Hao et al., 2019). **(B)** fabrication of the Cu$_2$O@TAPB-Tp-COF-based PEC aptasensor for the detection of *E. coli* (Huo et al., 2023). 1,3,5-tris(4-aminophenyl)-benzene (TAPB), 1,3,5-triformylphloroglucinol (Tp), covalent−organic framework (COF).

affected by interfacial charge recombination and interfacial reaction kinetics (Xin et al., 2022). Therefore, designing photosensitive materials with different component interfaces in close contact and abundant active sites may be an effective method to accelerate charge transfer. Given the homogeneously distributed pores, good biocompatibility and rich functionality, covalent−organic frameworks (COFs) are widely utilized as platforms for fabricating biosensors to sensitively analyze various analytes. Huo et al. (2023) established a novel Cu$_2$O-constrained photoactive COF network as a sensitive and selective platform for the PEC detection of *E. coli* (Figure 4B). The COF synthesized using 1,3,5-tris(4-aminophenyl)-benzene (TAPB) and 1,3,5-triformylphloroglucinol (Tp) as building blocks acted as the scaffold for encapsulating Cu$_2$O nanoparticles (denoted as Cu$_2$O@TAPB-Tp-COF). Given the high photoelectric conversion efficiency, large porous structure, rich functionality and encapsulation ability towards metal nanoparticles of Cu$_2$O@TAPB-Tp-COF, the manufactured PEC aptasensor exhibited an ultralow detection limit of 2.5 CFU/mL within a range of 1.0×10^1 to 1.0×10^4 CFU/mL toward *E. coli*. In PEC sensing, the recognition and photoelectric conversion interfaces play a crucial role in charge recombination and transfer dynamics. Therefore, it is necessary to explore electrode interfaces with more active sites and more effective biological stationary technology.

3.2.2 Signal amplification

For PEC detection, quantitative detection is usually achieved by photoelectron transfer at the electrode/electrolyte interface and photocurrent response after interface changes (Shu and Tang, 2019). However, due to the influence of substrate in food, it is challenging to achieve sensitive detection of trace objects. Signal amplification strategies are essential in developing a highly sensitive PEC immunoassay system. Moreover, gaining a profound understanding of PEC signal amplification strategies will significantly enhance the development of advanced sensors. Standard signal amplification strategies include enzyme-mediated catalytic precipitation (Song et al., 2023) and DNA amplification (Yuan et al., 2020).

Enzyme-mediated catalytic precipitation is a simple and effective method of producing insoluble products on the electrode surface, resulting in changes in the photocurrent signal (Zhuang et al., 2015). However, natural enzymes have some problems, such as poor stability, high cost and harsh storage conditions. To overcome these shortcomings, nanozyme, a nanomaterial with enzyme-like properties, has emerged as the most promising alternative due to its good stability and low cost (Chi et al., 2024; Wang et al., 2020). Luo et al. (2022) used a single layer of Cu-C$_3$N$_4$ nano-enzyme as the signal amplifier for the highly selective and ultra-sensitive detection of *S. aureus* through the steric hindrance effect. The Cu–C$_3$N$_4$@Apt nanozyme acted as a

FIGURE 5
Schematic diagram showing **(A)** synthesis of Cu−C$_3$N$_4$−TiO$_2$. **(B)** preparation of Cu−C$_3$N$_4$@Apt. **(C)** construction of PEC sensor and detection of *S. aureus* (Luo et al., 2022) and **(D)** working mechanism of the sensors (Zhu L. et al., 2021). Glutaraldehyde (GLD), F-doped Tin Oxide (FTO).

peroxidase to catalyze the oxidation of 4-chloro-1-naphthol (4-CN) to produce an insoluble precipitate on the electrode surface and resulted in a significant decrease in photocurrent. Based on the signal amplification of Cu-C$_3$N$_4$@Apt nanozyme, a PEC sensor was successfully constructed to detect *S. aureus* (Figures 5A–C). The sensor had a linear range of $1.0 \times 10^1 \sim 1.0 \times 10^8$ CFU/mL with LOD as low as 3.4 CFU/mL. Additionally, the ability of the sensor to detect *S. aureus* that had been added to orange juice and milk was also verified, and the recovery rate was 91% ~ 113%. Enzyme-mediated catalytic precipitation has been employed as an effective and simple signal amplification strategy owing to its inhibition effect on interfacial mass and electron transfer. However, most enzyme-mediated catalytic

precipitation reactions belong to the signal-off mode, resulting in limited signal variation.

To detect trace or even trace objects, a DNA amplification strategy was introduced into the construction process of the PEC biosensor. Currently, the DNA amplification strategy applied in the PEC biosensor mainly includes hybridization chain reaction (HCR) (Zong et al., 2024) and rolling circle amplification (RCA) with nuclease-assisted recycling amplification (Zhang K. et al., 2018). Generally, these strategies amplify photocurrent signals by expanding DNA fragments, thus enhancing the number of sensitisers and mimetic enzymes. Zhu et al. (2021) constructed a PEC aptasensor using exonuclease I–assisted amplification and the initial identification of

aptamers. As shown in Figure 5D, WO$_3$ was used as the photoactive material. In contrast, the sensitization effect of CdTe QDs and the shear impact of exonuclease I were used to amplify the signal, achieving highly sensitive detection. The LOD was 45 CFU/mL in the concentration range of $1.3 \times 10^1 \sim 1.3 \times 10^7$ CFU/mL. This construction strategy provides a novel approach for the identification of *Listeria monocytogenes*. The DNA amplification strategy can effectively improve the sensitivity of the PEC biosensor, but several deficiencies still hinder its further development, such as its complicated operation and high cost.

3.2.3 Dual-mode detection platform

The PEC method has unique advantages and characteristics (Zhao et al., 2015). However, with the increasing demand for sensitivity and accuracy in detecting foodborne pathogens, single-mode biosensors are susceptible to various factors, such as different manual operation, unstable experimental environments and differences in substrate morphology and loads from batch to batch. Therefore, a new output signal is introduced, and dual-mode biosensors are developed. This can simultaneously introduce dual-channel detection into the recognition system, allowing multiple response signals to be output under the same or different test conditions. In this case, each signal was independent and free from interference. Therefore, the experimental results can be mutually verified, further improving the accuracy. In the case of a difference in the sensitivity of the two detection modes, the detection range of the analytes can be broadened, thus realizing the primary screening and sensitive detection of the samples (Zhang J. et al., 2021). Zhang's team built a CL and PEC dual-mode biosensor for *S. aureus* assay based on Porphyrin-Based Porous Organic Polymer (FePor-TPA) (Zheng et al., 2023). As shown in Figure 6A, on the one hand, the 2D FePor-TPA thin film shows a sensitive photocurrent response and outstanding catalase catalytic activity, which can decompose H$_2$O$_2$ to O$_2$. The produced O$_2$ as an electron donor further improved the photoelectric signal of the 2D FePor-TPA thin film. On the other hand, under acidic conditions caused by gluconic acid, FePor-TPA showed excellent peroxidase activity, which can oxidize TMB (Tetramethylbenzidine) to a chromogenic product. Then, a CL-detecting platform was realized. During the detection process, more targets generated more H$_2$O$_2$ and gluconic acid. As a result, a 'signal-on' and dual-mode detection platform with high sensitivity and selectivity was constructed for detecting *S. aureus*. Liu et al. (2023) combined PEC and SERS to construct a dual-mode biosensor. A photoactive heterostructure was formed by combining C$_3$N$_4$ and MXene via simple electrostatic self-assembly, as they possess well-matched band-edge energy levels. Subsequently, *in situ* growth of gold nanoparticles on the formed surface resulted in better PEC performance and SERS activity because of the synergistic effects of surface plasmon resonance and the Schottky barrier (as shown in Figure 6B). Experimental results revealed that the effective combination of PEC and SERS was achieved for amplification detection of *S. aureus* with a detection range of $5.0 \sim 1.0 \times 10^8$ CFU/mL (PEC) and $1.0 \times 10^1 \sim 1.0 \times 10^8$ CFU/mL (SERS) and a detection limit of 0.70 CFU/mL (PEC) and 1.35 CFU/mL (SERS), respectively (Figure 6C). Dual-mode biosensors were beneficial to compensate for the shortcomings of single-mode biosensors, such as large assay consumption, less information acquisition and poor results accuracy. The construction of more types of dual-mode biosensors by

combining PEC with other analytical methods (FL, EC, etc.) has received increasing attention.

4 Conclusion and perspective

Over the past few decades, methods for detecting foodborne pathogens have developed rapidly. With the continuous exploration of photoactive materials and sensing strategies, PEC biosensors with strong specificity and high sensitivity have gradually attracted increasing attention. This review summarizes the progress of the PEC biosensor in detecting foodborne pathogens in recent years. The main focus is on the design of photoactive materials (improving the photoelectric properties of materials and expanding the spectral absorption range of materials) and the construction of sensing strategies (realizing the effective fixation of target objects and signal amplification). The PEC biosensor has reached very low detection limits for some of the major foodborne pathogens in food, such as *S. aureus* and *E. coli*. Moreover, the capability and accuracy of actual sample analysis and its application in detecting foodborne pathogens have been demonstrated. Compared to the results of traditional techniques, the PEC biosensor exhibits good accuracy, confirming the effectiveness of this method for real sample detection. Importantly, this method will provide an ideal alternative for the rapid, ultra-sensitive and selective detection of foodborne pathogens in food.

Compared with traditional approaches to electrochemical and spectral analysis, PEC sensing technology is still in the initial stage of development due to its short history. The following strategies may provide new possibilities for the detection of foodborne pathogens.

4.1 Dual-photoelectrode self-powered PEC biosensors

Traditional PEC sensors are mostly single-photoelectrodes, which have certain limitations. For example, the photoanode may react with reducing substances in the sample, and the photocathode photoelectric response is poor. To solve these problems, developing dual-photoelectrode self-powered sensors has become an attractive strategy that eliminates the effect of reducing substances and enables sensitive detection.

4.2 High-throughput detection

It is common to perform PEC sensing on a single interface for single analyte detection, which limits detection efficiency and is not suitable for rapidly screening mass samples. Selective and sensitive quantification of multiple analytes in a system can significantly reduce the cost of detection and improve the efficiency of analysis. It is highly desired in practical application. Designing sensing arrays coupled with the light-addressing strategy is an effective method. For this strategy, the concentration of different targets can be easily detected in turns by merely moving the light source from one sensing area to another. At the same time, a higher throughput can be conveniently obtained by
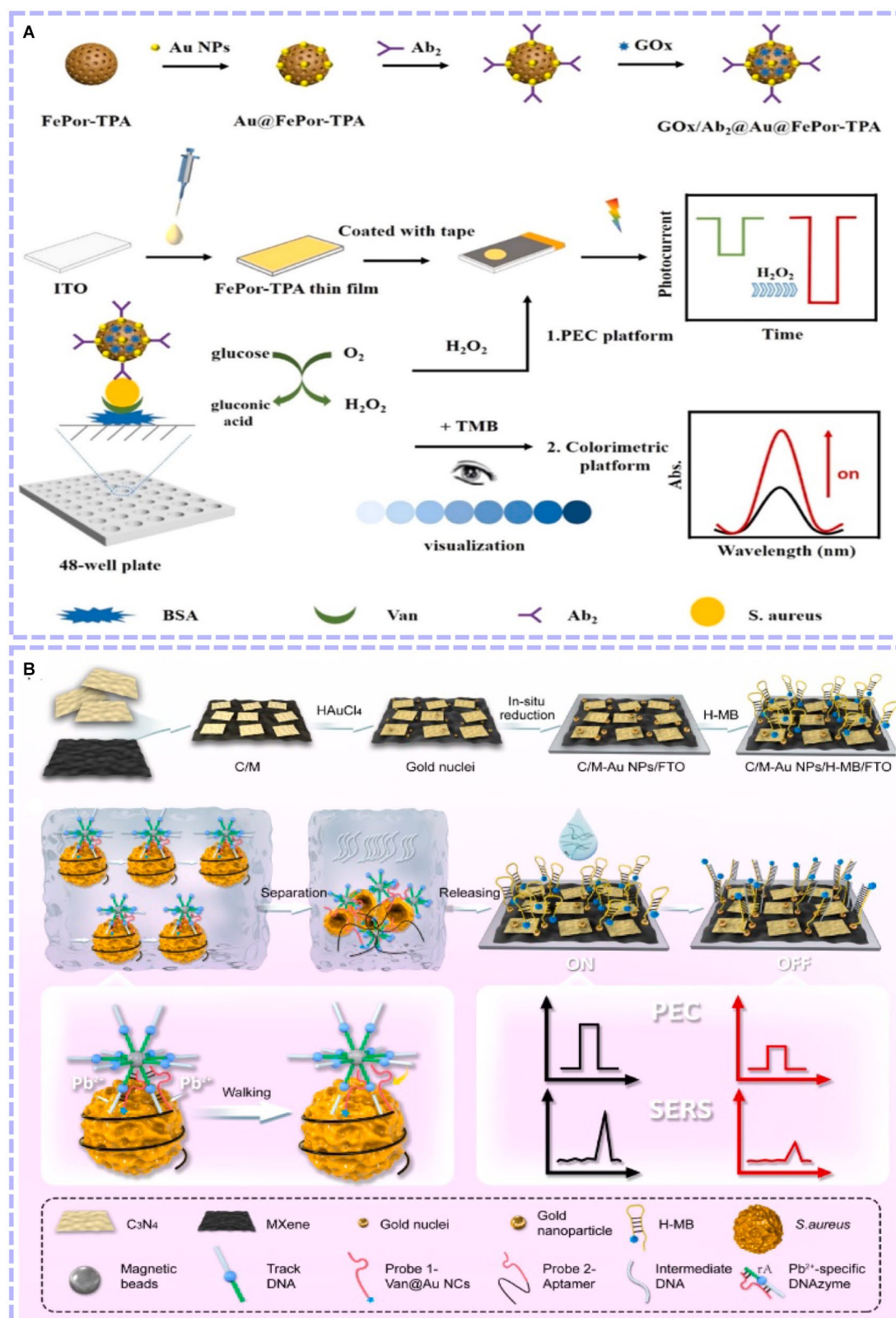
FIGURE 6
(A) Principle of the constructed dual-mode immunosensor for *S. aureus* detection and performance of the biosensor (Zheng et al., 2023).
(B) Schematic illustration of the dual-mode sensing platform and performance of the biosensor (Liu et al., 2023). Porphyrin-based porous organic polymer (FePor-TPA), vancomycin (Van), antibody (Ab).

merely enlarging the size of the substrate electrode and increasing the number of separated sensing zones.

4.3 Portable commercialization

The ultimate goal of all developed PEC bio-sensing devices is to achieve commercialization. However, most current efforts are being conducted in laboratory settings, with limited exploration in real-world settings. Portable PEC analyzers have great potential for environmental monitoring and have attracted widespread attention. Developing split-type PEC biosensors and integrating PEC bio-sensing with arrays, microfluidics and chips would contribute to high-throughput and automation. Additionally, PEC sensors are used in combination with mobile phones to enable intelligent detection. In summary, with the rapid development of nanotechnology and biotechnology in recent years, PEC analysis will play a more critical role in the field of food safety in the future.

Author contributions

XD: Conceptualization, Funding acquisition, Investigation, Project administration, Supervision, Writing – original draft, Writing – review & editing. AH: Writing – original draft, Writing – review & editing, Conceptualization, Investigation. LH: Writing – review & editing. CC: Writing – review & editing. TY: Funding acquisition, Supervision, Writing – original draft, Writing – review & editing.

Conflict of interest

The authors declare that the research was conducted in the absence of any commercial or financial relationships that could be construed as a potential conflict of interest.

Publisher's note

All claims expressed in this article are solely those of the authors and do not necessarily represent those of their affiliated organizations, or those of the publisher, the editors and the reviewers. Any product that may be evaluated in this article, or claim that may be made by its manufacturer, is not guaranteed or endorsed by the publisher.

References

Acunzo, A., Scardapane, E., De Luca, M., Marra, D., Velotta, R., and Minopoli, A. (2022). Plasmonic nanomaterials for colorimetric biosensing: a review. *Chemosensors* 10:136. doi: 10.3390/chemosensors10040136

Argudín, M., Mendoza, M., González-Hevia, M., Bances, M., Guerra, B., and Rodicio, M. (2012). Genotypes, exotoxin gene content, and antimicrobial resistance of *Staphylococcus aureus* strains recovered from foods and food handlers. *Appl. Environ. Microbiol.* 78, 2930–2935. doi: 10.1128/AEM.07487-11

Arumugam, G. M., Karunakaran, S. K., Galian, R. E., and Pérez-Prieto, J. (2022). Recent Progress in lanthanide-doped inorganic perovskite nanocrystals and Nanoheterostructures: a future vision of bioimaging. *Nano* 12:2130. doi: 10.3390/nano12132130

Bettazzi, F., and Palchetti, I. (2018). Photoelectrochemical genosensors for the determination of nucleic acid cancer biomarkers. *Curr. Opin. Electrochem.* 12, 51–59. doi: 10.1016/j.coelec.2018.07.001

Capita, R., Felices-Mercado, A., García-Fernández, C., and Alonso-Calleja, C. (2019). Characterization of *Listeria monocytogenes* originating from the Spanish meat-processing chain. *Food Secur.* 8:542. doi: 10.3390/foods8110542

Cesewski, E., and Johnson, B. N. (2020). Electrochemical biosensors for pathogen detection. *Biosens. Bioelectron.* 159:112214. doi: 10.1016/j.bios.2020.112214

Chen, A., Huang, A., and Ju, P. (2024). Photoelectrochemical pathogenic bacteria sensing platform integrated with sterilization function based on the g-C$_3$N$_4$ nanosheets decorated with AuNPs and poly (3-thiophene boronic acid). *Microchem. J.* 196:109680. doi: 10.1016/j.microc.2023.109680

Chen, J., Park, B., Huang, Y. W., Zhao, Y., and Kwon, Y. (2017). Label-free SERS detection of *Salmonella Typhimurium* on DNA aptamer modified ag NR substrates. *J. Food Meas. Charact.* 11, 1773–1779. doi: 10.1007/s11694-017-9558-6

Chen, Y., Yin, H., Li, F., Zhou, J., Wang, L., Wang, J., et al. (2020). Polydopamine-sensitized WS$_2$/black-TiO$_2$ heterojunction for histone acetyltransferase detection with enhanced visible-light-driven photoelectrochemical activity. *Chem. Eng. J.* 393:124707. doi: 10.1016/j.cej.2020.124707

Chi, J., Ju, P., Bi, F., Wang, S., Jiang, T., Wen, S., et al. (2024). MXene@ MnIn$_2$S$_4$-gated organic Photoelectrochemical transistors with Nanozyme-mediated multiple quenching effects for ultrasensitive detection of Okadaic acid, advanced functional materials. *Early View*. 2407201. doi: 10.1002/adfm.202407201

Ding, L., Wei, J., Qiu, Y., Wang, Y., Wen, Z., Qian, J., et al. (2021). One-step hydrothermal synthesis of telluride molybdenum/reduced graphene oxide with Schottky barrier for fabricating label-free photoelectrochemical profenofos aptasensor. *Chem. Eng. J.* 407:127213. doi: 10.1016/j.cej.2020.127213

Dini, D., Calvete, M. J. F., and Hanack, M. (2016). Nonlinear optical materials for the smart filtering of optical radiation. *Chem. Rev.* 116, 13043–13233. doi: 10.1021/acs.chemrev.6b00033

Dong, X., Liu, D., Meng, X., and You, T. (2022). Research progress on photoelectrochemical sensors for contamination analysis in agricultural fields. *Anal. Sci.* 38, 459–481. doi: 10.2116/analsci.21SAR09

Dong, G., Wang, H., Yan, Z., Zhang, J., Ji, X., Lin, M., et al. (2020). Cadmium sulfide nanoparticles-assisted intimate coupling of microbial and photoelectrochemical processes: mechanisms and environmental applications. *Sci. Total Environ.* 740:140080. doi: 10.1016/j.scitotenv.2020.140080

Feng, X., Lin, L., Duan, R., Qiu, J., and Zhou, S. (2022). Transition metal ion activated near-infrared luminescent materials. *Prog. Mater. Sci.* 129:100973. doi: 10.1016/j.pmatsci.2022.100973

Fu, Y., Zou, K., Liu, M., Zhang, X., Du, C., and Chen, J. (2020). Highly selective and sensitive Photoelectrochemical sensing platform for VEGF165 assay based on the switching of photocurrent polarity of CdS QDs by porous Cu$_2$O-CuO flower. *Anal. Chem.* 92, 1189–1196. doi: 10.1021/acs.analchem.9b04319

Ge, R., Lin, X., Dai, H., Wei, J., Jiao, T., Chen, Q., et al. (2022). Photoelectrochemical sensors with near-infrared-responsive reduced graphene oxide and MoS$_2$ for quantification of *Escherichia Coli O157:H7*. *ACS Appl. Mater. Interfaces* 14, 41649–41658. doi: 10.1021/acsami.2c13292

Ge, L., Liu, Q., Hao, N., and Kun, W. (2019). Recent developments of photoelectrochemical biosensors for food analysis. *J. Mater. Chem. B* 7, 7283–7300. doi: 10.1039/C9TB01644A

Ge, R., Zhang, S.-M., Dai, H.-J., Wei, J., Jiao, T.-H., Chen, Q.-M., et al. (2023). G-Quadruplex/hemin-mediated polarity-switchable and photocurrent-amplified system for *Escherichia coli O157:H7* detection. *J. Agric. Food Chem.* 71, 16807–16814. doi: 10.1021/acs.jafc.3c06052

Guldimann, C., and Johler, S. (2018). An introduction to current trends in foodborne pathogens and diseases. *Curr. Clin. Microbiol. Rep.* 5, 83–87. doi: 10.1007/s40588-018-0093-y

Haddour, N., Cosnier, S., and Gondran, C. (2004). Electrogeneration of a biotinylated poly(pyrrole–ruthenium(ii)) film for the construction of photoelectrochemical immunosensor. *Chem. Commun.* 21, 2472–2473. doi: 10.1039/B410727F

Han, H., Wei, X., Wei, Y., Zhang, X., Li, X., Jiang, J., et al. (2017). Isolation, characterization, and bioinformatic analyses of lytic *Salmonella Enteritidis* phages and tests of their antibacterial activity in food. *Curr. Microbiol.* 74, 175–183. doi: 10.1007/s00284-016-1169-7

Hao, H., Hao, S., Hou, H., Zhang, G., Hou, Y., Zhang, Z., et al. (2019). A novel label-free photoelectrochemical immunosensor based on CdSe quantum dots sensitized Ho^{3+}/Yb^{3+}-TiO$_2$ for the detection of *Vibrio parahaemolyticus*. *Methods* 168, 94–101. doi: 10.1016/j.ymeth.2019.06.005

Hao, N., and Wang, K. (2016). Recent development of electrochemiluminescence sensors for food analysis. *Anal. Bioanal. Chem.* 408, 7035–7048. doi: 10.1007/s00216-016-9548-2

Hou, Y., Zhu, L., Hao, H., Zhang, Z., Ding, C., Zhang, G., et al. (2021). A novel photoelectrochemical aptamer sensor based on rare-earth doped Bi$_2$WO$_6$ and Ag$_2$S for the rapid detection of *Vibrio parahaemolyticus*. *Microchem. J.* 165:106132. doi: 10.1016/j.microc.2021.106132

Hsieh, P.-Y., Wu, J.-Y., Chang, T.-F. M., Chen, C.-Y., Sone, M., and Hsu, Y.-J. (2020). Near infrared-driven photoelectrochemical water splitting: review and future prospects. *Arab. J. Chem.* 13, 8372–8387. doi: 10.1016/j.arabjc.2020.05.025

Huo, E., Shahab, S., Dang, H., Jia, Q., and Wang, M. (2023). Triazine-based covalent–organic framework embedded with cuprous oxide as the bioplatform for photoelectrochemical aptasensing *Escherichia coli*. *Microchim. Acta* 190:407. doi: 10.1007/s00604-023-05987-6

Jiang, S., Wang, Y., Cheng, H., Zhang, G., Hou, H., Bi, G., et al. (2024). Multifunctional photoelectrochemical platform based on layer-by-layer assembly of au/Bi$_2$MoO$_6$/V$_2$CTx for simultaneous detection and inactivation of *Salmonella enteritidis*. *J. Photochem. Photobiol. A Chem.* 451:115535. doi: 10.1016/j.jphotochem.2024.115535

Jiang, J., Xia, J., Zang, Y., and Diao, G. (2021). Electrochemistry/Photoelectrochemistry-based Immunosensing and Aptasensing of carcinoembryonic antigen. *Sensors* 21:7742. doi: 10.3390/s21227742

Kuang, Y., Yamada, T., and Domen, K. (2017). Surface and Interface engineering for Photoelectrochemical water oxidation. *Joule* 1, 290–305. doi: 10.1016/j.joule.2017.08.004

Kümmel, J., Stessl, B., Gonano, M., Walcher, G., Bereuter, O., Fricker, M., et al. (2016). *Staphylococcus aureus* entrance into the dairy chain: tracking *S. aureus* from dairy cow to cheese. *Front. Microbiol.* 7:1603. doi: 10.3389/fmicb.2016.01603

Leng, W., Wu, X., Xiong, Z., Shi, T., Sun, Q., Yuan, L., Gao, R., et al. (2022). Study on antibacterial properties of mucus extract of snakehead (Channa argus) against Escherichia coli and its application in chilled fish fillets preservation. *Lwt-Food Sci. Technol.* 167:113840. doi: 10.1016/j.lwt.2022.113840

Li LingZhi, L. L., Meng HongMei, M. H., Dan, G. D. G., Li Yang, L. Y., and MengDie, J. M. J. (2019). Molecular mechanisms of Vibrio parahaemolyticus pathogenesis. *Microbiol. Res.* 222, 43–51. doi: 10.1016/j.micres.2019.03.003

Li, J., Li, C., Shi, C., Aliakbarlu, J., Cui, H., and Lin, L. (2022). Antibacterial mechanisms of clove essential oil against Staphylococcus aureus and its application in pork. *Int. J. Food Microbiol.* 380:109864. doi: 10.1016/j.ijfoodmicro.2022.109864

Li, M., Xiong, C., Zheng, Y., Liang, W., Yuan, R., and Chai, Y. (2018). Ultrasensitive Photoelectrochemical biosensor based on DNA tetrahedron as Nanocarrier for efficient immobilization of CdTe QDs-methylene blue as signal probe with near-zero background noise. *Anal. Chem.* 90, 8211–8216. doi: 10.1021/acs.analchem.8b01641

Li, X., Yuan, Y., Pan, X., Zhang, L., and Gong, J. (2019). Boosted photoelectrochemical immunosensing of metronidazole in tablet using coral-like g-C$_3$N$_4$ nanoarchitectures. *Biosens. Bioelectron.* 123, 7–13. doi: 10.1016/j.bios.2018.09.084

Li, F., Zhu, G., Jiang, J., Yang, L., Deng, F., and Arramel, X. (2024). A review of updated S-scheme heterojunction photocatalysts. *J. Mater. Sci. Technol.* 177, 142–180. doi: 10.1016/j.jmst.2023.08.038

Lima, C. M., Souza, I. E. G. L., dos Santos Alves, T., Leite, C. C., Evangelista-Barreto, N. S., and de Castro Almeida, R. C. (2017). Antimicrobial resistance in diarrheagenic *Escherichia coli* from ready-to-eat foods. *J. Food Sci. Technol.* 54, 3612–3619. doi: 10.1007/s13197-017-2820-4

Liu, R., Ali, S., Haruna, S. A., Ouyang, Q., Li, H., and Chen, Q. (2022). Development of a fluorescence sensing platform for specific and sensitive detection of pathogenic bacteria in food samples. *Food Control* 131:108419. doi: 10.1016/j.foodcont.2021.108419

Liu, R., Ali, S., Haruna, D., Zhang, Y., Lu, P., and Chen, Q. (2023). A Sensitive Nucleic Acid Detection Platform for Foodborne Pathogens Based on CRISPR-Cas13a System Combined with Polymerase Chain Reaction. *Food Anal. Methods* 16, 356–366. doi: 10.1007/s12161-022-02419-8

Liu, R., Zhang, Y., Ali, S., Haruna, S. A., He, P., Li, H., et al. (2021). Development of a fluorescence aptasensor for rapid and sensitive detection of *Listeria monocytogenes* in food. *Food Control* 122:107808. doi: 10.1016/j.foodcont.2020.107808

Liu, F., Zhao, J., Liu, X., Zhen, X., Feng, Q., Gu, Y., et al. (2023). PEC-SERS dual-mode detection of foodborne pathogens based on binding-induced DNA Walker and C$_3$N$_4$/

MXene-au NPs accelerator. *Anal. Chem.* 95, 14297–14307. doi: 10.1021/acs.analchem.3c02529

Long, D., Tu, Y., Chai, Y., and Yuan, R. (2021). Photoelectrochemical assay based on SnO$_2$/BiOBr p–n heterojunction for ultrasensitive DNA detection. *Anal. Chem.* 93, 12995–13000. doi: 10.1021/acs.analchem.1c02745

Low, J., Yu, J., Jaroniec, M., Wageh, S., and Al-Ghamdi, A. A. (2017). Heterojunction Photocatalysts. *Adv. Mater.* 29:1601694. doi: 10.1002/adma.201601694

Luo, S., Liu, F., Gu, S., Chen, K., Yang, G., Gu, Y., et al. (2022). Nanozyme-mediated signal amplification for ultrasensitive photoelectrochemical sensing of *Staphylococcus aureus* based on cu-C$_3$N$_4$-TiO$_2$ heterostructure. *Biosens. Bioelectron.* 216:114593. doi: 10.1016/j.bios.2022.114593

Lv, J., Xie, J., Mohamed, A. G. A., Zhang, X., and Wang, Y. (2022). Photoelectrochemical energy storage materials: design principles and functional devices towards direct solar to electrochemical energy storage. *Chem. Soc. Rev.* 51, 1511–1528. doi: 10.1039/D1CS00859E

Lv, S., Zhang, K., Zhu, L., and Tang, D. (2020). ZIF-8-assisted NaYF$_4$:Yb,tm@ZnO converter with exonuclease III-powered DNA Walker for near-infrared light responsive biosensor. *Anal. Chem.* 92, 1470–1476. doi: 10.1021/acs.analchem.9b04710

Ma, L., Chen, K., Dang, H., and Wang, M. (2023). Establishment of a photoactive heterojunction of triazine covalent-organic polymer and copper (II) selenide: Photoelectrochemical aptasensing strategy for efficiently detecting *Salmonella typhimurium*. *Microchem. J.* 193:109162. doi: 10.1016/j.microc.2023.109162

Miles, D. W., Ross, T., Olley, J., and McMeekin, T. A. (1997). Development and evaluation of a predictive model for the effect of temperature and water activity on the growth rate of *Vibrio parahaemolyticus*. *Int. J. Food Microbiol.* 38, 133–142. doi: 10.1016/S0168-1605(97)00100-1

Mitsubayashi, K., Toma, K., Iitani, K., and Arakawa, T. (2022). Gas-phase biosensors: a review. *Sensors Actuators B Chem.* 367:132053. doi: 10.1016/j.snb.2022.132053

Munekata, P. E., Pateiro, M., Rodríguez-Lázaro, D., Domínguez, R., Zhong, J., and Lorenzo, J. M. (2020). The role of essential oils against pathogenic *Escherichia coli* in food products. *Microorganisms* 8:924. doi: 10.3390/microorganisms8060924

Naresh, V., and Lee, N. (2021). A review on biosensors and recent development of nanostructured materials-enabled biosensors. *Sensors* 21:1109. doi: 10.3390/s21041109

Palomino-Camargo, C., Gonzalez-Munoz, Y., Perez-Sira, E., and Aguilar, V. H. (2018). Delphi methodology in food safety management and foodborne disease prevention. *Rev. Peru Med. Exp. Salud Publica* 35, 483–490. doi: 10.17843/rpmesp.2018.353.3086

Paniel, N., and Noguer, T. (2019). Detection of *Salmonella* in food matrices, from conventional methods to recent aptamer-sensing technologies. *Food Secur.* 8:371. doi: 10.3390/foods8090371

Pye, H. V., Thilliez, G., Acton, L., Kolenda, R., Al-Khanaq, H., Grove, S., et al. (2023). Strain and serovar variants of *Salmonella enterica* exhibit diverse tolerance to food chain-related stress. *Food Microbiol.* 112:104237. doi: 10.1016/j.fm.2023.104237

Raut, V. S., Lokhande, C. D., and Killedar, V. V. (2017). Photoelectrochemical studies on electrodeposited indium doped CdSe thin films using aqueous bath. *J. Electroanal. Chem.* 788, 137–143. doi: 10.1016/j.jelechem.2017.02.010

Sakamoto, D., Shiratani, M., and Seo, H. (2022). Near-infrared light harvesting of upconverting Y$_2$O$_3$:Er^{3+} nanoparticles and their photovoltaic application. *Electrochim. Acta* 436:141407. doi: 10.1016/j.electacta.2022.141407

Scallan, E., Hoekstra, R. M., Angulo, F. J., Tauxe, R. V., Widdowson, M. A., Roy, S. L., et al. (2011). Foodborne illness acquired in the United States—major pathogens. *Emerg. Infect. Dis.* 17, 7–15. doi: 10.3201/eid1701.P11101

Scharff, R. L., Besser, J., Sharp, D. J., Jones, T. F., Peter, G. S., and Hedberg, C. W. (2016). An economic evaluation of PulseNet: a network for foodborne disease surveillance. *Am. J. Prev. Med.* 50, S66–S73. doi: 10.1016/j.amepre.2015.09.018

Schirone, M., Visciano, P., Tofalo, R., and Suzzi, G. (2019). Editorial: foodborne pathogens: hygiene and safety. *Front. Microbiol.* 10:1974. doi: 10.3389/fmicb.2019.01974

Sheng, P., Yao, L., Yang, P., Yang, D., Lu, C., Cao, K., et al. (2020). The origin of enhanced photoelectrochemical activity in metal-ion-doped ZnO/CdS quantum dots. *J. Alloys Compd.* 822:153700. doi: 10.1016/j.jallcom.2020.153700

Shi, J., Chen, Z., Zhao, C., Shen, M., Li, H., Zhang, S., et al. (2022). Photoelectrochemical biosensing platforms for tumor marker detection. *Coord. Chem. Rev.* 469:214675. doi: 10.1016/j.ccr.2022.214675

Shi, X.-M., Mei, L.-P., Zhang, N., Zhao, W.-W., Xu, J.-J., and Chen, H.-Y. (2018). A polymer dots-based Photoelectrochemical pH sensor: simplicity, high sensitivity, and broad-range pH measurement. *Anal. Chem.* 90, 8300–8303. doi: 10.1021/acs.analchem.8b02291

Shu, J., Qiu, Z., Lv, S., Zhang, K., and Tang, D. (2018). Plasmonic enhancement coupling with defect-engineered TiO$_2$−x: a mode for sensitive Photoelectrochemical biosensing. *Anal. Chem.* 90, 2425–2429. doi: 10.1021/acs.analchem.7b05296

Shu, J., and Tang, D. (2019). Recent advances in Photoelectrochemical sensing: from engineered photoactive materials to sensing devices and detection modes. *Anal. Chem.* 92, 363–377. doi: 10.1021/acs.analchem.9b04199

Sivula, K., and van de Krol, R. (2016). Semiconducting materials for photoelectrochemical energy conversion. *Nat. Rev. Mater.* 1:15010. doi: 10.1038/natrevmats.2015.10

Song, P., Wang, M.-L., Duan, Y.-X., Wang, A.-J., Xue, Y., Mei, L.-P., et al. (2023). Bifunctional photoelectrochemical aptasensor based on heterostructured Ag$_3$PO$_4$/ag/TiO$_2$ nanorod array for determination of two tumor markers. *Microchim. Acta* 190:85. doi: 10.1007/s00604-023-05654-w

Sun, J., He, Y., He, S., Liu, D., Lu, K., Yao, W., et al. (2022). A self-powered photoelectrochemical cathodic molecular imprinting sensor based on au@TiO$_2$ nanorods photoanode and Cu$_2$O photocathode for sensitive detection of sarcosine. *Biosens. Bioelectron.* 204:114056. doi: 10.1016/j.bios.2022.114056

Sun, Y., Zhang, X., Wang, G., Lin, S., Zeng, X., Wang, Y., et al. (2016). PI3K-AKT signaling pathway is involved in hypoxia/thermal-induced immunosuppression of small abalone *Haliotis diversicolor*. *Fish Shellfish Immunol.* 59, 492–508. doi: 10.1016/j.fsi.2016.11.011

Tao, Q., Tang, N., Jiang, Y., Chen, B., Liu, Y., Xiong, X., et al. (2023). Double bipolar electrode electrochemiluminescence color switch for food-borne pathogens detection. *Biosens. Bioelectron.* 237:115452. doi: 10.1016/j.bios.2023.115452

Taylor, B. J., Quinn, A. R., and Kataoka, A. (2019). *Listeria monocytogenes* in low-moisture foods and ingredients. *Food Control* 103, 153–160. doi: 10.1016/j.foodcont.2019.04.011

Todd, E. (2020). Food-borne disease prevention and risk assessment. *Int. J. Environ. Res. Public Health* 17:129. doi: 10.3390/ijerph17145129

Vongkamjan, K., Benjakul, S., Vu, H. T. K., and Vuddhakul, V. (2017). Longitudinal monitoring of *Listeria monocytogenes* and Listeria phages in seafood processing environments in Thailand. *Food Microbiol.* 66, 11–19. doi: 10.1016/j.fm.2017.03.014

Wang, X., Chen, H., Zhang, J., Zhou, H., Meng, X., Wang, N., et al. (2024). Photoelectrochemical sensor for the detection of *Escherichia coli* O157:H7 based on TPA-NO$_2$ and dual-functional polythiophene films. *Food Chem.* 441:138299. doi: 10.1016/j.foodchem.2023.138299

Wang, J., Cui, X., Liang, L., Li, J., Pang, B., and Li, J. (2024). Advances in DNA-based electrochemical biosensors for the detection of foodborne pathogenic bacteria. *Talanta* 275:126072. doi: 10.1016/j.talanta.2024.126072

Wang, G., Li, L., Zheng, H., Li, Q., Huang, J., Zhang, L., et al. (2023). Bifunctional strategy toward constructing perovskite/Upconversion lab-on-paper Photoelectrochemical device for sensitive detection of *malathion*. *ACS Nano* 17, 13418–13429. doi: 10.1021/acsnano.3c01692

Wang, B., Wang, H., Lu, X., Zheng, X., and Yang, Z. (2023). Recent advances in electrochemical biosensors for the detection of foodborne pathogens: current perspective and challenges. *Food Secur.* 12:2795. doi: 10.3390/foods12142795

Wang, G.-L., Yuan, F., Gu, T., Dong, Y., Wang, Q., and Zhao, W.-W. (2018). Enzyme-initiated Quinone-chitosan conjugation chemistry: toward a general in situ strategy for high-throughput Photoelectrochemical enzymatic bioanalysis. *Anal. Chem.* 90, 1492–1497. doi: 10.1021/acs.analchem.7b04625

Wang, Z., Zhang, R., Yan, X., and Fan, K. (2020). Structure and activity of nanozymes: inspirations for de novo design of nanozymes. *Mater. Today* 41, 81–119. doi: 10.1016/j.mattod.2020.08.020

Xiao, M., Zhu, M., Yuan, R., and Yuan, Y. (2023). Dual-sensitized heterojunction PDA/ZnO@ MoS$_2$ QDs combined with multilocus domino-like DNA cascade reaction for ultrasensitive photoelectrochemical biosensor. *Biosens. Bioelectron.* 227:115151. doi: 10.1016/j.bios.2023.115151

Xin, C., Cheng, Y., Wang, J., Sun, Q., Liu, E., Hu, X., et al. (2022). Hole storage interfacial regulation of Sb2Se3 photocathode with significantly enhanced Photoelectrochemical performance. *Langmuir* 39, 627–637. doi: 10.1021/acs.langmuir.2c02999

Xu, L., Bai, X., and Bhunia, A. K. (2021). Current state of development of biosensors and their application in foodborne pathogen detection. *J. Food Prot.* 84, 1213–1227. doi: 10.4315/JFP-20-464

Xu, Y., Hassan, M. M., Sharma, A. S., Li, H., and Chen, Q. (2023). Recent advancement in nano-optical strategies for detection of pathogenic bacteria and their metabolites in food safety. *Crit. Rev. Food Sci. Nutr.* 63, 486–504. doi: 10.1080/10408398.2021.1950117

Yan, K., Karthick Kannan, P., Doonyapisut, D., Wu, K., Chung, C.-H., and Zhang, J. (2021). Advanced functional electroactive and photoactive materials for monitoring the environmental pollutants. *Adv. Funct. Mater.* 31:2008227. doi: 10.1002/adfm.202008227

Yang, H., Chen, H., Cao, L., Wang, H., Deng, W., Tan, Y., et al. (2020). An immunosensor for sensitive photoelectrochemical detection of *Staphylococcus aureus* using ZnS–Ag$_2$S/polydopamine as photoelectric material and Cu$_2$O as peroxidase mimic tag. *Talanta* 212:120797. doi: 10.1016/j.talanta.2020.120797

Yang, X., Gao, Y., Ji, Z., Zhu, L.-B., Yang, C., Zhao, Y., et al. (2019). Dual functional molecular imprinted polymer-modified Organometal Lead halide perovskite: synthesis and application for Photoelectrochemical sensing of salicylic acid. *Anal. Chem.* 91, 9356–9360. doi: 10.1021/acs.analchem.9b01739

Yang, Y., Tan, H., Cheng, B., Fan, J., Yu, J., and Ho, W. (2021). Near-infrared-responsive Photocatalysts. *Small Methods* 5:e2001042. doi: 10.1002/smtd.202001042

Yang, G., Wang, H., Dong, Y., Li, Z., and Wang, G. L. (2020). High-throughput photoelectrochemical determination of E. coli O157: H7 by modulation of the anodic photoelectrochemistry of CdS quantum dots via reversible deposition of MnO$_2$. *Microchim. Acta* 187, 1–9. doi: 10.1007/s00604-019-3968-6

Yang, H., Zhao, X., Wang, H., Deng, W., Tan, Y., Ma, M., et al. (2019). Sensitive photoelectrochemical immunoassay of *Staphylococcus aureus* based on one-pot electrodeposited ZnS/CdS heterojunction nanoparticles. *Analyst* 145, 165–171. doi: 10.1039/c9an02020a

Yin, M., Liu, C., Ge, R., Fang, Y., Wei, J., Chen, X., et al. (2022). Paper-supported near-infrared-light-triggered photoelectrochemical platform for monitoring *Escherichia coli* O157:H7 based on silver nanoparticles-sensitized-upconversion nanophosphors. *Biosens. Bioelectron.* 203:114022. doi: 10.1016/j.bios.2022.114022

Yu, H., Guo, W., Lu, X., Xu, H., Yang, Q., Tan, J., et al. (2021). Reduced graphene oxide nanocomposite based electrochemical biosensors for monitoring foodborne pathogenic bacteria: a review. *Food Control* 127:108117. doi: 10.1016/j.foodcont.2021.108117

Yuan, Y., Hu, T., Zhong, X., Zhu, M., Chai, Y., and Yuan, R. (2020). Highly sensitive Photoelectrochemical biosensor based on quantum dots sensitizing Bi$_2$Te$_3$ Nanosheets and DNA-amplifying strategies. *ACS Appl. Mater. Interfaces* 12, 22624–22629. doi: 10.1021/acsami.0c04536

Zang, Y., Lei, J., and Ju, H. (2017). Principles and applications of photoelectrochemical sensing strategies based on biofunctionalized nanostructures. *Biosens. Bioelectron.* 96, 8–16. doi: 10.1016/j.bios.2017.04.030

Zhang, J., Gao, Y., Zhang, X., Feng, Q., Zhan, C., Song, J., et al. (2021). "Dual signal-on" Split-type Aptasensor for TNF-alpha: integrating MQDs/ZIF-8@ZnO NR arrays with MB-liposome-mediated signal amplification. *Anal. Chem.* 93, 7242–7249. doi: 10.1021/acs.analchem.1c00415

Zhang, Z., Liu, Q., Zhang, M., You, F., Hao, N., Ding, C., et al. (2021). Simultaneous detection of enrofloxacin and ciprofloxacin in milk using a bias potentials controlling-based photoelectrochemical aptasensor. *J. Hazard. Mater.* 416:125988. doi: 10.1016/j.jhazmat.2021.125988

Zhang, K., Lv, S., Lu, M., and Tang, D. (2018). Photoelectrochemical biosensing of disease marker on p-type cu-doped Zn$_{0.3}$Cd$_{0.7}$S based on RCA and exonuclease III amplification. *Biosens. Bioelectron.* 117, 590–596. doi: 10.1016/j.bios.2018.07.001

Zhang, G., Shan, D., Dong, H., Cosnier, S., Al-Ghanim, K. A., Ahmad, Z., et al. (2018). DNA-mediated nanoscale metal–organic frameworks for ultrasensitive Photoelectrochemical enzyme-free immunoassay. *Anal. Chem.* 90, 12284–12291. doi: 10.1021/acs.analchem.8b03762

Zhao, W.-W., Xiong, M., Li, X.-R., Xu, J.-J., and Chen, H.-Y. (2014). Photoelectrochemical bioanalysis: a mini review. *Electrochem. Commun.* 38, 40–43. doi: 10.1016/j.elecom.2013.10.035

Zhao, W.-W., Xu, J.-J., and Chen, H.-Y. (2015). Photoelectrochemical bioanalysis: the state of the art. *Chem. Soc. Rev.* 44, 729–741. doi: 10.1039/C4CS00228H

Zhao, W. W., Xu, J. J., and Chen, H. Y. (2016). Photoelectrochemical detection of metal ions. *Analyst* 141, 4262–4271. doi: 10.1039/C6AN01123C

Zhao, Y., Zhu, L., Jiang, S., Zhang, G., Hou, H., Bi, G., et al. (2024). A novel photoelectrochemical phage sensor based on WO$_3$/Bi$_2$S$_3$ for *Escherichia coli* detection. *Colloids Surf. A Physicochem. Eng. Asp.* 686:133392. doi: 10.1016/j.colsurfa.2024.133392

Zheng, Z., Ma, L., Li, B., and Zhang, X. (2023). Dual-modal biosensor for *Staphylococcus aureus* detection based on a porphyrin-based porous organic polymer FePor-TPA with excellent peroxidase-like Catalase-like, and Photoelectrochemical Properties. *Anal. Chem.* 95, 13855–13863. doi: 10.1021/acs.analchem.3c01950

Zhou, Y., Shi, Y., Wang, F.-B., and Xia, X.-H. (2019). Oriented self-assembled monolayer of Zn(II)-Tetraphenylporphyrin on TiO$_2$ electrode for Photoelectrochemical analysis. *Anal. Chem.* 91, 2759–2767. doi: 10.1021/acs.analchem.8b04478

Zhu, A., Ali, S., Jiao, T., Wang, Z., Ouyang, Q., and Chen, Q. (2023). Advances in surface-enhanced Raman spectroscopy technology for detection of foodborne pathogens. *Compr. Rev. Food Sci. Food Saf.* 22, 1466–1494. doi: 10.1111/1541-4337.13118

Zhu, L., Hao, H., Ding, C., Gan, H., Jiang, S., Zhang, G., et al. (2021). A novel Photoelectrochemical aptamer sensor based on CdTe quantum dots enhancement and exonuclease I-assisted signal amplification for *Listeria monocytogenes* detection. *Food Secur.* 10:2896. doi: 10.3390/foods10122896

Zhu, S., Tang, Y., Shi, B., Zou, W., Wang, X., Wang, C., et al. (2021). Oligonucleotide-mediated the oxidase-mimicking activity of Mn$_3$O$_4$ nanoparticles as a novel colorimetric aptasensor for ultrasensitive and selective detection of *Staphylococcus aureus* in food. *Sensors Actuators B Chem.* 349:130809. doi: 10.1016/j.snb.2021.130809

Zhu, P., Wang, P., Kan, L., Sun, G., Zhang, Y., and Yu, J. (2015). An enhanced photoelectrochemical immunosensing platform: supramolecular donor–acceptor arrays by assembly of porphyrin and C60. *Biosens. Bioelectron.* 68, 604–610. doi: 10.1016/j.bios.2015.01.050

Zhu, Y.-C., Xu, Y.-T., Xue, Y., Fan, G.-C., Zhang, P.-K., Zhao, W.-W., et al. (2019). Three-dimensional CdS@carbon Fiber networks: innovative synthesis and application as a general platform for Photoelectrochemical bioanalysis. *Anal. Chem.* 91, 6419–6423. doi: 10.1021/acs.analchem.9b01186

Zhuang, J., Lai, W., Xu, M., Zhou, Q., and Tang, D. (2015). Plasmonic AuNP/g-C$_3$N$_4$ nanohybrid-based photoelectrochemical sensing platform for ultrasensitive monitoring of polynucleotide kinase activity accompanying DNAzyme-catalyzed precipitation amplification. *ACS Appl. Mater. Interfaces* 7, 8330–8338. doi: 10.1021/acsami.5b01923

Zong, C., Kong, L., Li, C., Xv, H., Lv, M., Chen, X., et al. (2024). Light-harvesting iridium (III) complex-sensitized NiO photocathode for photoelectrochemical bioanalysis. *Microchim. Acta* 191:223. doi: 10.1007/s00604-024-06321-4

Glossary

AA	ascorbic acid
BCP	biocatalytic precipitation
CDC	Centers for Disease Control and Prevention
CB	conduction band
COP	covalent–organic polymer
COF	covalent–organic framework
CL	colourimetric
E.coli	*Escherichia coli*
EC	electrochemical
FL	fluorescent
HCR	hybridisation chain reaction
ITO	Indium tin oxide
LOD	limit of detection
N-GQDs	Nitrogen-doped graphene quantum dots
NIR	near-infrared
NC	nanocluster
PEC	photoelectrochemical
FePor-TPA	Porphyrin-Based Porous Organic Polymer
QDs	quantum dots
RCA	rolling circle amplification
rGO	Reduced Graphene Oxide
S. aureus	*Staphylococcus aureus*
SERS	Surface-enhanced Raman scatting
TMB	tetramethylbenzidine
TAPB	1,3,5-tris(4-aminophenyl)-benzene
TAPT	2,4,6-Tris(4-aminophenyl)-1,3,5-Triazine
Tp	2,4,6-trihydroxy-1,3,5-benzenetricarbaldehyde
UV–Vis	ultraviolet–visible
UCNPs	up-converting nanophosphors
VB	valence band
4-CN	4-chloro-1-naphthol

Hyperspectral imaging combined with deep learning models for the prediction of geographical origin and fungal contamination in millet

Saimei Nie[1,2†], Wenbin Gao[3†], Shasha Liu[1]*, Mo Li[3], Tao Li[3], Jing Ren[3], Siyao Ren[3] and Jian Wang[4]*

[1]College of Science and Technology, Hebei Agricultural University, Huanghua, Hebei, China, [2]Intensive Care Unit of Wangjing Hospital, China Academy of Chinese Medical Sciences, Beijing, China, [3]College of Life Science, CangZhou Normal University, Cangzhou, Hebei, China, [4]College of Chemistry and Chemical Engineering, Cangzhou Normal University, Cangzhou, China

Millet is one of the major coarse grain crops in China. Its geographical origin and *Fusarium* fungal contamination with ergosterol and deoxynivalenol have a direct impact on food quality, so the rapid prediction of the geographical origins and fungal toxin contamination is essential for protecting market fairness and consumer rights. In this study, 600 millet samples were collected from twelve production areas in China, and traditional algorithms such as random forest (RF) and support vector machine (SVM) were selected to compare with the deep learning models for the prediction of millet geographical origin and toxin content. This paper firstly develops a deep learning model (wavelet transformation-attention mechanism long short-term memory, WT-ALSTM) by combining hyperspectral imaging to achieve the best prediction effect, the wavelet transformation algorithm effectively eliminates noise in the spectral data, while the attention mechanism module improves the interpretability of the prediction model by selecting spectral feature bands. The integrated model (WT-ALSTM) based on selected feature bands achieves optimal prediction of millet origin, with its accuracy exceeding 99% on both the training and prediction datasets. Meanwhile, it achieves optimal prediction of ergosterol and deoxynivalenol content, with the coefficient of determination values exceeding 0.95 and residual predictive deviation values reaching 3.58 and 3.38 respectively, demonstrating excellent model performance. The above results suggest that the combination of hyperspectral imaging with a deep learning model has great potential for rapid quality assessment of millet. This study provides new technical references for developing portable and rapid hyperspectral imaging inspection technology for on-site assessment of agricultural product quality in the future.

KEYWORDS

millet, hyperspectral imaging, deep learning model, geographical origin, fungal contamination

1 Introduction

Millet (*Setaria italica* (L.) Beauv.) is the seed of the grass species in the family of *Poaceae*, and it is considered one of the oldest cultivated crops (Yang et al., 2012). It originated in the Yellow River basin of China and became one of the major cereal crops in ancient China. At present, China is the main production area for millet, accounting for 80% of the world's

production (Wu and Qu, 2018). Millet has rich nutrients and provides various essential amino acids, fats, vitamins, minerals, and other nutritional components for the human body (He et al., 2007; Dasa and Nguyen, 2020; Yang et al., 2021; Shi et al., 2023). Many pharmacological studies have indicated that millet has various health benefits, including lowering blood glucose levels (Balli et al., 2023), anti-tumor properties (Saleem et al., 2023), reducing cholesterol levels, as well as anti-inflammatory effects (Onipe and Ramashia, 2022). Attributed to its combined medicinal and nutritional value, millet is highly favored in several regions of China (Mahajan et al., 2021).

Millet from different regions differs in quality and price. In China, the five provinces of Shaanxi, Shanxi, Gansu, Ningxia, and Inner Mongolia account for 15.6% of the national millet production (Yang et al., 2019), Hebei, Shandong, and Henan provinces account for 64.3% of the national millet production, while the three northeastern provinces (Heilongjiang, Jilin, and Liaoning) account for 13.9% of the national millet production (Wu and Qu, 2018). The Wu'an millet (HBWA) from Wu'an City, Hebei Province, the Chaoyang millet (LNCY) from Chaoyang City, Liaoning Province, and the Qinzhou millet (SXQX) from Qinxian County, Shanxi Province are certified as Protected Geographical Indication (PGI) products in China. These three production areas have unique natural environments such as altitude, climate, and soil, along with strict and standardized planting regulations, so millet products in these areas have better quality and higher market value. However, there are often cases in the market where inferior products are sold as high-quality ones and non-PGI products from other regions are falsely labeled as PGI products, seriously disrupting market order. Therefore, it is of great significance to implement source tracing and brand protection measures for millet products.

Pathogenic fungi of the *Fusarium* genus are common in the production of grains such as millet (Femenias et al., 2021; Teixido-Orries et al., 2023). Infection by *Fusarium* species usually leads to a sharp decrease in crop yield, and the fungal toxin residues caused by *Fusarium* microbial contamination have a serious impact on the quality of millet, ultimately leading to agricultural economic losses (Dowell et al., 1999). The number of microorganisms of the *Fusarium* genus attached to the surface of grains is linearly related to the content of ergosterol ($C_{28}H_{44}O$, ZC), a metabolite produced by these microorganisms. The ZC content in grains is widely adopted as an important criterion for evaluating the degree of fungal contamination and grain quality (He et al., 2007). Meanwhile, deoxynivalenol ($C_{15}H_{20}O_6$, DON), also known as vomitoxin, is a mycotoxin secreted by microorganisms of *Fusarium* species. DON is widely present in millet grains and has high toxicity. It can cause vomiting, diarrhea, miscarriage, and other damage to humans and animals. The World Health Organization has identified DON as one of

the high-risk food contaminants (Yao and Long, 2020; Zhao et al., 2020). Therefore, efficient and rapid detection of ZC and DON content in millet grains has great significance for determining the degree of *Fusarium* fungal contamination and ensuring millet quality and food safety.

Traditional methods for determining the origin of agricultural products mainly rely on the mineral element content of the target, stable isotope ratios with regional variations (Wang et al., 2022b), chemical fingerprinting of the target substance (Yan et al., 2023), etc. The conventional quantitative detection methods for the content prediction of low-concentration toxins of DON and ZC mainly include high-performance liquid chromatography (HPLC), high-performance liquid chromatography-mass spectrometry tandem (HPLC-MS) (Antonios et al., 2010), enzyme-linked immunosorbent assay (ELISA), thin layer chromatography (TLC) (Rocha et al., 2017), etc. Though these evaluation methods have advantages such as high accuracy and sensitivity, they have some defects, including sample destruction, high detection costs, low time efficiency (inability to conduct batch testing in a single run), and environmental contamination due to the use of organic reagents (Wang et al., 2024a; Wang et al., 2024b). These issues should not be ignored.

The external environmental factors of millet planting include soil and climate in the production area, which lead to differences in crop chemical fingerprint spectra (Lu et al., 2014). Meanwhile, fungal contamination causes the denaturation of chemical nutrients, resulting in significant differences in hyperspectral characteristics (Teixido-Orries et al., 2023). Hyperspectral imaging (HSI) technology could produce chemical reflectance data across hundreds of bands to reflect the physical and chemical information of the measured samples (An et al., 2023). In recent years, HSI technology has gained increasing popularity as a rapid inspection technique that can meet the demands of today's market for fast and batch testing. HSI has great advantages such as non-destructive sample detection, high throughput, fast detection speed, and environmental friendliness in experimental techniques (Wang et al., 2024a; Wang et al., 2024b). At present, combining HSI technology with classic machine learning algorithms is a common method for the rapid prediction of geographical origins and chemical compositions of various agricultural products. Traditional machine learning algorithms, such as PLSDA (partial least squares discriminant analysis), random forest (RF) and support vector machine (SVM) have achieved generally satisfactory results in previous hyperspectral research, and they have obvious advantages such as short training time, simple computation, and strong generalization ability. HSI combined with models such as RF and SVM has been successfully applied to the identification of origins for cereal of Coix seeds (Wang et al., 2023) as well as to the quality or variety identification of small grains such as wheat (Safdar et al., 2023), oats (Teixido-Orries et al., 2023), and sorghum (Bu et al., 2023). The combination of HSI with chemometric models like partial least squares regression (PLSR) has been applied to the prediction of DON and ZC content in corn and wheat (Femenias et al., 2021; Borras-Vallverdu et al., 2024), various saponin content in ginseng (Wang et al., 2024a; Wang et al., 2024b), as well as starch and protein content in Coix seeds (Wang et al., 2023). However, it is worth noting that traditional model parameter optimization involves a certain degree of human subjectivity, and model optimization often cannot take into account data feature extraction to improve model performance (Wang et al., 2023; Zhang et al., 2020). Deep learning based on neural networks can address the above concerns.

Abbreviations: AM, attention mechanism; R, coefficient of determination; CNN, convolutional neural networks; DON, deoxynivalenol; ZC, ergosterol; HSI, hyperspectral imaging; HPLC-MS, high-performance liquid chromatography-mass spectrometry tandem; LSTM, long short-term memory; MAE, mean absolute error; MSC, multiplicative scatter correction; ORI, original data without denoising processing; PGI, protected geographical indication; PLSDA, partial least squares discriminant analysis; PLSR, partial least squares regression; RF, random forest; RNNs, recurrent neural networks; RMSE, root mean square error; RPD, residual predictive deviation; SNV, standard normal variate; SVM, support vector machine; WT, wavelet transformation; WT-ALSTM, wavelet transformation-attention mechanism long short-term memory.

Currently, combining HSI with artificial intelligence deep learning models to predict the quality of agricultural products has been a prominent research focus. Compared to traditional machine learning algorithms (including RF and SVM), deep learning models, like recurrent neural networks (RNNs) and long short-term memory (LSTM), have more evident advantages such as self-learning, self-reasoning, and no need for subjective parameter selection. As a result, these models can make more objective and reliable predictions than traditional algorithms (Li et al., 2021). Existing research has shown that using feature data extracted from HSI to reduce the dimensionality of hyperspectral data can simplify model calculations and improve prediction efficiency (Wang et al., 2022d; Wang et al., 2024a). Meanwhile, by assigning variable weights to HSI bands, the application of deep learning attention mechanism (AM) modules allows for the selection of important feature wavelengths. This enhances not only the prediction performance of the model but also the interpretability of deep learning (Wang et al., 2023). Additionally, denoising complex and redundant hyperspectral data across multiple bands provides an important means for improving model prediction effectiveness (Wang et al., 2022c; Wang et al., 2022d). However, there is a lack of research both domestically and internationally on the application of HSI technology combined with deep learning models, including data denoising, to the prediction of millet origin, fungal microbial contamination, and toxin content.

Considering this, this study aims to: (1) establish a large-scale hyperspectral database for millet from multiple origins; (2) compare the effectiveness of LSTM with traditional machine learning models such as RF, SVM, and partial least squares discriminant analysis (PLSDA or PLSR) in predicting the origin of millet and the content of fungal toxins, to determine the optimal prediction model; (3) reveal the effects of combining different denoising methods, including multiplicative scatter correction (MSC), wavelet transformation (WT), and standard normal variate (SNV), with prediction models, and determine the optimal combination; (4) evaluate the effectiveness of the deep learning AM algorithm in selecting feature bands, to provide more options for reducing the dimensionality of HSI data and improving the interpretability of prediction models in the future. This study attempts to achieve rapid quality inspection of millet by combining HSI with deep learning models, thereby providing references for the further development of portable, intelligent agricultural product inspection equipment in the future.

2 Materials and methods

2.1 Sample collection and preparation

Millet samples were collected from 12 major production areas in 9 provinces of China from October 2022 to January 2023, including three high-quality samples from regions designated with PGI status (Table 1). In the sample collection, uniformly sized and clean millet seeds were selected and naturally air-dried. All the samples were collected from 10 plots in each production area, and 5 parallel samples (500 g each) were selected from each plot. Finally, 50 samples (10×5) were collected from each production area, and 600 sets of HSI data ($10 \times 5 \times 12$) were acquired from all 12 production areas. In terms of origin prediction, to ensure the stability of the samples, the test samples are stored at a low temperature of 4°C for a long time.

TABLE 1 The distribution of twelve production areas of millet.

Production areas	Longitude and latitude
Mizhi County, Shaanxi Province (SXMZ)	37°48′32″N/110°22′35″E
Longjiang County, Heilongjiang Province (HLJLJ)	47°15′55″N/123°12′51″E
Yi'nan County, Shandong Province (SDYN)	35°31′31″N/118°20′31″E
Daning County, Shanxi Province (SXDN)	36°28′10″N/110°45′27″E
Shouyang County, Shanxi Province (SXSY)	36°42′23″N/ 112°50′1″E
Wu'an City, Hebei Province (HBWA)	**36°41′ 48″N/114°17′ 13″E**
Yu County, Hebei Province (HBYX)	40°4′2″N/115°0′52″E
Chaoyang City, Liaoning Province (LNCY)	**41°37′ 51″N/120°31′ 39″E**
Qingyang City, Gansu Province (GSQY)	35°42′23″N/107°42′31″E
Fuxin City, Liaoning Province (LNFX)	42°3′28″N/121°6′53″E
Chifeng City, Inner Mongolia Autonomous Region (NMGCF)	42°16′5″N/ 118°57′58″E
Qin County, Shanxi Province (SXQX)	**36°42′ 23″N/112°50′ 1″E**

The areas marked in bold are regions designated with PGI status.

Regarding fungal toxin contamination, millet samples were processed in a controlled environment with a temperature of 20°C and a humidity of 70% for 30 days, resulting in toxin enrichment. After data collection, all samples were processed into 50-mesh powder (stored at a low temperature of 4°C) for subsequent chemical content analysis (600 sets) to benchmark and correct the prediction effect of the established model.

2.2 Acquisition of hyperspectral data

Hyperspectral data was collected using a visible and shortwave/longwave near-infrared imaging spectrometer (VIS-NIR-HSI, HySpex VNIR-1800/HySpex SWIR 384, Norsk ElektroOptikk, Oslo, Norway). The VIS-NIR-HSI spectrometer has a wavelength range of 350–1000 nm covering visible light and short wave near-infrared parts. The SWIR spectrometer has a wavelength range of 900–2550 nm covering short and middle short-wave near-infrared parts, showing higher sensitivity to organic compounds. The spectrometer mainly consists of two tungsten halogen lamps (150 W/12 V, H-LAM, Norsk ElektroOptikk, Oslo, Norway), two lenses (VNIR and SWIR), a conveyor belt, and a data analysis computer. The two tungsten halogen lamps were used as light sources, angled at 45 degrees. The two lenses, VNIR and SWIR, were set up with exposure times of 3.5 ms and 4.5 ms, respectively. The spectral resolution was approximately 5 nm, and the samples were positioned 22 cm from the lenses. The conveyor belt moved at a speed of 2.5 mm/s. To avoid noise fluctuations at the edges of the wavelength range, the effective spectral information collected from 410 to 950 nm and 950 to 2500 nm, covering 396 bands in total, was manually merged. After the collection of the HSI data, black and white board correction was performed on the original hyperspectral images to eliminate the influence of external factors such as instrument and current on the sample data (Wang et al., 2023). Finally, ENVI 5.3 software (Research Systems Inc., Boulder, CO, United States) was employed to extract the

regions of interest and calculate the relative reflectance of the regions of interest.

2.3 Measurement of ZC and DON content in millet samples

2.3.1 Extraction and HPLC quantification of ZC and DON in millet samples

As previously documented in literature, the main organic nutritional components of millet include protein (10–15%), amylose (10–28%), and fat (3–5%), leading to the frequent contamination with *Fusarium* fungal and high levels of ergosterol and deoxynivalenol content (He et al., 2007; Dasa and Nguyen, 2020; Yang et al., 2021; Shi et al., 2023). According to the operating procedures listed in GBT 25221-2010 (General Administration of Quality Supervision, 2011), ZC was extracted from millet samples followed by quantification. First, 5 g of the above-mentioned sample powder was taken, and through processes such as cold condensation reflux extraction, rotary evaporation concentration, and nitrogen blow drying, ZC extraction solution dissolved in n-hexane was obtained. Then, quantitative detection was performed using HPLC (1290, Agilent, United States) with an Inertsil ODS-3 silica column (length: 250 mm, inner diameter: 4.6 mm, particle size: 5 μm). The detection conditions were as follows: the mobile phase consisted of n-hexane: isopropanol = 99:1 (v/v), with an elution time of 18 min. The flow rate was set to 2 mL/min, the column temperature was 40°C, the detection wavelength was 282 nm, and the injection volume was 10 μL.

Following the method described in GB5009.111-2016 (General Administration of Quality Supervision, 2017) (2016), DON was extracted from the millet samples, and its content was determined. First, 2 g of the millet sample powder was placed in a 50 mL centrifuge tube, and 20 mL of acetonitrile-water solution (84% acetonitrile, v/v) was added. Then, the mixture was subjected to ultrasonic extraction for 20 min, followed by centrifugation at 10,000 r/min for 5 min to obtain the supernatant, which was reserved for detection. Next, the solution to be tested was purified using an immunoaffinity column (IAC-030-3, PriboLab, China). The column was eluted with methanol, and the eluate was subjected to nitrogen blow drying to obtain the DON extract. Subsequently, quantitative detection was performed using HPLC (1290, Agilent, United States) with a Waters ACQUITY UPLC HSS T3 column (2.1 mm × 100 mm, 1.8 μm, Waters, United States). The detection conditions were as follows: the mobile phase consisted of 80% methanol solution (methanol: water = 80:20, v/v), with an elution time of 20 min. The flow rate was set to 0.8 mL/min, the column temperature was 35°C, the detection wavelength was 218 nm, and the injection volume was 10 μL.

2.3.2 Preparation of standard solutions for ZC and DON

First, 20 mg of ZC standard (57-87-4, Sigma-Aldrich, United States) was dissolved in 100 mL of n-hexane to prepare the stock solution (200 μg/mL). Then, by using the purchased 200 μg/mL DON standard solution (CRM46911, Sigma-Aldrich, United States) and based on the test results of the mixed sample (20 samples were randomly selected from different origins), working solutions in the concentration range of 0.01–100 μg/mL were prepared using acetonitrile solvent to establish the standard quantitative curve. The detection limit and quantification limit of the method were determined based on a signal-to-noise ratio of 3:1 (Supplementary Table S1). Finally, the chemical indicator content of millet samples was determined based on the standard content curve.

2.4 Model data analysis

2.4.1 Spectral data preprocessing

In the modeling process, appropriate preprocessing methods are usually employed to mitigate noise interference during data collection, thereby improving model prediction effectiveness and stability. This study compared three spectral preprocessing methods: SNV, MSC, and WT. Among them, SNV and MSC are commonly utilized to eliminate scattering effects in spectral data, and they are widely used to perform scattering correction (Wu et al., 2019). WT, characterized by its high resolution and good time-frequency properties, performs a multiscale detailed analysis of signals through scaling and shifting operations, thus greatly reducing random noise to smooth the spectrum (He et al., 2018).

2.4.2 Prediction models for millet origin and chemical indicators

Four models, PLSDA, SVM, RF, and LSTM, were utilized in this study for origin prediction. Meanwhile, the prediction of the two chemical indicators was achieved using four regression models: PLSR, SVM, RF, and LSTM.

The PLSDA model explores the linear relationship between spectral data (X) and the predicted region (Y) based on the correlation between variables X and Y (Wang et al., 2023). In this study, leave-one-out cross-validation was employed to determine the optimal number of latent variables (between 5–10) for the PLSDA model based on the minimum root mean square error (RMSE) obtained through cross-validation. SVM is a classic machine learning method that constructs a hyperplane to achieve better separation of observations (Liang et al., 2020). It can well handle complex spectral data, including linear and nonlinear patterns (Yu et al., 2019). This study used the radial basis kernel function for SVM modeling. Optimization was conducted for both the penalty factor (C) and the kernel parameter (γ), with reference ranges defined as 100 to 2500 for C and 2^{-8} to 2^8 for γ. The RF model integrates the predictions of multiple decision trees through a majority voting scheme. It introduces two random factors, namely the number of trees (*n*-tree) and the number of variables to consider at each split (mtry), to enhance prediction accuracy and avoid overfitting. In this study, through leave-one-out cross-validation, it was determined that *n*-tree of 500 and mtry of 2 are suitable for balancing model accuracy and efficiency (Liu et al., 2020; Jia et al., 2021). The PLSR model, unlike PLSDA, is used to solve regression prediction problems. In the PLSR model, latent variables measure the covariance between the independent variables and the target variable to achieve higher prediction accuracy. In this study, leave-one-out cross-validation was employed, and based on the minimum RMSE value obtained through cross-validation, the optimal number of latent variables for the model was determined to range between 6 and 10.

The LSTM model is a classic deep-learning neural network that can capture long-term dependencies in information. It addresses the common issue of gradient vanishing or explosion in large amounts of spectral data by introducing gate mechanisms. In this study, an LSTM model with 64 hidden units was

constructed, and its detailed architecture is illustrated in Figure 1. In the LSTM layer, two types of states were constructed: the output state (at time step t denoted as *ht*) and the cell state (at time step *t* denoted as *ct*). These states are controlled by input gates (*it*), forget gates (*ft*), cell candidate gates (*gt*), and output gates (*ot*). These gates enable the network to determine whether to discard or add information, thus forgetting and remembering the corresponding information. In the model training process, the LSTM model combines input weights, recurrent weights, and bias parameters with a dropout strategy to ensure a balance between performance and computational complexity, thus preventing overfitting (Mou et al., 2021). In the LSTM layer initializer, the parameter settings include "Orthogonal" and "Dropout rate = 0.2." In the fully connected initializer, the parameter settings include "Kaiming" and "Bach size = 40." The parameter settings of the optimizer are "Adam," "Loss = MSE (content prediction)," and "Loss = Cross Entropy (origin prediction)."

The AM originated from research on human vision and can be employed to extract the important features for variable selection. The screening process of AM involves two steps: (1) calculating the attention distribution on all input information, and (2) computing the weighted average of input information based on the attention distribution (Fan et al., 2022) (Figure 2). AM can help the LSTM model eliminate redundant information based on the information content and importance of the target value, thereby enhancing the model's generalization performance.

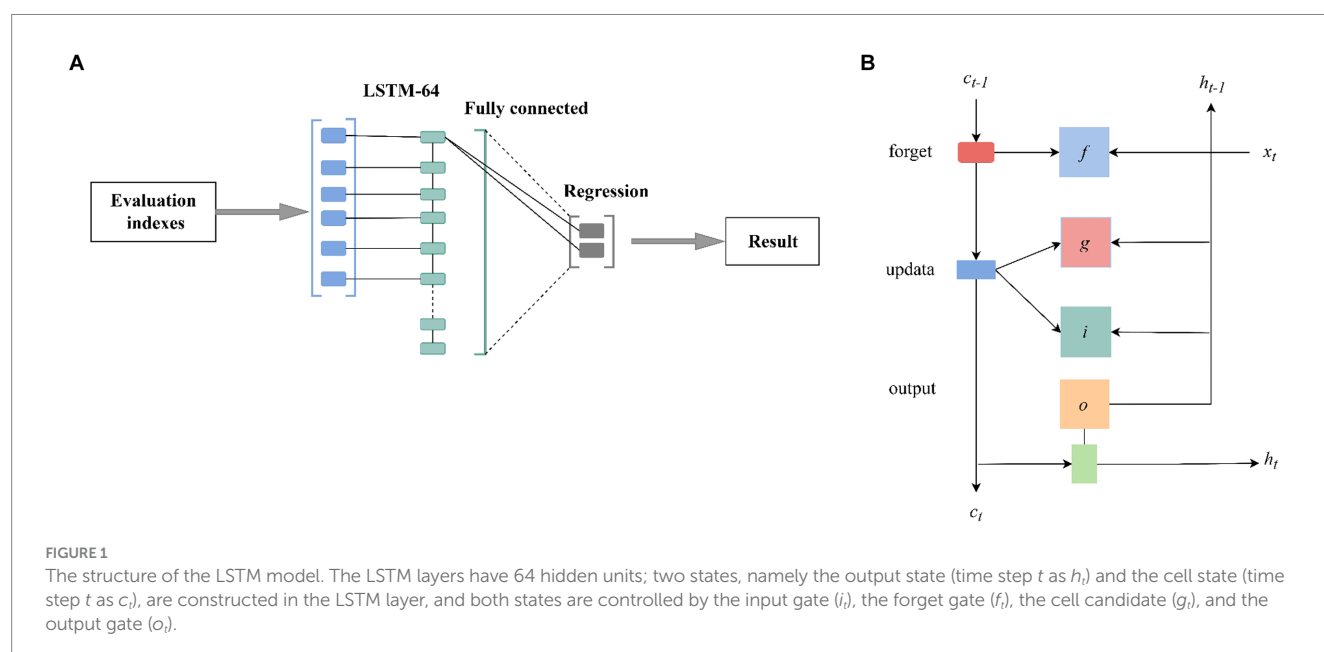### 2.4.3 Model data splitting and performance evaluation

In the model analysis, the SPXY algorithm (based on joint *x–y* distance) (Galvao et al., 2005) was utilized to randomly split the 600 samples (10 plots × 5 replicates × 12 origins) into a training set (420 samples) and a prediction set (180 samples) at a ratio of 7:3. The main advantage of the SPXY algorithm lies in its consideration of the variability of multidimensional spatial data, including both *x* and *y* dimensions. The model parameters were selected and optimized through 5-fold cross-validation. All models were implemented with Python 3.9 software in the Spyder environment. The performance of the models in predicting the origin of millet was evaluated in terms of the accuracy on the prediction set. For content prediction, metrics such as mean absolute error (MAE), coefficient of determination (R), RMSE, and residual predictive deviation (RPD) were employed to evaluate the performance of the regression models (Wang et al., 2023).

3 Results

3.1 Explicable wavelengths selected via attention mechanism in origin discrimination and chemical content prediction

By using the AM algorithm to assign weights to all bands, the top 15 variables with higher weights were selected for predicting the origin and the content of the two chemical indicators in millet (as shown in Figure 3). As for origin prediction, the feature bands are related to the differences in the main organic compound content of millet from different production areas. Specifically, the wavelengths at 998 nm are related to the third overtone region of –CH (CH/CH2/CH3) and the third overtone region of –OH from oil nutrients (Weinstock et al., 2006; Balbino et al., 2022); the wavelengths at 1156 nm and 1521 nm are, respectively, related to the second overtone regions of –OH and –CH (CH/CH2/CH3) and the first overtone region of –NH from protein in the protein compound (Wang et al., 2013; Lv et al., 2016); the wavelength at 1254, 1276, 1314, and 1467 nm are closely related to the starch compounds and reflect the –CH second overtone and combination (Workman and Weyer, 2007; Ma et al., 2017). Additionally, the wavelengths at 486, 546, and 562 nm in the visible light range represent potential color differences in millet samples due to environmental factors in different production areas.

FIGURE 1
The structure of the LSTM model. The LSTM layers have 64 hidden units; two states, namely the output state (time step *t* as h_t) and the cell state (time step *t* as c_t), are constructed in the LSTM layer, and both states are controlled by the input gate (i_t), the forget gate (f_t), the cell candidate (g_t), and the output gate (o_t).
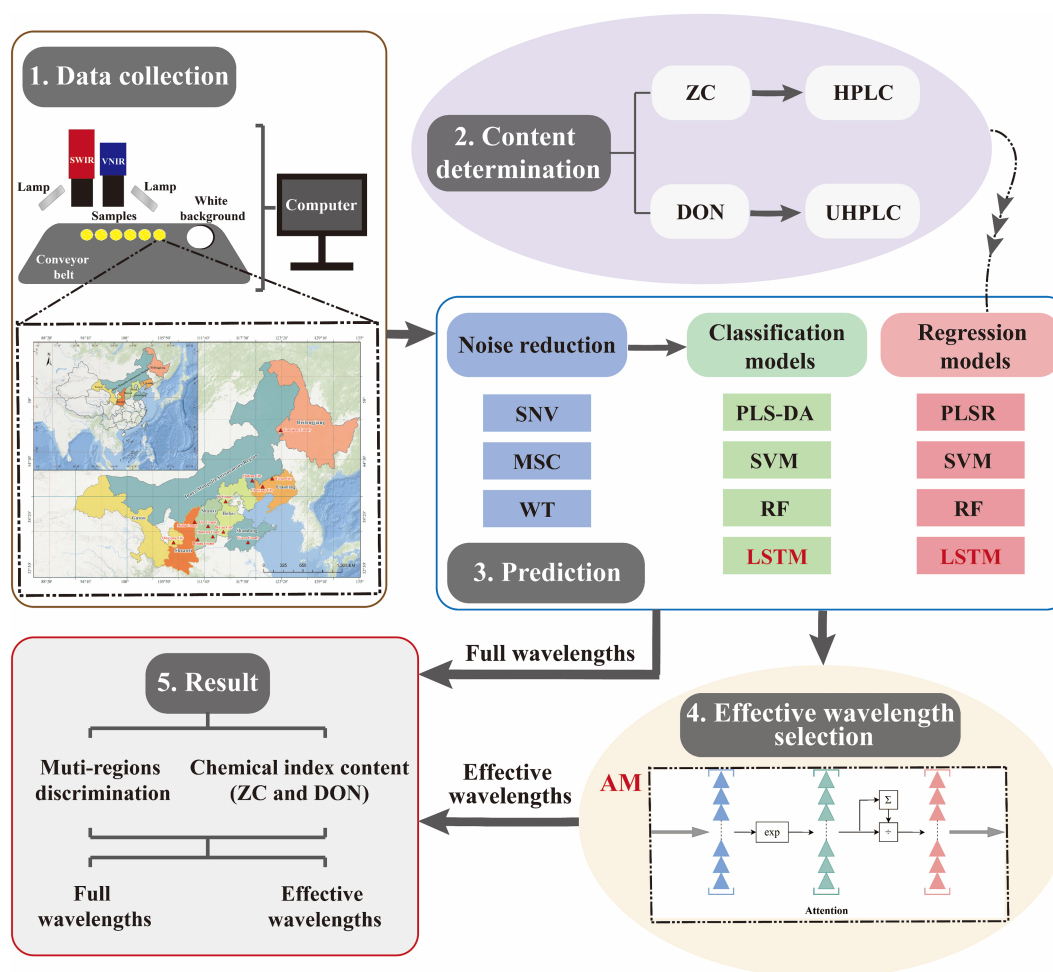
FIGURE 2
The workflow of the proposed method. It mainly includes spectral data acquisition, chemical composition analysis, model prediction (including data denoising, origin discrimination, and content regression prediction), and feature wavelength selection by the AM algorithm (AM focuses on the important part of the target while ignoring the rest by calculating the attention distribution and weighting the average value based on all input information).

In the prediction of DON and ZC content, the main feature wavelengths indicate that the contamination by fungi of the *Fusarium* genus mainly leads to changes in the organic properties of millet and potential discoloration. Regarding DON, wavelengths in the visible light range of 486, 546, and 562 nm represent potential color differences in millet caused by various environmental factors in different production areas. Meanwhile, the wavelengths at 1396 and 1412 nm are associated with the moisture content of millet (Femenias et al., 2021). The wavelengths at 1123, 1145, and 1167 nm correspond to the second overtone regions of –OH and –CH (CH/CH2/CH3) in the protein compound (Wang et al., 2013; Lv et al., 2016); additionally, the wavelengths at 1592 and 1614 nm bands are related to the –NH stretch first overtone and –CH first overtone in the protein compound (Eldin and Akyar, 2011).

As for the ZC group, the wavelengths at 638, 660, 676, and 714 nm represent potential color differences in millet caused by environmental factors in different production areas. The wavelengths at 909 and 968 nm are, respectively, related to the third overtone region of –CH

(CH/CH2/CH3) and the third overtone region of –OH from oil nutrient (Weinstock et al., 2006; Balbino et al., 2022). The effective spectra of 1118 nm and 1150 nm correspond to the second overtone regions of –OH and –CH (CH/CH2/CH3) in the protein compound (Wang et al., 2013; Lv et al., 2016); additionally, the wavelength at 1423 nm is associated to the moisture content of millet (Femenias et al., 2021).

3.2 Results of geographical origin discrimination of XM

3.2.1 Results of geographical origin discrimination based on full wavelengths

Based on the full spectrum of HSI, the results of millet origin discrimination using PLSDA, SVM, RF, and LSTM prediction models combined with three preprocessing methods (SNV, MSC, and WT) are presented in Table 2. The results showed that compared to the group of using original data without denoising processing (ORI), the
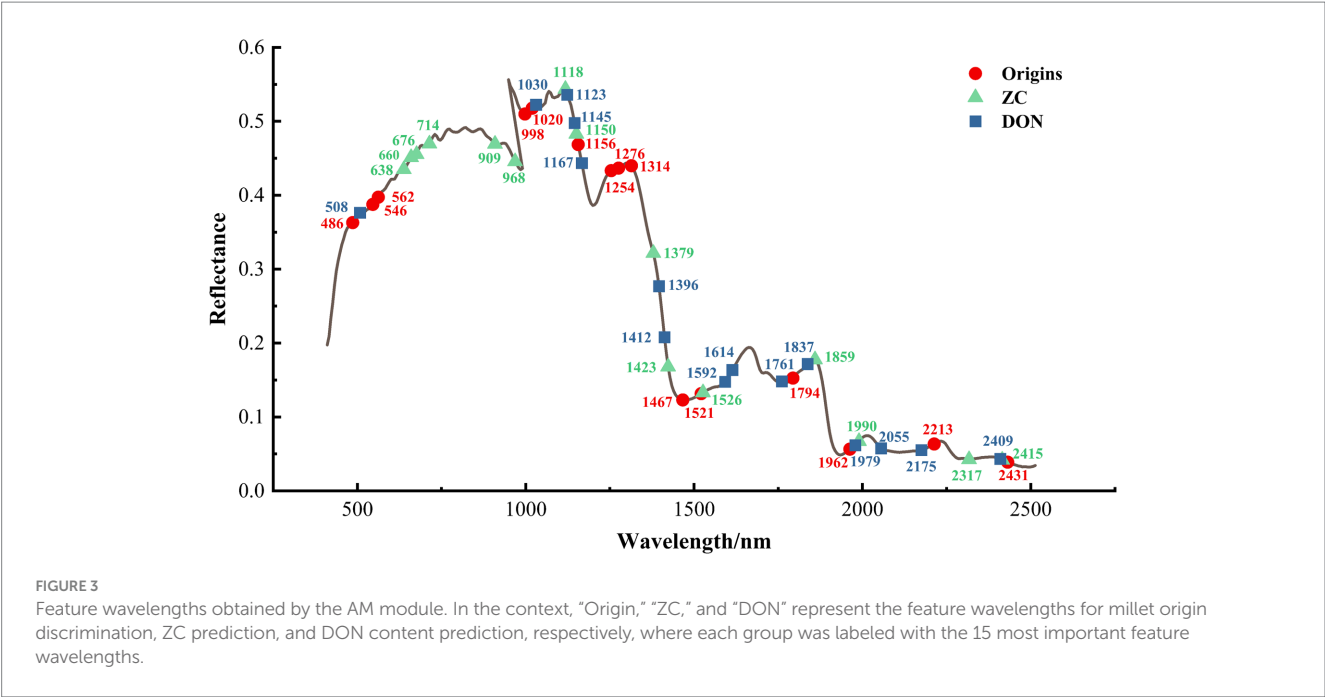
FIGURE 3
Feature wavelengths obtained by the AM module. In the context, "Origin," "ZC," and "DON" represent the feature wavelengths for millet origin discrimination, ZC prediction, and DON content prediction, respectively, where each group was labeled with the 15 most important feature wavelengths.

TABLE 2 Models for muti-regions discrimination based on full wavelengths.

Pretreatments	PLSDA (%)		SVM (%)		RF (%)		LSTM (%)	
	Train	Test	Train	Test	Train	Test	Train	Test
ORI	80.7	77.3	100.0	65.0	95.2	60.6	100	82.2
SNV	81.8	80.1	100.0	50.6	95.2	60.6	98.8	80.6
MSC	93.0	83.5	100.0	55.0	96.0	57.8	98.6	85.6
WT	94.8	92.6	100.0	87.8	99.3	85.6	99.0	94.4

ORI represents the original data without denoising processing; SNV, MSC, and WT represent three preprocessing groups, respectively.

three preprocessing groups exhibited higher origin prediction accuracy, reflecting the effectiveness of denoising methods. Among them, the WT preprocessing group obtained the best results, with the accuracy of prediction exceeding 85% for all models. The WT-LSTM model achieved the highest prediction performance for millet origin discrimination, with the highest accuracy reaching 94.4% on the prediction set.

3.2.2 Improved effect of geographical origin discrimination based on the selected wavelengths

After using the selected feature wavelengths, PLSDA, SVM, RF, and LSTM models showed higher overall accuracy on both the training and prediction sets (Table 3), with their prediction accuracy all exceeding 85%, demonstrating the effectiveness of the AM algorithm in selecting feature wavelengths. Overall, the WT data denoising preprocessing method showed the best results, with improvements in prediction accuracy across all models. In terms of regression models, the LSTM model combined with different data preprocessing methods achieved a prediction accuracy of over 98% on the prediction set. Overall, the WT-LSTM model achieved the best performance, with training and testing accuracy of 99.5 and 99.4%, respectively.

3.3 Results of DON and ZC content prediction

3.3.1 Results of DON and ZC content prediction based on full wavelengths

The results of ZC and DON content prediction based on the full wavelength are presented in Table 4. In the content prediction of both chemical indicators, after WT preprocessing, all models exhibited higher R values, lower MAE and RMSE values, and higher RPD values (all above 2.50) compared to other preprocessing groups, indicating good model performance and the outstanding denoising effect of the WT method. From the perspective of content regression models, the LSTM model obtained higher R values than the traditional PLSR, SVM, and RF models, reflecting a better linear relationship; meanwhile, the LSTM model obtained significantly lower MAE and RMSE values than other models, indicating that the LSTM model had smaller prediction errors. Additionally, the RPD values of the LSTM model are generally the highest, demonstrating the excellent predictive performance of the model. Overall, the WT-LSTM model is the best model for ZC and DON content prediction, with the highest R values (all above 0.90), lowest MAE and RMSE values, and RPD values all above 3.30, demonstrating the excellent predictive performance of these models (Table 4).

TABLE 3 Models for muti-regions discrimination based on effective wavelengths.

Pretreatments	PLSDA (%)		SVM (%)		RF (%)		LSTM (%)	
	Train	Test	Train	Test	Train	Test	Train	Test
ORI	93.1	87.2	100.0	86.1	97.8	85.6	98.6	96.1
SNV	93.8	87.8	100.0	88.3	98.6	89.4	97.9	97.2
MSC	95.7	91.7	100.0	89.4	100	91.7	99.3	97.8
WT	97.9	95.6	100.0	96.7	99.0	92.8	99.5	99.4

TABLE 4 The content prediction results of two chemical indicators by full wavelengths.

Models	Pretreatments	Test (ZC)				Test (DON)			
		R	MAE	RMSE	RPD	R	MAE	RMSE	RPD
PLSR	ORI	0.735	0.0624	0.0937	2.41	0.731	0.0346	0.0452	2.39
	MSC	0.765	0.0612	0.0889	2.53	0.796	0.0297	0.0356	2.69
	SNV	0.777	0.0611	0.0869	2.60	0.803	0.0212	0.0320	2.74
	WT	0.789	0.0610	0.0855	2.67	0.842	0.0179	0.0287	2.86
SVM	ORI	0.765	0.0600	0.0880	2.58	0.765	0.0325	0.0423	2.57
	MSC	0.742	0.0598	0.0901	2.50	0.778	0.0318	0.0431	2.63
	SNV	0.780	0.0609	0.0865	2.71	0.831	0.0188	0.0286	2.88
	WT	0.849	0.0512	0.0832	2.93	0.854	0.0165	0.0269	2.91
RF	ORI	0.759	0.0615	0.0899	2.49	0.702	0.0387	0.0467	2.22
	MSC	0.798	0.0547	0.0831	2.66	0.839	0.0170	0.0266	2.80
	SNV	0.854	0.0516	0.0824	2.99	0.854	0.0163	0.0254	2.91
	WT	0.880	0.0477	0.0730	3.17	0.867	0.0154	0.0239	2.93
LSTM	ORI	0.847	0.0501	0.0798	2.90	0.849	0.0166	0.0248	2.89
	MSC	0.866	0.0486	0.0768	3.06	0.874	0.0142	0.0228	3.11
	SNV	0.887	0.0469	0.0734	3.18	0.860	0.0151	0.0297	2.98
	WT	0.905	0.0454	0.0708	3.38	0.970	0.0101	0.0173	3.65

Evaluation metrics for model performance include R, MAE, RMSE, and RPD; three methods for noise reduction are MSC, WT, and SNV; four prediction models are PLSR, SVM, RF, and LSTM.

3.3.2 Improved effect of ZC and DON content prediction based on the selected wavelengths

As shown in the above prediction results using the full spectrum, the WT preprocessing method exhibited the best denoising effect. Meanwhile, redundant spectral data can lead to issues such as high model complexity, long data processing times, and poor predictive performance. However, these issues can be addressed by selecting effective wavelengths. In this section, feature wavelengths are extracted using the AM algorithm, and four regression models (PLSR, SVM, RF, and LSTM) were combined with the WT preprocessing method to predict the content of two chemical indicators. The results are presented in Table 5. In the content prediction of the two chemical indicators, the four models using selected wavelengths all obtained better results than those using the full spectrum group (higher R and RPD values, lower RMSE values), demonstrating the effectiveness of feature wavelength selection. Moreover, compared to the ORI group, the WT data denoising group demonstrated better prediction results (higher R and RPD values, lower RMSE values), highlighting the outstanding denoising effect of the WT method.

For the content prediction of the two chemical indicators, the WT-LSTM model demonstrated the best performance. Its R values

both exceeded 0.95, and the RPD values were higher than 3.50, indicating outstanding predictive capabilities of the model (Table 5). In the prediction of ZC content, compared to the full wavelength group (WT-LSTM), the R value of the selected full wavelength group was increased by 5.52%, the MAE and RMSE values were significantly decreased by about 47.97 and 41.78%, respectively, and the RPD value was increased by 5.9%. In the prediction of DON content, compared to the full wavelength group (WT-LSTM), the R value of the selected full wavelength group was increased by 0.41%, while the MAE and RMSE values were, respectively, decreased by approximately 6.93 and 4.62%, and the RPD value is increased by 1.1%, remaining at a similar level (Table 5).

4 Discussion

The quality attributes of millet determine its commercial value, and there is high variability in the quality and price of millet on the market. Due to differences in growing regions and environmental factors, millet from different origins has significant differences in appearance and nutritional content, leading to notable price disparities

TABLE 5 The content prediction results of two chemical indicators by effective wavelengths.

Models	Pretreatments	Test (ZC)				Test (DON)			
		R	MAE	RMSE	RPD	R	MAE	RMSE	RPD
PLSR	ORI	0.897	0.0469	0.0721	3.28	0.876	0.0140	0.0231	3.13
	WT	0.922	0.0395	0.0613	3.40	0.924	0.0123	0.0195	3.38
SVM	ORI	0.884	0.0470	0.0720	3.19	0.910	0.0230	0.0202	3.29
	WT	0.916	0.0414	0.0652	3.33	0.954	0.0111	0.0185	3.55
RF	ORI	0.869	0.0482	0.0772	3.04	0.899	0.0228	0.0217	3.30
	WT	0.925	0.0396	0.0602	3.47	0.922	0.0120	0.0190	3.41
LSTM	ORI	0.934	0.0365	0.0554	3.51	0.946	0.0114	0.0188	3.47
	WT	0.955	0.0236	0.0412	3.58	0.974	0.0094	0.0165	3.69

(Wang et al., 2022a). The frequent occurrence of counterfeit geographical indications undermines market fairness and brand value. Meanwhile, during storage or processing, grains such as millet are susceptible to mycotoxin contamination (Zhao et al., 2020; Femenias et al., 2021; Teixido-Orries et al., 2023), posing serious issues of food safety and quality (Bai et al., 2024). Therefore, developing a rapid and accurate method to predict the geographical origin and fungal contamination of millet is crucial for preventing fraud and protecting consumer rights. HSI emerges as a promising non-destructive detection technique, and it is widely used in the assessment of agricultural product quality (Wang et al., 2021).

Currently, HSI research has achieved good results in predicting the content of low-concentration compounds, such as toxins (DON and ZC) in maize and wheat (Femenias et al., 2021; Borras-Vallverdu et al., 2024), and ginsenosides in *Panax ginseng* (Wang et al., 2024a; Wang et al., 2024b), overcoming the challenges of trace compound prediction. In this study, HSI combined with a deep learning model (WT-ALSTM) also obtained satisfactory results in millet origin classification, with training and testing accuracy of 99.5 and 99.4%, respectively. In the prediction of low-concentration compounds, such as ZC and DON, the WT-ALSTM model's RPD values exceeded 3.0, and the R values were greater than 0.9, demonstrating the excellent predictive performance and the immense potential of HSI technology for low-concentration compound prediction. Furthermore, the WT-ALSTM model made satisfactory regression predictions, outperforming traditional and individual deep learning models. The AM model's characteristic bands provided reasonable explanatory and satisfactory prediction outcomes. Generally, the combination of the WT-ALSTM model with HSI technology provides a promising approach for developing portable equipment for rapid and effective quality prediction of millet in the future.

Hyperspectral data involve diverse noise sources, which may originate from instruments or samples. Preprocessing methods are commonly used to improve the prediction performance of models. The WT denoising method used in this study is typically sensitive to various sources of noise such as environmental conditions, instrument errors, and sample variations (He et al., 2018; Wang et al., 2022c). Existing studies, including predictions of total polysaccharides and total flavonoid content in Chrysanthemum (He et al., 2018), and assessments of total alkylamide content (TALC) and volatile oil content (VOC) in Sichuan pepper (Wang et al., 2022c), all validated the applicability of the WT denoising method to HSI data. Similarly,

in this study, the AM module was used as a feature wavelength selection method, which significantly reduced the computational burden caused by redundant data, contributing to higher model performance. Consistent with this study, the combination of the AM module with deep learning models in the field of HSI research has also yielded some encouraging results. For example, the CLSTM model successfully used the AM module to screen feature bands for predicting starch and protein content in Coix seed (Wang et al., 2023); the fusion of the AM module and the SCNN model can successfully predict wheat's susceptibility to herbicide stress (Chu et al., 2022); additionally, the AM module was combined with CNN models to predict single particle oil content in maize seeds (Zhang et al., 2022).

The deep learning model LSTM used in this study demonstrated higher prediction performance than traditional machine learning models. The LSTM module, integrated with multi-layer neural networks, shows a strong capability to handle complex and nonlinear spectral data (Fan et al., 2022). Furthermore, compared to traditional machine learning models, the LSTM model enhances compatibility with spectral time-series sequences through gated recurrent units and improves generalization and stability through dropout strategies to address overfitting issues (Wang et al., 2023). Similar studies in the literature, such as the prediction of amino acid content in beef (Dong et al., 2024) and corn variety identification (Wang et al., 2018), have confirmed the outstanding prediction performance of LSTM models and the advantages of deep learning models in terms of self-inference, avoidance of subjective parameter tuning, and more objective and reliable model output, indicating that they can be successfully used in food research in the future (Wang et al., 2023).

In future research, considering the great challenges posed by external environmental factors, simultaneously normalizing and denoising both spectral and chemical content data can suppress the impact of individual differences. Meanwhile, collecting more representative samples from various geographical origins can further improve the applicability and reliability of prediction models. Compared to traditional spectral techniques, HSI has the advantage of acquiring both spectral and image information from samples. With the prominent advantages of deep learning techniques in processing image information, it is necessary to integrate image and spectral information to further develop prediction models for millet samples, thereby broadening the application scope of HSI technology. Moreover, based on the effective wavelengths selected by the AM module in HSI, further efforts should be made to develop

specialized, portable, and miniaturized hyperspectral systems to meet the demand for on-site rapid testing in future markets.

Data availability statement

The original contributions presented in the study are included in the article/Supplementary material, further inquiries can be directed to the corresponding authors.

Author contributions

SN: Writing – original draft. WG: Writing – original draft. SL: Writing – review & editing. ML: Data curation, Formal analysis, Writing – review & editing. TL: Data curation, Formal analysis, Writing – review & editing. JR: Data curation, Formal analysis, Writing – review & editing. SR: Data curation, Writing – review & editing. JW: Writing – review & editing.

Funding

Acknowledgments

Conflict of interest

The authors declare that the research was conducted in the absence of any commercial or financial relationships that could be construed as a potential conflict of interest.

Publisher's note

All claims expressed in this article are solely those of the authors and do not necessarily represent those of their affiliated organizations, or those of the publisher, the editors and the reviewers. Any product that may be evaluated in this article, or claim that may be made by its manufacturer, is not guaranteed or endorsed by the publisher.

Supplementary material

The Supplementary material for this article can be found online at: https://www.frontiersin.org/articles/10.3389/fsufs.2024.1454020/full#supplementary-material

References

An, D., Zhang, L., Liu, Z., Liu, J., and Wei, Y. (2023). Advances in infrared spectroscopy and hyperspectral imaging combined with artificial intelligence for the detection of cereals quality. *Crit. Rev. Food Sci. Nutr.* 63, 9766–9796. doi: 10.1080/10408398.2022.2066062

Antonios, D., Guitton, V., Darrozes, S., Pallardy, M., and Azouri, H. (2010). Monitoring the levels of deoxynivalenol (DON) in cereals in Lebanon and validation of an HPLC/UV detection for the determination of DON in crushed wheat (bulgur). *Food Addit. Contam. Part B Surveill.* 3, 45–51. doi: 10.1080/19440040903514507

Bai, R., Zhou, J., Wang, S., Zhang, Y., Nan, T., Yang, B., et al. (2024). Identification and classification of Coix seed storage years based on hyperspectral imaging technology combined with deep learning. *Food Secur.* 13:30498. doi: 10.3390/foods13030498

Balbino, S., Vincek, D., Trtanj, I., Egredija, D., Gajdos-Kljusuric, J., Kraljic, K., et al. (2022). Assessment of pumpkin seed oil adulteration supported by multivariate analysis: comparison of GC-MS, colourimetry and NIR spectroscopy data. *Food Secur.* 11:835. doi: 10.3390/foods11060835

Balli, D., Bellumori, M., Masoni, A., Moretta, M., Palchetti, E., Bertaccini, B., et al. (2023). Proso millet (*Panicum miliaceum* L.) as alternative source of starch and phenolic compounds: a study on twenty-five worldwide accessions. *Molecules* 28:6339. doi: 10.3390/molecules28176339

Borras-Vallverdu, B., Marin, S., Sanchis, V., Gatius, F., and Ramos, A. J. (2024). NIR-HSI as a tool to predict deoxynivalenol and fumonisins in maize kernels: a step forward in preventing mycotoxin contamination. *J. Sci. Food Agric.* 104, 5495–5503. doi: 10.1002/jsfa.13388

Bu, Y., Jiang, X., Tian, J., Hu, X., Han, L., Huang, D., et al. (2023). Rapid nondestructive detecting of sorghum varieties based on hyperspectral imaging and convolutional neural network. *J. Sci. Food Agric.* 103, 3970–3983. doi: 10.1002/jsfa.12344

Chu, H., Zhang, C., Wang, M., Gouda, M., Wei, X., He, Y., et al. (2022). Hyperspectral imaging with shallow convolutional neural networks (SCNN) predicts the early herbicide stress in wheat cultivars. *J. Hazard. Mater.* 421:126706. doi: 10.1016/j.jhazmat.2021.126706

Dasa, F., and Nguyen, B. (2020). Relation among proximate compositions, rheological properties and injera making quality of millet varieties. *Adv. Crop. Sci. Technol.* 8:453.

Dong, F., Bi, Y., Hao, J., Liu, S., Yi, W., Yu, W., et al. (2024). A new comprehensive quantitative index for the assessment of essential amino acid quality in beef using Vis-NIR hyperspectral imaging combined with LSTM. *Food Chem.* 440:138040. doi: 10.1016/j.foodchem.2023.138040

Dowell, F., Ram, M., and Seitz, L. (1999). Predicting scab, vomitoxin, and ergosterol in single wheat kernels using near-infrared spectroscopy. *Cereal Chem.* 76, 573–576. doi: 10.1094/CCHEM.1999.76.4.573

Eldin, A., and Akyar, I. (2011). Near infrared spectroscopy. Wide spectra of quality control. 237–248

Fan, J., Bi, S., Xu, R., Wang, L., and Zhang, L. (2022). Hybrid lightweight deep-learning model for sensor-fusion basketball shooting-posture recognition. *Measurement* 189:110595. doi: 10.1016/j.measurement.2021.110595

Femenias, A., Gatius, F., Ramos, A., Sanchis, V., and Marin, S. (2021). Near-infrared hyperspectral imaging for deoxynivalenol and ergosterol estimation in wheat samples. *Food Chem.* 341:128206. doi: 10.1016/j.foodchem.2020.128206

Galvao, R., Araujo, M., Jose, G., Pontes, M., Silva, E., and Saldanha, T. (2005). A method for calibration and validation subset partitioning. *Talanta* 67, 736–740. doi: 10.1016/j.talanta.2005.03.025

General Administration of Quality Supervision (2011), inspection and quarantine of the People's Republic of China, standardization administration. Inspection of grain and oils-determination of ergosterol in grain-Normal phase high performance liquid chromatography: GB/T 25221-2010, 12. Beijing: Standards Press of China, 1–8.

General Administration of Quality Supervision (2017), inspection and quarantine of the People's Republic of China, standardization administration. Determination of deoxynivalenol and its acetylated derivatives in national food safety standards: GB5009.111-2016 [S]. Beijing: Standards Press of China, 1–21.

He, J., Chen, L., Chu, B., and Zhang, C. (2018). Determination of total polysaccharides and total flavonoids in *Chrysanthemum morifolium* using near-infrared hyperspectral imaging and multivariate analysis. *Molecules* 23:2395. doi: 10.3390/molecules23092395

He, X., Guo, D., Lan, S., Zhang, H., Li, W., Ding, J., et al. (2007). Feasibility of ergosterol as an index to estimate grain safety degree. *Grain Storage.* 6, 22–26.

Jia, P., Shang, T., Zhang, J., and Sun, Y. (2021). Inversion of soil pH during the dry and wet seasons in the Yinbei region of Ningxia, China, based on multi-source remote sensing data. *Geoderma Reg.* 25:e00399. doi: 10.1016/j.geodrs.2021.e00399

Li, X., Yi, X., Liu, Z., Liu, H., Chen, T., Niu, G., et al. (2021). Application of novel hybrid deep leaning model for cleaner production in a paper industrial wastewater treatment system. *J. Clean. Prod.* 294:126343. doi: 10.1016/j.jclepro.2021.126343

Liang, K., Huang, J., He, R., Wang, Q., Chai, Y., and Shen, M. (2020). Comparison of Vis-NIR and SWIR hyperspectral imaging for the non-destructive detection of DON levels in *Fusarium* head blight wheat kernels and wheat flour. *Infrared Phys. Technol.* 106:103281. doi: 10.1016/j.infrared.2020.103281

Liu, G., Zhou, X., Li, Q., Shi, Y., Guo, G., Zhao, L., et al. (2020). Spatial distribution prediction of soil as in a large-scale arsenic slag contaminated site based on an integrated model and multi-source environmental data. *Environ. Pollut.* 267:115631. doi: 10.1016/j.envpol.2020.115631

Lu, W., Jiang, Q., Shi, H., Niu, Y., Gao, B., and Yu, L. (2014). Partial least-squares-discriminant analysis differentiating Chinese wolfberries by UPLC-MS and flow injection mass spectrometric (FIMS) fingerprints. *J. Agric. Food Chem.* 62, 9073–9080. doi: 10.1021/jf502156n

Lv, C., Jiang, X., Zhang, Y., Zhang, X., and Mao, W. (2016). Variable selection based near infrared spectroscopic quantitative analysis on wheat crude protein content. *Trans. Chin. Soc. Agric. Mach.* 47, 340–346. doi: 10.6041/j.issn.1000-1298.2016.S0.052

Ma, H., Wang, J., Chen, Y., Cheng, J., and Lai, Z. (2017). Rapid authentication of starch adulterations in ultrafine granular powder of Shanyao by near-infrared spectroscopy coupled with chemometric methods. *Food Chem.* 215, 108–115. doi: 10.1016/j.foodchem.2016.07.156

Mahajan, P., Bera, M., Panesar, P., and Chauhan, A. (2021). Millet starch: a review. *Int. J. Biol. Macromol.* 180, 61–79. doi: 10.1016/j.ijbiomac.2021.03.063

Mou, L., Zhou, C., Zhao, P., Nakisa, B., Rastgoo, M., Jain, R., et al. (2021). Driver stress detection via multimodal fusion using attention-based CNN-LSTM. *Expert Syst. Appl.* 173:114693. doi: 10.1016/j.eswa.2021.114693

Onipe, O., and Ramashia, S. (2022). Finger millet seed coat-a functional nutrient-rich cereal by-product. *Molecules* 27:227837. doi: 10.3390/molecules27227837

Rocha, D., Oliveira, M., Furlong, E., Junges, A., Paroul, N., Valduga, E., et al. (2017). Evaluation of the TLC quantification method and occurrence of deoxynivalenol in wheat flour of southern Brazil. *Food. Additives Contamin.* 34, 2220–2229. doi: 10.1080/19440049.2017.1364872

Safdar, L. B., Dugina, K., Saeidan, A., Yoshicawa, G. V., Caporaso, N., Gapare, B., et al. (2023). Reviving grain quality in wheat through non-destructive phenotyping techniques like hyperspectral imaging. *Food. Energy. Secur.* 12:e498. doi: 10.1002/fes3.498

Saleem, S., Mushtaq, N., Shah, W., Rasool, A., Hakeem, K., Seth, C., et al. (2023). Millets as smart future food with essential phytonutrients for promoting health. *J. Food. Compost. Anal.* 124:105669. doi: 10.1016/j.jfca.2023.105669

Shi, P., Zhao, Y., Qin, F., Liu, K., and Wang, H. (2023). Understanding the multi-scale structure and physicochemical properties of millet starch with varied amylose content. *Food Chem.* 410:135422. doi: 10.1016/j.foodchem.2023.135422

Teixido-Orries, I., Molino, F., Femenias, A., Ramos, A., and Marin, S. (2023). Quantification and classification of deoxynivalenol-contaminated oat samples by near-infrared hyperspectral imaging. *Food Chem.* 417:135924. doi: 10.1016/j.foodchem.2023.135924

Wang, Y., Kang, L., Zhao, Y., Xiong, F., Yuan, Y., Nie, J., et al. (2022b). Stable isotope and multi-element profiling of Cassiae semen tea combined with chemometrics for geographical discrimination. *J. Food. Compost. Anal.* 107:104359. doi: 10.1016/j.jfca.2021.104359

Wang, X., Liao, W., An, D., and Wei, Y. (2018). Maize haploid identification via LSTM-CNN and hyperspectral imaging technology. arXiv doi: 10.48550/arXiv.1805.09105

Wang, B., Sun, J., Xia, L., Liu, J., Wang, Z., Li, P., et al. (2021). The applications of hyperspectral imaging technology for agricultural products quality analysis: a review. *Food Rev. Int.* 39, 1043–1062. doi: 10.1080/87559129.2021.1929297

Wang, Y., Wang, S., Bai, R., Li, X., Yuan, Y., Nan, T., et al. (2024a). Prediction performance and reliability evaluation of three ginsenosides in *Panax ginseng* using hyperspectral imaging combined with a novel ensemble chemometric model. *Food Chem.* 430:136917. doi: 10.1016/j.foodchem.2023.136917

Wang, L., Wang, Q., Liu, H., Liu, L., and Du, Y. (2013). Determining the contents of protein and amino acids in peanuts using near-infrared reflectance spectroscopy. *J. Sci. Food Agric.* 93, 118–124. doi: 10.1002/jsfa.5738

Wang, F., Wang, C., and Song, S. (2022a). Origin identification of foxtail millet (*Setaria italica*) by using green spectral imaging coupled with chemometrics. *Infrared Phys. Technol.* 123:104179. doi: 10.1016/j.infrared.2022.104179

Wang, Y., Wang, S., Yuan, Y., Li, X., Bai, R., Wan, X., et al. (2024b). Fast prediction of diverse rare ginsenoside contents in *Panax ginseng* through hyperspectral imaging assisted with the temporal convolutional network-attention mechanism (TCNA) deep learning. *Food Control* 162:110455. doi: 10.1016/j.foodcont.2024.110455

Wang, Y., Xiong, F., Zhang, Y., Wang, S., Yuan, Y., Lu, C., et al. (2023). Application of hyperspectral imaging assisted with integrated deep learning approaches in identifying geographical origins and predicting nutrient contents of Coix seeds. *Food Chem.* 404:134503. doi: 10.1016/j.foodchem.2022.134503

Wang, Y., Yang, J., Yu, S., Fu, H., He, S., Yang, B., et al. (2022c). Prediction of chemical indicators for quality of *Zanthoxylum* spices from multi-regions using hyperspectral imaging combined with chemometrics. *Front. Sustain. Food. Syst.* 6:1036892. doi: 10.3389/fsufs.2022.1036892

Wang, Y., Zhang, Y., Yuan, Y., Zhao, Y., Nie, J., Nan, T., et al. (2022d). Nutrient content prediction and geographical origin identification of red raspberry fruits by combining hyperspectral imaging with chemometrics. *Front. Nutr.* 9:980095. doi: 10.3389/fnut.2022.980095

Weinstock, B., Janni, J., Hagen, L., and Wright, S. (2006). Prediction of oil and oleic acid concentrations in individual corn (*Zea mays* L.) kernels using near-infrared reflectance hyperspectral imaging and multivariate analysis. *Appl. Spectrosc.* 60, 9–16. doi: 10.1366/000370206775382631

Workman, J. R., and Weyer, L. (2007). Practical guide to interpretive near-infrared spectroscopy, vol. *344*. Boca Raton: CRC Press.

Wu, Y., Peng, S., Xie, Q., Han, Q., Zhang, G., and Sun, H. (2019). An improved weighted multiplicative scatter correction algorithm with the use of variable selection: application to near-infrared spectra. *Chemometr. Intell. Lab. Syst.* 185, 114–121. doi: 10.1016/j.chemolab.2019.01.005

Wu, L., and Qu, L. (2018). A review on the resource and processing of the millet. *Food Res Dev* 39, 191–196. doi: 10.5555/20183280206

Yan, Y., Abdulla, R., Ma, Q., and Aisa, H. (2023). Comprehensive identification of chemical fingerprint and screening of potential quality markers of *Aloe vera* (L.) Burm. f. from different geographical origins via ultra-high-performance liquid chromatography hyphenated with quadrupole-orbitrap-high-resolution mass spectrometry combined with chemometrics. *J. Chromatogr. Sci.* 61, 312–321. doi: 10.1093/chromsci/bmad009

Yang, L., Li, R., Cui, Y., Qin, X., and Li, Z. (2021). Comparison of nutritional compositions of foxtail millet from the different cultivation regions by UPLC-Q-Orbitrap HRMS based metabolomics approach. *J. Food Biochem.* 45:e13940. doi: 10.1111/jfbc.13940

Yang, X., Wan, Z., Perry, L., Lu, H., Wang, Q., Zhao, C., et al. (2012). Early millet use in northern China. *Proc. Natl. Acad. Sci. USA* 109, 3726–3730. doi: 10.1073/pnas.1115430109

Yang, Y., Zhang, H., Wang, R., Deng, L., Qin, L., Chen, E., et al. (2019). Determination of yellow pigment content in foxtail millet. *J. Chin. Cereal. Oil. Assoc.* 34, 121–125.

Yao, Y., and Long, M. (2020). The biological detoxification of deoxynivalenol: a review. *Food Chem. Toxicol.* 145:111649. doi: 10.1016/j.fct.2020.111649

Yu, X., Wang, J., Wen, S., Yang, J., and Zhang, F. (2019). A deep learning based feature extraction method on hyperspectral images for nondestructive prediction of TVB-N content in Pacific white shrimp (*Litopenaeus vannamei*). *Biosyst. Eng.* 178, 244–255. doi: 10.1016/j.biosystemseng.2018.11.018

Zhang, L., An, D., Wei, Y., Liu, J., and Wu, J. (2022). Prediction of oil content in single maize kernel based on hyperspectral imaging and attention convolution neural network. *Food Chem.* 395:133563. doi: 10.1016/j.foodchem.2022.133563

Zhang, C., Wu, W., Zhou, L., Cheng, H., Ye, X., and He, Y. (2020). Developing deep learning based regression approaches for determination of chemical compositions in dry black goji berries (*Lycium ruthenicum* Murr.) using near-infrared hyperspectral imaging. *Food Chem.* 319:126536. doi: 10.1016/j.foodchem.2020.126536

Zhao, T., Chen, M., Jiang, X., Shen, F., He, X., Fang, Y., et al. (2020). Integration of spectra and image features of Vis/NIR hyperspectral imaging for prediction of deoxynivalenol contamination in whole wheat flour. *Infrared Phys. Technol.* 109:103426. doi: 10.1016/j.infrared.2020.103426

An electrochemical sensor for simultaneous voltammetric detection of ascorbic acid and dopamine enabled by higher electrocatalytic activity of co-modified MCM-41 mesoporous molecular sieve

Guoxin Ma[1]*, Qiang Shi[2], Xiuli Hou[1], Yuxin Peng[1] and Qian Liu[1]*

[1]School of Agricultural Engineering, Jiangsu University, Key laboratory of Modern Agricultural Equipment and Technology (Ministry of Education), Zhenjiang, China, [2]School of Science and Technology, Shanghai Open University, Shanghai, China

It is of great value to develop effective methods for accurately and simultaneously detecting ascorbic acid (AA) and dopamine (DA) in the field of biochemistry. This work reports a nonenzymatic electrochemical sensor for the simultaneous detection of AA and DA by employing a Co-modified MCM-41 (CoMCM-41) mesoporous molecular sieve as an efficient electrocatalytic material, which was synthesized by a two-step hydrothermal method. Subsequently, the high structural organization of the CoMCM-41 mesoporous structure was characterized, and the electrocatalytic performance of CoMCM-41 toward AA and DA oxidation was then evidenced by the catalytic effect of different electrodes modified with or without CoMCM-41. By virtue of the superior electrocatalytic activity of the CoMCM-41, a much wider peak potential difference (ΔE_{pa}) of 310 mV was obtained for the oxidation of AA and DA in their mixture solution, and the parameters that influenced the electrochemical signals of the modified electrode were also optimized. Under optimal conditions, a good linear response to AA and DA was observed on the CoMCM-41 modified electrode. For individual detection of AA and DA, the linear ranges were 7 ~ 105 μM and 5 ~ 110 μM respectively, while the linear response range was 20 ~ 100 μM for simultaneous detection of AA and DA. Satisfactory recovery results were obtained when the fabricated sensor was applied to determine AA in orange juice and DA in madopar pill samples.

KEYWORDS

electrochemical sensor, simultaneous detection, ascorbic acid, dopamine, mesoporous molecular sieve

1 Introduction

Electrochemically active biomolecules such as dopamine (DA) and ascorbic acid (AA) are important biomedical compounds that play a crucial role in the human metabolism process (Liang et al., 2023). Dopamine, the most significant catecholamine, is an important neurotransmitter widely distributed in the brain for message transfer in the mammalian central nervous system. Dysfunctions of the dopaminergic system are related to neurological disorders such as schizophrenia, Parkinson's disease, and so forth (Li et al., 2021; Xia et al.,

2023). Ascorbic acid, also known as vitamin C, is an important water-soluble cytosolic chain-breaking antioxidant in the mammalian brain. In the presence of several neurotransmitter amines, including DA, AA has been used to prevent and treat the common cold, mental illness, and cancer (Yang et al., 2023; Xu et al., 2021). Considering the vital functions of biomolecules mentioned above, it is essential to develop practical methods to accurately and rapidly detect DA and AA in neurochemistry and biochemistry fields. Because of their analogous properties, selective and simultaneous DA and AA determination has attracted much attention in biomedical chemistry and diagnostic research.

Numerous efficient methods, including colorimetry (Hao et al., 2023), chemometric-assisted kinetic spectrophotometry (Moghadam et al., 2011), and ultraviolet–visible spectrophotometry (El-Zohry and Hashem, 2013), have been developed in past years for the determination of DA and AA. Compared with those methods, electrochemical sensing has the merits of simple operation, low cost, high sensitivity, and rapid response (Zhang et al., 2020). However, DA and AA have similar electrochemical properties on bare electrodes, which complicate the identification of their oxidation potential. Also, the overlap of their volt–ampere responses could hinder their simultaneous determination (Peng et al., 2022). To overcome those shortcomings, various outstanding functionalized nanomaterials, including noble metal/alloy nanoparticles (Demirkan et al., 2020; Yang et al., 2019), polymers (Li et al., 2020; Zhang et al., 2020), and carbon-based materials (Zhao et al., 2019; Arya Nair et al., 2022; Han et al., 2024) have been introduced as modifying materials. Mesoporous molecular sieves have been vigorously pursued since ExxonMobil introduced M41S materials in 1992 (Beck et al., 1992; Kresge et al., 1992). Due to their unique pore structure and large specific surface area, silica-based mesoporous materials are very attractive and convenient for immobilizing different catalysts in various electrocatalytic fields ranging from oxygen reduction and biomass oxidation to electrochemical sensing (Chen et al., 2013; Zhang et al., 2017; Terra et al., 2019; Feng et al., 2019; Zablocka et al., 2019). Mobil composition of matter No. 41 (MCM-41) is a promising candidate for a silica-based catalyst and catalyst support for electrochemical sensors due to its hexagonally arranged uniform pore structure and high thermal stability (Jin et al., 2017). Nevertheless, most of those silica-based materials are electronic insulators, and incorporating an additional material, such as noble metal nanoparticles (Iminova et al., 2015), semiconductor quantum dots (Pabbi and Mittal, 2017), and carbon-based materials (Abraham et al., 2015) is commonly required to improve the charge transfer efficiency of silica-based materials for electrochemical applications (Eguílaz et al., 2018). A previous report found that the catalytic efficiency of MCM-41 was improved by heteroatom loading (Hassan et al., 2017), which provided a novel candidate catalyst for fabricating electrochemical sensors with good performance. The incorporation of metallic ions such as V, Fe and Co in the network structure of MCM-41 molecular sieves has showed good results for the oxidation of organic molecules (Cánepa et al., 2017), however, few studies have been reported the use of such mesoporous materials modified with transition metal of Co in the oxidation and simultaneous detection of biomedical compounds of AA and DA.

In the present study, an effective electrochemical sensor for simultaneous detection of AA and DA was developed by using Co-modified MCM-41 (CoMCM-41) as the electrocatalytic material

(Scheme 1). X-ray diffraction (XRD) analysis, transmission electron microscopy (TEM) and scanning electron microscopy (SEM) were used to characterize the as-prepared CoMCM-41 materials or CoMCM-41 based film. Then the electrochemical performance of the CoMCM-41 modified electrodes toward the oxidation of AA and DA were investigated by cyclic voltammetry (CV) and differential pulse voltammetry (DPV) techniques. The peak-to-peak separation potential between the oxidation peaks of AA and DA on CoMCM-41 modified electrodes was bigger enough for simultaneous detection of them. Finally, the electrochemical characteristics of CoMCM-41 modified electrodes for the individual and simultaneous detection of AA and DA were investigated by a DPV method. More importantly, real sample analysis was done by using the proposed CoMCM-41 based electrochemical sensing method.

2 Experimental

2.1 Chemicals and solutions

Sodium silicate ($Na_2SiO_3 \cdot 9H_2O$), sodium meta-aluminates ($NaAlO_2$), cobalt chlorate ($CoCl_2 \cdot 6H_2O$), cetyltrimethyl ammonium bromide (CTAB) were purchased from Shanghai Chemical Reagent Co., P. R. China. AA and DA were obtained from the Fourth Chemical Reagent Company of Shanghai and Sigma-Aldrich (United States), respectively. Phosphate-buffered saline (PBS, 0.1 M) solution of different pH were prepared by mixing stock solutions of NaH_2PO_4 and Na_2HPO_4, and then adjusted by H_3PO_4 or NaOH solution. Pill of madopar was obtained from Roche medical company (Shanghai). All of the chemicals were of analytical reagent grade and were used without further purification. All other aqueous solutions were prepared with deionized water.

2.2 Apparatus

XRD measurement was carried out with a Rigaku D Max 2500 PC X-ray diffractometer. Surface area and pore size distribution were measured using an NOVA2000 surface area and pore size analyzer from Quntachrome Corporation, the surface area was calculated with Brunauer–Emmett–Teller (BET) method and pore size distribution, pore volume was calculated with Barrett–Joyner–Halenda (BJH) method (Barrett et al., 1951). TEM image was taken with a JEOL 2100 TEM (JEOL, Japan) operated at 200 kV, and SEM was obtained with a JSM-6480 field-emission scanning electron microscope. All electrochemical experiments including CV and DPV were performed with a CHI660 electrochemical workstation (Chenhua, Shanghai, China). A conventional three-electrode electrochemical system was used for all electrochemical experiments, which consisted of a glassy carbon electrode (GCE) working electrode, a Pt wire auxiliary electrode and a saturated calomel reference electrode (SCE), respectively.

2.3 Synthesis of CoMCM-41

With some modifications, the CoMCM-41 mesoporous molecular sieves were synthesized by a reported two-step hydrothermal method

(Zhao et al., 2007). A composition of 2.13 g of Na$_2$SiO$_3$·9H$_2$O, 0.12 g of NaAlO$_2$, and 1.43 g of CoCl$_2$·6H$_2$O was dissolved in 50 mL of deionized water and mixed with a H$_2$SO$_4$/deionized water solution (volume ratio 1:1) to adjust the pH value of the solution to equal 11.0. The gel was stirred for 3 h at 90°C, then transferred into a 100 mL Teflon-inner-container stainless steel water boiler and kept in an oven at 200°C for 5 h. The reaction mixture was cooled to room temperature and poured into another beaker containing 10.23 g of Na$_2$SiO$_3$·9H$_2$O. The sample was stirred, creating the colloidal suspension liquid precursor (sample I). 4.85 g of CTAB was added to 25 mL water in another beaker, creating a transparent, glue-like suspension liquid (sample II). Sample I was slowly dropped into sample II with vigorous stirring, and the pH was adjusted to 11.0 using H$_2$SO$_4$ solution. After 1 h of stirring, the mixture was introduced to the boiler and kept in an oven at 130°C for 48 h. Finally, the CoMCM-41 was obtained after cooling, filtering, rinsing with deionized water, and drying at 120°C for 24 h.

2.4 Preparation of CoMCM-41 modified electrode

A bare GCE was polished successively with 1, 0.3, and 0.05 μm alumina slurries. Then, it was rinsed with doubly distilled water and sonicated in ethanol and doubly distilled water for 5 min. A suspension of CoMCM-41 (10 mg/mL) was obtained by dispersing 10 mg CoMCM-41 in 10 mL of a 0.2% chitosan (CHI) solution. 10 μL of CoMCM-41 suspension was dropped to cover the surface of the electrode, then the CoMCM-41 modified electrode (denoted as CoMCM–CHI/GCE) was kept at 4°C for 12 h to dry, then stored for further use. With the help of the CHI employed in the CoMCM–CHI/GCE, the CoMCM-41 particles could be embedded on the surface of electrode much easier and successfully.

3 Results and discussion

3.1 Characterization of CoMCM-41

Figure 1A shows XRD patterns of the as-prepared CoMCM-41 at small angles. As shown, the sample had a distinct diffraction peak at (100) at 2θ of 2.3°, showing the high structural organization of the mesoporous structure (Zhao et al., 2007). The adsorption–desorption isotherms and pore size distribution curves of the sample are shown in Figure 1B, which shows that the adsorption–desorption isotherms of the sample were typical type IVs, indicating its mesoporous framework (Beck et al., 1992). Adsorption and desorption isotherms of the sample were obviously abrupt in a relative pressure range of 0.4–0.6, demonstrating that CoMCM-41 had a mesoporous larger pore size, which was consistent with the pore size distribution curve of CoMCM-41 in Figure 1C. It can be clearly seen form the TEM image (Figure 1D) that the as-prepared CoMCM-41 exhibited a mesoporous structure (Zhao et al., 2007). These results above indicated the successfully synthesized of CoMCM-41 mesoporous material. By virtue of its electrocatalytic activity, CoMCM-41 was then used for construction a sensing platform toward electrochemically active biomolecules of AA and DA. After the modification of electrodes, SEM was

employed to characterize the morphology of the CoMCM–CHI film on the surface of GCE. Figure 1E shows the surface image of a pure layer of CHI, which formed a flat and homogeneous film across the entire section. However, after the CoMCM-41 particles were embedded by CHI on the electrode surface, the rugged appearance was observed obviously for the CoMCM–CHI film (Figure 1F), which indicated the successful modification of the CoMCM–CHI/GCE.

3.2 CV behavior of AA and DA on the modified electrode

Figure 2A illustrates the CV responses of bare GCE, CHI/GCE, and CoMCM-CHI/GCE recorded in 0.1 M PBS (pH 4.0) in the presence of 120 μM AA. It can be seen that the AA showed an irreversible oxidation peak and a much smaller CV peak response on the bare GCE (curve a). The anodic peak current of AA at the CHI/GCE (curve b) showed no obvious change compared with the bare GCE, whereas at the CoMCM–CHI/GCE (curve c), the peak current of the AA was 2.3 times larger than that of the bare GCE, and the peak potential shifted more negatively. At the same time, the anodic peak current of DA at the bare GCE showed a small anodic peak with a peak potential of approximately 500 mV (curve a in Figure 2B). An observed change of anodic peak current and a peak potential shift of 90 mV was obtained at the CHI/GCE (curve b), whereas a 2.1 times larger anodic peak current compared to the bare GCE was observed at the CoMCM–CHI/GCE (curve c). Those phenomena are clear evidence of the catalytic effect of the chemically modified electrode toward the oxidation of AA and DA. The CV responses of CoMCM–CHI/GCE scanned under different scan rate from 10 to 100 mV/s was displayed in Figures 3A,C, and it can be clear seen that the peak currents of the electrode were increased gradually with the increasing of the scan rate. As shown in Figures 3B–D, the peak currents of the CoMCM–CHI/GCE for the oxidation of AA and DA were linearly proportional to the scan rates in the range of 10~100 mV/s, indicating an adsorption-controlled electrode process for the electro-oxidation of AA and DA at the CoMCM–CHI/GCE (Han et al., 2023).

3.3 Optimization of the experimental conditions

The concentration of CoMCM-41 at the peak current of DA was investigated firstly. As shown in Figure 4A, the peak current of AA increased with the increase in CoMCM-41 concentration from 4.0 to 8.0 mg/mL, and little change of the peak current was observed when the CoMCM-41 content exceeded 8.0 mg/mL. Figure 4B shows that the peak current of DA increased with the increase in CoMCM-41 concentration from 4.0 to 10.0 mg/mL. Because of the sensitivity of the current response, 10.0 mg/mL of CoMCM-41 gel was chosen for electrode modification in this work. The effect of the pH value of PBS on the oxidation potential of AA and DA was studied in the range of 2.0 to 8.0 (Figure 4C). As shown, the peak potential of AA (curve a) shifted negatively by 75 mV/pH with the increase in pH. When pH < 5.0, the minimum potential was at pH = 5.0, and the peak potential stayed constant when pH > 5.0. Although the peak potential of DA (curve b) was proportional to pH, it shifted negatively by 60 mV/pH
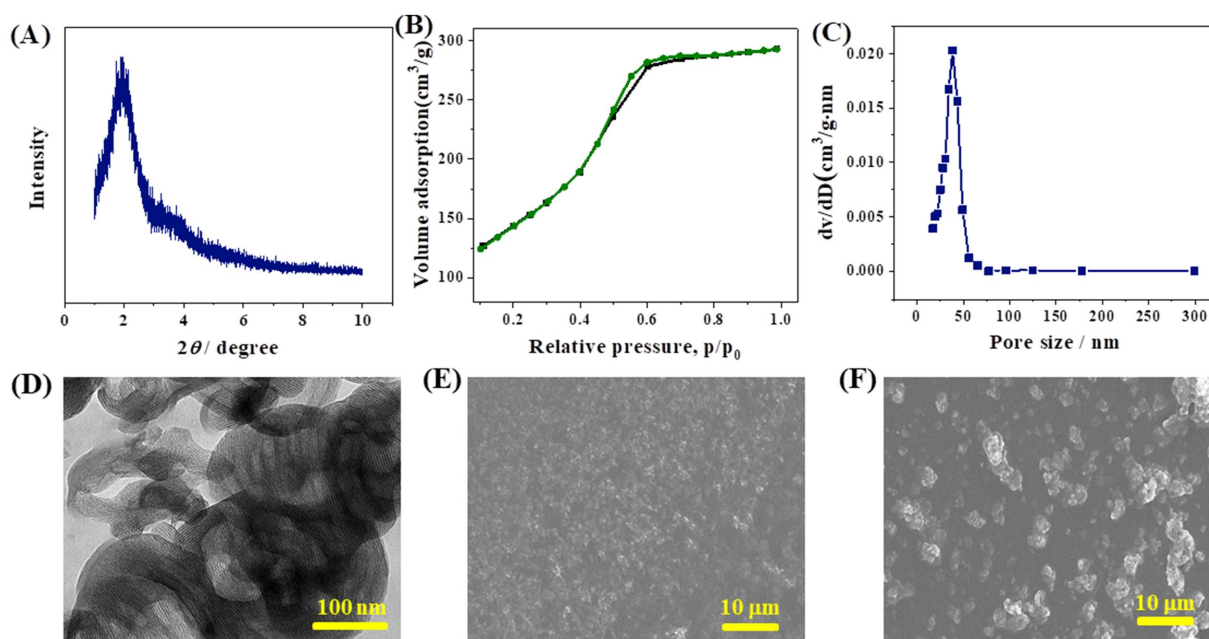
FIGURE 1
(A) XRD patterns of the as-prepared CoMCM-41; (B) adsorption and desorption isotherms of CoMCM-41; (C) the pore size distribution curve of CoMCM-41; (D) TEM image of CoMCM-41; SEM images of GCE modified with (E) 0.2% CHI and (F) CoMCM-41 dispersed in 0.2% CHI.
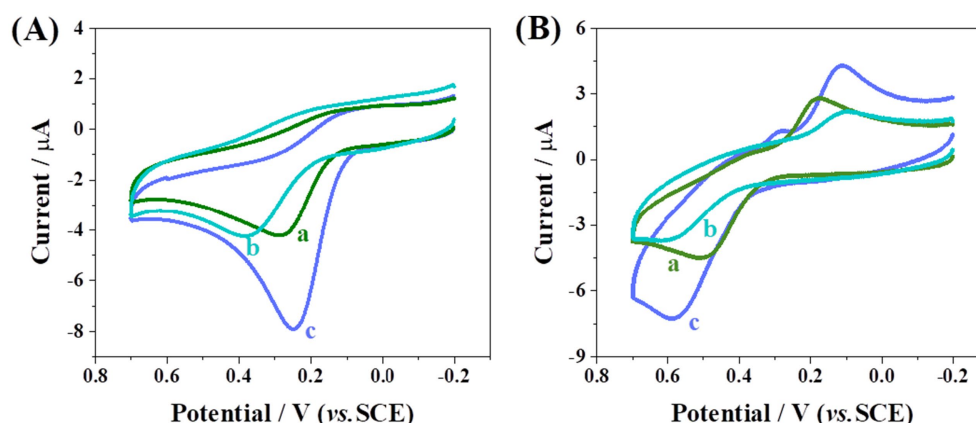

FIGURE 2
CV curves of bare GCE (a), CHI/GCE (b) and CoMCM-CHI/GCE (c) in 0.1 M PBS (pH 4.0) in the presence of 120 μM (A) AA and (B) DA, respectively.

with the increase in solution pH. Therefore, 0.1 M PBS with a pH of 4.0 was selected for the following experiment.

3.4 Oxidation of mixture of AA and DA at CoMCM–CHI/GCE

Ascorbic acid and DA always exist together in a biological environment, but simultaneous determination of AA and DA is difficult on a bare GCE and other solid electrodes. In this work, the peak potentials could be distinguished at the CoMCM–CHI/GCE. The CV behavior of an AA and DA mixed solution was studied on the bare GCE, the CHI/GCE, and the CoMCM–CHI/GCE. As shown in

Figure 4D, the AA and DA showed 2 broad anodic peaks of 380 mV and 530 mV, respectively at the bare GCE (curve b). Only one overlapped peak (380 mV) was at the CHI/GCE (curve a). For the CoMCM–CHI/GCE, two well-defined peaks were observed at approximately 280 mV and 590 mV, corresponding to AA and DA oxidation, respectively, (curve c). The peak potential difference (ΔE_{pa}) between the oxidation of AA and DA reached 310 mV, which was attributed to the promoted adsorption of these molecules on the porous nanostructure of CoMCM-41 film with high surface area and these abundant active sites (Zhang et al., 2018; Peng et al., 2023). More importantly, the ΔE_{pa} of 310 mV obtained in this work was much bigger than those reported in the recent works listed in Table 1 (Peng et al., 2022; Yang et al., 2023; Celik Cogal et al., 2024; Jia et al., 2024; Darabi et al., 2023), indicating
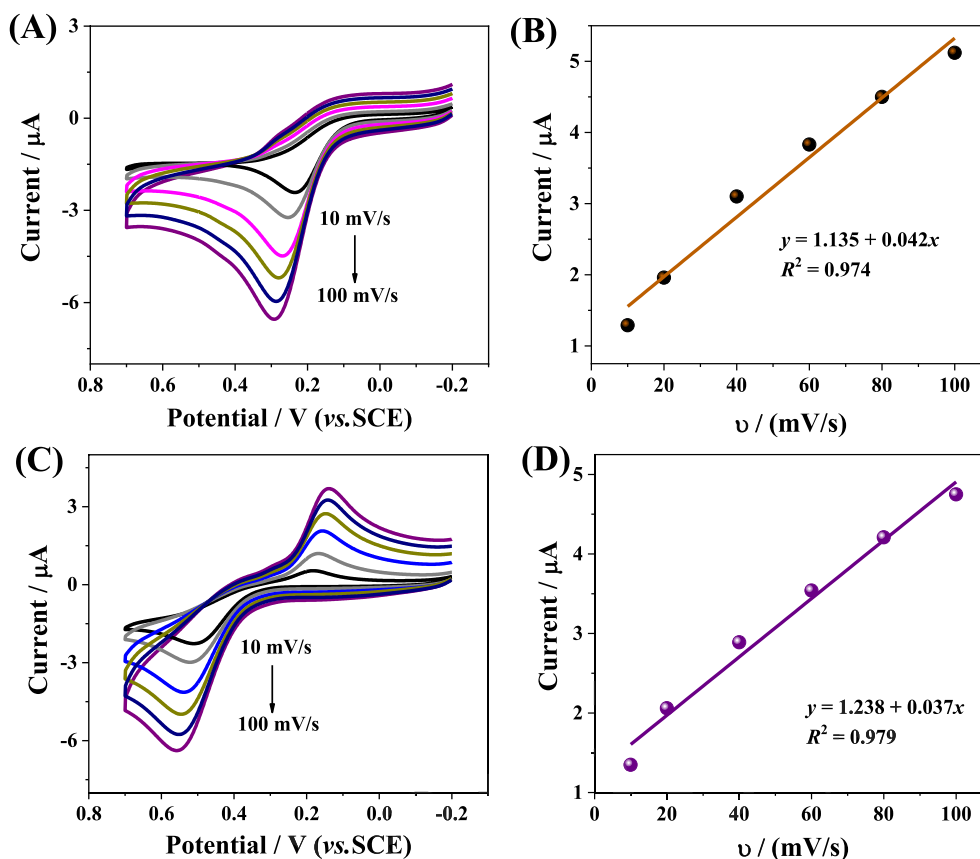
FIGURE 3
CV curves of CoMCM–CHI/GCE in 0.1 M PBS (pH 4.0) with 20 μM (A) AA and (C) DA at various scan rates of 10, 20, 40, 60, 80, and 100 mV/s. The corresponding plots of peak current versus scan rate for (B) AA and (D) DA, respectively.

the high catalytic oxidation activity of the proposed CoMCM–CHI/GCE for simultaneous determination of AA and DA.

3.5 Simultaneous determination of AA and DA

The electro-oxidation processes of AA and DA in the mixture were investigated by DPV when the concentration of one species changed while that of another species remained constant. Figure 5A gives the DPV recordings of the CoMCM–CHI/GCE with various DA concentrations in the presence of 100 μM of AA. As shown, the peak currents increased with the increasing of DA concentrations. The oxidation peak current was proportional to the DA concentration, and there was a linear relation between the oxidation peak currents of DA and its concentration over a range of 5 ~ 110 μM. The linear regression equation was $I\,(\mu A) = 0.184 + 0.030 C_{DA}$ (μM), $R^2 = 0.985$ (Figure 5B), and the limit of detection (LOD) was 1.7 μM ($S/N = 3$). Similarly, as shown in Figures 5C,D, the oxidation peak currents were proportional to the AA concentrations in the range of 7 ~ 105 μM with a LOD of 2.1 μM ($S/N = 3$). The linear regression equation was $I\,(\mu A) = 0.138 + 0.404 C_{AA}$ (μM), $R^2 = 0.994$. To demonstrate the analytical performance of the CoMCM–CHI based sensor, the linear response range and LOD were compared with previous reports in the literatures. As depicted in Table 1, the proposed sensor exhibited better or comparable performance toward AA

and DA detection. Those results demonstrated that the CoMCM–CHI/GCE proposed in this work is a promising candidate for the simultaneous determination of AA and DA in a mixture without cross interference.

Subsequently, the DPV responses of the CoMCM–CHI/GCE recorded in 0.1 M PBS (pH 4.0) with various concentrations of the two species were also investigated. As depicted in Figure 6A, the electrochemical responses of the CoMCM–CHI/GCE were increased gradually with the increasing of the concentrations of the two species from 20 to 100 μM, respectively and the oxidation peak currents of AA and DA were clearly separated from each other, which indicated that the electrochemical detection of the two species can be resolved well from their mixed solutions, resulted in the high accuracy of the sensor from the mutual interference. Figure 6B indicates that the oxidation peak currents of CoMCM–CHI/GCE increased linearly with increasing concentrations of both AA and DA in the concentration range of 20 ~ 100 μM, which demonstrated that the proposed CoMCM-41 based electrochemical sensor was possible to discriminate and simultaneously detect AA and DA in their mixture solution by the conventional DPV method.

3.6 Real sample analysis

The CoMCM–CHI/GCE was applied to measure AA in orange juice using a standard addition method; the results are listed in
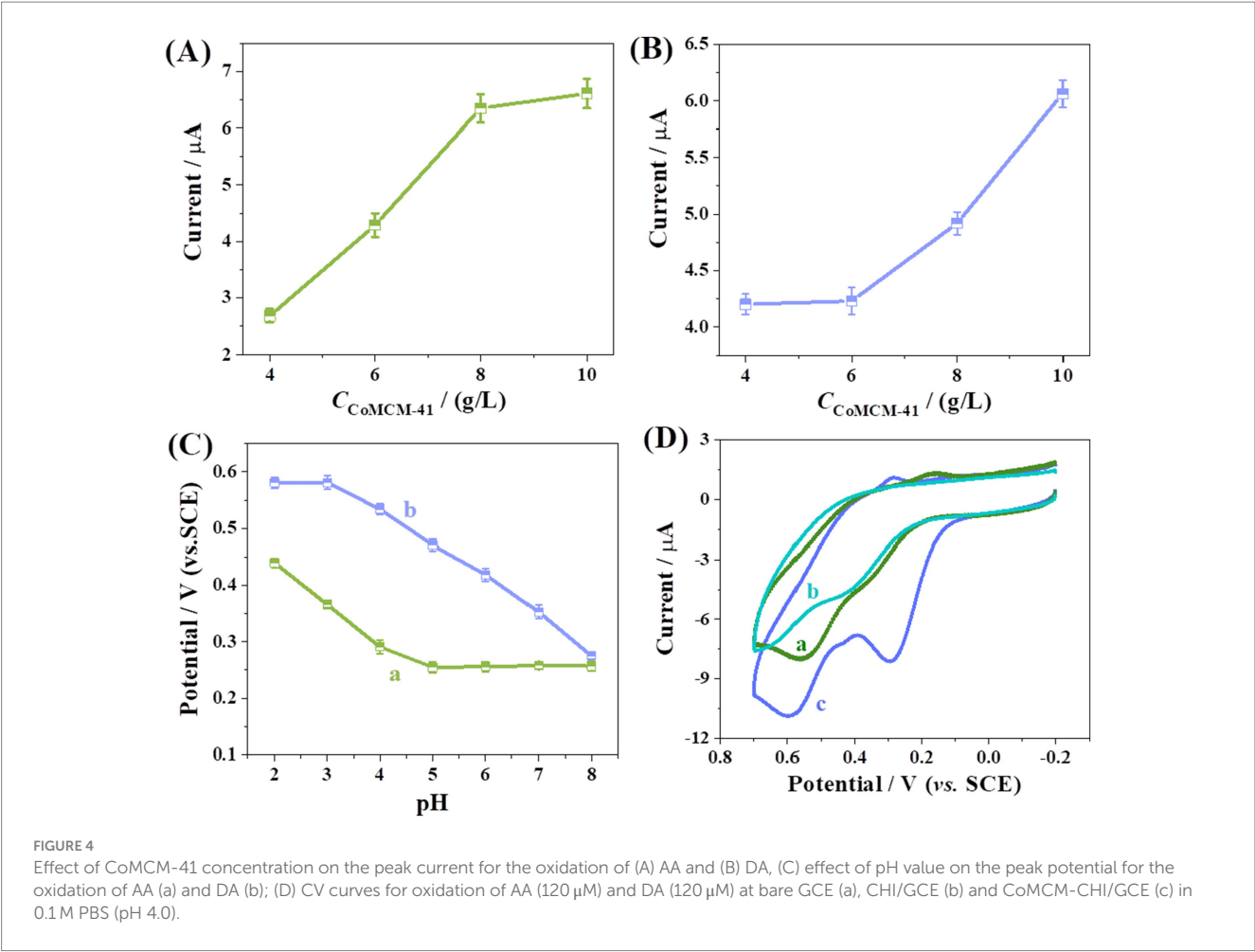
FIGURE 4
Effect of CoMCM-41 concentration on the peak current for the oxidation of (A) AA and (B) DA, (C) effect of pH value on the peak potential for the oxidation of AA (a) and DA (b); (D) CV curves for oxidation of AA (120 μM) and DA (120 μM) at bare GCE (a), CHI/GCE (b) and CoMCM-CHI/GCE (c) in 0.1 M PBS (pH 4.0).

TABLE 1 Comparison of ΔE_{pa} between AA and DA, CoMCM-CHI/GCE for AA and DA detection with different modified electrodes.

Modified electrodes	ΔE_p (V)	Linear range (μM)		LOD (μM)		References
		AA	DA	AA	DA	
3D-KSC/C$_{CSBP}$[a]/GCE	0.24	1,980–6,000	14.1–100	660	4.6	Peng et al. (2022)
PtCo/N-CNSs[b] electrode	0.19	30–1,900	0.5–80	1.02	0.12	Yang et al. (2023)
GCE-Co/MoSe$_2$/PPy@CNF[c]	0.16	30–3,212	1.2–536	6.32	0.45	Celik Cogal et al. (2024)
Ti$_3$C$_2$T$_x$/TiO$_2$ NWs[d]/GCE	0.14	300–1,800	2–9 and 9–33	6.61	0.093	Jia et al. (2024)
rGO/PPy-Pt[e]/GCE	0.19	800–2,100	30–1,400	0.12	0.071	Darabi et al. (2023)
CoMCM-CHI/GCE	0.31	7–105	5–110	2.1	1.7	This work

3D-KSC/C$_{CSBP}$[a]: N-doped carbon nanosheets/three-dimensional porous carbon.
PtCo/N-CNSs[b]: PtCo nanocrystals/porous N-doped carbon nanospheres.
PPy@CNF[c]: polypyrrole hybrid-based carbon nanofiber.
Ti$_3$C$_2$T$_x$/TiO$_2$ NWs[d]: Ti$_3$C$_2$T$_x$/TiO$_2$ nanowires.
rGO/PPy-Pt[e]: reduced graphene oxide/polypyrrole-platinum nanocomposite.

Table 2. As is shown, the recoveries and relative standard deviation for the determination of AA were in the ranges of 98.61–101.71% and 0.39–2.15%, respectively. That modified electrode was also applied to determine the recovery of a madopar pill in spiking DA using the standard addition method. One madopar pill was dispersed in 5 mL PBS to fit into the linear range of DA. The samples were diluted 12.5 times with PBS (pH 4.0) for detection. The diluted sample was spiked with various concentrations of DA, and its DPV could be obtained by the modified electrode. The recovery results are listed in Table 3. The recoveries and relative standard deviation for the determination of AA were in the ranges of 98.09–100.64% and 1.31–2.32%, respectively. Those recoveries and precisions were acceptable, showing that the modified electrode could be efficiently applied to determine AA and DA in real samples. Furthermore, to verify the reliability and accuracy
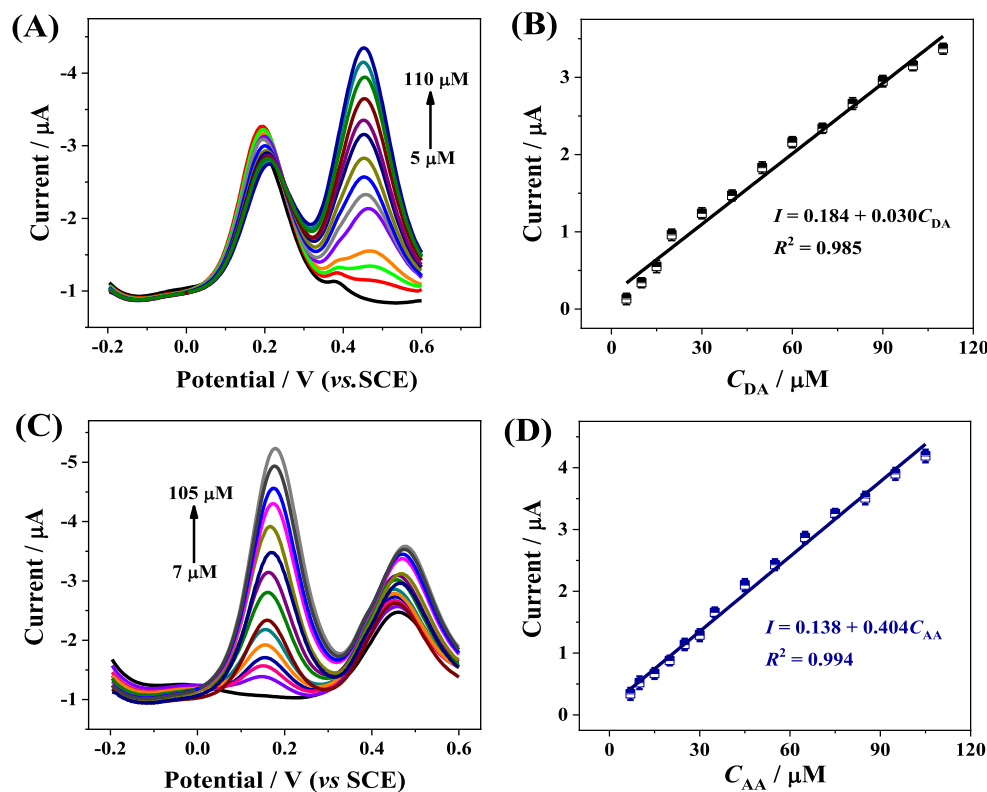
FIGURE 5
(A) DPV curves of CoMCM-CHI/GCE in 0.1 M PBS (pH 4.0) with different DA concentrations (from bottom to top: 0, 5, 10, 15, 20, 30, 40, 50, 60, 70, 80, 90, 100, 110 μM) in the presence of 100 μM AA, (B) the calibration plot for DA detection, (C) DPV curves of CoMCM-CHI/GCE in 0.1 M PBS (pH 4.0) with different AA concentrations (from bottom to top: 0, 7, 10, 15, 20, 25, 30, 35, 45, 55, 65, 75, 85, 95, 105 μM) in the presence of 100 μM DA, (D) the calibration plot for AA detection.
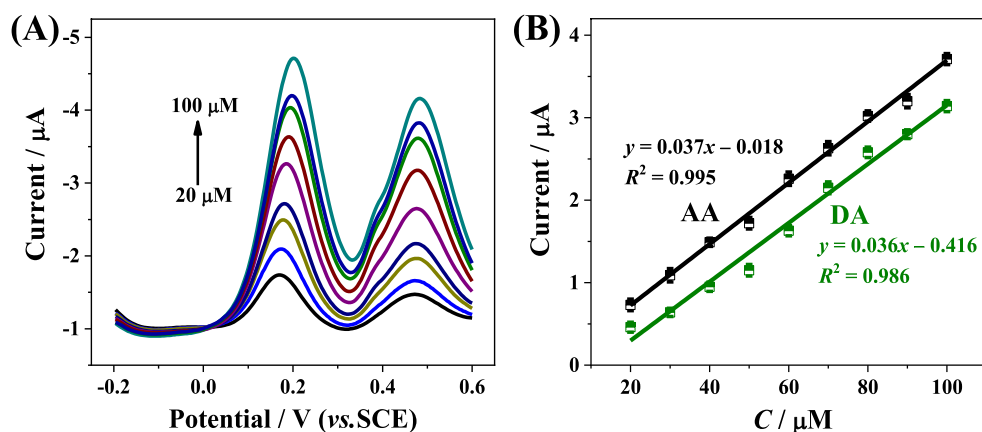

FIGURE 6
(A) DPV curves of CoMCM-CHI/GCE for simultaneous detection of AA and DA in 0.1 M PBS (pH 4.0) with their changed concentrations (20, 30, 40, 50, 60, 70, 80, 90, and 100 μM from bottom to top), (B) the calibration plots for simultaneous detection of AA and DA.

of the proposed electrochemical sensing method, high-performance liquid chromatography (HPLC) was applied to detect these spiked samples for comparison. The consistency between the two methods shown in Tables 2, 3 confirmed the accuracy of the proposed electrochemical sensor for AA and DA detection.
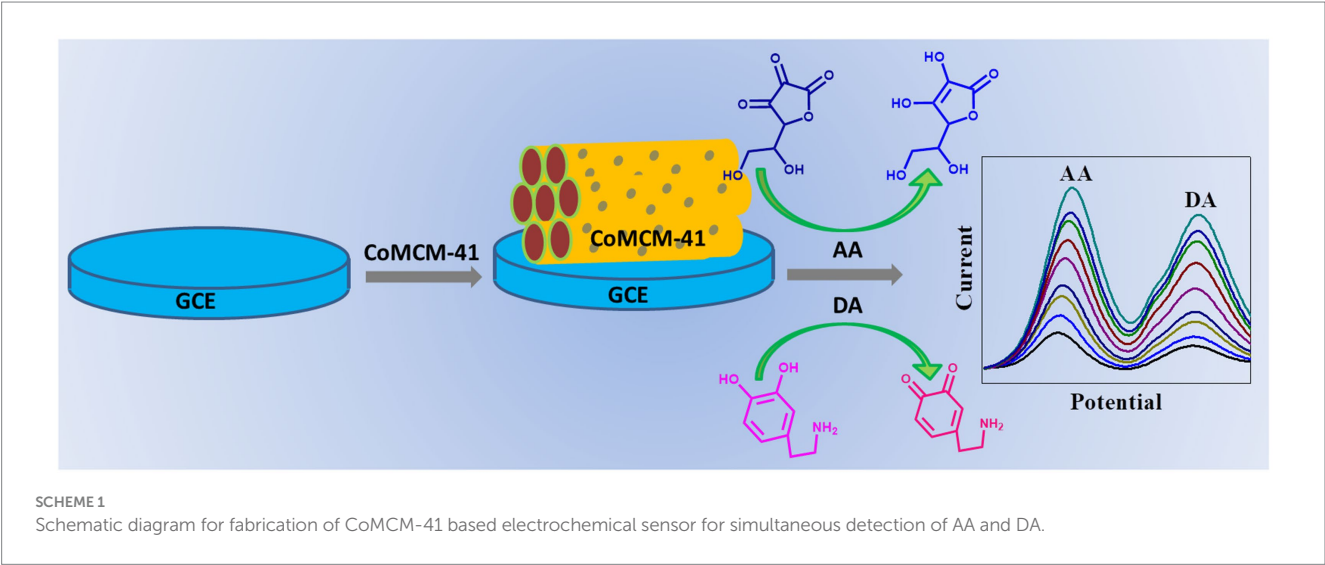
4 Conclusion

In summary, Co-containing mesoporous molecular sieves of CoMCM-41 were synthesized successfully by introducing Co-saponite into the pore wall. XRD characterization, adsorption–desorption

TABLE 2 Determination of AA in orange juice with the proposed electrochemical sensor and standard HPLC method ($n = 5$).

Samples	Electrochemical sensor					HPLC
	Detected (µM)	Added (µM)	Found (µM)	Recovery	RSD	Found (µM)
1	6.88	70.00	76.71	99.78%	0.39%	75.42
2	13.76	70.00	83.90	100.16%	1.28%	Not tested
3	20.64	70.00	90.18	99.49%	2.15%	Not tested
4	27.70	70.00	96.35	98.61%	1.73%	Not tested
5	34.62	70.00	106.41	101.71%	2.04%	103.35

TABLE 3 Determination of DA in madopar pills with the proposed electrochemical sensor and standard HPLC method ($n = 5$).

Samples	Electrochemical sensor					HPLC
	Detected (µM)	Added (µM)	Found (µM)	Recovery	RSD	Found (µM)
1	29.91	70.00	99.10	99.19%	1.47%	98.74
2	44.86	70.00	115.57	100.62%	2.32%	Not tested
3	59.81	70.00	130.64	100.64%	1.40%	Not tested
4	74.77	70.00	142.01	98.09%	1.31%	Not tested
5	89.72	70.00	158.88	99.47%	1.43%	156.36

SCHEME 1
Schematic diagram for fabrication of CoMCM-41 based electrochemical sensor for simultaneous detection of AA and DA.

isotherms and pore size distribution curves indicated the high structural organization of the mesoporous structure. Employing the as-prepared CoMCM-41 as an ideal electrode modification material, the novel CoMCM–CHI/GCE had remarkable electrocatalytic activity for the oxidation of AA and DA simultaneously, and it needs to be emphasized that the proposed CoMCM–CHI/GCE showed a wider separation of peak currents between the oxidation of AA and DA. Good linear response to AA and DA was observed on the CoMCM-41 modified electrode, and satisfactory recovery results were obtained when the fabricated sensor was applied to determine AA in orange juice and DA in madopar pill samples. Those properties indicated that the CoMCM–CHI/GCE is promising for efficient AA and DA measurements in actual samples.

Data availability statement

The raw data supporting the conclusions of this article will be made available by the authors, without undue reservation.

Author contributions

GM: Data curation, Writing – review & editing. QS: Data curation, Writing – review & editing. XH: Writing – review & editing. YP: Writing – review & editing. QL: Supervision, Writing – original draft, Writing – review & editing.

Funding

Conflict of interest

The authors declare that the research was conducted in the absence of any commercial or financial relationships that could be construed as a potential conflict of interest.

Publisher's note

References

Abraham, S., Srivastava, S., Kumar, V., Pandey, S., Rastogi, K., Nirala, N. R., et al. (2015). Enhanced electrochemical biosensing efficiency of silica particles supported on partially reduced graphene oxide for sensitive detection of cholesterol. *J. Electroanal. Chem.* 757, 65–72. doi: 10.1016/j.jelechem.2015.09.016

Arya Nair, J. S., Saisree, S., Aswathi, R., and Sandhya, K. Y. (2022). Ultra-selective and real-time detection of dopamine using molybdenum disulphide decorated graphene-based electrochemical biosensor. *Sensors Actuators B Chem.* 354:131254. doi: 10.1016/j.snb.2021.131254

Barrett, E. P., Joyner, L. G., and Halenda, P. P. (1951). The determination of pore volume and area distributions in porous substances. I. Computations from nitrogen isotherms. *J. Am. Chem. Soc.* 73, 373–380. doi: 10.1021/ja01145a126

Beck, J. S., Vartuli, J. C., Roth, W. J., Leonowicz, M. E., Kresge, C. T., Schmitt, K. D., et al. (1992). A new family of mesoporous molecular sieves prepared with liquid crystal templates. *J. Am. Chem. Soc.* 114, 10834–10843. doi: 10.1021/ja00053a020

Cánepa, A. L., Elías, V. R., Vaschetti, V. M., Sabre, E. V., Eimer, G. A., and Casuscelli, S. G. (2017). Selective oxidation of benzyl alcohol through eco-friendly processes using mesoporous V-MCM-41, Fe-MCM-41 and co-MCM-41 materials. *Appl. Catal. A* 545, 72–78. doi: 10.1016/j.apcata.2017.07.039

Celik Cogal, G., Cogal, S., Machata, P., Uygun Oksuz, A., and Omastová, M. (2024). Electrospun cobalt-doped 2D-MoSe₂/polypyrrole hybrid-based carbon nanofibers as electrochemical sensing platforms. *Microchim. Acta* 191:75. doi: 10.1007/s00604-023-06078-2

Chen, P. K., Lai, N. C., Ho, C. H., Hu, Y. W., Lee, J. F., and Yang, C. M. (2013). New synthesis of MCM-48 sanospheres and facile replication to mesoporous platinum nanospheres as highly active electrocatalysts for the oxygen reduction reaction. *Chem. Mater.* 25, 4269–4277. doi: 10.1021/cm402349f

Darabi, R., Karimi-Maleh, H., Akin, M., Arikan, K., Zhang, Z., Bayat, R., et al. (2023). Simultaneous determination of ascorbic acid, dopamine, and uric acid with a highly selective and sensitive reduced graphene oxide/polypyrrole-platinum nanocomposite modified electrochemical sensor, and folic acid. *Electrochim. Acta* 457:142402. doi: 10.1016/j.electacta.2023.142402

Demirkan, B., Bozkurt, S., Cellat, K., Arıkan, K., Yılmaz, M., Şavk, A., et al. (2020). Palladium supported on polypyrrole/reduced graphene oxide nanoparticles for simultaneous biosensing application of ascorbic acid, dopamine, and uric acid. *Sci. Rep.* 10:2946. doi: 10.1038/s41598-020-59935-y

Eguílaz, M., Villalonga, R., and Rivas, G. (2018). Electrochemical biointerfaces based on carbon nanotubes-mesoporous silica hybrid material: bioelectrocatalysis of hemoglobin and biosensing applications. *Biosens. Bioelectron.* 111, 144–151. doi: 10.1016/j.bios.2018.04.004

El-Zohry, A. M., and Hashem, E. Y. (2013). Environmental method to determine dopamine and ascorbic acid simultaneously via derivative spectrophotometry. *J. Spectrosc.* 2013:260376. doi: 10.1155/2013/260376

Feng, Y. H., Li, W. L., Meng, M. J., Yin, H. B., and Mi, J. L. (2019). Mesoporous Sn(IV) doping MCM-41 supported Pd nanoparticles for enhanced selective catalytic oxidation of 1,2-propanediol to pyruvic acid. *Appl Catal B* 253, 111–120. doi: 10.1016/j.apcatb.2019.04.051

Han, E., Li, L., Gao, T., Pan, Y. Y., and Cai, J. R. (2024). Nitrite determination in food using electrochemical sensor based on self-assembled MWCNTs/AuNPs/poly-melamine nanocomposite. *Food Chem.* 437:137773. doi: 10.1016/j.foodchem.2023.137773

Han, E., Pan, Y. Y., Li, L., and Cai, J. R. (2023). Bisphenol a detection based on nano gold-doped molecular imprinting electrochemical sensor with enhanced sensitivity. *Food Chem.* 426:136608. doi: 10.1016/j.foodchem.2023.136608

Hao, P. P., Liu, Z. C., Wang, Z. W., Xie, M., and Liu, Q. Y. (2023). Colorimetric sensor arrays for antioxidant recognition based on Co₃O₄ dual-enzyme activities. *Analyst* 148, 3843–3850. doi: 10.1039/D3AN00939D

Hassan, H. M. A., Betiha, M. A., Elshaarawy, R. F. M., and Samy El-Shall, M. (2017). Promotion effect of palladium on Co₃O₄ incorporated within mesoporous MCM-41 silica for CO oxidation. *Appl. Surf. Sci.* 402, 99–107. doi: 10.1016/j.apsusc.2017.01.061

Iminova, Y. V., Tananaiko, O. Y., Rozhanchuk, T. S., Gruzina, T. G., Reznichenko, L. S., Malysheva, M. L., et al. (2015). Electrodes modified by a biocomposite film based on silica and gold nanoparticles for the determination of glucose. *J. Anal. Chem.* 70, 1247–1253. doi: 10.1134/S1061934815080109

Jia, D. Z., Yang, T., Wang, K., Zhou, L. L., Wang, E. H., Chou, K. C., et al. (2024). Facile in-situ synthesis of Ti₃C₂Tₓ/TiO₂ nanowires toward simultaneous determination of ascorbic acid, dopamine and uric acid. *J. Alloys Compd.* 985:173392. doi: 10.1016/j.jallcom.2023.173392

Jin, T., Yuan, W. H., Xue, Y. J., Wei, H., Zhang, C. Y., and Li, K. B. (2017). Co-modified MCM-41 as an effective adsorbent for levofloxacin removal from aqueous solution: optimization of process parameters, isotherm, and thermodynamic studies. *Environ. Sci. Pollut. Res.* 24, 5238–5248. doi: 10.1007/s11356-016-8262-0

Kresge, C. T., Leonowicz, M. E., Roth, W. J., Vartuli, J. C., and Beck, J. S. (1992). Ordered mesoporous molecular sieves synthesized by a liquid-crystal template mechanism. *Nature* 359, 710–712. doi: 10.1038/359710a0

Li, D. D., Liu, M., Zhan, Y. Z., Su, Q., Zhang, Y. M., and Zhang, D. D. (2020). Electrodeposited poly(3,4-ethylenedioxythiophene) doped with graphene oxide for the simultaneous voltammetric determination of ascorbic acid, dopamine and uric acid. *Microchim. Acta* 187:94. doi: 10.1007/s00604-019-4083-4

Li, Z. H., Zhang, X., Huang, X. W., Zou, X. B., Shi, J. Y., Xu, Y. W., et al. (2021). Hypha-templated synthesis of carbon/ZnO microfiber for dopamine sensing in pork. *Food Chem.* 335:127646. doi: 10.1016/j.foodchem.2020.127646

Liang, X. H., Yu, A. X., Bo, X. J., Du, D. Y., and Su, Z. M. (2023). Metal/covalent-organic frameworks-based electrochemical sensors for the detection of ascorbic acid, dopamine and uric acid. *Coordin. Chem. Rev.* 497:215427. doi: 10.1016/j.ccr.2023.215427

Moghadam, M. R., Dadfarnia, S., Haji Shabani, A. M., and Shahbazikhah, P. (2011). Chemometric-assisted kinetic–spectrophotometric method for simultaneous determination of ascorbic acid, uric acid, and dopamine. *Anal. Biochem.* 410, 289–295. doi: 10.1016/j.ab.2010.11.007

Pabbi, M., and Mittal, S. K. (2017). Electrochemical algal biosensor based on silica coated ZnO quantum dots for selective determination of acephate. *Anal. Methods* 9, 1672–1680. doi: 10.1039/C7AY00111H

Peng, W. J., Cai, L. X., Lu, Y. N., and Zhang, Y. Y. (2023). Preparation of Mn-co-MCM-41 molecular sieve with thermosensitive template and its degradation performance for rhodamine B. *Catalysts* 13:991. doi: 10.3390/catal13060991

Peng, X., Xie, Y., Du, Y., Song, Y. H., and Chen, S. H. (2022). Ultra-selective and real-time detection of dopamine using molybdenum disulphide decorated graphene-based electrochemical biosensor. *J. Electroanal. Chem.* 904:115850. doi: 10.1016/j.jelechem.2021.115850

Terra, J. C. S., Moores, A., and Moura, F. C. C. (2019). Amine-functionalized mesoporous silica as a support for on-demand release of copper in the a(3)-coupling reaction: ultralow concentration catalysis and confinement effect. *ACS Sustain. Chem. Eng.* 7, 8696–8705. doi: 10.1021/acssuschemeng.9b00576

Xia, Y. H., Li, G. L., Zhu, Y. F., He, Q. G., and Hu, C. P. (2023). Facile preparation of metal-free graphitic-like carbon nitride/graphene oxide composite for simultaneous determination of uric acid and dopamine. *Microchem. J.* 190:108726. doi: 10.1016/j.microc.2023.108726

Xu, X. C., Luo, Z. J., Ye, K., Zou, X. B., Niu, X. H., and Pan, J. M. (2021). One-pot construction of acid phosphatase and hemin loaded multifunctional metal–organic framework nanosheets for ratiometric fluorescent arsenate sensing. *J. Hazar. Mater.* 412:124407. doi: 10.1016/j.jhazmat.2020.124407

Yang, L., Wang, A. J., Weng, X. X., and Feng, J. J. (2023). Well-dispersed strawberry-like PtCo nanocrystals/porous N-doped carbon nanospheres for multiplexed assays. *Microchem. J.* 187:108421. doi: 10.1016/j.microc.2023.108421

Yang, H., Zhao, J., Qiu, M. J., Sun, P., Han, D. X., Niu, L., et al. (2019). Hierarchical bi-continuous Pt decorated nanoporous au-Sn alloy on carbon fiber paper for ascorbic acid, dopamine and uric acid simultaneous sensing. *Biosens. Bioelectron.* 124-125, 191–198. doi: 10.1016/j.bios.2018.10.012

Zablocka, I., Wysocka-Zolopa, M., and Winkler, K. (2019). Electrochemical detection of dopamine at a gold electrode modified with a polypyrrole-mesoporous silica molecular sieves (MCM-48) film. *Int. J. Mol. Sci.* 20:111. doi: 10.3390/ijms20010111

Zhang, W. J., Liu, L., Li, Y. G., Wang, D. Y., Ma, H., Ren, H. L., et al. (2018). Electrochemical sensing platform based on the biomass-derived microporous carbons for simultaneous determination of ascorbic acid, dopamine, and uric acid. *Biosens. Bioelectron.* 121, 96–103. doi: 10.1016/j.bios.2018.08.043

Zhang, Z. X., Liu, Y., Meng, W. J., Wang, J., Li, W., Wang, H., et al. (2017). One-pot synthesis of Ni nanoparticle/ordered mesoporous carbon composite electrode materials for electrocatalytic reduction of aromatic ketones. *Nanoscale* 9, 17807–17813. doi: 10.1039/C7NR06602C

Zhang, S., Xu, F., Liu, Z. Q., Chen, Y. S., and Luo, Y. L. (2020). Novel electrochemical sensors from poly [N-(ferrocenyl formacyl) pyrrole]@multi-walled carbon nanotubes nanocomposites for simultaneous determination of ascorbic acid, dopamine and uric acid. *Nanotechnology* 31:085503. doi: 10.1088/1361-6528/ab53bb

Zhang, X. N., Zhu, M. C., Jiang, Y. J., Wang, X., Guo, Z. M., Shi, J. Y., et al. (2020). Simple electrochemical sensing for mercury ions in dairy product using optimal Cu^{2+}-based metal-organic frameworks as signal reporting. *J. Hazar. Mater.* 400:123222. doi: 10.1016/j.jhazmat.2020.123222

Zhao, Q., Chu, J. Y., Jiang, T. S., and Yin, H. B. (2007). Synthesis and stability of CoMCM-41 mesoporous molecular sieve using cetyltrimethyl ammonium bromide as a template by two-step hydrothermal method, colloids and surfaces a: Physicochem. *Eng. Aspects* 301, 388–393. doi: 10.1016/j.colsurfa.2007.01.002

Zhao, Y. N., Zhou, J., Jia, Z. M., Huo, D. Q., Liu, Q. Y., Zhong, D. Q., et al. (2019). In-situ growth of gold nanoparticles on a 3D-network consisting of a MoS_2/rGO nanocomposite for simultaneous voltammetric determination of ascorbic acid, dopamine and uric acid. *Microchim. Acta* 186:92. doi: 10.1007/s00604-018-3222-7

Check for updates

A covalent organic framework-derived pretreatment for pesticides in vegetables and fruits

Ai-Jun Huang[1], Xiu-Xiu Dong[2], Shu Tan[3], Kai Chen[1],
Meiling Zhang[1], Bingrong Li[1], Hao Deng[4], Fan He[5], Hui Ni[5],
Hongwu Wang[1]* and Zi-Jian Chen[1]*

[1]Laboratory of Quality and Safety Risk Assessment for Agro-Products, Ministry of Agriculture and
Rural Affairs, School of Food and Pharmaceutical Engineering, Zhaoqing University, Zhaoqing, China,
[2]School of Agricultural Engineering, Jiangsu University, Zhenjiang, Jiangsu Province, China, [3]Zhaoqing
Branch Center of Guangdong Laboratory for Lingnan Modern Agricultural Science and Technology,
Zhaoqing, Guangdong, China, [4]Key Laboratory of Tropical Fruit and Vegetable Cold-Chain of Hainan
Province, Institute of Agro-products of Processing and Design, Hainan Academy of Agricultural
Sciences, Haikou, China, [5]Fujian Provincial Key Laboratory of Food Microbiology and Enzyme
Engineering, Xiamen, China

Sample pretreatment is an essential procedure in pesticide analysis, as the matrix
effect can significantly influence the results. In this study, a covalent organic
framework (COF) was synthesized using 1,2,4,5-tetrakis-(4-formylphenyl)benzene
(TFPB) and benzidine (BD) to mitigate the matrix effect in vegetable and fruit
samples. This COF was then used to develop a solid-phase extraction (CSPE)
method. In addition, the COF was used to create a magnetic COF (MCOF) for
use in magnetic solid-phase extraction (MSPE). The synthesized COF and MCOF
were thoroughly characterized using scanning electron microscopy (SEM) for
morphological analysis, Fourier-transform infrared spectroscopy (FT-IR) for chemical
bond identification, and N_2 adsorption−desorption measurements for porosity and
surface area assessment. Key pretreatment parameters such as buffers, dilution
rate, sorbent dosage, extraction time, elution solvent, and reuse number were
optimized. The developed CSPE and MSPE showed excellent purification ability
for the matrix of vegetable and fruit samples. The reuse test demonstrated that
the synthesized COF and MCOF can be reused up to 15 times. Moreover, the
developed CSPE and MSPE showed acceptable recoveries in spiked recovery tests,
suggesting that these pretreatment methods were feasible for sample purification
in pesticide analysis.

KEYWORDS

pesticide, covalent organic framework, pretreatment, solid phase extraction, magnetic
solid-phase extraction

Introduction

Pesticides are widely used in agricultural production to control pests and diseases, making
them the backbone of the agri-food sector in its endeavor to secure food production (Chen
Z. Y. et al., 2023; Li H. et al., 2022; Ma et al., 2023). However, pesticides are typically used in
large quantities, so they pose potential risks to organisms across various environments and
demonstrate toxicity toward human beings (Meng et al., 2022; Zhang et al., 2023). Moreover,
high levels of pesticide residue in food may cause chronic poisoning and even cancer (Pedroso

et al., 2022; Yang et al., 2018). Therefore, to protect consumers from the hazards of pesticides, it is necessary to improve the monitoring of pesticide residues in foods.

Instrumental methods are commonly used for the detection of pesticide residues in foods due to their high accuracy, precision, reproducibility, and selectivity. Several instrumental methods for pesticide analysis have been reported, including HPLC-MS/MS (Dong et al., 2023), GC–MS/MS (Harischandra et al., 2021), AChE sensor (Dai et al., 2024), immunoassays (Guo et al., 2024), and electrochemical sensors (Ding et al., 2024). In non-targeted food safety analysis, it is crucial to ensure that the sample pretreatment eliminates matrix effects and retains chemical contaminants (Wang et al., 2021). Previous studies have reported advanced materials for cleaning up the extracts from vegetable or fruit samples, including carbon nitride materials (Pan et al., 2022), molecularly imprinted polymers (Abdulhussein et al., 2021), metal–organic frameworks (MOFs) (Liu et al., 2022), and covalent organic frameworks (COFs) (Wang et al., 2021). COFs possess metal-free π-conjugated backbone structures connected by covalent bonds and feature large specific surface areas, good thermal stability, and abundant pores (Dong et al., 2024; Liu et al., 2024; Zhang et al., 2024). Hence, COFs can effectively adsorb organic compounds and eliminate the interference of macromolecular impurities in the matrix by the size exclusion effect (Lin et al., 2020), making them suitable materials for sample pretreatment.

In this study, a novel COF was synthesized using 1,2,4,5-tetrakis-(4-formylphenyl)benzene (TFPB) and benzidine (BD) to remove the matrix effect of vegetable and fruit samples (Scheme 1). The COF was used to prepare a solid-phase extraction (CSPE) method. It was further used to prepare a magnetic COF (MCOF) for the development of magnetic solid-phase extraction (MSPE). Moreover, key pretreatment parameters including buffers, dilution rate, dosage of sorbent, time for extraction, elution solvent, and number of reuses were optimized. Both pretreatment methods were used for pesticide analysis, and the results of the recovery test were verified using HPLC-MS/MS to evaluate the accuracy, reliability, and practicability of the two developed pretreatment methods.

Materials and methods

Materials and reagents

Pesticide standards were purchased from Tanmo Technology Ltd. (Beijing, China). 1,2,4,5-Tetrakis-(4-formylphenyl)benzene (TFPB), benzidine (BD), N-2-hydroxyethylpiperazine-N-ethane-sulfonic acid (Hepes), Tris-(hydroxymethyl)-aminomethane (Tris), and 1,4-dioxane were purchased from Aladdin Chemical Technology Co., Ltd. (Shanghai, China). Amino magnetic beads (5 mg/mL) were supplied by Beaver Biomedical Co., Ltd. (Suzhou, China). Boric acid, acetonitrile, acetone, N,N-dimethylformamide (DMF), methanol, and ethanol were supplied by Damao Chemical Technology Co., Ltd. (Tianjin, China).

Instruments

Absorbance was measured using an HBS-Scan Y microplate reader (DeTie Biotechnology Co., Ltd., China). Centrifuge (TGL-15B)

was purchased from Anting Scientific Instrument Factory (Shanghai, China). HPLC-MS/MS analysis was performed using a 1,290 Infinity-6495 system (Agilent Technologies, Inc., CA, USA) using a liquid chromatography column (Welch, 100 × 2.1 mm, 3.5 μm).

Preparation of COF

The synthesis of COF was according to the method reported by Li et al. (2023). Briefly, 19.8 mg of TFPB and 14.7 mg of BD were dissolved in 4 mL of 1,4-dioxane, respectively. Afterward, the two solutions were mixed, and 1 mL of 6 mol/L acetic acid was added subsequently. The mixture was rested at room temperature for 72 h in the dark. The product was washed with ethanol three times and dried at 60°C. Then, 10 mg of COF was added into a 3-mL SPE column to prepare CSPE.

Preparation of MCOF

First, 19.8 of mg TFPB and 14.7 mg of BD were separately dissolved in 4 mL of 1,4-dioxane each. Afterward, 1.0 mL of amino magnetic beads was added to the BD solution before adding the TFPB solution. Then, 6 M acetic acid was added and mixed. The mixture was rested at room temperature for 72 h in the dark. The product (MCOF) was washed with ethanol three times and dried at 60°C. The MCOF powder was used to develop MSPE.

Optimization of CSPE and MSPE

To develop CSPE and MSPE, several parameters were optimized, including types of diluents, dilution rate, types of eluents, and addition amount for COF and MCOF. The removal percentage of the matrix (R%) and elution efficiency (E%) were calculated using the following equations:

$$R(\%) = \frac{A_S - A_P}{A_S} \times 100\%$$

$$E(\%) = \frac{A_E}{A_S} \times 100\%$$

Here, A_S, A_P, and A_E are the absorption values at 666 nm for sample extract, purified solution, and eluent, respectively. The conditions for single-factor optimization are summarized in Supplementary Tables S1, S2.

Procedures of CSPE and MSPE

For the purification of CSPE, 3 mL of acetonitrile was added to the column for activation. Then, 1 mL of sample extract was loaded into the CSPE, and the flow speed was kept at 0.5 mL/min. After purification, the CSPE was renewed by washing with 5 mL of acetone.

For the purification of MSPE, 5 mg of MCOF was added to a 1.5 mL centrifuge tube. Afterward, 1 mL of acetonitrile was added for

activation with the assistance of a vortex mixer for 30 s. Acetonitrile was removed after magnetic separation. The sample extract (1 mL) was subsequently loaded for 10-s vortex mixing. The pure extract was obtained after magnetic separation. The MCOF was renewed by washing with 3 mL of acetone after purification.

Sample purification

The sample purification step was performed according to the China National Food Safety Standard (GB 2763–2021, 2021). First, 10 g of samples (cucumber, Chinese cabbage, green grape, and pomelo) was homogenized and mixed with 10 mL of acetonitrile in a 50 mL polypropylene centrifuge tube. Then, 4 g of $MgSO_4$, 1 g of NaCl, 1 g of sodium citrate, 0.5 g of sodium dihydrogen citrate, and a ceramic homogenizer were added and the tube was shaken vigorously for 1 min, followed by centrifuging for 5 min at 4200 r/min. Next, 1 mL of the upper layer was purified using a CSPE column or MSPE, respectively. The purified solution was filtered using a 0.22-μm membrane and analyzed using HPLC-MS/MS. The HPLC-MS/MS parameters are summarized in the Supplementary Tables S3, S4.

Results and discussion

Identification of COF and MCOF

This study synthesized SCOF and MCOF for sample purification owing to their large surface areas for matrix absorption. As shown in Figure 1, scanning electron microscopy (SEM) images revealed surface microstructures of COF and MCOF, displaying porous morphology. The irregular particle morphology of COF was observed in Figure 1A, and its dense porous morphology was clearly shown in

Figure 1B, demonstrating the large surface area of COF. Based on the synthesized COF, the MCOF was further prepared. The SEM micrograph (Figure 1C) of the MCOF distinctly exhibited a spherical morphology, notably different from that of the COF. Moreover, the porous nanoflower morphology is clearly illustrated in Figure 1D, which can be attributed to the uniform growth of COF on the surface of amino magnetic beads.

To further analyze the structural characteristics of MCOF, a transmission electron microscope (TEM) was used. The TEM image of MCOF clearly showed that the Fe_3O_4 core was covered by the nanoflower structure of COF (Figures 2A,B). The element mapping graph showed the presence of Fe and O elements in the MCOF (Figures 2C,D), which can be attributed to the Fe_3O_4 core. Moreover, the Fe_3O_4 core was encapsulated by a nanoflower layer of C and N elements, with their presence being attributed to the formation of the C=N group (Figures 2E,F). The energy-dispersive spectrum of MCOF also verified the existence of Fe, O, C, and N elements (Figure 2G).

Fourier-transform infrared (FT-IR) spectroscopy was further carried out to verify the conversion of COF and MCOF (Figure 3A). The broad bands located at 3500 cm^{-1} to 3,300 cm^{-1} belong to the N-H vibrations of amidogen (Chen Z. J. et al., 2023). The peak at 1620 cm^{-1} for COF and MCOF can be ascribed to the stretching vibration of the C=N group (Li W. et al., 2022). For COF and MCOF, the peaks ranging from 1,520 cm^{-1} to 1,430 cm^{-1} are indicative of the benzene ring (Wang et al., 2024), whereas the peaks between 860 cm^{-1} and 800 cm^{-1} correspond to the para-substitution of the benzene ring. These characteristics can be attributed to the structural elements of BD and TFPB. The weak stretching vibration of the Fe-O bond was observed at 587 cm^{-1} for MCOF (Li and Row, 2018). All the FT-IR spectra confirmed the successful synthesis of both COF and MCOF.

The XRD patterns of COF and MCOF are shown in Figure 3B. Both COF and MCOF showed a strong diffraction peak at 2.22° (2θ), which was assigned to (100) diffractions (Li et al., 2023).
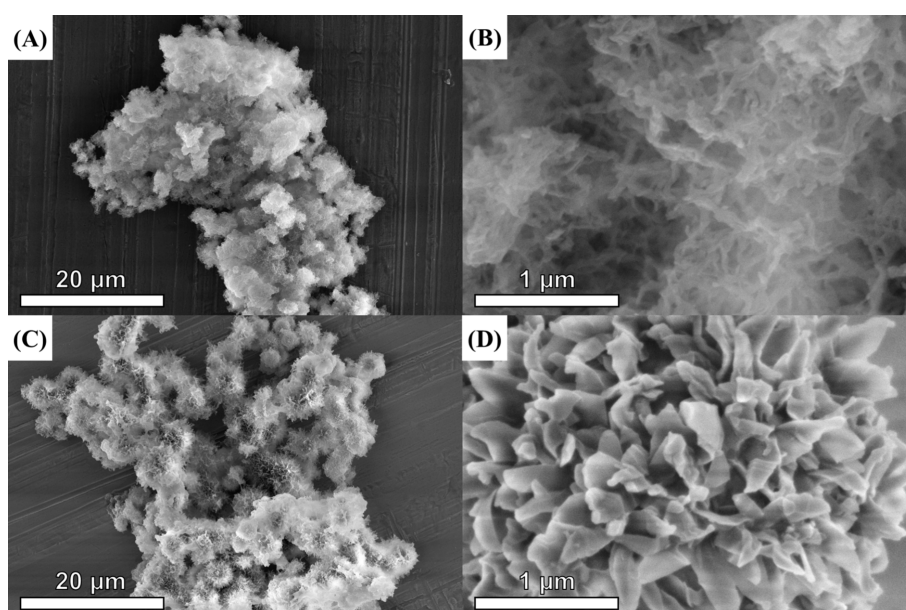
FIGURE 1
The SEM image of (A,B) COF and (C,D) MCOF.

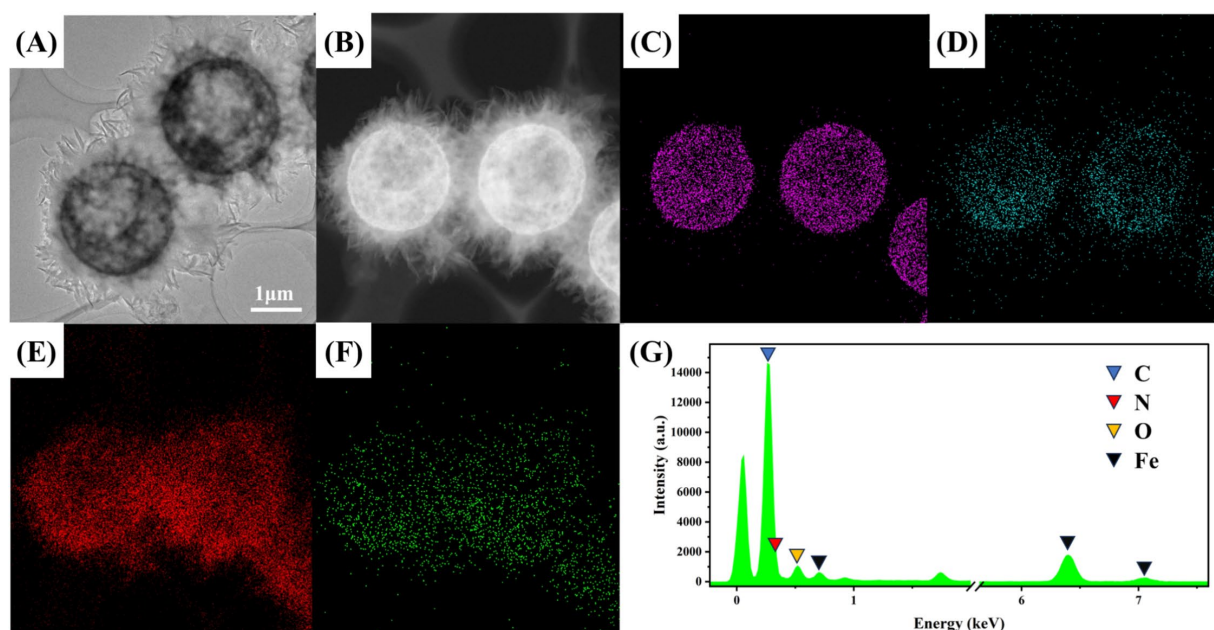**FIGURE 2**
(A) The TEM image of MCOF; (B) the high-angle annular dark field (HAADF) of MCOF; the elemental mapping for MCOF: (C) C, (D) O, (E) N, and (F) Fe; and (G) the energy-dispersive spectrometer spectrum of MCOF.
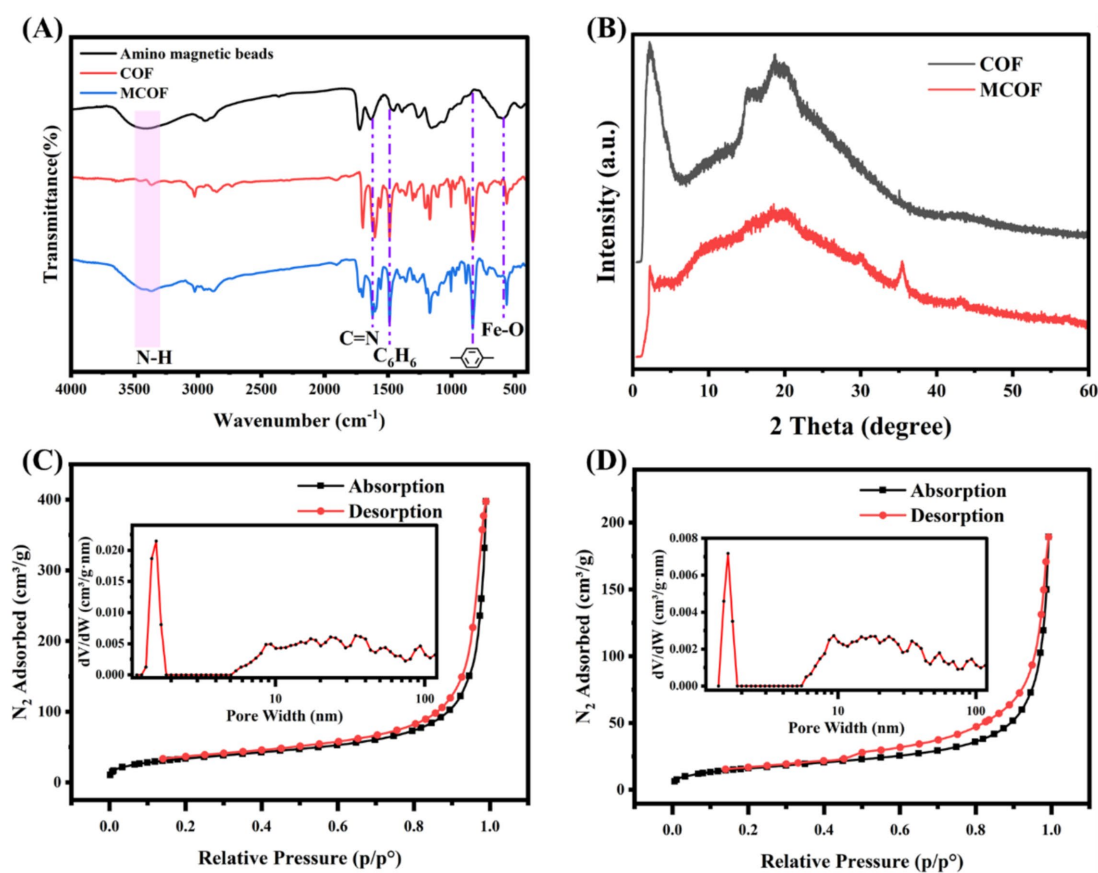

FIGURE 3
(A) The FT-IR spectrum for amino magnetic beads, COF, and MCOF; (B) the XRD of COD and MCOF; and the N_2 adsorption−desorption isotherms of (B) COF and (C) MCOF.
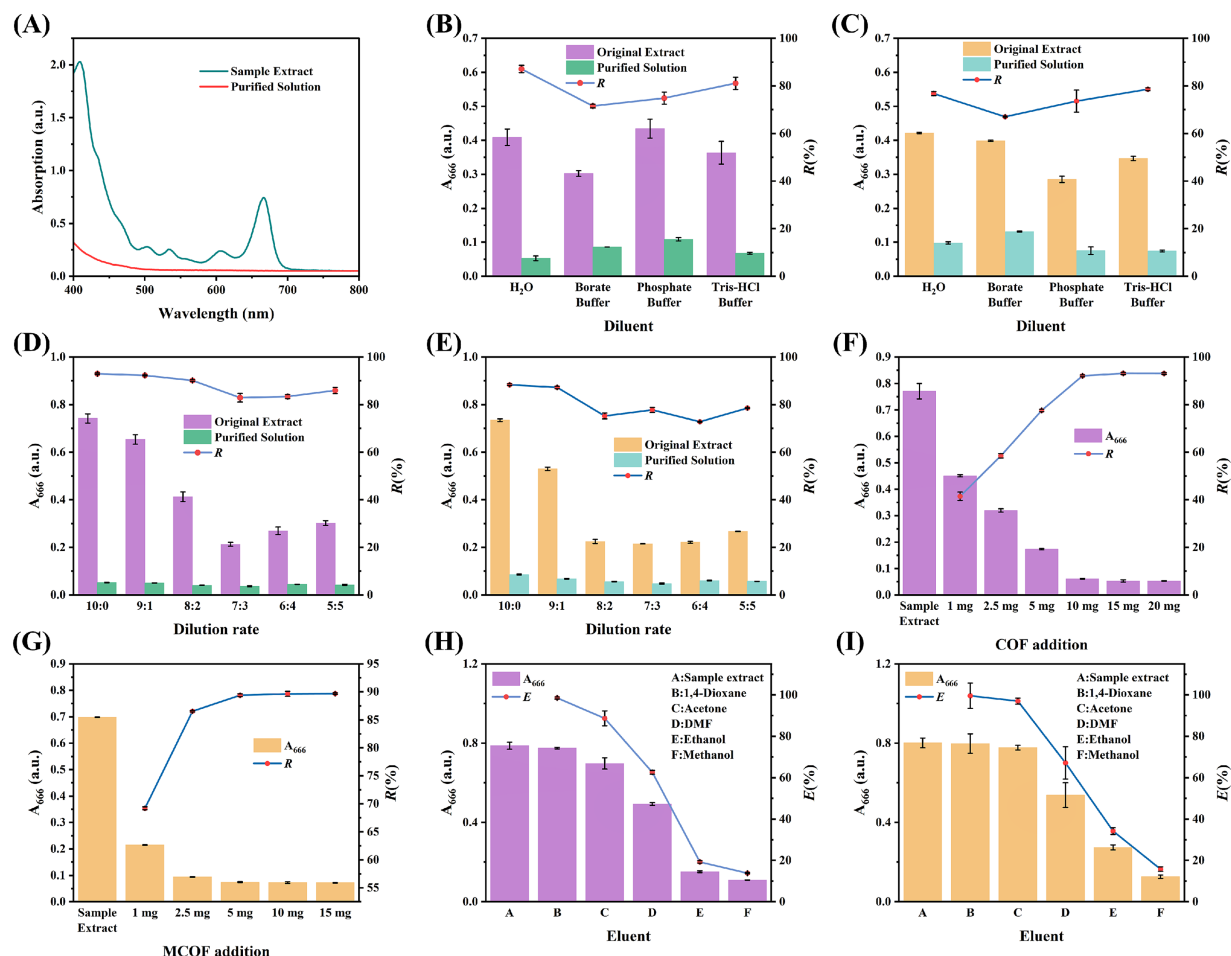
FIGURE 4

(A) The UV–Vis spectrum of sample extract and purified solution; the diluent optimization for (B) CSPE and (C) MSPE; the dilution rate diluent optimization for (D) CSPE and (E) MSPE; the optimization of COF and MCOF addition for (F) CSPE and (G) MSPE, respectively; and the eluent optimization for (H) CSPE and (I) MSPE.

Moreover, the broad diffraction band over the range of 15–25° indicates partial crystallinity within the two-dimensional COF and MCOF (Akyuz, 2020; Koonani and Ghiasvand, 2024). For MCOF, the strong diffraction peak at 35.5° and weak diffraction peaks at 30.1°, 43.1°, and 57.0° belonged to (311), (220), (400), and (511) diffractions for Fe_3O_4, respectively (Sajid et al., 2023). The above results indicated that the crystalline structure of COF and MCOF was well-retained. Moreover, the magnetic property of MCOF was investigated using a vibrating sample magnetometer (VSM). The hysteresis curve (Supplementary Figure S3) showed superparamagnetic behavior, with a coercivity of 36.4 Oe and a magnetization of 11.3 emu/g, indicating that MCOF can be used for efficient magnetic separation.

To further analyze the porosity of COF and MCOF, N_2 gas adsorption/desorption isotherm was used. As shown in Figures 3C,D, the adsorption/desorption isotherm exhibited hysteresis loops with characteristic IV-type patterns, indicative of the concurrent presence of both micropores and mesopores within the COF and MCOF (An et al., 2023; Wu et al., 2024). The BJH pore distribution pattern of COF and MCOF (Figures 3C,D inset) revealed that the pore size was approximately 1.59 nm. The BET-specific surface area of COF was 122.0 m^2/g. However, due to the core of the amino magnetic bead, the

BET-specific surface area of MCOF only reached up to 58.3 m^2/g. Hence, COF with high specific surface area and micropores can be effectively used for the absorption of matrix from food samples.

Development of CSPE and MSPE purification

Lettuce was used as a vegetable sample to optimize the parameters for the purification capacity of CSPE and MSPE. The UV–Vis spectrum of the lettuce sample extract exhibited a distinct absorption peak at 666 nm, whereas no prominent peaks were discernible within the range of 500 nm to 800 nm (Figure 4A). Therefore, the characteristic absorption peak at 666 nm was used as an indicator to evaluate the optimization parameters. For MCOF preparation, the usage of amino magnetic beads was optimized. As the amount of amino magnetic beads increased, the $R\%$ also increased accordingly (Supplementary Figure S1). Hence, the MCOF prepared using 1 mL of amino magnetic beads was used for subsequent optimization and MSPE development. For the diluent optimization, a parallel trend in $R\%$ was observed, and water demonstrated the highest $R\%$ for both CSPE and MSPE. Consequently,
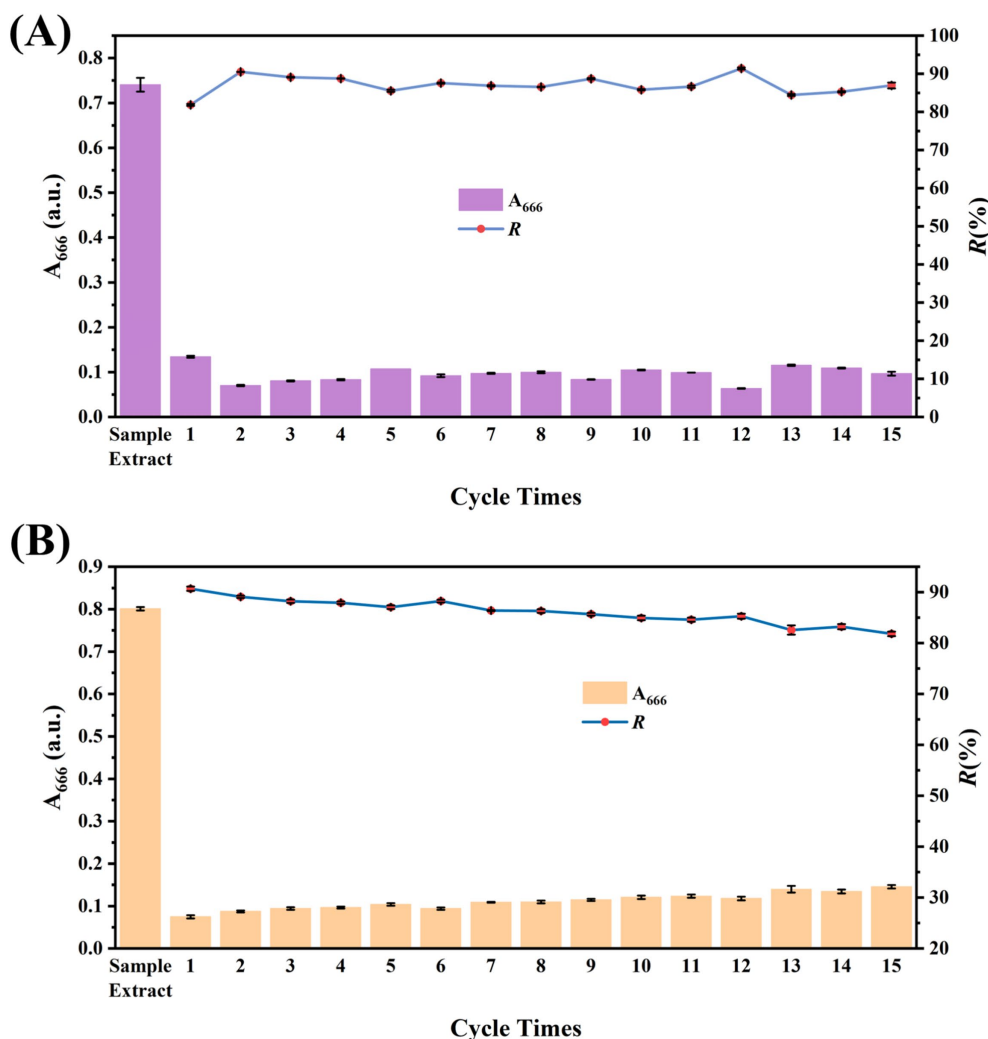
FIGURE 5
The reusability of (A) CSPE and (B) MSPE.

water was determined to be the optimal diluent (Figures 4B,C). Based on the optimized diluent, the effect of dilution rate on $R\%$ was further studied. For CSPE, as the dilution rate increased, the $R\%$ showed a decreasing trend, while the highest $R\%$ was observed for sample extract without dilution and MSPE (Figures 4D,E). Thus, it was inferred that the sample extract can be directly purified using CSPR or MSPE without any diluent, which is simple, convenient, and low-cost. For MSPE, the vortex time was investigated, and the results indicated that the matrix was removed after 10 s of vertexing, thereby demonstrating the remarkable purification ability of MCOF (Supplementary Figure S2).

The addition amounts of COF and MCOF for CSPE and MSPE were further optimized, respectively. As the amount of COF increased, the $R\%$ for both CSPE and MSPE also increased (Figures 4F,G). The CSPE and MSPE achieved the highest R% with the addition of 10 mg of COF and 5 mg of MCOF, respectively, which were chosen as the optimal addition amounts. The eluent was further studied to investigate the feasibility of the reuse of COF and MCOF. As shown in Figures 4H,I, 1,4-dioxane exhibited remarkable elution capacity and achieved the highest E%. In contrast, alcohols (ethanol and methanol) showed poor elution ability. Therefore, 1,4-dioxane was chosen as the

optimal eluent. Under the optimized conditions, the developed CSPE showed stable purification capacity during 15 reuse cycles, while the purification capacity of MSPE decreased slightly. However, the $R\%$ remained above 80% (Figures 5A,B). These results indicated that the synthesized COF and MCOF were suitable materials for low-cost pretreatment of vegetable and fruit samples.

Recovery test

To assess the accuracy of the developed CSPE and MSPE, the recovery test was carried out. Samples (cucumber, Chinese cabbage, green grape, and pomelo) were spiked with 10 pesticides, respectively. Then, they were purified using CSPE and MSPE and analyzed using HPLC-MS/MS. The results are summarized in Tables 1, 2. The recoveries of CSPE and MSPE were 76–92% and 77.3–95.1%, respectively, with the coefficient of variances (CVs) of 1.75–9.55% and 1.63–12.9%, respectively. The results indicated acceptable recoveries, which can fulfill the pesticide maximum residue limits (MRLs) set by the Chinese government (GB 2763–2021, 2021), the

TABLE 1 Recovery of ten pesticides from spiked food samples using CSPE.

Sample		Pesticide[a]									
		Dimethoate	Isocarbophos	Isofenphos-Methyl	Coumaphos	Profenofos	Carbofuran	Carbaryl	Isoprocarb	Fenobucarb	Propoxur
Cucumber	Unspiked mean ± SD[b] (µg/L)	0.29 ± 0.03	0.07 ± 0.01	0.25 ± 0.03	0.2 ± 0.02	0.23 ± 0.02	0.11 ± 0.01	0.39 ± 0.01	0	0.04 ± 0	0
	Measured mean ± SD (µg/L)	8.03 ± 0.38	8.65 ± 0.42	9.02 ± 0.55	9.07 ± 0.5	9.23 ± 0.5	9.01 ± 0.58	9.43 ± 0.53	8.97 ± 0.61	7.64 ± 0.73	8.03 ± 0.46
	Recovery (%)	77.4	85.8	87.7	88.7	90	89	90.4	89.7	76	80.3
	CV[c] (%)	4.73	4.86	6.1	5.51	5.42	6.44	5.62	6.8	9.55	5.73
Chinese cabbage	Unspiked mean ± SD (µg/L)	0.29 ± 0.02	0.13 ± 0.01	0.18 ± 0.02	0.22 ± 0.02	0.21 ± 0.02	0.08 ± 0.01	0.36 ± 0.05	0	0.01 ± 0	0
	Measured mean ± SD (µg/L)	9.18 ± 0.41	8.8 ± 0.62	8.96 ± 0.31	9.04 ± 0.31	9.41 ± 0.48	9.22 ± 0.29	9.4 ± 0.33	9.07 ± 0.29	8.3 ± 0.52	8.51 ± 0.57
	Recovery (%)	88.9	86.7	87.8	88.2	92	91.4	90.4	90.7	82.9	85.1
	CV (%)	4.47	7.05	3.46	3.43	5.1	3.15	3.51	3.2	6.27	6.7
Green grape	Unspiked mean ± SD (µg/L)	0.26 ± 0.02	1.25 ± 0.09	0.13 ± 0	0.19 ± 0.02	0.22 ± 0.01	0.03 ± 0	0.36 ± 0.04	0	0	0
	Measured mean ± SD (µg/L)	8.71 ± 0.43	10.25 ± 0.28	9.14 ± 0.4	9.35 ± 0.49	9.02 ± 0.46	8.92 ± 0.34	9.56 ± 0.5	9.11 ± 0.41	8.38 ± 0.57	8.56 ± 0.29
	Recovery (%)	84.5	90	90.1	91.6	88	88.9	92	91.1	83.8	85.6
	CV (%)	4.94	2.73	4.38	5.24	5.1	3.81	5.23	4.5	6.8	3.39
Pomelo	Unspiked mean ± SD (µg/L)	0.29 ± 0.03	0.1 ± 0.01	0.22 ± 0.02	0.27 ± 0	0.25 ± 0.04	0.32 ± 0.01	0.38 ± 0.02	0.15 ± 0.02	0	8.87 ± 1.03
	Measured mean ± SD (µg/L)	9.2 ± 0.68	8.61 ± 0.39	8.57 ± 0.5	9.15 ± 0.63	9.06 ± 0.75	9.15 ± 0.16	9.09 ± 0.7	8.92 ± 0.65	8.93 ± 0.16	17.72 ± 1.4
	Recovery (%)	89.1	85.1	83.5	88.8	88.1	88.3	87.1	87.7	89.3	88.5
	CV (%)	7.39	4.53	5.83	6.89	8.28	1.75	7.7	7.29	1.79	7.9

[a]The spiked level of each pesticide is 10 µg/mL; [b]SD, standard deviation; [c]CV, coefficient of variance, which was obtained from intra-assay.

TABLE 2 Recovery of 10 pesticides from spiked food samples using MSPE.

Sample		Pesticide									
		Dimethoate	Isocarbophos	Isofenphos-Methyl	Coumaphos	Profenofos	Carbofuran	Carbaryl	Isoprocarb	Fenobucarb	Propoxur
Cucumber	Unspiked mean ± SD (μg/L)	0.29 ± 0.01	0.08 ± 0	0.23 ± 0.01	0.2 ± 0	0.3 ± 0	0.05 ± 0	0.42 ± 0.04	0	0	0
	Measured mean ± SD (μg/L)	9.15 ± 1.18	8.43 ± 0.57	8.19 ± 0.25	8.36 ± 0.25	8.58 ± 0.14	8.21 ± 0.16	8.64 ± 0.26	8.5 ± 0.15	8.24 ± 0.37	7.83 ± 0.32
	Recovery (%)	88.6	83.5	79.6	81.6	82.8	81.6	82.2	85	82.4	78.3
	CV (%)	12.9	6.76	3.05	2.99	1.63	1.95	3.01	1.76	4.49	4.09
Chinese cabbage	Unspiked mean ± SD (μg/L)	0.29 ± 0.03	0.14 ± 0.01	0.1 ± 0	0.19 ± 0.01	0.21 ± 0.03	0.05 ± 0	0.37 ± 0.02	0	0	0
	Measured mean ± SD (μg/L)	8.36 ± 0.36	7.87 ± 0.31	8.08 ± 0.55	8.34 ± 0.38	8.45 ± 0.27	8.47 ± 0.25	8.63 ± 0.38	8.54 ± 0.31	8.16 ± 0.49	8.22 ± 0.63
	Recovery (%)	80.7	77.3	79.8	81.5	82.4	84.2	82.6	85.4	81.6	82.2
	CV (%)	4.31	3.94	6.81	4.56	3.2	2.95	4.4	3.63	6	7.66
Green grape	Unspiked mean ± SD (μg/L)	0.29 ± 0.01	1.12 ± 0.12	0.13 ± 0.01	0.18 ± 0.03	0.25 ± 0.02	0.03 ± 0	0.38 ± 0	0	0	0
	Measured mean ± SD (μg/L)	8.7 ± 0.34	10.25 ± 0.64	9.4 ± 0.19	9.06 ± 0.57	9.2 ± 0.17	8.99 ± 0.3	9.61 ± 0.35	9.24 ± 0.25	9.3 ± 0.23	8.76 ± 0.47
	Recovery (%)	84.1	91.3	92.7	88.8	89.5	89.6	92.3	92.4	93	87.6
	CV (%)	3.91	6.24	2.02	6.29	1.85	3.34	3.64	2.71	2.47	5.37
Pomelo	Unspiked mean ± SD (μg/L)	0.25 ± 0.03	0.07 ± 0	0.19 ± 0	0.33 ± 0.04	0.23 ± 0.03	0.32 ± 0	0.39 ± 0.02	0.01 ± 0	0.09 ± 0	9.53 ± 1.24
	Measured mean ± SD (μg/L)	8.53 ± 0.42	8.44 ± 0.19	8.51 ± 0.33	8.7 ± 0.39	9.16 ± 0.95	8.68 ± 0.38	9.2 ± 0.48	8.93 ± 0.19	8.96 ± 0.45	19.04 ± 0.59
	Recovery (%)	82.8	83.7	83.2	83.7	89.3	83.6	88.1	89.2	88.7	95.1
	CV (%)	4.92	2.25	3.88	4.48	10.37	4.38	5.22	2.13	5.02	3.1

SCHEME 1
The development of CSPE and MSPE.
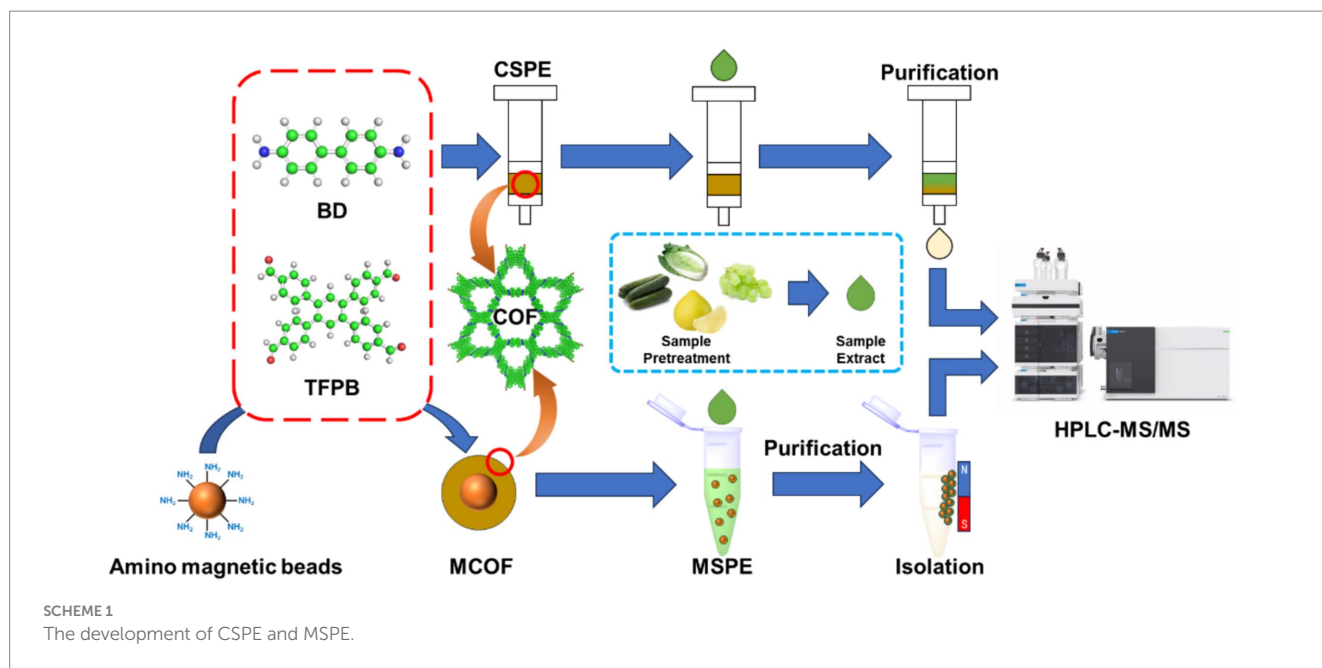
European Union (EU Plant Pesticides Database, n.d.), the USA (States Environmental Protection Agency (EPA), n.d.), and the Codex Alimentarius Commission (Codex Alimentarius Commission Pesticide Index, n.d.). These findings demonstrated the accuracy and practicability of the developed CSPE and MSPE. Moreover, the developed MSPE required less usage and more convenient steps compared to CSPE. However, the CSPE showed potential for online HPLC or GC analysis. Therefore, these two formats of purification can both be used for monitoring, depending on the purification step that is required.

Conclusion

This study synthesized a COF and further prepared an MCOF to develop CSPE and MSPE, respectively. The synthesized materials were characterized using SEM and FT-IR analyses. The results indicated the successful synthesis of COF and MCOF. The parameter optimization test suggested that the sample extract can be directly purified by CSPE and MSPE without dilution, which is simple, convenient, and efficient. Furthermore, the synthesized COF and MCOF can be regenerated and reused up to 15 times, which reduces the cost of sample purification. The recovery test showed acceptable recoveries for vegetable and fruit samples, which fulfill the MRLs set by most countries and organizations. In summary, the developed CSPE and MSPE are ideal purification methods and show potential for pesticide analysis in vegetable and fruit samples.

Data availability statement

The original contributions presented in the study are included in the article/Supplementary material, further inquiries can be directed to the corresponding authors.

Author contributions

A-JH: Writing – original draft. X-XD: Data curation, Methodology, Writing – review & editing. ST: Data curation, Methodology, Writing – original draft. KC: Methodology, Writing – original draft. MZ: Methodology, Writing – original draft. BL: Methodology, Writing – original draft. HD: Methodology, Project administration, Writing – original draft. FH: Methodology, Project administration, Writing – review & editing. HN: Methodology, Project administration, Writing – review & editing. HW: Supervision, Writing – review & editing. Z-JC: Supervision, Writing – review & editing.

Funding

Conflict of interest

The authors declare that the research was conducted in the absence of any commercial or financial relationships that could be construed as a potential conflict of interest.

The author(s) declared that they were an editorial board member of Frontiers, at the time of submission. This had no impact on the peer review process and the final decision.

Publisher's note

All claims expressed in this article are solely those of the authors and do not necessarily represent those of their affiliated organizations, or those of the publisher, the editors and the reviewers. Any product that may be evaluated in this article, or claim that may be made by its manufacturer, is not guaranteed or endorsed by the publisher.

Supplementary material

The Supplementary material for this article can be found online at: https://www.frontiersin.org/articles/10.3389/fsufs.2024.1472174/full#supplementary-material

References

Abdulhussein, A. Q., Jamil, A. K. M., and Bakar, N. K. A. (2021). Magnetic molecularly imprinted polymer nanoparticles for the extraction and clean-up of thiamethoxam and thiacloprid in light and dark honey. *Food Chem.* 359:129936. doi: 10.1016/j.foodchem.2021.129936

Akyuz, L. (2020). An imine based COF as a smart carrier for targeted drug delivery: from synthesis to computational studies. *Micropor. Mesopor. Mat.* 294:109850. doi: 10.1016/j.micromeso.2019.109850

An, Y. F., Zhang, H., Geng, D. X., Fu, Z. J., Liu, Z. M., He, J., et al. (2023). Double redox-active polyimide-based covalent organic framework induced by lithium ion for boosting high-performance aqueous Zn^{2+} storage. *Chem. Eng. J.* 477:147275. doi: 10.1016/j.cej.2023.147275

Chen, Z. J., Huang, A. J., Dong, X. X., Zhang, Y. F., Zhu, L., Luo, L., et al. (2023). A simple and sensitive fluoroimmunoassay based on the nanobody-alkaline phosphatase fusion protein for the rapid detection of fenitrothion. *Front. Sustainable Food Syst.* 7:1320931. doi: 10.3389/fsufs.2023.1320931

Chen, Z. Y., Sun, Y., Shi, J. Y., Zhang, W., Zhang, X. N., Hang, X. W., et al. (2023). Convenient self-assembled PDADMAC/PSS/au@ag NRs filter paper for swift SERS evaluate of non-systemic pesticides on fruit and vegetable surfaces. *Food Chem.* 424:136232. doi: 10.1016/j.foodchem.2023.136232

Codex Alimentarius Commission Pesticide Index. (n.d.) Pesticide Index. Available online at: http://www.fao.org/fao-who-codexalimentarius/codex-texts/dbs/pestres/pesticides/en/ (Accessed October 21, 2024).

Dai, Y., Xu, W., Wen, X. Y., Fan, H. Z., Zhang, Q., Zhang, J., et al. (2024). Smartphone-assisted hydrogel platform based on BSA-CeO2 nanoclusters for dual-mode determination of acetylcholinesterase and organophosphorus pesticides. *Microchim. Acta* 191:185. doi: 10.1007/s00604-024-06268-6

Ding, L. H., Guo, J. W., Chen, S., and Wang, Y. W. (2024). Electrochemical sensing mechanisms of neonicotinoid pesticides and recent progress in utilizing functional materials for electrochemical detection platforms. *Talanta* 273:125937. doi: 10.1016/j.talanta.2024.125937

Dong, M., Pan, Q. Q., Meng, F. F., Yao, X. H., You, S. Q., Shan, G. G., et al. (2024). Trinuclear cu-based covalent organic framework: π-conjugated framework regulating electron delocalization to promote photoreduction CO_2. *J. Colloid Interf. Sci.* 662, 807–813. doi: 10.1016/j.jcis.2024.02.129

Dong, Y. B., Yao, X. L., Zhang, W. P., and Wu, X. M. (2023). Development of simultaneous determination method of pesticide high toxic metabolite 3,4-Dichloroaniline and 3,5 Dichloroaniline in chives using HPLC-MS/MS. *Food Secur.* 12:2875. doi: 10.3390/foods12152875

EU Plant Pesticides Database. (n.d.) Pesticide Residues. Available online at: https://ec.europa.eu/food/plant/pesticides/eu-pesticides-database/start/screen/mrls (Accessed October 21, 2024).

GB 2763–2021. (2021). China national food safety standard—maximum residue limits for pesticides in food.

Guo, M. W., Pang, J. R., Wang, Y., Bi, C. H., Xu, Z. L., Shen, Y. D., et al. (2024). Nanobodies-based colloidal gold immunochromatographic assay for specific detection of parathion. *Anal. Chim. Acta* 1310:342717. doi: 10.1016/j.aca.2024.342717

Harischandra, N. R., Pallavi, M. S., Bheemanna, M., PavanKumar, K., Chandra Sekhara Reddy, V., Udaykumar, N. R., et al. (2021). Simultaneous determination of 79 pesticides in pigeonpea grains using GC-MS/MS and LC-MS/MS. *Food Chem.* 347:128986. doi: 10.1016/j.foodchem.2020.128986

Koonani, S., and Ghiasvand, A. (2024). A highly porous fiber coating based on a Zn-MOF/COF hybrid material for solid-phase microextraction of PAHs in soil. *Talanta* 267:125236. doi: 10.1016/j.talanta.2023.125236

Li, H., Hassan, M. M., He, Z., Haruna, S. A., Chen, Q., and Ding, Z. (2022). A sensitive silver nanoflower-based SERS sensor coupled novel chemometric models for simultaneous detection of chlorpyrifos and carbendazim in food. *LWT-Food Sci. Technol.* 167:113804. doi: 10.1016/j.lwt.2022.113804

Li, G., and Row, K. H. (2018). Ternary deep eutectic solvent magnetic molecularly imprinted polymers for the dispersive magnetic solid-phase microextraction of green tea. *J. Sep. Sci.* 41, 3424–3431. doi: 10.1002/jssc.201800222

Li, W., Wang, R., Jiang, H. X., Chen, Y., Tang, A. N., and Kong, D. M. (2022). Controllable synthesis of uniform large-sized spherical covalent organic frameworks for facile sample pretreatment and as naked-eye indicator. *Talanta* 236:122829. doi: 10.1016/j.talanta.2021.122829

Li, W., Wang, X. H., Liu, J. Q., Jiang, H. X., Cao, D. X., Tang, A. N., et al. (2023). Efficient food safety analysis for vegetables by a heteropore covalent organic framework derived silicone tube with flow-through purification. *Talanta* 265:124880. doi: 10.1016/j.talanta.2023.124880

Lin, X. P., Wang, X. Q., Wang, J., Yuan, Y. W., Di, S. S., Wang, Z. W., et al. (2020). Magnetic covalent organic framework as a solid-phase extraction absorbent for sensitive determination of trace organophosphorus pesticides in fatty milk. *J. Chromatogr. A* 1627:461387. doi: 10.1016/j.chroma.2020.461387

Liu, J. L., Lin, M. X., Huang, J., Zhang, C. R., Qi, J. X., Cai, Y. J., et al. (2024). sp²-c linked cu-based metal-covalent organic framework for chemical and photocatalysis synergistic reduction of uranium. *Chem. Eng. J.* 491:151982. doi: 10.1016/j.cej.2024.151982

Liu, G. Y., Zhang, X., Lu, M., Tian, M. S., Liu, Y., Wang, J., et al. (2022). Adsorption and removal of organophosphorus pesticides from Chinese cabbages and green onions by using metal organic frameworks based on the mussel-inspired adhesive interface. *Food Chem.* 393:133337. doi: 10.1016/j.foodchem.2022.133337

Ma, L., Han, E., Yin, L., Xu, Q., Zou, C., Bai, J., et al. (2023). Simultaneous detection of mixed pesticide residues based on portable Raman spectrometer and au@ag nanoparticles SERS substrate. *Food Control* 153:109951. doi: 10.1016/j.foodcont.2023.109951

Meng, Z., Cui, J., Li, R., Sun, W., Bao, X., Wang, J., et al. (2022). Systematic evaluation of chiral pesticides at the enantiomeric level: a new strategy for the development of highly effective and less harmful pesticides. *Sci. Total Environ.* 846:157294. doi: 10.1016/j.scitotenv.2022.157294

Pan, Y. C., Liu, X., Liu, J., Wang, J. P., Liu, J. X., Gao, Y. X., et al. (2022). Determination of organophosphorus in dairy products by graphitic carbon nitride combined molecularly imprinted microspheres with ultra performance liquid chromatography. *Food Chem X* 15:100424. doi: 10.1016/j.fochx.2022.100424

Pedroso, T. M. A., Benvindo-Souza, M., de Araújo Nascimento, F., Woch, J., Dos Reis, F. G., de Melo, E., et al. (2022). Cancer and occupational exposure to pesticides: a bibliometric study of the past 10 years. *Environ. Sci. Pollut. R.* 29, 17464–17475. doi: 10.1007/s11356-021-17031-2

Sajid, M., Shuja, S., Rong, H., and Zhang, J. (2023). Size-controlled synthesis of Fe3O4 and Fe3O4@SiO2 nanoparticles and their superparamagnetic properties tailoring. *Progress in Natural Science: Materials International* 33, 116–119. doi: 10.1016/j.pnsc.2022.08.003

States Environmental Protection Agency (EPA). (n.d.) Code of Federal Regulations (40 CFR Part 180). Available online at: https://www.govinfo.gov/content/pkg/CFR-2014-title40-vol24/xml/CFR-2014-title40-vol24-part180.xml

Wang, X. H., Li, W., Jiang, H. X., Chen, Y., Gao, R. Z., Tang, A. N., et al. (2021). Heteropore covalent organic framework-based composite membrane prepared by in situ growth on non-woven fabric for sample pretreatment of food non-targeted analysis. *Microchim. Acta* 188:235. doi: 10.1007/s00604-021-04889-9

Wang, S. L., Liang, N. N., Hu, X. T., Li, W. T., Guo, Z. A., Zhang, X. A., et al. (2024). Carbon dots and covalent organic frameworks based FRET immunosensor for sensitive detection of *Escherichia coli* O157:H7. *Food Chem.* 447:138663. doi: 10.1016/j.foodchem.2024.138663

Wu, S. P., Shi, W. J., Cui, L. J., and Xu, C. (2024). Enhancing contaminant rejection efficiency with ZIF-8 molecular sieving in sustainable mixed matrix membranes. *Chem. Eng. J.* 482:148954. doi: 10.1016/j.cej.2024.148954

Yang, N., Wang, P., Xue, C. Y., Sun, J., Mao, H. P., and Oppong, P. K. (2018). A portable detection method for organophosphorus and carbamates pesticide residues based on multilayer paper chip. *J. Food Process Eng.* 41:e12867. doi: 10.1111/jfpe.12867

Zhang, X., Zhou, Y., Huang, X., Hu, X., Huang, X., Yin, L., et al. (2023). Switchable aptamer-fueled colorimetric sensing toward agricultural fipronil exposure sensitized with affiliative metal-organic framework. *Food Chem.* 407:135115. doi: 10.1016/j.foodchem.2022.135115

Zhang, Q. L., Zhu, N., Lu, Z. Y., He, M., Chen, B. B., and Hu, B. (2024). Magnetic covalent organic frameworks as sorbents in the chromatographic analysis of environmental organic pollutants. *J. Chromatogr. A* 1728:465034. doi: 10.1016/j.chroma.2024.465034

Check for updates

A hapten design strategy to enhance the selectivity of monoclonal antibodies against malachite green

Min-Fu Wu[1†], Nuo Xu[2†], Sha Li[1,3]*, Yi-Lan Huang[2], Min-Hua Wu[4], Jia-Dong Li[1], Ri-Sheng Chen[2], Wen-Ming Xiong[5], Yong-Jun Li[5], Hong-Tao Lei[6], Xin-An Huang[7] and Zhen-Lin Xu[6]

[1]Department of Food Science, Foshan Polytechnic, Foshan, China, [2]School of Food Science, Guangdong Pharmaceutical University, Zhongshan, China, [3]School of Health Sciences Research, Research Institute for Health Sciences, Chiang Mai University, Chiang Mai, Thailand, [4]Department of Histology and Embryology, Guangdong Medical University, Zhanjiang, China, [5]Guangzhou Vocational College of Technology and Business, Guangzhou, China, [6]Guangdong Provincial Key Laboratory of Food Quality and Safety, College of Food Science, South China Agricultural University, Guangzhou, China, [7]Tropical Medicine Institute and South China Chinese Medicine Collaborative Innovation Center, Guangzhou University of Chinese Medicine, Guangzhou, China

Malachite green (MG), a triphenylmethane dye, is used in the aquaculture industry as a disinfectant and insect repellent due to its potent bactericidal and pesticidal properties. However, its use poses potential environmental and health risks. This study analyzed and designed two haptens using computer simulation. Serum data confirmed the feasibility of introducing an arm at the dimethylamine group. Subsequently, a highly selective monoclonal antibody strain was successfully prepared based on the hapten. After optimizing the working conditions of indirect competitive enzyme-linked immunosorbent assay (IC-ELISA), the IC_{50} value was 0.83 ng/mL, with a detection limit (IC_{10}) of 0.08 ng/mL and a linear range of 0.19−3.52 ng/mL. The developed monoclonal antibody exhibited a crossover rate of less than 0.1% with other similar structures and can be used to establish an immunoassay.

KEYWORDS

malachite green, monoclonal antibody, molecular simulation, IC-ELISA, hapten design

1 Introduction

Malachite green (MG) is a toxic triphenylmethane compound known for its strong bactericidal, fungicidal, and antiparasitic properties, making it one of the most effective drugs used in aquaculture (Hu et al., 2021; Wang et al., 2023). In fish, MG metabolizes into the more toxic leucomalachite green (LMG), which can persist in the organism for extended periods (Teepoo et al., 2020). Upon human ingestion, MG can induce apoptosis, trigger tumor formation, and damage DNA, leading to carcinogenesis (He et al., 2023). This has raised significant concerns globally. Health Canada has prohibited the sale of fish products containing MG or LMG residues exceeding 1 ng/g, a threshold stricter than the European Union's 2 ng/g standard. Many countries and regions, including China and the United States, have imposed strict bans on its use in aquaculture (Zhou et al., 2019). Despite these regulations, some vendors continue to use MG illegally due to its low cost, effective antimicrobial properties, and the lack of suitable alternatives.

Current detection methods for MG rely primarily on large-scale instrumentation techniques such as liquid chromatography (Faraji et al., 2020), liquid chromatography-mass

spectrometry (Chen et al., 2020; Hussain Hakami et al., 2021), ionization mass spectrometry (Xiao et al., 2020), capillary electrophoresis (Pradel and Tong, 2017), and Raman spectroscopy (Su et al., 2024; Zhang et al., 2024). Although these methods can accurately detect trace amounts of MG in aquatic products, they are time-consuming, costly, require specialized personnel, and are unsuitable for rapid on-site screening of large sample volumes. Therefore, there is a growing need for a rapid and highly specific detection method for monitoring MG residue levels. Immunoassay methods, as a novel analytical approach, offer advantages such as low cost, speed, simplicity (Wu et al., 2024), high sensitivity (Wang et al., 2024), and accuracy (Shin et al., 2024), potentially overcoming the limitations of traditional instrumental methods (Abdelhamid et al., 2024; Sayee et al., 2024; Yue et al., 2024). The effectiveness of immunoassays largely depends on obtaining antibodies with high specificity and affinity, which is critically influenced by the structure of the hapten.

Developing specific antibodies for MG has been a significant challenge. Xing et al. (2009) synthesized LMG derivatives with amino groups on the benzene ring as immunogenic haptens, while Oplatowska et al. (2011) used carboxyl-MG as the immunogenic hapten. Both methods successfully produced monoclonal antibodies (mAbs) but exhibited high cross-reactivity with crystal violet (CV). Shen et al. (2011) designed a novel immunogenic hapten with a carboxyl methoxy group directly on the phenyl ring; however, the resulting mAb also showed high cross-reactivity with CV. To address this issue, this study employed computer simulations of existing hapten research to identify key antigenic epitopes of malachite green. A novel hapten strategy was developed, leading to the successful production of highly selective and sensitive mAbs. Optimized using the indirect competitive enzyme-linked immunosorbent assay (IC-ELISA), the detection limit achieved was 0.08 ng/mL, facilitating the establishment of a specific immunoassay method for malachite green.

2 Materials and methods

2.1 Materials and instruments

Methyl aniline, N,N-dimethyl aniline, zinc chloride, 2,3-dichloro-5,6-dicyanobenzoquinone (DDQ), 1-(3-dimethylaminopropyl)-3-ethylcarbodiimide (EDC), N,N-dimethylformamide (DMF), and N-hydroxysuccinimide (NHS) were obtained from Aladdin Reagent Company. All other reagents used in the study met or exceeded analytical reagent grade standards. Female Balb/c mice were provided by the Guangdong Medical Laboratory Animal Center (SCXK (Yue) 2018-0002) and were subsequently housed and maintained at the South China Agricultural University Animal Center (SYXK (Yue) 2019-0136).

2.2 Synthesis of the MG hapten H1

As shown in Figure 1, Step 1: Add 7 g (6.5 mmol) of N-methylaniline to a 250 mL single-necked flask. Dissolve it completely in 100 mL of anhydrous methanol. Then, add 17 g (19.7 mmol) of methyl acrylate and 3 mL of triethylamine. React in an 85°C oil bath overnight to obtain compound 1 (8.8 g, 70%).

Step 2: Add 100 mL of anhydrous ethanol to dissolve 8.8 g (4.5 mmol) of compound 1 in a 250 mL single-necked flask. Then add 4.6 mL (4.5 mmol) of benzaldehyde, 5.7 mL (4.5 mmol) of N,N-dimethylaniline, and 20 g (13.5 mmol) of zinc chloride. React at 100°C in an oil bath overnight. Concentrate the solution, adjust the pH to 8 with 10% aqueous sodium hydroxide, add an appropriate amount of ethyl acetate, and then pump-filter to obtain compound 2 (2 g, 10%).

Step 3: Dissolve 2 g (4.96 mmol) of compound 2 in 10 mL of methanol in a 100 mL single-necked flask. Add 10 mL of 10% aqueous sodium hydroxide solution and react at 70°C in an oil bath overnight. Concentrate the solution, adjust the pH to 8 with dilute hydrochloric acid, extract with an appropriate amount of ethyl acetate, and purify the residue by column chromatography (PE:EA = 15:1; 10:1; 1:1; EA) to obtain compound 3.

Step 4: Dissolve compound 3 in 20 mL of acetonitrile in a 100 mL single-necked vial. Slowly add 10 mL of an acetonitrile solution with DDQ while stirring. The color of the reaction solution will immediately darken. Stir the reaction for 0.5 h. Perform column chromatography purification to obtain a small amount of the target product MG-H1.

2.3 Synthesis of the MG hapten H2

As shown in Figure 2, Dissolve 1.5 g (10 mmol) of p-carboxybenzaldehyde in 60 mL of anhydrous ethanol in a 250 mL flask. Add 4 g (3 mmol) of zinc chloride and 4 mL (3.15 mmol) of N,N-diethylaniline, and reflux overnight. Prepare a 3:2 mixture of acetonitrile and methanol, then add DDQ to completely dissolve the compound. Weigh compound 4 into a 100 mL single-necked vial, add the mixture, evaporate the solvent, wash off the DDQ with ether, and purify the residue by column chromatography to obtain the green product MG-H2.

2.4 Computer simulation of 3D structures and electrostatic potential maps

The three-dimensional (3D) energy-minimized structure of the MG hapten was constructed using Sybyl 8.1 (provided by Professor Xin'an Huang from Guangzhou University of Chinese Medicine). Initially, a sketch was created and then geometrically optimized using the standard Tripos force field, incorporating non-bonded interactions and Gasteiger-Hückel charges with an 8 Å cutoff, a termination gradient of 0.005 kcal/(molÅ), and dielectric constants based on previous research. The surface electrostatic potential of the obtained structure was generated using the MOLCAD surface program in Sybyl 8.1 with Gasteiger-Hückel charges.

2.5 Synthesis of immunogens and coating antigens

Immunogens and coating antigens were synthesized using previously established methods. Immunogens were prepared by conjugating haptens with carrier proteins, such as lactoglobulin (LF). Coating antigens were prepared by conjugating all haptens with
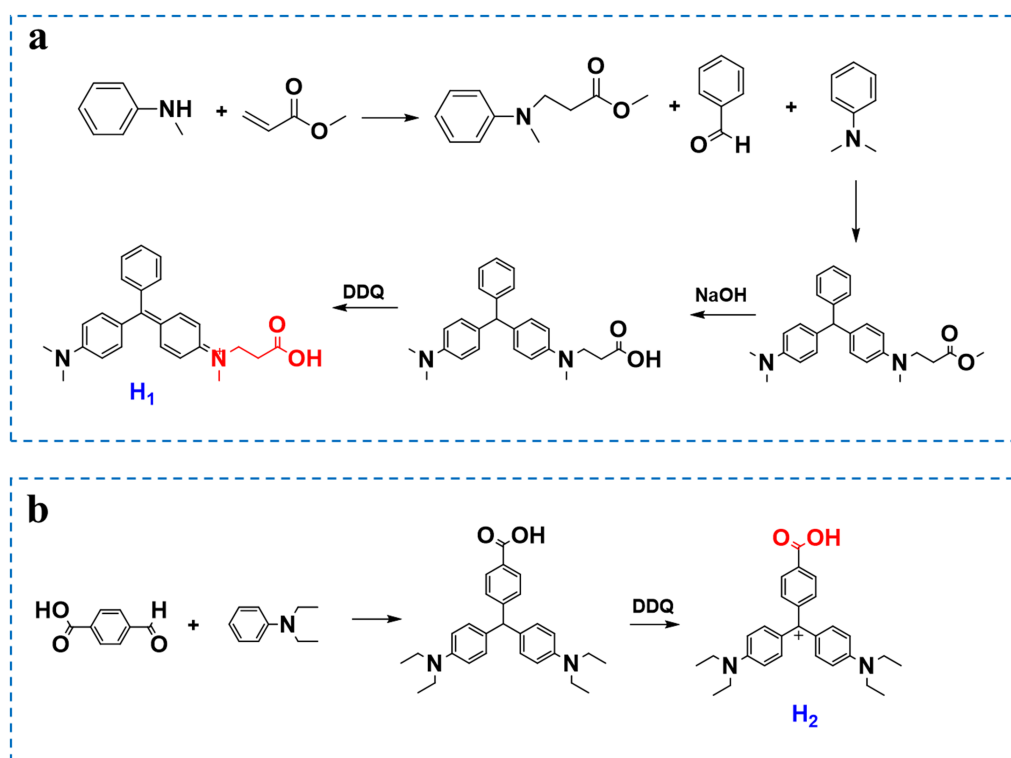
FIGURE 1
The synthetic route of hapten H1 **(a)** and the synthetic route of hapten H2 **(b)**.

bovine serum albumin (BSA). The structure of the final conjugates was verified using ultraviolet–visible (UV–vis) spectral data.

2.6 Hybridoma cell line preparation and screening

Female BALB/c mice aged 6–8 weeks were subcutaneously immunized with the immunogen, with four immunizations at 3-week intervals. A mouse exhibiting the highest titer against each immunogen was selected as the spleen cell donor for hybridoma production. Spleen cells from the immunized mouse were fused with SP2/0 myeloma cells, which had been revived 10 days prior to fusion, using 50% PEG 1500 as the fusion agent. The hybridoma cells were distributed in a 96-well cell culture plate and cultured in a medium containing 80% Dulbecco's Modified Eagle's Medium (DMEM), 20% Fetal Bovine Serum (FBS), and Hypoxanthine-Aminopterin-Thymidine (HAT). After 2 weeks, the medium was replaced with Hypoxanthine-Thymidine (HT). Cells were incubated in a cell culture incubator (37°C, 5% CO2). After 7 days, antibody titer and binding characteristics in the culture supernatant were tested using the same method as for serum. Cells with high affinity and specificity were subcloned using limited dilution until a stable monoclonal cell line secreting antibodies was obtained.

2.7 Production of mAbs

Animal experiments strictly adhere to the guidelines of Chinese laws and regulations, the studies involving animals were reviewed and approved by the Animal Ethics Committee of South China Agricultural University. The animal immunization and hybridoma preparation process was carried out according to the previously established protocol. Male BALB/c mice aged 10–12 weeks were injected with liquid paraffin. After 1 week, hybridoma cells were injected into the mice. Two weeks later, ascitic fluid was collected from mice with noticeably enlarged abdomens. Proteins were precipitated using ammonium sulfate and then purified using Protein A columns. Protein content was determined by ultraviolet spectrophotometry using the following formula: Protein Concentration/(mg/mL) = [1.45 A_{280}−0.74 A_{260}] × Dilution Factor.

2.8 Optimization and characterization of antibody performance

The IC-ELISA method was used to optimize working conditions, including antigen coating, antibody working concentration, and organic solvent tolerance. After optimization, a competitive IC-ELISA method was employed to establish a standard curve and determine the specificity of mAbs against MG analogs. The cross-reactivity rate was calculated using the formula:

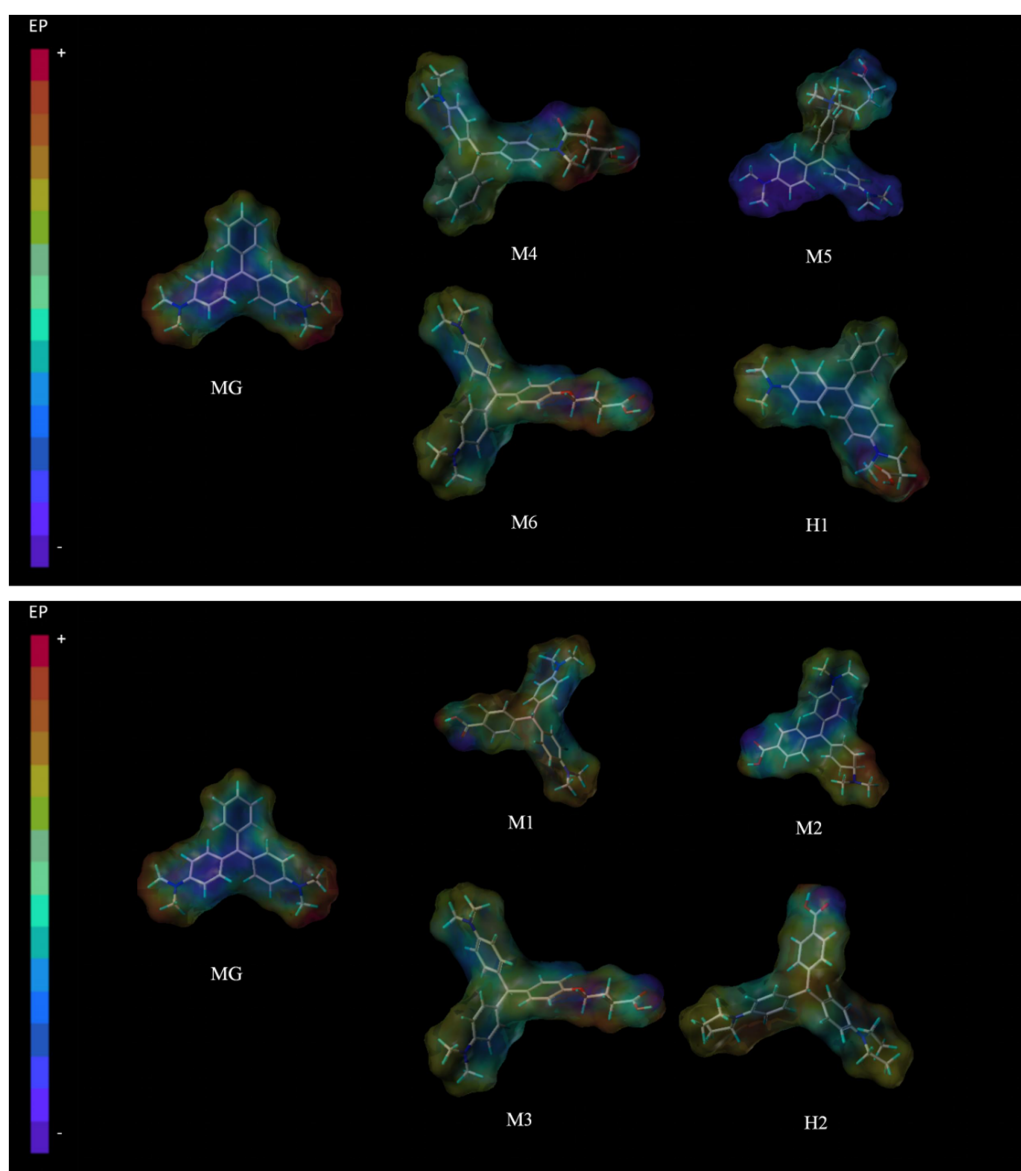$$CR\% = \frac{IC_{50}\left(analyte\right)}{IC_{50}\left(analogue\right)} \times 100\%$$

FIGURE 2
Three-dimensional structure and surface electrostatic potential image of MG haptens.

3 Discussion

3.1 Hapten design

The design of haptens is paramount in antibody preparation. Recent hapten designs targeting MG have primarily focused on introducing reactive groups onto the benzene ring without incorporating dimethylamino groups. However, the prevailing trend in recent years has neglected the presence of dimethylamino groups, despite the fact that numerous monoclonal antibodies (mAbs) produced using these designs exhibit significant cross-reactivity with crystal violet, suggesting that the dimethylamino group could be a crucial factor contributing to this cross-reactivity. To validate this hypothesis, we conducted a systematic review of the latest advancements in the field and performed in-depth analyses utilizing computational modeling techniques.

As depicted in Figure 2, due to the strong electron-donating property of nitrogen atoms, the structure of MG is highly negatively charged, thereby facilitating the formation of hydrogen bonds. In contrast, crystal violet possesses similar dimethylamino antigenic epitopes, which may undermine the selectivity of the prepared antibodies toward malachite green. Introducing spacer arms onto the benzene ring results in a more positively charged overall structure, disrupting the original high negative charge state. Notably, the charge associated with the central double bonds resembles that of the parent drug, and the incorporation of spacer arms alongside dimethylamino groups has minimal impact on the overall charge distribution. Consequently, we propose a novel hapten design (Hapten 1), which not only incorporates dimethylamino groups to enhance antigen selectivity but also retains the central double bonds to mimic the immunogenicity of the parent drug. Furthermore, to further

enhance antibody coating efficiency, we devised another hapten (Hapten 2) featuring exposed dimethylamino groups, thereby strengthening its interaction capabilities with antibodies. This design strategy not only improves the immune recognition efficiency of antigens but also lays a solid foundation for the subsequent development of highly sensitive and selective immunoassay methods.

3.2 Production of mAbs

H1-LF and H2-LF were used as immunogens, and H1-BSA and H2-BSA were used as coating antigens for mouse immunization, respectively. After the fourth immunization, mouse serum was collected to determine antibody titer and affinity for MG (Table 1). Absorbance and corresponding inhibition rates of MG were used as evaluation criteria. For H2-LF, serum from mouse 3 exhibited the strongest recognition of MG at 200 ng/mL, with inhibition rates of 27 and 30% for H1-BSA and H2-BSA, respectively. For H1-LF, serum from mouse 2 showed inhibition rates of 63 and 45% for H2-BSA and H1-BSA, respectively. Both H1 and H2 haptens induced strong immune responses against MG, but H1-LF, enhanced by H2-BSA, demonstrated significant improvements in titer and inhibition rate. Consequently, mouse 2 (H1-LF) was selected for cell fusion experiments.

3.3 Antibody characterization and purification

Following cell fusion, monoclonal antibody M1 was obtained from H2-LF. Protein G affinity chromatography was used for

purification due to its strong binding affinity with mammalian IgG. By adjusting the pH of the mobile phase, high-purity mAbs were achieved. The antibody was concentrated using dialysis bags covered with polyethylene glycol 20,000 at the bottom and surface. Observations were made every 30 min until the desired volume was reached. After a 4-h PBS dialysis exchange, the final concentration was determined to be 4.2 mg/mL.

As shown in Table 2, a comparison of the prepared monoclonal antibodies with previous studies revealed that the introduction of an arm onto the benzene ring that never contained a dimethylamino group resulted in a cross-reactivity with CV as high as 100%. Subsequently, the cross-reactivity decreased to 27% when an arm was introduced onto the dimethylamino group. This pattern also confirms that the dimethylamino group is the most crucial antigenic epitope for MG recognition. Based on this finding, this study further introduced a double bond to make the structure closer to MG. The successfully prepared monoclonal antibody not only outperformed previous studies in terms of sensitivity but also in specificity.

3.4 Optimization of antibody performance

Theoretically, a decrease in the concentration of the coated antigen leads to a decrease in its own antibody's competitive binding ability, while enhancing the competitive binding ability of the drug's antibody. To maintain stable working conditions, the antibody's working concentration needs to be adjusted upwards. In this experiment, the checkerboard method was used to optimize the concentrations of coated antigen and antibody. Under other consistent conditions, IC-ELISA was used to compare the IC_{50} values under different combinations of coated antigen and antibody concentrations. The resulting standard curve had the lowest IC_{50} value when the coated antigen concentration was 0.25 μg/mL and the antibody concentration was 125 ng/mL. Therefore, a coated antigen concentration of 0.25 μg/mL and an antibody concentration of 125 ng/mL were selected as the optimal working concentrations.

As shown in Figure 3, the buffer had little effect on MG. When the standards were diluted with PBST, the IC_{50} values were relatively low, indicating that PBST improved the detection sensitivity compared with distilled water. This enhancement may be attributed to the compositional similarity between PBST and the antibody diluent, which maintains the pH and ionic concentration of the buffer system, thus avoiding adverse effects on the antigen–antibody reaction. In contrast, buffers such as distilled water and phosphate buffer (PB) may disrupt this equilibrium and affect detection sensitivity. Therefore, PBST was chosen as the optimal diluent for the standard.

Due to the strong lipophilicity of MG, its standard solution mainly needs to be prepared with acetonitrile as the solvent. In the actual sample detection process, the concentration of organic solvents in the reaction system has an important influence on the biological activity of the antibody, the binding efficiency of antigen and antibody, and the solubility of the drug. Therefore, the concentration of acetonitrile in the PBST buffer solution was optimized to study the organic solvent tolerance of the antibody. The results showed that when the buffer contained a low concentration of acetonitrile, the PBST buffer could not dissolve the

TABLE 1 Results of rat antiserum to MG.
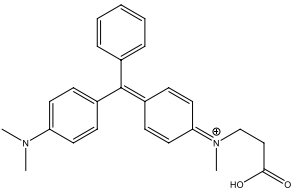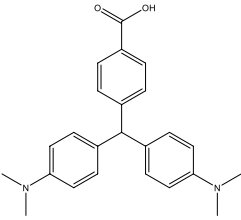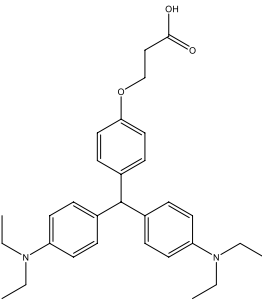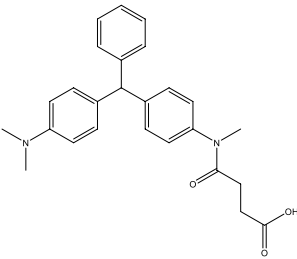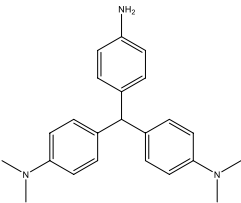
Coating antigen (1)	Immunogen: H1-LF		
	Rat one	Rat two	Rat three
H1-BSA	Titer: 1 K inhibition rate: 41%	Titer: 1 K inhibition rate: 45%	Titer: 2 K inhibition rate: 32%
H2-BSA	Titer: 16 K inhibition rate: 65%	Titer: 32 K inhibition rate: 63%	Titer: 32 K inhibition rate: 43%

Coating antigen	Immunogen: H2-LF		
	Rat one	Rat two	Rat three
H1-BSA	Titer: 16 K inhibition rate: 19%(2)	Titer: 16 K inhibition rate: 20%	Titer: 32 K inhibition rate: 27%
H2-BSA	Titer: 1 K inhibition rate: 23%	Titer: 1 K inhibition rate: 25%	Titer: 4 K inhibition rate: 30%

[a]Titer is defined as dilution factor of antiserum with the absorbance at 450 nm being situated at about 1.0–1.5 at coating concentration of 1 μg/mL.
[b]Inhibition rate was expressed as follow: inhibition (%) = [1-(B/B_0)] × 100. B_0 was mean absorbance of the wells in the absence of competitor. B was mean absorbance of the wells in the presence of competitor (0.2 mg/L of MG).

TABLE 2 Comparison of monoclonal antibodies to MG.

Structure	IC$_{50}$ (ng/mL)	Cross-reactivity	References
	0.83	<0.1%	This study
	–	100%	Yang et al. (2007)
	1.16	–	Wang et al. (2017)
	20	27%	Singh et al. (2011)
	0.9 ~ 2.6	29.07%	Xing et al. (2009)

FIGURE 3
The optimization of working conditions. Effects of coating antigen and antibody concentration (a), buffer (b) and amount of acetonitrile (c).
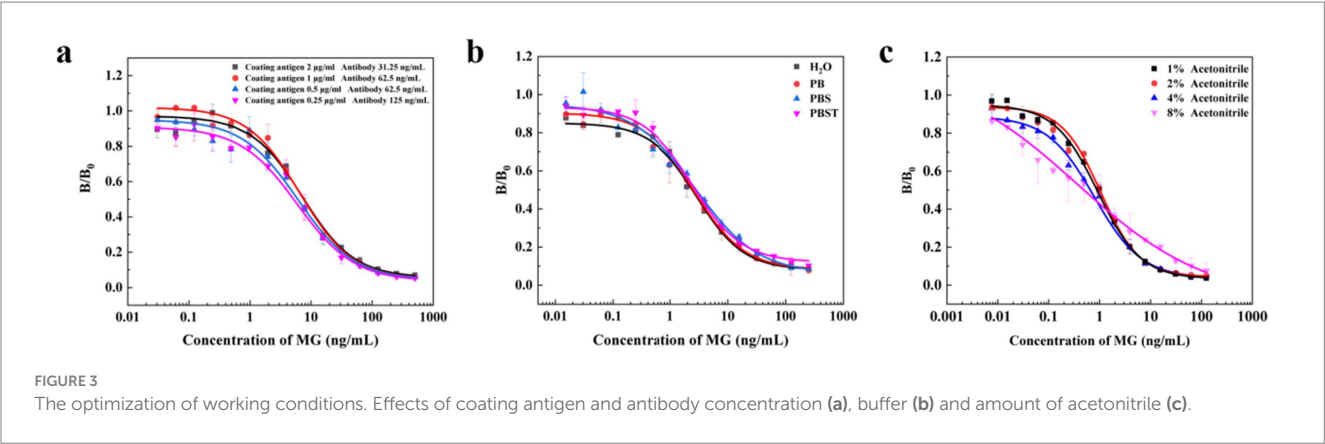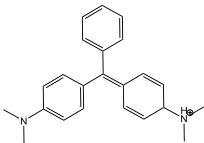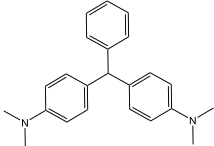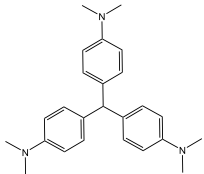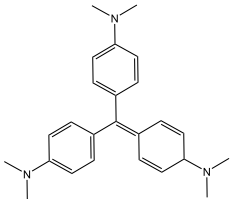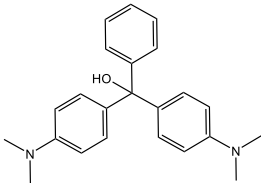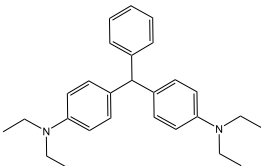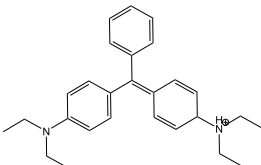
MG well, resulting in a higher IC_{50} value. When the acetonitrile content in the buffer was increased from 1 to 8%, the lowest IC_{50} ratio was observed at 4% acetonitrile content. However, when the acetonitrile content in the buffer reached 8%, some of the antibodies were inactivated due to the high concentration of organic solvent. Therefore, the PBST buffer containing 4% acetonitrile was selected as the optimal buffer system condition. In summary, after a series of optimization, the IC-ELISA standard curve of MG was established under the optimal experimental conditions: as shown in Figure 4, the IC_{50} value of MG detected by IC-ELISA was 0.83 ng/

mL, and the linear ranges was 0.19–3.52 ng/mL, and IC_{10} was 0.08 ng/mL.

3.5 Evaluation of antibody specificity

The specificity of the antibodies was evaluated using Malachite Green (MG), Leucomalachite Green (LMG), Crystal violet (CV), Leuco Crystal Violet (LCV), Einecs 284-783-6 (BG) and Leucobrilliant green (LBG) as structural analogs. As shown in

TABLE 3 Specificity of the anti-MG mAb.

Analyst	Structure	IC_{50} (ng/mL)	CR (%)
Malachite Green		0.83	100
Leucomalachite Green		>10,000	<0.1
Leuco Crystal Violet		>10,000	<0.1
Crystal violet		>10,000	<0.1
Solvent Green 1		>10,000	<0.1
Leucobrilliant green		>10,000	<0.1
Einecs 284-783-6		>10,000	<0.1

FIGURE 4
Standard curve for malachite green monoclonal antibody.
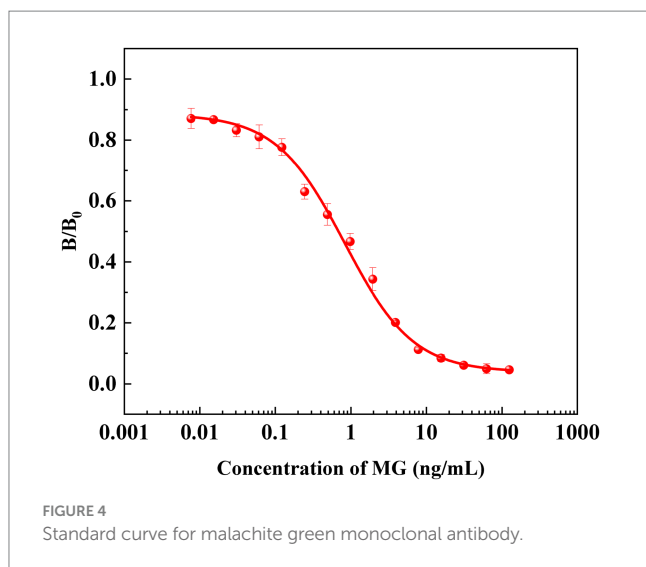
Table 3, the cross-reactivity of anti-MG mAb with other structural analogs was below 0.1. This indicates that the design of dimethylamino group effectively improves the selectivity of the antibody, and also proves that dimethylamino group is the key antigenic recognition epitope of malachite green, confirming the feasibility of our strategy. The antibody prepared in this study can be used to further develop highly sensitive and selective immunoassay methods (Figure 4).

4 Conclusion

In this study, two hapten were designed and synthesized, and computer simulations demonstrated that the spacer arm position of MG significantly affects the recognition of MG by the mAb. High-quality mAbs were subsequently prepared using these hapten, showing an IC_{50} value of 0.83 ng/mL, a detection limit (IC_{10}) of 0.08 ng/mL, and a linear range of 0.19–3.52 ng/mL. This study presents a novel strategy for designing MG hapten, with great potential for application in immunoassay methods.

Data availability statement

The raw data supporting the conclusions of this article will be made available by the authors, without undue reservation.

Ethics statement

Animal experiments strictly adhere to the guidelines of Chinese laws and regulations, the studies involving animals were reviewed and approved by the Animal Ethics Committee of South China Agricultural University.

Author contributions

M-FW: Writing – original draft, Writing – review & editing. NX: Writing – original draft. SL: Writing – review & editing. Y-LH: Writing – original draft. M-HW: Writing – review & editing. J-DL: Writing – original draft. R-SC: Writing – original draft. W-MX: Writing – review & editing. Y-JL: Writing – review & editing. H-TL: Writing – review & editing. X-AH: Writing – review & editing. Z-LX: Writing – review & editing.

Conflict of interest

The authors declare that the research was conducted in the absence of any commercial or financial relationships that could be construed as a potential conflict of interest.

Publisher's note

All claims expressed in this article are solely those of the authors and do not necessarily represent those of their affiliated organizations, or those of the publisher, the editors and the reviewers. Any product that may be evaluated in this article, or claim that may be made by its manufacturer, is not guaranteed or endorsed by the publisher.

References

Abdelhamid, A. G., Wick, M., and Yousef, A. E. (2024). Production of polyclonal antibodies and development of competitive ELISA for quantification of the Lantibiotic Paenibacillin. *Fermentation* 10:232. doi: 10.3390/fermentation10050232

Chen, Y., Xia, S., Han, X., and Fu, Z. (2020). Simultaneous determination of malachite green, chloramphenicols, sulfonamides, and fluoroquinolones residues in fish by liquid chromatography-mass spectrometry. *J. Anal. Methods Chem.* 2020, 1–12. doi: 10.1155/2020/3725618

Faraji, M., Adeli, M., and Noormohammadi, F. (2020). Deep eutectic solvent-based dispersive liquid-liquid micro-extraction for extraction of malachite green and crystal violet in water samples prior their determination using high performance liquid chromatography. *Int. J. Environ. An. Ch.* 102, 681–689. doi: 10.1080/03067319.2020.1724992

He, J., Mo, P., Luo, Y.-S., Yang, P.-H., and Ghafarifarsani, H. (2023). Strategies for solving the issue of malachite green residues in aquatic products: a review. *Aquac. Res.* 2023, 1–17. doi: 10.1155/2023/8578570

Hu, Y., Gao, Z., and Luo, J. (2021). Fluorescence detection of malachite green in fish tissue using red emissive Se,N,Cl-doped carbon dots. *Food Chem.* 335:127677. doi: 10.1016/j.foodchem.2020.127677

Hussain Hakami, A. A., Ahmed, M. A., Khan, M. A., AlOthman, Z. A., Rafatullah, M., Islam, M. A., et al. (2021). Quantitative analysis of malachite green in environmental samples using liquid chromatography-mass spectrometry. *Water* 13. doi: 10.3390/w13202864

Oplatowska, M., Connolly, L., Stevenson, P., Stead, S., and Elliott, C. T. (2011). Development and validation of a fast monoclonal based disequilibrium enzyme-linked immunosorbent assay for the detection of triphenylmethane dyes and their metabolites in fish. *Anal. Chim. Acta* 698, 51–60. doi: 10.1016/j.aca.2011.04.047

Pradel, J. S., and Tong, W. G. (2017). Determination of malachite green, crystal violet, brilliant green and methylene blue by micro-cloud-point extraction and nonlinear laser wave-mixing detection interfaced to micellar capillary electrophoresis. *Anal. Methods* 9, 6411–6419. doi: 10.1039/C7AY01706E

Sayee, R. H., Hosamani, M., Krishnaswamy, N., Shanmuganathan, S., Charan, M. S. S., Sheshagiri, G., et al. (2024). Monoclonal antibody based solid phase competition ELISA to detect FMDV serotype a specific antibodies. *J. Virol. Methods* 328. doi: 10.1016/j.jviromet.2024.114959

Shen, Y. D., Deng, X. F., Xu, Z. L., Wang, Y., Lei, H. T., Wang, H., et al. (2011). Simultaneous determination of malachite green, brilliant green and crystal violet in grass carp tissues by a broad-specificity indirect competitive enzyme-linked immunosorbent assay. *Anal. Chim. Acta* 707, 148–154. doi: 10.1016/j.aca.2011.09.006

Shin, J.-H., Lee, M.-J., Kim, Y.-J., Kim, T.-H., Choi, J.-H., and Oh, B.-K. (2024). Development of multi-HRP-conjugated branched PEI/antibody-functionalized gold nanoparticles for ultra-sensitive ELISA. *Biochip J.* 18, 419–426. doi: 10.1007/s13206-024-00165-z

Singh, G., Koerner, T., Gelinas, J.-M., Abbott, M., Brady, B., Huet, A.-C., et al. (2011). Design and characterization of a direct ELISA for the detection and quantification of leucomalachite green. *Food Addit. Contam. Part A Chem. Anal. Control Expo Risk Assess.* 28, 731–739. doi: 10.1080/19440049.2011.567360

Su, P., Wang, H., Liu, T., Li, X., Yu, L., Wang, X., et al. (2024). Adsorption-based preconcentration effect enhanced FRET and PET from rhodamine B to analyte malachite green for ultra-sensitive sensing application. *Microchem. J.* 203:110840. doi: 10.1016/j.microc.2024.110840

Teepoo, S., Wongtongdee, U., and Phapugrangkul, P. (2020). Development of qualitative and quantitative immunochromatographic strip test assay for rapid and simple detection of leucomalachite green residual in aquatic animals. *Food Chem.* 320:126613. doi: 10.1016/j.foodchem.2020.126613

Wang, L., He, Z., Guo, Y., Ran, X., Cheng, Y., and He, Z. (2024). A novel quantitative double antigen sandwich ELISA for detecting total antibodies against *Candida albicans* enolase 1. *Eur. J. Clin. Microbiol. Infect. Dis.* 43, 1815–1823. doi: 10.1007/s10096-024-04899-4

Wang, X., Yang, T., Chen, X., Fang, L., Yang, Y., Cao, G., et al. (2023). Quantitative detection of malachite green in sediment by a time-resolved immunofluorescence

method combined with a portable 3D printing equipment platform. *Sci. Total Environ.* 855:158897. doi: 10.1016/j.scitotenv.2022.158897

Wang, Y., Yang, J., Shen, Y., Sun, Y., Xiao, Z., Lei, H., et al. (2017). Novel haptens synthesis and development of a monoclonal antibody-based enzyme-linked immunosorbent assay for leuco-malachite green in fish. *Food Agric. Immunol.* 28, 1460–1476. doi: 10.1080/09540105.2017.1348490

Wu, Q., Ma, Z., Pan, Q., Liu, T., Zhang, Y., Xin, J., et al. (2024). A candidate competitive ELISA based on monoclonal antibody 3A8 for diagnosis of contagious bovine pleuropneumonia. *Appl. Microbiol. Biotechnol.* 108:290. doi: 10.1007/s00253-024-13127-0

Xiao, X., Chen, C., Deng, J., Wu, J., He, K., Xiang, Z., et al. (2020). Analysis of trace malachite green, crystal violet, and their metabolites in zebrafish by surface-coated probe nanoelectrospray ionization mass spectrometry. *Talanta* 217:121064. doi: 10.1016/j.talanta.2020.121064

Xing, W., He, L., Yang, H., Sun, C., Li, D., Yang, X., et al. (2009). Development of a sensitive and group-specific polyclonal antibody-based enzyme-linked immunosorbent assay (ELISA) for detection of malachite green and leucomalachite green in water and fish samples. *J. Sci. Food Agr.* 89, 2165–2173. doi: 10.1002/jsfa.3695

Yang, M.-C., Fang, J.-M., Kuo, T.-F., Wang, D.-M., Huang, Y.-L., Liu, L.-Y., et al. (2007). Production of antibodies for selective detection of malachite green and the related triphenyl methane dyes in fish and fishpond water. *J. Agric. Food Chem.* 55, 8851–8856. doi: 10.1021/jf071195y

Yue, S., Liu, Y., Zhou, R., Zhan, Z., Kang, L., Huang, L., et al. (2024). A highly sensitive and rapid colloidal gold immunoassay for Puerarin detection. *J. Agric. Food Chem.* 72, 8817–8822. doi: 10.1021/acs.jafc.4c00644

Zhang, Z., Li, H., Huang, L., Wang, H., Niu, H., Yang, Z., et al. (2024). Rapid identification and quantitative analysis of malachite green in fish via SERS and 1D convolutional neural network. *Spectrochim. Acta A Mol. Biomol. Spectrosc.* 320:124655. doi: 10.1016/j.saa.2024.124655

Zhou, X., Zhang, J., Pan, Z., and Li, D. (2019). Review of methods for the detection and determination of malachite green and Leuco-malachite green in aquaculture. *Crit. Rev. Anal. Chem.* 49, 1–20. doi: 10.1080/10408347.2018.1456314

Recent advances of optical sensors for point-of-care detection of phthalic acid esters

Lili Zhang[1], Mingming Chen[2], Hongwei Duan[3], Quan Bu[1] and Xiuxiu Dong[1]*

[1]School of Agricultural Engineering, Jiangsu University, Zhenjiang, Jiangsu, China, [2]School of Physics and Electronic Engineering, Jiangsu University, Zhenjiang, Jiangsu, China, [3]College of Mechanical and Electrical Engineering, Shihezi University, Shihezi, China

Phthalic acid esters (PAEs) are often added to plastics to enhance elasticity, transparency, durability and prolong service life as a kind of plasticizer. However, they are not chemically bonded to polymers and are difficult to degrade, which makes it easy for them to release into the environment and enter the human body from various potential sources. This results in environmental pollution and poses health risks. In order to protect ecosystem, ensure food safety and prevent disease, there is an urgent need for sensors that can achieve point-of-care detection of PAEs. Optical sensors have advantages of simplicity, portability and low cost, and have been widely applied to the detection of PAEs. In this review, we focus on introducing the recent advancements and trends in optical sensors for detection of PAEs represented by colorimetric (CL) sensors, fluorescence (FL) sensors and surface-enhanced Raman scattering (SERS) platform. Based on recognition strategies (e.g., label-free, aptamer, molecularly imprinted polymer, antibody and enzyme), the significant achievements of these optical sensors in the past 5 years are systematically classified and described in detail. Researchers can quickly know the development status of optical sensors for detection of PAEs in the past 5 years. This review highlights the strengths of each sensor type while also identifying their application limitations, providing researchers with valuable insights into future directions for optical sensor research.

KEYWORDS

phthalic acid esters, fluorescence, colorimetric, surface-enhanced Raman, detection
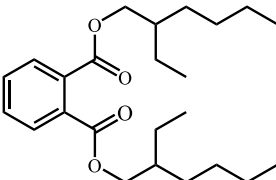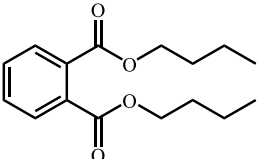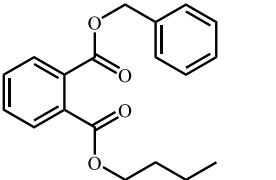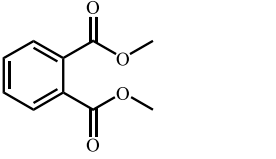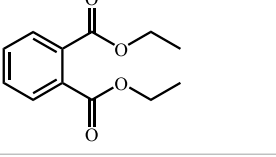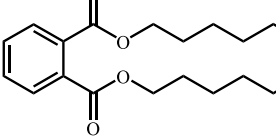
1 Introduction

Phthalic acid esters (PAEs) are a series of ester compounds containing benzene ring, which are composed of dialkyl or alkylaryl esters of 1,2-benzenedicarboxylic acid (Lee et al., 2019). PAEs as plasticizers are extensively added to personal care products (e.g., nail polish and shampoo), drugs, solvent adhesives, food packaging, medical equipment, building materials and agricultural films (Wang Y. et al., 2019; Abeysinghe et al., 2022). PAEs are not chemically bound to the polymer, so they can easily release into environment and finally enter human body from various potential sources, which will cause environmental pollution and health threatening (Zhang et al., 2021). With the development of industrialization, a large number of PAEs are used in plastic products. Studies have shown that PAEs can be detected in the air, soil, water of the Yangtze River and the ocean (Chen, 2019; Hidalgo-Serrano et al., 2022; Mi et al., 2019; Wang W. et al., 2018). PAEs in the environment will be absorbed during plant growth, and will also enter and accumulate in the organism. That could cause significant toxic and side effects such as plant growth retardation, yield decline and quality degradation and will also have a huge negative impact on the biota (Cao et al., 2022; Wang F. et al., 2022;

Sun et al., 2023; Zhang D. et al., 2023). PAEs have also been detected in agricultural products, most fermented food products and foods containing plastic packaging bags (Dong et al., 2019; Tan et al., 2018). These PAEs can cause harm to health after entering the human body through the food chain (Reyes and Price, 2018; Fu et al., 2023). Long-term intake of PAEs can affect neurotransmitter activity, lead to neurobehavioral disorders, and increase the risk of asthma in children (Kang et al., 2023; Garí et al., 2019; Huang P. C. et al., 2022; Zhao Y. et al., 2022). Up to now, there are more than 30 kinds of PAEs (Dong et al., 2024). Six kinds of PAEs including DEHP, DBP, butyl benzyl phthalate (BBP), dimethyl phthalate (DMP), diethyl phthalate (DEP) and di-n-octyl phthalate (DNOP) are listed as priority pollutants by the United States Environmental Protection Agency (USEPA), the European Union (EU) and China (Gong et al., 2024). The basic information about the above six PAEs is shown in Table 1.

The concentration of DEHP in drinking water should be lower than $8\,\mu g/L$ ($2.05 \times 10^{-8}\,mol/L$), which is one of the lowest molarity limits of pollutants including heavy metal ions, pesticides and polycyclic aromatic hydrocarbons recommended by the WHO (Net et al., 2015). China, the United States, Japan and other countries have regulated the content of these six PAEs in all toys and products of children to no more than 0.1% [Commission Regulation (EU), 2018]. China has put forward relevant suggestions on the maximum residue of PAEs in food. For example, the content of DEHP and DBP in liquor and other distilled liquor should not be higher than 5 and 1 mg/kg (Sate Administration for Market Regulation, 2019). About 600 million people around the world suffer from diseases after ingesting contaminated food every year, and about 10% of them die from diseases (World Health Organization, 2021). In recent years, food safety awareness has been widely spread among consumers, and

TABLE 1 Six kinds of PAEs in restricted list and their basic information.

Name	Abbreviation	Chemical molecular formula	Structural formulas	Samples with PAEs	Reference
Bis(2-ethylhexyl) phthalate	DEHP	$C_{24}H_{38}O_4$		Tap water, pork, bottled beverages, plastic particles	Zhang Y. et al. (2023), Wang Y. et al. (2021), and Tu et al. (2019)
Dibutyl phthalate	DBP	$C_{16}H_{22}O_4$		Pond water, liquor, fish, juice	Zhu et al. (2018), Chen et al. (2022), You et al. (2022), and You et al. (2022)
Benzyl butyl phthalate	BBP	$C_{19}H_{20}O_4$		Liquor, rice wine	Liu et al. (2018) and Li et al. (2019)
Dimethyl phthalate	DMP	$C_{10}H_{10}O_4$		Liquor, tap water, bottled beverages	Li et al. (2023)
Diethyl phthalat	DEP	$C_{12}H_{14}O_4$		River water	Zhu et al. (2019)
Di-n-octyl phthalate	DNOP	$C_{24}H_{38}O_4$		–	Abeysinghe et al. (2022)

"–" means that the research on the relevant detection in the real sample has not been found.

food safety analysis methods have been continuously improved. However, issues related to food safety incidents are still the focus of attention in many developing countries (Soon et al., 2020; Selva Sharma et al., 2024; Ding et al., 2022). Therefore, the development of sensors that can achieve point-of-care detection of PAEs is of great significance for the prevention and control of PAEs. Optical sensors have the advantages of simplicity, non-destructiveness and portability, which are expected to realize the point-of-care detection of PAEs. A series of optical sensors for quantitative detection of PAEs have been developed (Zhang C. et al., 2023; Pablo et al., 2023; Ly et al., 2021). However, there is a lack of systematic summary for the current research on colorimetric (CL) sensors, fluorescence (FL) sensors, surface-enhanced Raman scattering (SERS) platform and dual-mode optical sensors for detection of PAEs. Therefore, this review aims to summarize the recent advancements of optical sensors including CL, FL, SERS and dual-mode sensors for detection of PAEs, from the aspects of detection mechanism and application. As shown in Figure 1, CL, FL, SERS and dual-mode sensors for detection of PAEs are discussed as follows: (i) The CL sensors for detection of PAEs are divided into direct detection and indirect detection. (ii) The FL sensors for detection of PAEs are classified to direct detection and labeled with FL probe. (iii) The different metal materials (e.g., Ag, Au, and Au-Ag) are used to construct the Raman substrate in SERS sensing platform. (iv) The bifunctional materials in the dual-mode sensor are discussed. In addition, it is quick to understand the development status of optical sensors for detection of PAEs in the past 5 years and the future research directions of optical sensors by this review. In conclusion, this review provides guidance for the rapid, real-time and sensitive detection of PAEs by optical sensors.

2 Application of optical sensors for the detection of PAEs

Optical sensors detect small entities based on the interaction between light and matter with the strength of the principles of absorption, emission, and FL (Qin et al., 2022). When light interacts with objects, there are three forms of energy transfer: absorption, transmission and reflection. Owing to the differences in the internal biochemical components, texture and apparent morphology of the target compound, the optical signal is attenuated at different intensities. The optical sensors can collect the generated signal and visualize it into a spectral line through computers (Liu F. et al., 2023; Lu et al., 2020). Based on this, the type and concentration of the target can be determined. Optical sensors usually include a transducer component and a recognition unit that can interact selectively with targets. Various optical sensors currently have been developed for quantitative analysis include CL, FL, SERS. In these methods, color changes, FL generation and quenching, as well as changes in spectral patterns and peak shifts, are related to the concentration of the target. Moreover, the optical sensing system has immunity to electromagnetic interference, and can exhibit stable performance and high signal-to-noise ratio even in complex environments (Ma et al., 2023). Recently, optical sensors have also been widely used in the detection of PAEs. Next, the optical sensors for detection of PAEs will be described based on CL, FL, SERS, and dual-mode methods.

2.1 CL sensor for detection of PAEs

The CL methods can determine the content of the target by measuring or comparing the color depth of the colored substance solution. This method utilizes the absorption characteristics to the specific wavelength light of the colored substance to qualitatively analyze. The principle is that the color of the colored solution generated after the addition of the chromogenic agent or the color depth of the measured substance solution is proportional to the content of the substance (Wang Y. et al., 2022). The CL methods have many advantages: Firstly, CL methods allow in situ visual detection founded on color change without complex instruments (Jiang et al., 2022). Secondly CL sensor arrays provide an approach with simplicity and efficiency for the rapid detection and recognition of chemical substrates by utilizing digital imaging (Lin et al., 2023). Thirdly, CL sensors are easy to miniaturize and allow multiple analyses using a single control instrument at the central site. Fourthly, it can be used for the detection of explosive, flammable and toxic substances. In addition, it also has the advantages of high selectivity, non-destructiveness, fast response and low limit of detection (LOD) (Huang et al., 2018). In recent years, CL methods have made some progress in the detection of PAEs. The characteristics of CL sensors constructed in these works are shown in Table 2.

After converting PAEs into dyes, the total amount of PAEs at sub-micromolar levels can be easily determined by CL method. The CL method without recognition elements is known as direct detection. For example, the PAEs are hydrolyzed in sodium hydroxide solution, and then dehydrated to form phthalic anhydride. The product can be converted into a marker by reacting with resorcinol. The presence of PAEs can be determined by absorbance spectrophotometry (Yanagisawa and Fujimaki, 2019). This CL method provides a simple screening method for the detection of PAEs, but it cannot identify individual PAEs. Au nanomaterials display different colors according to their aggregation state, shape and size, which provide good platforms for the development of CL sensors in biological field. The development of Au nanomaterials has promoted the progress of CL detection (Yu et al., 2020). PAEs can cause the aggregation of functionalized Au nanoparticles (Au NPs), resulting in a change in the color of the solution, which provides a research idea for the detection of PAEs by CL sensors. Yan et al. (2021) proposed a simple and innovative CL method based on DBP-induced aggregation of arginine functionalized Au NPs (ARG-Au NPs). There is a strong non-covalent interaction between DBP and ARG-Au NPs (electrostatic, van der Waals force and hydrogen bonding), which leads to the decrease of electrostatic repulsion between the nanoparticles and aggregation. Therefore, the color of ARG-Au NPs changes from red to blue. When the concentration of DBP in the solution is more than 1.0 mg/L (3.59×10^{-6} mol/L), the color change of the solution can be obviously observed by the naked eye. In this system, DBP can be rapidly and semi-quantitatively detected without sample pretreatment technology and tedious operation. Recently, M13 bacteriophage-based sensors have also been widely studied for their flexible responses to changes in the target substance (Lee et al., 2023). The intermolecular interactions (or binding affinities) between the M13 bacteriophage and target chemicals can be regulated by genetic engineering techniques. When the external gas is exposed, the distance between the self-assembled M13 bacteriophage bundles will change, resulting in a change in the scattering color. The self-assembled structure has
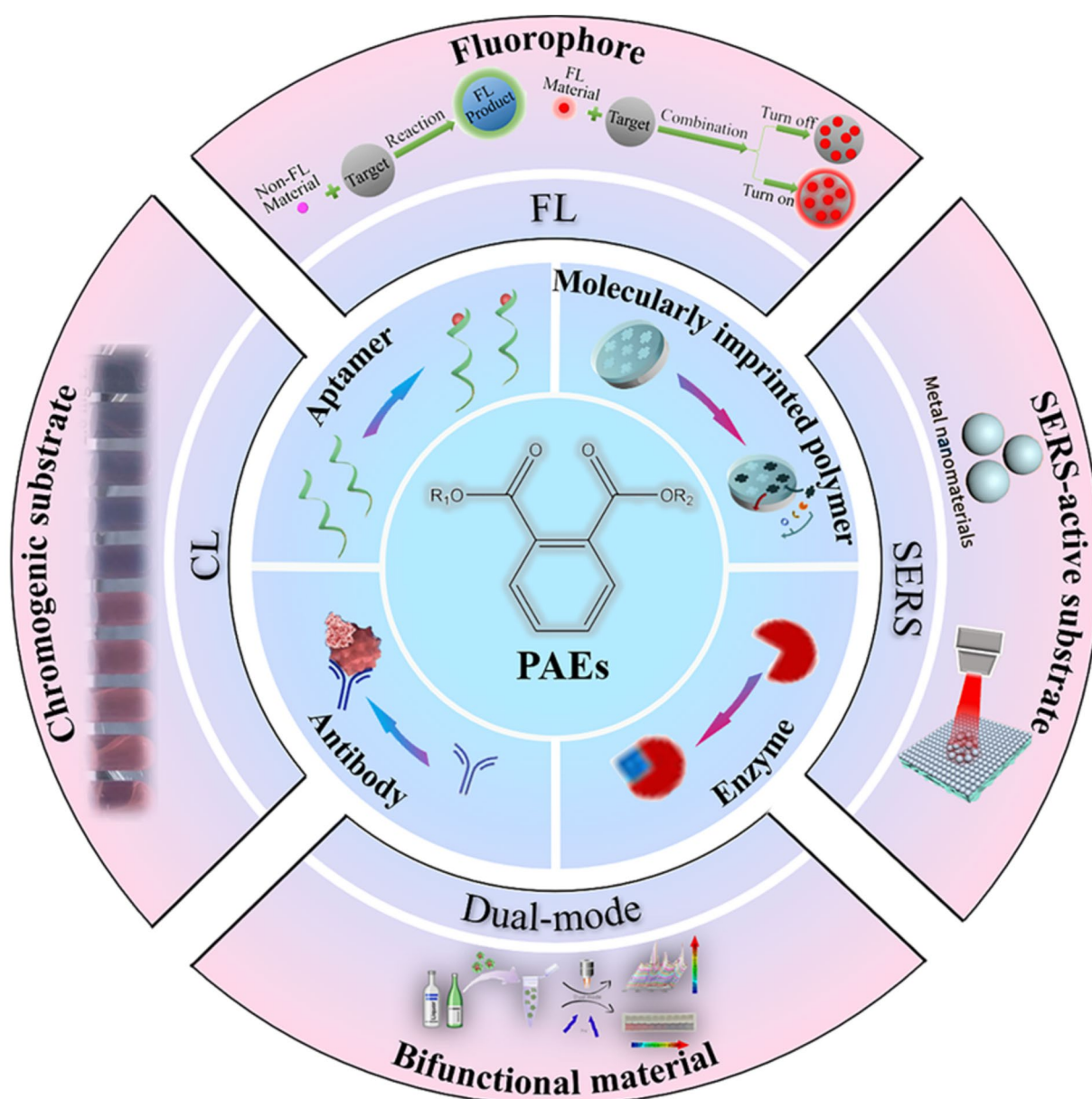
FIGURE 1
Schematic diagram of common optical sensors for detection of PAEs.

the characteristics of easy tunability and multi-functionality, so we have advantages in using M13 bacteriophage as sensor applications and biomaterials (Kim et al., 2023). Seol et al. (2019) studied the potential of CL sensors based on M13 bacteriophage for the analysis and detection of four PAEs (DEHP, DBP, DEP, and BBP) with similar molecular structures. The magnitude and pattern of the RGB color change vary due to the functional groups present in the PAEs structures. DEHP with a long alkyl chain causes a slight color change. BBP with an additional benzene ring has a large color change when measured. Because the tryptophan-histidine-tryptophan residues on the self-assembled phages contain imidazole and indole, the surface of the sensor constructed by the self-assembled phages can interact with the benzene ring in BBP by π-π interaction, resulting in a large color change. The CL sensor constructed in this study is

multifunctional and can be applied to on-site screening. Although direct detection mode is simple, the selectivity of the CL sensors is limited.

By introducing recognition elements such as aptamers and antibodies into the CL method, the selectivity of the sensor can be improved. Horseradish peroxidase (HRP) is a natural enzyme with high selectivity and excellent catalytic efficiency, which is often used in the study of CL sensors (Zhao T. et al., 2022; Wang D. N. et al., 2019). Zhu et al. (2018) constructed an ingenious HRP-based CL immunosensor for detection of trace DBP in Figure 2A. In the presence of HNO_3, a large amount of Cu (II) is released after Cu-MOFs@Ab$_2$ is captured by the antigen-primary Ab$_1$ complex. After the addition of sodium ascorbate, Cu (II) is further reduced to Cu (I), resulting in the inhibition of HRP-catalyzed colorless 3,3′, 5,5

TABLE 2 Characteristics of the developed CL sensors for detection of PAEs.

Target	Type of sensor	Functional nanomaterials	Recognition element	Type of signal response	Linear range (mol/L)	Limit of detection (mol/L)	Real sample	References
DBP	CL	ARG-Au NPs	Label-free	Turn on	$0.0 \sim 1.0 \times 10^{-5}$	1.8×10^{-7}	Liquor	Yan et al. (2021)
DBP	CL	HRP/Cu-MOFs@Ab/TMB	Antibody	Turn on	\	3.6×10^{-9}	Pure water, pond water, liquor	Zhu et al. (2018)
DMP DBP	CL	Pt@Au@Ab$_1$/Pt@Au@Ab$_2$	Antibody	Turn off	$2.6 \times 10^{-9} \sim 5.2 \times 10^{-7}$ $3.6 \times 10^{-9} \sim 1.2 \times 10^{-7}$	5.2×10^{-10}, 1.8×10^{-9}	Liquor, plastic bottled drinks	Li et al. (2023)
DEP DBP DEHP	CL	Au NPs	Aptamer	Turn on	$1.9 \times 10^{-6} \sim 7.7 \times 10^{-6}$ $1.2 \times 10^{-6} \sim 2.5 \times 10^{-6}$ $2.2 \times 10^{-6} \sim 8.5 \times 10^{-6}$	1.2×10^{-7} 2.8×10^{-7} 3.7×10^{-7}	–	Guo et al. (2021)
PAEs	CL	Mfold secondary structure	Aptamer	Turn on	$7.7 \times 10^{-12} \sim 2.6 \times 10^{-8}$	/	–	Chen et al. (2021)
DEHP	CL EC	H-Gr/TMB	Aptamer	Turn off	$5.1 \times 10^{-13} \sim 2.6 \times 10^{-10}$ $2.6 \times 10^{-13} \sim 2.6 \times 10^{-10}$	1.7×10^{-13} 8.5×10^{-14}	Water in plastic bottle	Zhang Y. et al. (2023)
PAEs	CL FL	HPEAPB/PDDB	MIP	Turn on/ off	\	4.0×10^{-5} 2.0×10^{-6}	–	Gong et al. (2017)

"\" means that the linear range is not clearly pointed out in the corresponding work, "/" means that the limit of detection is not clearly pointed out in the corresponding work, "–" means that the real sample is not examined in the corresponding work.

′-tetramethylbenzidine (TMB) to blue oxidation product (oxTMB). The method shows good accuracy and reproducibility and the proposed immunosensor indicates great potential for trace DBP determination from environmental and food samples. However, nanozymes have a wide range of applications in many fields such as the detection of biomedicine, biosensing, pollutant and antibacterial products because of their advantages of economy, stability and large-scale preparation, compared with natural enzymes. As a kind of nanomaterial with a variety of enzyme-like activities and enzymatic catalytic properties, nanozymes have become a new strategy for design of CL sensors. Single-atom nanozymes have received extensive attention due to their unique structures and high enzyme-like activities of atomically dispersed metal sites, among the multitudinous nanozyme materials. They have displayed tremendous potential to replace natural enzymes in the field of disease treatment, environmental control, biochemical analysis and other fields (Zhang T. et al., 2022; Wang M. et al., 2020; Cai et al., 2021; Liu et al., 2020; Wu et al., 2021; Wang et al., 2023; Niu et al., 2019). At the same time, the aptamer can quickly and conveniently detect the target, and it can be introduced into the CL sensors to detect PAEs, which can simultaneously identify a variety of PAEs with similar structures (Chen et al., 2021). Zhang Y. et al. (2023) realized the detection of DEHP by using the aptamer of hemin-graphene chloride (H-Gr) hybrid and DEHP. The H-Gr nanocomposites have intrinsic peroxidase-like activity that can catalyze the colorless TMB to generate blue oxTMB. The constructed sensor has the potential to be an efficient tool for the detection of DEHP in water samples. Au NPs can also be combined with recognition elements to achieve selective detection of PAEs. Based on DNA-modified Au NPs, a simple and rapid method for the detection of DEP, DBP and DEHP was proposed by Guo et al. (2021). After DNA modification (aptamer-B, aptamer-E

and aptamer-H), Au NPs can form aggregates in the presence of PAEs. Therefore, it can be observed that as the concentration of PAEs increases, the absorption ratio increases, and the solution shows an obvious color change from red to blue. Li et al. (2023) used a new strategy to combine Pt@Au nanozymes with high catalytic performance to create two catalytic signal probes: Pt@Au@Ab$_1$ and Pt@Au@Ab$_2$, which were specifically used to detect DMP and DBP, as shown in Figure 2B. These catalytic signal probes realize the simultaneous detection of DMP and DBP, which lay a foundation for the development of CL immunoassay. Although this CL sensor with indirect detection mode provides a powerful tool for simultaneous quantification of DMP and DBP in real samples, its linear ranges are relatively narrow. It is necessary to design novel materials with high activity and high stability to increase the sensitivity of sensors for detection of PAEs in real samples.

2.2 FL sensor for detection of PAEs

The generation of FL is that the material can emit light when it returns to the ground state after absorbing short-wave energy (Jablonski, 1933). The condition for the FL of organic molecules is that the energy level difference between the highest occupied molecular orbital and the lowest unoccupied molecular orbital is small. The presence of fluorophore is a necessary condition for the generation of fluorescence. The FL sensors include two elements: recognition group and fluorophore, which are commonly used methods for detection of substances. These two elements can be connected in a conjugate system to achieve the detection of the target. The FL of the fluorophore will be affected, when the analyte is identified, giving rise to changes in FL signals such as FL lifetime and FL intensity. The fluorophore can
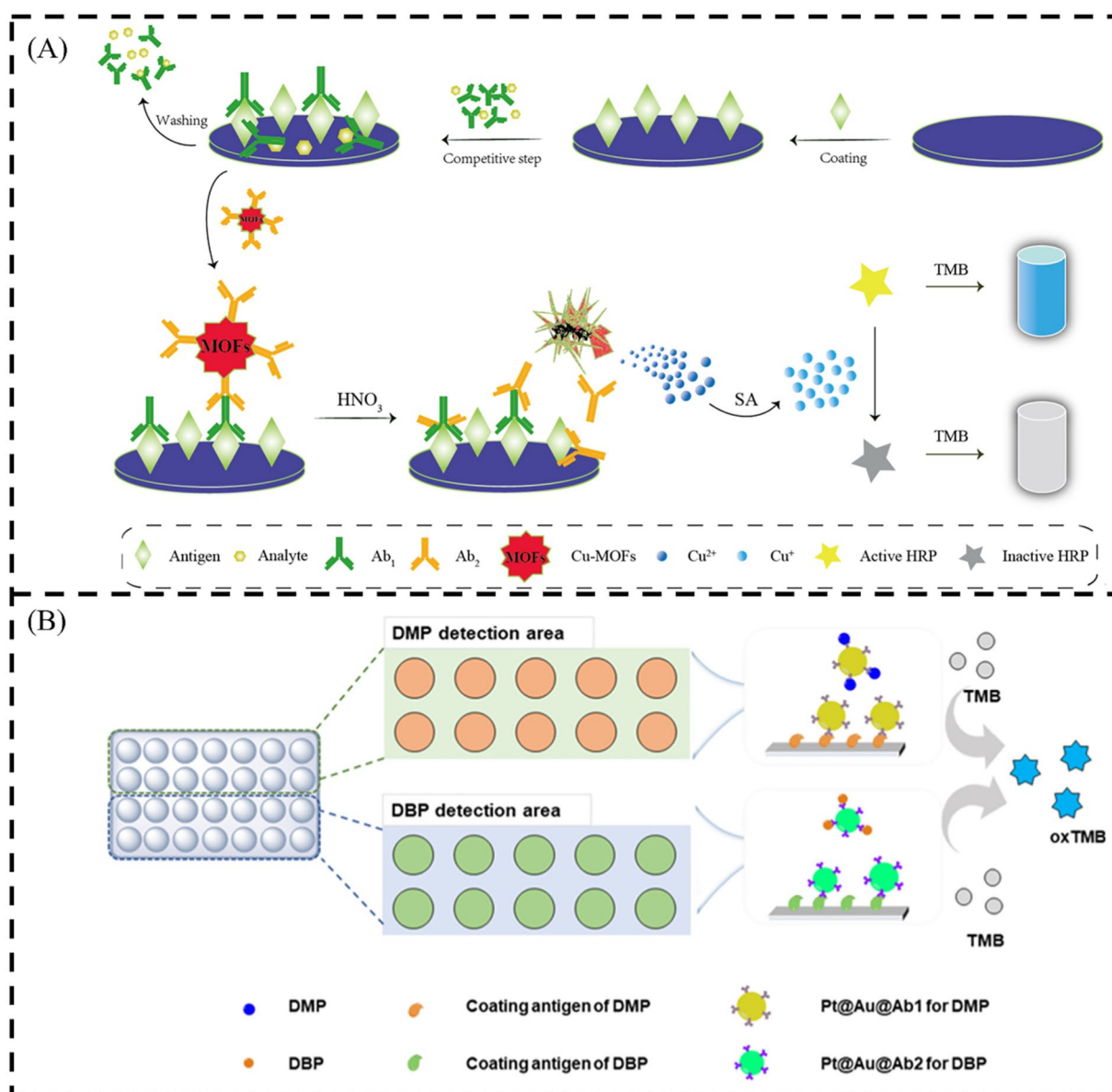
Scheme illustration of **(A)** the principle of the constructed CL immunosensor (Zhu et al., 2018) and **(B)** detection principle of the developed CL immunoassay (Li et al., 2023). Sodium ascorbate (SA).

convert the information of the analyte into a FL signal, so as to achieve simple and highly selective detection (Liu et al., 2020). Due to the increasing requirements for the detection ability and stability of FL sensors, more and more emerging nanomaterials (e.g., Au NPs, MoS₂ nanosheets, graphene oxide, and carbon nanotubes) have been applied to FL sensors to improve sensor performance. Nanomaterials have efficient FL quenching characteristics, which promote the development of FL sensors (Liu et al., 2020; Lan et al., 2018; Guo et al., 2011). The research on the detection of PAEs by FL method in recent years is summarized in Table 3.

It is well known that PAEs themselves do not emit light, but they can be converted into luminescent products. For example, PAEs are hydrolyzed into FL-free PAEs in a strong alkaline solution, which then react with hydroxyl free radicals generated during photo-Fenton process catalyzed by vermiculite-loaded BiFeO₃ to produce a

fluorescent product. The FL intensity is proportional to the concentration of PAEs, based on which the sensitive detection of PAEs can be realized (Zeng et al., 2017). In order to improve the FL intensity of PAEs derivatives, Qiu and Li (2018) proposed a simple method for detection of PAE derivatives by FL spectroscopy founded on a double-substitution modification. This method does not affect the function (stability and insulation) of the sensor. The detection of PAEs derivatives is more environmentally friendly, because the toxicity, mobility, and persistence of PAE derivatives are reduced to varying degrees compared with PAEs, and their amounts of bioaccumulation are not changed obviously. In order to realize the detection of PAEs, Lu et al. (2021) proposed a BODIPY fluorescent dye (3-(4-(5,5-difluoro-2-(4-(hydroxymethyl) phenyl))-1,3,7,9-tetramethyl5H-5l4,6l4-Bispyrrole [1,2-c:2′,1′-f] (Lee et al., 2019; Abeysinghe et al., 2022; Wang Y. et al., 2019) borothiaserine-10-yl)

phenyl)-2-(4-nitro) phenylnier (BCNOH) modified with p-nitrodiphenyl acrylonitrile and hydroxymethyl phenyl group, as shown in Figure 3A. BCNOH is turned on by PAEs to form a non-emission water caged BCNOH. The combination of water caged BCNOH and PAEs can generate nano FL dyes (nano-BCNOH). Hydroxymethyl phenyl group of BCNOH could bind more DBP. The trigger that turned on the FL emission is the interaction between p-nitrodiphenyl acrylonitrile and DBP. The results show that weakening the isomerization of water caged BODIPY dyes provides a potential method for turn-on FL sensors. Although the method is simple, it is not sensitive.

Fluorophores or fluorescent dyes have been used widely as mediums to gain readout signals in various assays or bioimaging due to their versatilities such as biocompatibility (Huang X. et al., 2022). Those fluorescent dyes-based techniques manipulate glycan-lectin interaction, base complementation, Ab-protein interaction, etc., for the selectivity analysis of molecular interactions of biomacromolecules (Luan et al., 2016). Although PAEs themselves do not emit light, they can be labeled with fluorescent labels for detection through emission (Savicheva et al., 2020) In recent years, quantum dots (QDs), as an emerging nanomaterial, have been widely used in the study of fluorescent sensors because of their ability to enhance FL signals. CdTe QDs can also be combined with MoS_2 QDs (Figure 3B) that provide self-calibration signals to construct a proportional FL sensor system for the detection of DEHP (Wang Y. et al., 2021). Zhou et al. (2017) synthesized a novel fluorescent molecularly imprinted polymer (SiO_2@QDs@MIP) based on Mn-doped ZnS QDs and SiO_2 nanoparticles. The composites exhibit outstanding molecular recognition ability of MIP and optical properties. It can recognize the template molecule DBP with high selectivity. The QDs of metal oxides [such as ZnO (Wang Y. et al., 2018)] or metal compounds [such as CdTe (Chen et al., 2022)] as optical materials can be combined with MIP to achieve selective detection of DEHP and DBP in Figure 4A. Graphene QDs (GQDs) can be quenched by Au NPs. Based on this, an aptasensor can be developed for detection of 11 PAEs (Lim et al., 2022). Carbon dots (CDs) have the characteristics of real-time and non-destructive detection. CDs have been widely applied in rapid detection. Some studies have used CDs to detect PAEs, such as Chen et al. (2023a) reported an ultrasensitive FL immunoassay using red CDs@SiO_2 (R-CDs@SiO_2) as tags for trace detection of DEP. SiO_2 as a nanocarrier can effectually enhance the utilization rate and bio-functionalization of CDs. In addition, R-CDs embedded in SiO_2 nanospheres (NS) can enhance sensitivity and amplify the FL signal. The FL immunosensor constructed by R-CDs@SiO_2 coupled with anti-DEP Ab can realize the selective recognition of DEP. Ashokan and Bhunia (2023) synthesized nitrogen and boron co-doped yellow FL CDs (B, N-C-dots). These B, N-C-dots selectively detect PAEs in aqueous solution, and the FL quenching rate is as high as 95% after PAEs treatment. The method for labeling amino-modified nucleic acid aptamers using double-emission CQDs provides more precise results and has a stronger anti interference ability compared with the single wavelength emission method. Therefore, the sensor can be used for detection of DBP in soybean oil and edible liquor (Wang X. et al., 2020). The tricolor ratiometric FL sensors have a wider range of color variations in the visual detection of DBP compared with single-emission or dual-emission sensors. It provides an ideal choice for intuitive and rapid detection of DBP in the aquatic products and environment (You et al., 2022). Other nanomaterials with efficient FL

quenching properties have also been used in the study of FL sensors. Zhu et al. (2019) established a dual-label time-resolved FL immunoassay using europium (Eu^{3+}) and samarium (Sm^{3+}) as fluorescent markers to detect DEP and DBP in aquatic environment. In order to shorten the detection time, Kim et al. (2020) proposed a non-equilibrium rapid replacement aptamer (NERRA) assay, which could perform ultra-fast (in 30 s) quantitative detection of PAEs without waiting for the reaction to reach equilibrium. The $PoPo_3$ dye is embedded into the aptamer of ssDNA by NERRA assay. When the intercalated dye is replaced by PAEs, it will quench in water. The change rate of FL is proportional to the concentration of PAEs. Based on this, PAEs in water can be selectively detected and quantified. As shown in Figure 4B, Dolai et al. (2021). combined the nanocomposites composed of poly-cyclodextrin and graphene oxide with the molecular imprinting of DBP. The molecular imprint inside the nanocomposite can achieve selective capture of DBP. After that, the "turn on" detection of the constructed FL sensor is realized by the competitive binding of graphene oxide and fluorescein. The combination of nanocomposites and paper strips can be used for rapid and simple read out detection of DBP in polluted water. In order to improve the impact of the inherent interior correction calibration on the environment and improve the accuracy and precision, Meng et al. (2022) combined the dual-output ratiometric FL assays with the enzyme-linked immunosorbent assay (ELISA) to construct a ratiometric FL immunoassay based on Ag NPs for the detection of DBP. Ag NPs are labeled on the Ag NPs@Ab_2 for signal amplification to regulate the concentration of H_2O_2. The addition of H_2O_2 can effectively quench the blue fluorescence of scopoletin and produce the red fluorescence of Amplex Red, when Ag NPs-Ab_2 and antigen–primary Ab_1 are linked by selective recognition. Founded on a new tetrahedral DNA nanostructure (TDN) -scaffold-DNAzyme (Tetrazyme), Zhu et al. (2021) established a high-throughput proportional FL amplification ELISA for the detection of DBP in aquatic systems. Among them, the HRP-mimicking enzyme is derived from the Tetrazyme formed by the precise folding of the G-quadruplex sequence on the three apexes of hemin and TDN. The rigid TDN can avoid the local crowding effect, thus providing a reasonable spatial spacing for the G-quadruplex sequence on the interface. In addition, it can also enhance the catalytic ability of the DNAzyme, thereby increasing the chance of collision between the substrate and the DNAzyme. In summary, the sensor provides a potential strategy for rapid detection of DBP in environmental water. However, the sensor suffers from various interferences such as non-selective binding and cross-fluorescence reactions in the actual environmental. In addition, the direct detection mode of FL methods is currently unable to achieve selective recognition of single PAE. To obtain the FL sensors with simplicity and portability, the composite materials combine function of recognition and signal amplification should be carried out.

2.3 SERS platform for detection of PAEs

SERS is an ultrasensitive vibrational spectroscopy technique for analyte characterization and determination. It has remarkable characteristics such as high resolution, fingerprint recognition, nondestructive and strong anti-interference ability to samples (Guo et al., 2020). Raman scattering is that when light interacts with matter, photons will exchange energy with molecules in matter, resulting in a

TABLE 3 Characteristics of the developed FL sensors for detection of PAEs.

Target	Type of sensor	Functional nanomaterials	Recognition element	Type of signal response	Linear range (mol/L)	Limit of detection (mol/L)	Real sample	References
DEHP	FL	MoS$_2$ QDs/CdTe-Apta	Aptamer	Turn off	$1.3 \times 10^{-8} \sim 7.7 \times 10^{-6}$	5.4×10^{-10}	Pork	Wang Y. et al. (2021)
DEHP	FL	ZnO QDs	MIP	Turn off	$5.0 \times 10^{-7} \sim 4.0 \times 10^{-5}$	/	Tap water	Wang Y. et al. (2018)
DBP	FL	SiO$_2$@QDs@ MIPs	MIP	Turn off	$5.0 \sim 5.0 \times 10$	/	Tap water	Zhou et al. (2017)
DBP	FL	CdTe QDs	MIP	Turn off	$5.0 \times 10^{-8} \sim 1.8 \times 10^{-5}$	1.6×10^{-9}	Water, fish, milk, juice	Chen et al. (2022)
DBP	FL	Dual-emission carbon QDs	Antibody	Turn on	$4.5 \times 10^{-8} \sim 5.4 \times 10^{-6}$	1.8×10^{-8}	Edible liquor	Wang X. et al. (2020)
DBP	FL	CdSe/ZnS QDs	MIP	Turn off	$7.2 \times 10^{-9} \sim 7.2 \times 10^{-5}$	2.3×10^{-9}	Fish, seawater	You et al. (2022)
DBP	FL	graphene oxide/ poly-cyclodextrin	MIP	Turn on	$2.5 \times 10^{-8} \sim 1 \times 10^{-6}$	2.4×10^{-8}	–	Dolai et al. (2021)
DBP	FL	TDN-scaffolded-DNAzyme (Tetrazyme)	Enzyme sensing	Turn on	\	6.1×10^{-10}	Pure water, river water, tap water, pond water	Zhu et al. (2021)
DEP	FL	R-CDs@SiO$_2$	Antibody	Turn off	\	5.0×10^{-12}	–	Chen et al. (2023a)
DBP DEP	FL	Eu^{3+}/Sm^{3+}	Antibody	Turn off	\	3.4×10^{-7} 2.8×10^{-7}	The inner rivers of Zhenjiang city	Zhu et al. (2019)
DBP DEHP	FL	nano-BCNOH	Label-free	Turn on	$5.0 \times 10^{-6} \sim 2.5 \times 10^{-4}$	5.0×10^{-6}	Rice yellow wine, liquor, spirits	Lu et al. (2021)
PAEs	FL	Au NP-gQD/ GQDs	Aptamer	Turn on	$2.6 \times 10^{-12} \sim 1.3 \times 10^{-7}$	1.0×10^{-11}	–	Lim et al. (2022)
PAEs	FL	B, NC-dots	Label-free	Turn off	\	/	Drinking water, industrial water, river water	Ashokan and Bhunia (2023)
PAEs	FL	Fluorescence PoPo$_3$ dye	Aptamer	Turn off	$2.6 \times 10^{-10} \sim 3.8 \times 10^{-6}$	2.6×10^{-10}	–	Kim et al. (2020)
PAEs	FL	VMT-BiFeO$_3$	Label-free	Turn on	$3.8 \times 10^{-7} \sim 4.8 \times 10^{-5}$	5.4×10^{-8}	–	Zeng et al. (2017)
PAEs	FL	BSA	Label-free	Turn on	\	/	–	Qiu and Li (2018)

"\" means that the linear range is not clearly pointed out in the corresponding work, "/" means that the limit of detection is not clearly pointed out in the corresponding work, "–" means that the real sample is not examined in the corresponding work.

slight change in the frequency and intensity of light. The signal intensity of SERS is vastly affected by the modification of Raman dyes in plasmonic hot spots and the compositional details and structural of the plasmonic nanostructures (Xue and Jiang, 2023). Therefore, the key to obtaining strong, controllable and quantifiable SERS signals is a strategy for high-yield and accurate synthesis of plasmonic nanostructures with strong enhanced electromagnetic fields and the controllable modification of the number and position of Raman dyes in plasmonic hotspots (Nam et al., 2016). The Raman activity of PAEs is poor, and the affinity of metal surface is very low, which greatly hinders the realization of direct and effective detection of PAEs by SERS. The equivalent charge oscillation on the metal surface can produce an electric field enhancement effect, which makes the Raman scattering signal of the material greatly enhanced. Therefore, the SERS platform for detection of PAEs are based on metal nanomaterials. The SERS platform characteristics currently used for detection of PAEs are shown in Table 4.

SERS is an ultra-sensitive analytical tool that usually measures single molecules by an obviously enhanced Raman scattering signal of molecules located near the surface of metals such as Au, Ag, and Cu
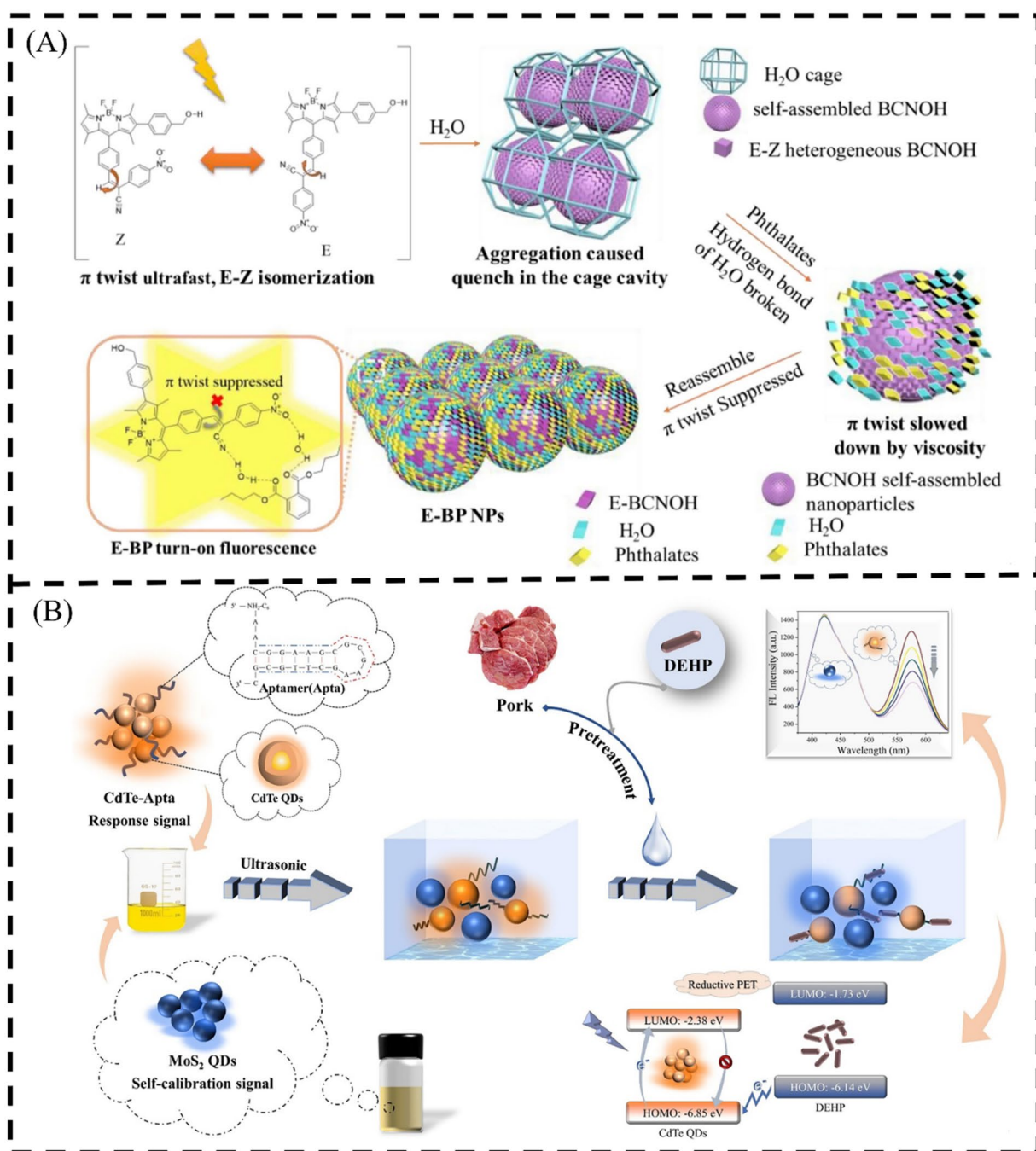
FIGURE 3
Schematic illustration of **(A)** BCNOH and phthalates and water assembled nanoparticles to turn on the FL emission (Lu et al., 2021) and **(B)** MoS$_2$ QDs/ CdTe-Apta for the DEHP detection assay (Wang Y. et al., 2021). Lowest Unoccupied Molecular Orbital (LOMO), Highest Occupied Molecular Orbital (HOMO).

(Zhang T. et al., 2023; Liu et al., 2024; Wang et al., 2024). As the first material to appear Raman signal, Ag has been studied a lot in recent years because of its strong Raman signal (Fleischmann et al., 1974; Li et al., 2016; Li et al., 2021). A high-density ordered SERS substrate based on triangular Ag NP (T Ag NP) array self-assembly is developed for detection of DBP (Xu S. et al., 2021). The sharp edges and ordered arrangement of T Ag NPs can offer uniform and sufficient hotspots for highly active and reproducible SERS effects. Wang et al. (2023) developed a two-dimensional (2D) Ag plate synergizing with a Ag sol

as a SERS substrate for the detection of potassium hydrogen phthalate (PHP), a hydrolysate of a PAE in Figure 5A. The results show that the detection of PHP by SERS platform is hopeful to offer a way for the detection of PAEs in fats and oils, and has prospect application prospects in food safety. By combining Ag with other metal nanomaterials, such as Fe$_3$O$_4$@MIP@Ag, the detection of DMP can be realized by SERS characterization. Ag@Fe$_3$O$_4$@Ag/β- cyclodextrin (CD) NPs as a SERS active substrate is shown in Figure 5B (Zhou et al., 2019). When malachite green is used as a probe molecule, the

FIGURE 4
Schematic illustration of **(A)** MIP@QDs for preparation (Wang Y. et al., 2018) and **(B)** the preparation of the poly-cyclodextrin−graphene oxide nanocomposite with DBP molecular imprinting. The a-CDs are spatially aligned in the imprinted polymer according to their interaction with DBP (Dolai et al., 2021). 2,2′-azobis(2-methylpropionitrile) (AIBN), Ethylene glycol dimethacrylate (EDGMA), 3-(Methacryloyloxy)propyltrimethoxysilane (KH-570), Tetrafluoroterephthalonitrile (TFN), Graphene oxide (GO).

substrate is proved to have good repeatability and sensitivity. Recently, MOFs have received extensive attention in the research of SERS platforms due to their excellent absorption capacity to capture target molecules entering the electromagnetic field. In the detection of sensors, Ag nanowires (NWs) are embedded in functionalized metal–organic frameworks ZIF-67 (ZIF-67@Ag NWs) composite as substrate to construct a platform for highly sensitive detection of six kinds of PAEs (Xu et al., 2023). In addition, Ag NPs can also be grown on the surface of MOFs octahedron UIO-66 (UIO-66@Ag NPs) with large specific surface area and high porosity to form a composite SERS substrate for detection of DEHP. The prepared UIO-66 @ Ag NPs substrate has good adsorption performance for DEHP, and it can

reduce the aggregation of Ag NPs, thereby increasing the "hot spots" formed by local surface plasmon resonance (LSPR) of Ag NPs. This work preliminarily discusses the SERS enhancement mechanism of UIO-66@Ag NPs substrate, and the SERS signal enhancement factor of the platform is calculated to be about 1.1×10^7. The results show that this method provides a suitable way for the monitoring of DEHP in plastics by studying advanced SERS sensing materials (Xu H. et al., 2021). Ag can also be combined with non-metallic materials to prepare high-performance SERS substrates. The most common is to combine with SiO_2 to prepare composite materials such as self-assembly of monodisperse SiO_2 colloidal spheres on silicon wafers, and then coating Ag layer on them to prepare SERS substrates. Ag NPs

can also be gathered together and coated with silica. The obtained Ag/SiO$_2$ SERS substrates can achieve rapid and sensitive detection of PAEs (Tu et al., 2019; Wu et al., 2018).

Although the Raman signal of Ag is very good, Ag NPs are easily oxidized in the air, giving rise to the weakening of the surface plasmon resonance effect and affecting the Raman enhancement effect. Therefore, it is also a research direction to explore other metal materials with better performance to replace Ag NPs. Au NPs, with antibacterial activity, unique surface plasmon resonance effect and biocompatibility, are intermediates between metal blocks and atoms. Spherical Au NPs have potential applications in optics due to their low toxicity, good photoelectric properties, excellent biocompatibility and high surface-to-volume ratio. Au NPs can increase surface compatibility by surface modification with different substances. Therefore, a SERS detection platform based on Au NPs can be constructed for the analysis of PAEs (Liu L. et al., 2023). Simply, the analyte BBP molecules can be loaded into the nanogaps with SERS activity in the Au array by inducing the self-assembly of Au NPs at the organic/water interface, thereby achieving sensitive detection of BBP (Liu et al., 2018). Au NPs are easily anchored and growth on bio-inspired polydopamine MIP (PDA-MIP) coating to form a three-dimensional (3D) architecture, as shown in Figure 6A. The distribution and particle size of PDA and Au NPs can be well controlled through adjusting the reaction conditions. The Au NP/PDA-MIP nanocomposite can be used to construct an excellent SERS sensing platform for selective recognition of PAEs (Yang et al., 2020).

The anisotropic growth of bimetallic nanostructures can not only skillfully integrate the two properties into one nanoarchitecture, but also highly improve the original properties. Therefore, people are committed to synthesize anisotropic bimetallic nanostructures by selectively growing a second material on the template nanostructures (Yang et al., 2023). Among them, anisotropic Au-Ag bimetallic nanostructures are prominent SERS platforms (Zhang et al., 2018). Wang Q. et al. (2021) combined the SERS strategy with plasmonic core–shell Au NS@Ag nanocubes (Au NCs) with abundant LSPR as substrates and successfully used it for sensitive and rapid detection of BBP in liquor. As shown in the Figure 6B, the synthesized Au@Ag NCs composed of Ag cuboid shells and Au nanorod (NR) cores can produce broader and richer plasmon resonance modes than Au NRs (Wang Q. et al., 2021). In this system, the unique core-shell Au@Ag NCs are used as SERS active substrates. The SERS sensing platform based on this SERS substrate realizes the detection of BBP content in liquor samples, and the LOD is as low as 1.3 mg/kg. Therefore, the unique bimetallic material provides an effective tool for the sensitive and rapid detection of PAEs in liquor samples. Ansah et al. (2022) proposed an Ag-Au bimetallic nanocomposite (SGBMNC) with internal hot spots to construct a SERS sensing platform for PAEs detection. Compared with the traditional SERS platform without internal hotspots, Au significantly enhances the plasmonic activity by replacing Ag NPs to provide the hotspots area for SGBMNC by galvanic replacement reaction (GRR). During the GRR process, the analyte diffuses to the proposed interior hotspots, and sensitive detection can be achieved within 10 s. Zhang J. F. et al. (2022) synthesized Au@Ag@b-CD NPs with a particle size about 13 nm, and successfully modified b-CD on its surface. An efficient synthetic method for the preparation of a SERS substrate is proposed, that is, Au@Ag@b-CDNPs and analytes are self-assembled into a coffee ring pattern through the coffee ring effect. This effect can make Au@Ag@b-CD NPs and PAEs gather to the edge together to achieve concentration enrichment. In addition, the b-CD modified on the surface of Au@Ag@b-CD with core-shell structure has a cavity structure, which can adsorb the analyte into the hydrophobic cavity through host-guest recognition, so as to achieve the purpose of enriching the analyte concentration. In the process of enrichment, the concentration of the analyte surface is improved. In addition, the analyte and other substances in the analyte solution can be effectively separated in this process. SERS seems to be a promising technique to fabricate a simple and universal biosensor, but it depends on Ag, Au and Ag-Au materials. To popularize the application of SERS method in practical detection, more low-cost and high-stability materials should be designed.

2.4 Dual-mode sensor for detection of PAEs

The above-mentioned individual methods for detection of PAEs still have some challenges in ensuring the accuracy of their results. The results obtained by the dual-mode measurement method can be mutually confirmed, and the accuracy of the detection results can be effectively improved by self-correction. The bifunctional materials are required for construction of dual-mode sensors. For example, Li et al. (2019) provided an effective and selective dual-mode sensor for the detection of trace BBP by constructing β-CD stabilized Au NPs (Au NPs@β-CD) colloids in Figure 7A. As switchable Raman reporters and macromolecular binder, BBP could assemble Au NPs@β-CD into photonic clusters with various shapes. The Au NPs@β-CD cluster triggered by BBP has rich hot spots in SERS mode, so it can amplify the corresponding SERS signal, and the LOD is 1.0×10^{-8} mol/L. In CL mode, the Au NPs@β-CD cluster is used as the chromogenic substrate, and the distinguishable response of CL can be accurately quantified by UV–Vis spectroscopy. The LOD of BBP can reach 1.49×10^{-8} mol/L. In addition, the combination of FL and CL to construct a multifunctional chemical sensor is expected to be used for low-cost, accurate and simple detection of trace PAEs (Gong et al., 2017). Chen et al. (2023b) constructed a dual-mode immunoassay based on blue CDs@SiO$_2$@MnO$_2$ (B-CDs@SiO$_2$@MnO$_2$), which could simultaneously detect DEP by FL method and CL method, as show in Figure 7B. In this system, MnO$_2$ nanosheets have oxidase-like activity. Under acidic conditions, colorless TMB can be oxidized to yellow TMB^{2+} and the color of the solution also changes. Moreover, the FL of B-CDs@SiO$_2$ is quenched by MnO$_2$ nanosheets. After the addition of ascorbic acid, MnO$_2$ nanosheets are reduced to Mn^{2+}, and the fluorescence of B-CDs@SiO$_2$ is restored. The experimental results show that the results of the constructed dual-mode immunosensor have good consistency, and it can be considered that the dual-mode immunosensor is reliable for the detection of DEP. Figure 7C shows that a simple preparation method of dual-mode nanocomposites for sensitive detection of PAEs by coupling SERS and up conversion FL as signal can be proposed (Rong et al., 2021). In the sensing system based on Au NPs modified up conversion NPs (UCNPs), UCNPs are used as signal molecules, Au NPs are applied as SERS substrates, and aptamer is used as recognition tags for PAEs. The method has been successfully applied to food packaging and spiked food samples. At the same time, the EC-CL dual-mode sensor can be constructed by combining the H-Gr complex with the aptamers of DEHP for detection of DEHP (Zhang Y. et al., 2023). The principle is that the H-Gr nanocomposite has peroxidase-like activity, which can catalyze the chromogenic substrate TMB to produce a blue oxTMB in

TABLE 4 Characteristics of the developed SERS platform for detection of PAEs.

Target	Type of sensor	Functional nanomaterials	Recognition element	Type of signal response	Linear range (mol/L)	Limit of detection (mol/L)	Real sample	References
DEHP	SERS	Ag/SiO$_2$	Aptamer	Turn on	$8.0\times10^{-12}\sim1.8\times10^{-7}$	8.00×10^{-12}	Tap water, bottled beverages	Tu et al. (2019)
DEHP	SERS	UIO-66@Ag NPs	Label-free	Turn off	$1.0\times10^{-11}\sim1.0\times10^{-4}$	3×10^{-12}	Plastic particles	Xu H. et al. (2021)
DBP	SERS	TAg NPS	Label-free	Turn on	$5.0\times10^{-7}\sim5.0\times10^{-5}$	1.0×10^{-7}	–	Xu S. et al. (2021)
BBP	SERS	Au NPs	Label-free	Turn on	\	3.8×10^{-6}	Liquor	Liu et al. (2018)
BBP	SERS	Au NS@Ag NCs	Label-free	Turn on	\	1.0×10^{-9}	Liquor	Wang Q. et al. (2021)
BBP	SERS	Ag@Fe$_3$O$_4$@Ag/β- CD	Label-free	Turn on	\	3.8×10^{-6}	Liquor	Zhou et al. (2019)
DMB	SERS	Fe$_3$O$_4$@MIPs@Ag	MIP	Turn on	$1.0\times10^{-10}\sim1.0\times10^{-3}$	4.2×10^{-11}	Laboratory tap water	Zhang T. et al. (2023)
DMP BBP DEHP	SERS	Au NP/PDA-MIP	MIP	Turn on	$1.0\times10^{-10}\sim1.0\times10^{-3}$	1.0×10^{-10} 1.0×10^{-10} 1.0×10^{-9}	–	Yang et al. (2020)
DEHP BBP DBP	SERS	Ag/SiO$_2$	Label-free	Turn on	\	2.6×10^{-4}	–	Wu et al. (2018)
PAEs	SERS	2D silver plate	Label-free	Turn on	$1.0\times10^{-9}\sim1.0\times10^{-2}$	1.0×10^{-9}	Edible oil	Wang et al. (2023)
PAEs	SERS	ZIF-67@Ag NWs	Label-free	Turn on	$1.0\times10^{-12}\sim1.0\times10^{-2}$	3.0×10^{-13}	Three plastics	Xu et al. (2023)
PAEs	SERS	Ag–Au	Label-free	Turn on	$3.6\times10^{-9}\sim3.6\times10^{-4}$	3.2×10^{-9}	–	Ansah et al. (2022)
PAEs	SERS	Au@Ag@b-CD	Label-free	Turn on	$1.0\times10^{-8}\sim1.0\times10^{-4}$	2.0×10^{-10}	–	Zhang J. F. et al. (2022)

"\" means that the linear range is not clearly pointed out in the corresponding work, "–" means that the real sample is not examined in the corresponding work.

CL mode. Moreover, H-Gr can be used as an *in situ* probe in EC mode, and the formed DEHP-aptamer complex will reduce the EC signal of H-Gr. The strategy of dual-mode detection of DEHP proposed in this study has a wide linear range and has the potential to be applied to the detection of DEHP in water samples. Compared with the EC sensors, the PEC sensors with higher sensitivity have been used to construct a PEC-CL dual-mode sensors. For example, the MXene/In$_2$S$_3$/In$_2$O$_3$ composite material can be used to construct a PEC-CL dual-mode aptasensor for the ultra-sensitive detection of DEHP (Zhang et al., 2024). The linear range of the constructed sensor is $1.0\times10^{-13}\sim2.0\times10^{-10}$ mol/L, and the LOD is 2.0×10^{-14} mol/L. This research provides a good prospect for the detection of PAEs by dual-mode sensors. In view of the high accuracy of dual-mode sensor, more dual-mode sensors are worth designing and developing.

3 Summary and perspectives

High toxicity, wide distribution and harmfulness are the characteristics of PAEs. PAEs in the environment not only affect the growth of plants, but also accumulate in organisms and eventually enter the human body. Long-term intake of PAEs can lead to obvious depressive behavior and neurobehavioral disorders, and can increase

the risk of asthma in children. In order to prevent and control the pollution of PAEs, several countries have introduced relevant limit standards in water, toys and food. The relevant limit standards of PAEs and their actual limitation of low concentration in the environment determine that it is very important to realize the sensitive detection of trace PAEs. Optical sensors have the advantages of simplicity, high selectivity, simple operation, portability and low cost, which have been applied to the detection of PAEs. Among them, CL sensors, FL sensors and SERS sensing platforms have been focused on due to their excellent detection performance, and have achieved encouraging results in the detection of PAEs. This review mainly discusses (i) the CL methods without recognition elements and the CL methods combined with aptamers and antibodies with high selectivity; (ii) the FL methods with fluorescent products or fluorescent tag; (iii) the SERS methods using Ag and Au for signal amplification, and (iv) the dual-mode methods with high accuracy. The latest research above shows that optical sensors are moving toward a broader prospect. However, due to some limitations of the optical sensor, its application in practice has not been greatly expanded. The sensitivity of CL sensors still needs to be improved. And the range of sample that detected by optical sensors has certain limitations. There is also lots of space for improvement in the portability of the detection device. The types of substances that
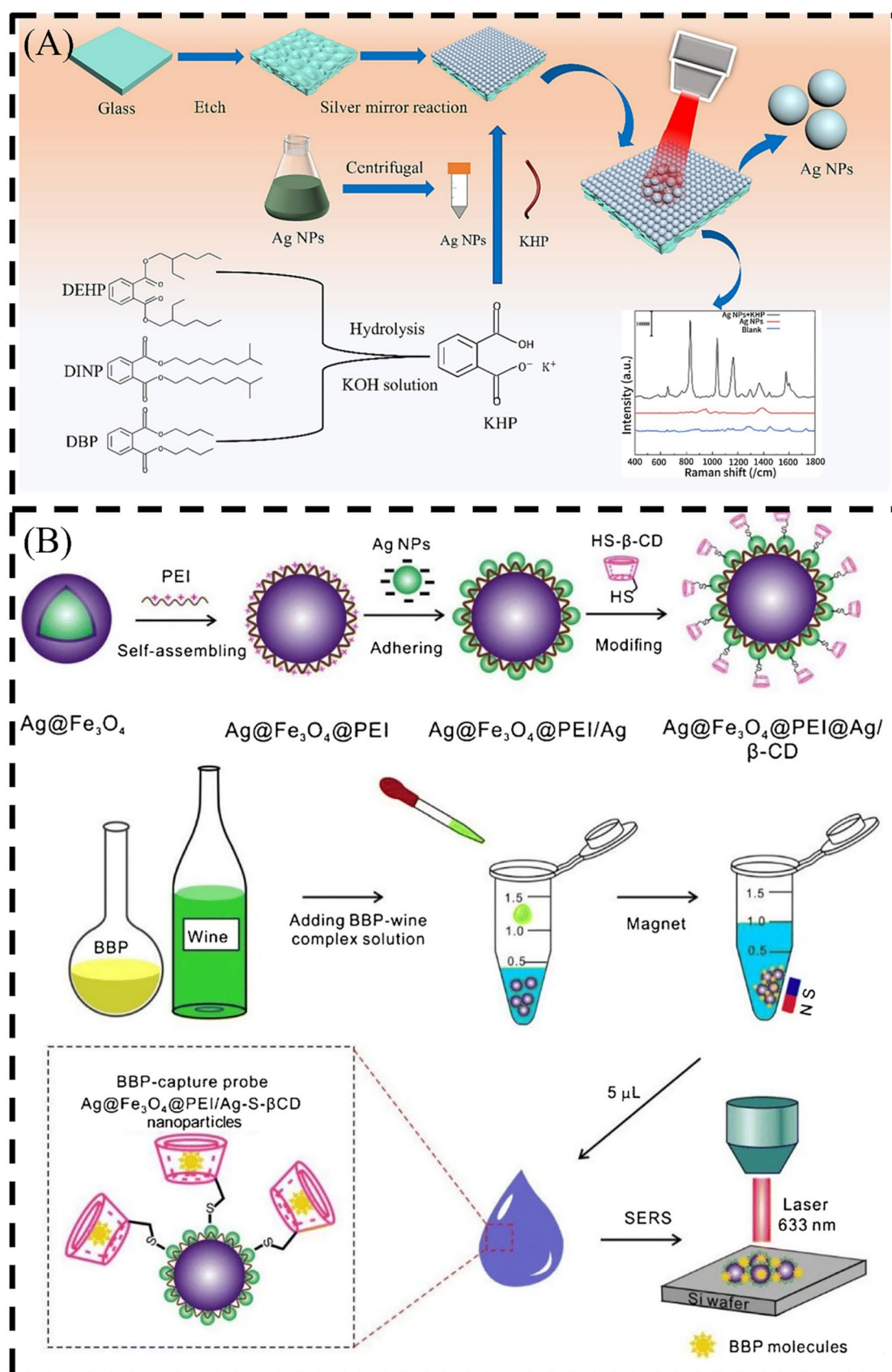
FIGURE 5
Schematic illustration of **(A)** SERS detection of PAEs in oil (Wang et al., 2023) and **(B)** the SERS detection of BBP and Ag@Fe₃O₄@Ag/β-CD NPs (Zhou et al., 2019). Polyethylenimine (PEI).

FIGURE 6
Scheme illustration of **(A)** the preparation of Au NP/PDA-MIP/SPE and the constructed SERS-active platform for PAEs selective recognition in different real samples (Yang et al., 2020) and **(B)** the Au NS@Ag NCs and it use as a SERS active platform for the detection of BBP (Wang Q. et al., 2021). Dopamine (DA), Hexadecyl trimethyl ammonium chloride (CTAC).
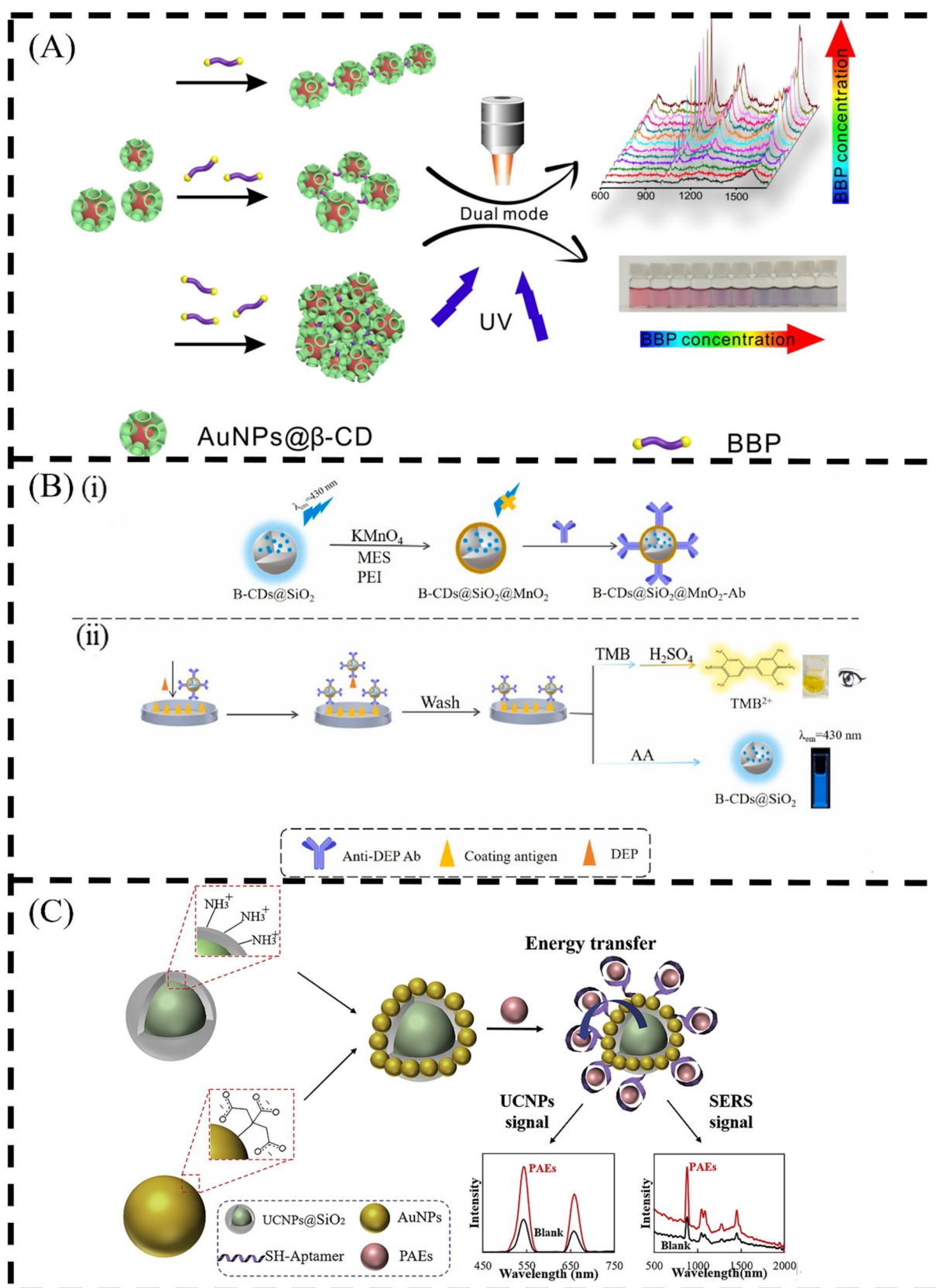
FIGURE 7
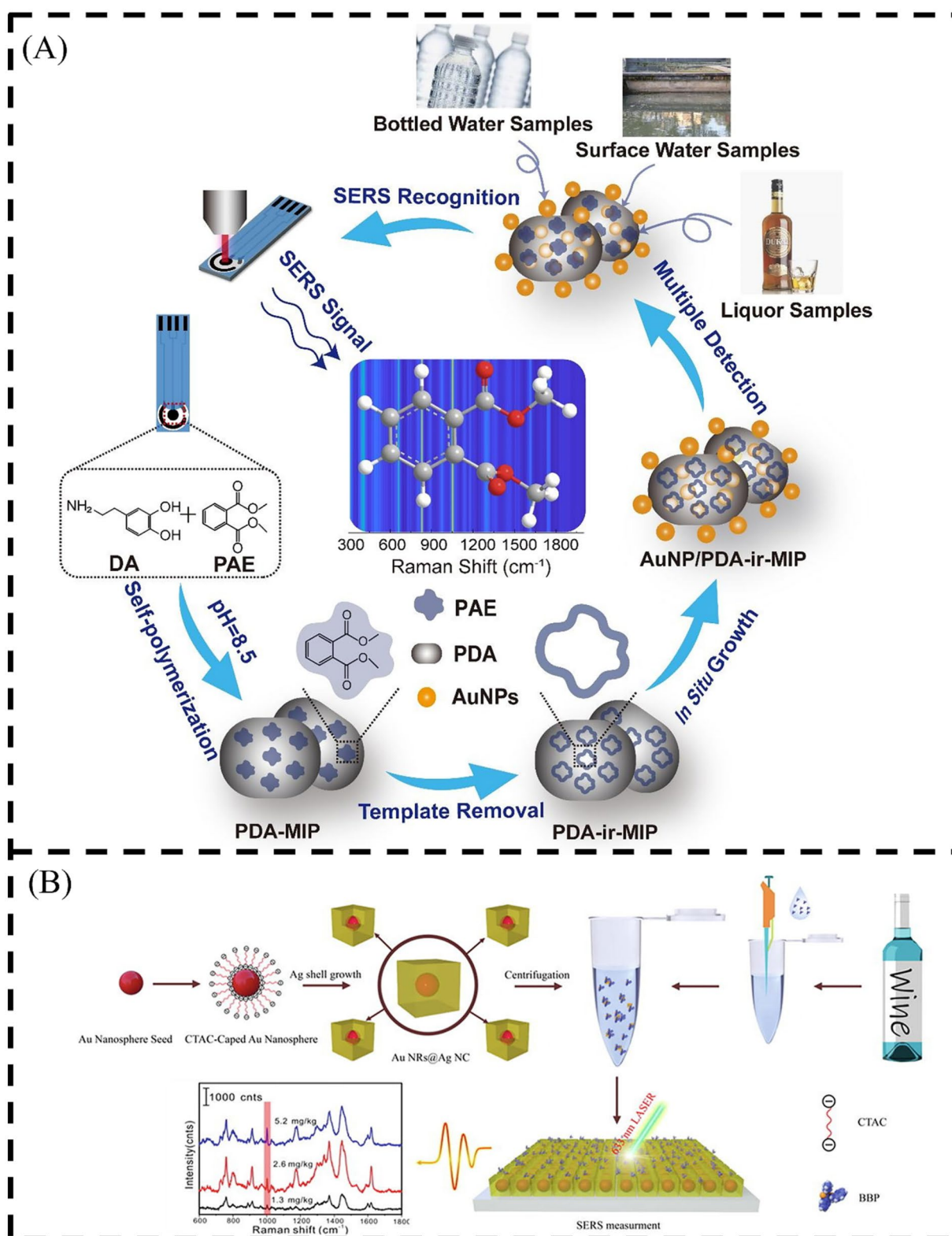Schematic illustration of **(A)** the BBP-mediated AuNPs@β-CD assembly and its dual-modal sensing of BBP (Li et al., 2019); **(B)** antibody labeled B-CDs@SiO₂@MnO₂ nanocomposite (i), dual-modal immunosensor for detection of DEP (ii) (Chen et al., 2023b) and **(C)** FL and SERS dual-mode sensors for detection of PAEs. Inset: upconversion emission and Raman spectral changes in spectra and photographs (Rong et al., 2021). Ultraviolet (UV), 2-morpholineethanesulfonic acid (MES), Polyethylenimine (PEI), Ascorbic acid (AA).

applied by the FL sensor are very limited. The enhancement of SERS signal requires the introduction of precious metals Ag and Au, and it is necessary to find materials that can replace precious metals to reduce costs.

In the future research, the practical application of optical sensors can be expanded from the following aspects. The range of samples that detected by optical sensors should be expanded to obtain a wider range of application. More types of receptors need to be designed and explored. We can try to combine optical sensors with other transmission or storage technologies (e.g., smart phones, shared networks) to achieve real-time detection of PAEs on online platforms. It is more portable and cheaper to combine the optimized design of the optical sensors with the paper sensing system. And it can also realize the separation and simultaneous detection of multiple targets. Through programming and other technical means, the data collected by the optical sensors is processed to achieve a more convenient, fast and intuitive purpose. The optimization and development of optical sensors from the above aspects will help them consolidate their own advantages, expand their application scope, and facilitate the development of their hot fields.

Author contributions

LZ: Data curation, Writing – original draft, Conceptualization. MC: Writing – review & editing, Supervision, Conceptualization. HD: Investigation, Funding acquisition, Writing – review & editing. QB: Writing – review & editing, Investigation, Funding acquisition. XD: Writing – original draft, Supervision, Project administration, Conceptualization, Writing – review & editing, Funding acquisition.

Conflict of interest

The authors declare that the research was conducted in the absence of any commercial or financial relationships that could be construed as a potential conflict of interest.

Publisher's note

All claims expressed in this article are solely those of the authors and do not necessarily represent those of their affiliated organizations, or those of the publisher, the editors and the reviewers. Any product that may be evaluated in this article, or claim that may be made by its manufacturer, is not guaranteed or endorsed by the publisher.

References

Abeysinghe, H., Wickramasinghe, G., Perera, S., and Etampawala, T. (2022). MWCNT buckypaper as electrochemical sensing platform: a rapid detection technology for phthalic acid esters in solutions. *Chem. Select* 7:e202201900. doi: 10.1002/slct.202201900

Ansah, I. B., Lee, S. H., Mun, C., Kim, D. H., and Park, S. G. (2022). Interior hotspot engineering in ag–au bimetallic nanocomposites by in situ galvanic replacement reaction for rapid and sensitive surface-enhanced Raman spectroscopy detection. *Int. J. Mol. Sci.* 23:11741. doi: 10.3390/ijms231911741

Ashokan, I., and Bhunia, S. K. (2023). Boron and nitrogen co-doped bright yellow fluorescent carbon dots as real-time selective detection of phthalic acid plasticizer in aqueous medium. *J. Photochem. Photobiol. A Chem.* 437:114489. doi: 10.1016/j.jphotochem.2022.114489

Cai, Y., Liu, C., Wang, J., Liu, X., Zhang, Y., Yang, S., et al. (2021). CuxO nanorods with excellent regenerable NADH peroxidase mimics and its application for selective and sensitive fluorimetric ethanol sensing. *Anal. Chim. Acta* 1186:339126. doi: 10.1016/j.aca.2021.339126

Cao, Y. R., Li, J., Wu, R. B., et al. (2022). Phthalate esters in seawater and sediment of the northern South China Sea: occurrence, distribution, and ecological risks. *Sci. Total Environ.* 811:151412. doi: 10.1016/j.scitotenv.2021.151412

Chen, H. (2019). Distribution, source, and environmental risk assessment of phthalate esters (PAEs) in water, suspended particulate matter, and sediment of a typical Yangtze River Delta City, China. *Environ. Sci. Pollut. Res.* 26, 24609–24619. doi: 10.1007/s11356-019-05259-y

Chen, S., Fu, J., Zhou, S., Zhao, P., Wu, X., Tang, S., et al. (2022). Rapid recognition of di-n-butyl phthalate in food samples with a near infrared fluorescence imprinted sensor based on zeolite imidazolate framework-67. *Food Chem.* 367:130505. doi: 10.1016/j.foodchem.2021.130505

Chen, B., Li, L., Yang, Q., Liu, B., Hu, Y., Zhang, M., et al. (2023a). Fluorescence signal amplification: red carbon dots@SiO$_2$-induced ultra-sensitive immunoassay for diethyl phthalate. *J. Fluoresc.* 33, 487–495. doi: 10.1007/s10895-022-03100-3

Chen, B., Li, L., Yang, Q., and Zhang, M. (2023b). Self-corrected dual-optical immunosensors using carbon dots@SiO$_2$@MnO$_2$ improving diethyl phthalate detection accuracy. *Talanta* 261:124652. doi: 10.1016/j.talanta.2023.124652

Chen, Y. Q., Wang, Z. M., and Liu, S. Y. (2021). A highly sensitive and group-targeting aptasensor for total phthalate determination in the environment. *J. Hazard. Mater.* 412:125174. doi: 10.1016/j.jhazmat.2021.125174

Commission Regulation (EU). (2018). Amending Annex XVII to Regulation (EC) no 1907/2006 of the European Parliament and of the Council Concerning the Registration, Evaluation, Authorisation and Restriction of Chemicals (REACH) as Regards Certain Substances Classified as Carcinogenic, Mutagenic or Toxic for Reproduction (CMR), Category 1A or 1B [S/OL]. Available at: https://eur-lex.europa.eu/legal-content/EN/TXT/?uri=celex%3A32018R1513#ntr2-L_2018256EN.01000101-E0002 (Accessed October 10, 2018).

Ding, X., Ahmad, W., Zareef, M., Rong, Y., Zhang, Y., Wu, J., et al. (2022). MIL-101(Cr)-induced nano-optical sensor for ultra-sensitive detection of enrofloxacin in aquatic products using a fluorescence turn-on mechanism via upconversion nanoparticles. *Sensors Actuators B Chem.* 365:131915. doi: 10.1016/j.snb.2022.131915

Dolai, J., Ali, H., and Jana, N. R. (2021). Selective capturing and fluorescence "turn on" detection of dibutyl phthalate using a molecular imprinted nanocomposite. *New J. Chem.* 45, 19088–19096. doi: 10.1039/D1NJ04169J

Dong, W., Guo, R., Sun, X., Li, H., Zhao, M., Zheng, F., et al. (2019). Assessment of phthalate ester residues and distribution patterns in baijiu raw materials and baijiu. *Food Chem.* 283, 508–516. doi: 10.1016/j.foodchem.2019.01.069

Dong, X., Zhang, L., Ge, M., Wu, M., Niu, Q., et al. (2024). Recent advances of sensitive electrochemical sensing platforms for rapid detection of phthalate acid esters. *Instrumentation* 11, 1–15. doi: 10.15878/j.instr.202400185

Fleischmann, M., Hendra, P. J., and McQuillan, A. J. (1974). Raman spectra of pyridzne adsorbed at a sliver electrode. *Chem. Phys. Lett.* 26, 163–166. doi: 10.1016/0009-2614(74)85388-1

Fu, L., Song, S., Luo, X., Luo, Y., Guo, C., Liu, Y., et al. (2023). Unraveling the contribution of dietary intake to human phthalate internal exposure. *Environ. Pollut.* 337:122580. doi: 10.1016/j.envpol.2023.122580

Garí, M., Koch, H. M., Pälmke, C., Jankowska, A., Wesołowska, E., Hanke, W., et al. (2019). Determinants of phthalate exposure and risk assessment in children from Poland. *Environ. Int.* 127, 742–753. doi: 10.1016/j.envint.2019.04.011

Gong, C. B., Ou, X. X., Liu, S., Jin, Y. L., Huang, H. R., Tang, Q., et al. (2017). A molecular imprinting-based multifunctional chemosensor for phthalate esters. *Dyes Pigments* 137, 499–506. doi: 10.1016/j.dyepig.2016.10.047

Gong, X., Xiong, L., Xing, J., Deng, Y., Qihui, S., Sun, J., et al. (2024). Implications on freshwater lake-river ecosystem protection suggested by organic micropollutant (OMP) priority list. *J. Hazard. Mater.* 461:132580. doi: 10.1016/j.jhazmat.2023.132580

Guo, X., Li, J., Arabi, M., Wang, X., Wang, Y., Chen, L., et al. (2020). Molecular-imprinting-based surface-enhanced Raman scattering sensors. *ACS Sensors* 5, 601–619. doi: 10.1021/acssensors.9b02039

Guo, Z., Ren, J., Wang, J., and Wang, E. (2011). Single-walled carbon nanotubes based quenching of free FAM-aptamer for selective determination of ochratoxin A. *Talanta* 85, 2517–2521. doi: 10.1016/j.talanta.2011.08.015

Guo, R. H., Shu, C. C., Chuang, K. J., and Hong, G. B. (2021). Rapid colorimetric detection of phthalates using DNA-modified gold nanoparticles. *Mater. Lett.* 293:129756. doi: 10.1016/j.matlet.2021.129756

Hidalgo-Serrano, M., Borrull, F., Marcé, R. M., and Pocurull, E. (2022). Phthalate esters in marine ecosystems: analytical methods, occurrence and distribution. *Trends Anal. Chem.* 151:116598. doi: 10.1016/j.trac.2022.116598

Huang, P. C., Cheng, P. K., Chen, H. C., Shiue, I., Chang, W. T., Huang, H. I., et al. (2022). Are phthalate exposure related to oxidative stress in children and adolescents with asthma? A cumulative risk assessment approach. *Antioxidants* 11:1315. doi: 10.3390/antiox11071315

Huang, X., Sun, W., Li, Z., Shi, J., Zhang, N., Zhang, Y., et al. (2022). Hydrogen sulfide gas sensing toward on-site monitoring of chilled meat spoilage based on ratio-type fluorescent probe. *Food Chem.* 396:133654. doi: 10.1016/j.foodchem.2022.133654

Huang, X. W., Zou, X. B., Shi, J. Y., Zhi-hua, L., and Jie-wen, Z. (2018). Colorimetric sensor arrays based on chemo-responsive dyes for food odor visualization. *Trends Food Sci. Technol.* 81, 90–107. doi: 10.1016/j.tifs.2018.09.001

Jablonski, A. (1933). Efficiency of anti-stokes fluorescence in dyes. *Nature* 131, 839–840. doi: 10.1038/131839b0

Jiang, H., Lin, H., Lin, J., Adade, S. Y. S. S., Chen, Q., Xue, Z., et al. (2022). Non-destructive detection of multi-component heavy metals in corn oil using nano-modified colorimetric sensor combined with near-infrared spectroscopy. *Food Control* 133:108640. doi: 10.1016/j.foodcont.2021.108640

Kang, J. S., Baek, J. H., Yeong, S. M., et al. (2023). Long-term exposure changes the environmentally relevant bis(2-ethylhexyl) phthalate to be a neuro-hazardous substance disrupting neural homeostasis in emotional and cognitive functions. *Environ. Pollut.* 324:121387. doi: 10.1016/j.envpol.2023.121387

Kim, S. J., Lee, Y., Choi, E. J., Lee, J. M., Kim, K. H., Oh, J. W., et al. (2023). The development progress of multi-array colourimetric sensors based on the M13 bacteriophage. *Nano Conv.* 10, 1–12. doi: 10.1186/s40580-022-00351-5

Kim, D., Lim, H. J., Ahn, Y. G., Chua, B., and Son, A. (2020). Development of non-equilibrium rapid replacement aptamer assay for ultra-fast detection of phthalic acid esters. *Talanta* 219:121216. doi: 10.1016/j.talanta.2020.121216

Lan, L., Chen, D., Yao, Y., Peng, X., Wu, J., Li, Y., et al. (2018). Phase-dependent fluorescence quenching efficiency of MoS_2 nanosheets and their applications in multiplex target biosensing. *ACS Appl. Mater. Interfaces* 10, 42009–42017. doi: 10.1021/acsami.8b15677

Lee, Y., Kim, S. J., Kim, Y. J., Kim, Y. H., Yoon, J. Y., Shin, J., et al. (2023). Sensor development for multiple simultaneous classifications using genetically engineered M13 bacteriophages. *Biosens. Bioelectron.* 241:115642. doi: 10.1016/j.bios.2023.115642

Lee, Y. M., Lee, J. E., Choe, W., Kim, T., Lee, J. Y., Kho, Y., et al. (2019). Distribution of phthalate esters in air, water, sediments, and fish in the Asan Lake of Korea. *Environ. Int.* 126, 635–643. doi: 10.1016/j.envint.2019.02.059

Li, J., Dong, S., Tong, J., Zhu, P., Diao, G., Yang, Z., et al. (2016). 3D ordered silver nanoshells silica photonic crystal beads for multiplex encoded SERS bioassay. *Chem. Commun.* 52, 284–287. doi: 10.1039/C5CC08332J

Li, J., Hu, X., Zhou, Y., Zhang, L., Ge, Z., Wang, X., et al. (2019). β-Cyclodextrin-stabilized au nanoparticles for the detection of butyl benzyl phthalate. *ACS Appl. Nano Mat.* 2, 2743–2751. doi: 10.1021/acsanm.9b00258

Li, J., Li, W., Rao, Y., Shi, F., Yu, S., Yang, H., et al. (2021). Synthesis of highly ordered AgNPs-coated silica photonic crystal beads for sensitive and reproducible 3D SERS substrates. *Chin. Chem. Lett.* 32, 150–153. doi: 10.1016/j.cclet.2020.10.043

Li, W., Zhang, X., Zhang, H., Zhang, C., Chen, Y., Li, C., et al. (2023). A nanozymatic-mediated smartphone colorimetric sensing platform for the detection of dimethyl phthalate (DMP) and dibutyl phthalate (DBP). *Biosensors* 13:919. doi: 10.3390/bios13100919

Lim, H. J., Jin, H., Chua, B., and Son, A. (2022). Clustered detection of eleven phthalic acid esters by fluorescence of graphene quantum dots displaced from gold nanoparticles. *ACS Appl. Mater. Interfaces* 14, 4186–4196. doi: 10.1021/acsami.1c21756

Lin, H., Wang, F., Lin, J., Yang, W., Kang, W., Jiang, H., et al. (2023). Detection of wheat toxigenic aspergillus flavus based on nano-composite colorimetric sensing technology. *Food Chem.* 405:134803. doi: 10.1016/j.foodchem.2022.134803

Liu, Z., Ge, D., Zhao, C., Shi, J., Zeng, Z., Fang, Z., et al. (2024). A porous silicon composite with irregular silver nano-dendritic particles: a rapid optical sensor for trace detection of malachite green in freshwater fish. *Anal. Methods* 16, 608–614. doi: 10.1039/D3AY02044D

Liu, J., Li, J., Li, F., Zhou, Y., Hu, X., Xu, T., et al. (2018). Liquid–liquid interfacial self-assembled au NP arrays for the rapid and sensitive detection of butyl benzyl phthalate (BBP) by surface-enhanced Raman spectroscopy. *Anal. Bioanal. Chem.* 410, 5277–5285. doi: 10.1007/s00216-018-1184-6

Liu, M., Mou, J., Xu, X., Zhang, F., Xia, J., Wang, Z., et al. (2020). High-efficiency artificial enzyme cascade bio-platform based on MOF-derived bimetal nanocomposite for biosensing. *Talanta* 220:121374. doi: 10.1016/j.talanta.2020.121374

Liu, F., Yang, R., Chen, R., Guindo, M. L., He, Y., Zhou, J., et al. (2023). Digital techniques and trends for seed phenotyping using optical sensors. *J. Adv. Res.* 63, 1–16. doi: 10.1016/j.jare.2023.11.010

Liu, X. X., Ying, Y. B., and Ping, J. F. (2020). Structure, synthesis, and sensing applications of single-walled carbon nanohorns. *Biosens. Bioelectron.* 167:112495. doi: 10.1016/j.bios.2020.112495

Liu, L., Zhang, T., Wu, Z., Zhang, F., Wang, Y., Wang, X., et al. (2023). Universal method for label-free detection of pathogens and biomolecules by surface-enhanced Raman spectroscopy based on gold nanoparticles. *Anal. Chem.* 95, 4050–4058. doi: 10.1021/acs.analchem.2c04525

Lu, R., Van Beers, R., Saeys, W., Li, C., Cen, H., et al. (2020). Measurement of optical properties of fruits and vegetables: a review. *Postharvest Biol. Technol.* 159:111003. doi: 10.1016/j.postharvbio.2019.111003

Lu, J. Y., Wang, J. X., Li, Y., Chen, Q. Y., Qu, L. L., Meng, S. C., et al. (2021). A water caged BODIPY as fluorescence sensor of phthalates. *Sensors Actuators B Chem.* 331:129396. doi: 10.1016/j.snb.2020.129396

Luan, C., Yang, Z. X., and Chen, B. A. (2016). Signal improvement strategies for fluorescence detection of biomacromolecules. *J. Fluoresc.* 26, 1131–1139. doi: 10.1007/s10895-016-1806-3

Ly, N. H., Son, S. J., Jang, S., Lee, C., Lee, J. I., and Joo, S. W. (2021). Surface-enhanced Raman sensing of semi-volatile organic compounds by plasmonic nanostructures. *Nano* 11:2619. doi: 10.3390/nano11102619

Ma, C., Jiang, N., Sun, X., Kong, L., Liang, T., Wei, X., et al. (2023). Progress in optical sensors-based uric acid detection. *Biosens. Bioelectron.* 237:115495. doi: 10.1016/j.bios.2023.115495

Meng, H., Yao, N., Zeng, K., Zhu, N., Wang, Y., Zhao, B., et al. (2022). A novel enzymefree ratiometric fluorescence immunoassay based on silver nanoparticles for the detection of dibutyl phthalate from environmental waters. *Biosensors* 12:125. doi: 10.3390/bios12020125

Mi, L. J., Xie, Z., Zhao, Z., et al. (2019). Occurrence and spatial distribution of phthalate esters in sediments of the Bohai and yellow seas. *Sci. Total Environ.* 653, 792–800. doi: 10.1016/j.scitotenv.2018.10.438

Nam, J. M., Oh, J. W., Lee, H., and Suh, Y. D. (2016). Plasmonic nanogap-enhanced raman scattering with nanoparticles. *Acc. Chem. Res.* 49, 2746–2755. doi: 10.1021/acs.accounts.6b00409

Net, S., Sempéré, R., Delmont, A., Paluselli, A., and Ouddane, B. (2015). Occurrence, fate, behavior and ecotoxicological state of phthalates in different environmental matrices. *Environ. Sci. Technol.* 49, 4019–4035. doi: 10.1021/es505233b

Niu, X., Shi, Q., Zhu, W., Liu, D., Tian, H., Fu, S., et al. (2019). Unprecedented peroxidase-mimicking activity of single-atom nanozyme with atomically dispersed Fe–Nx moieties hosted by MOF derived porous carbon. *Biosens. Bioelectron.* 142:111495. doi: 10.1016/j.bios.2019.111495

Pablo, L. V., Marie, G., Guillaume, R., and Menu, M. J. (2023). A review on solution- and vapor-responsive sensors for the detection of phthalates. *Anal. Chim. Acta* 1282:341828. doi: 10.1016/j.aca.2023.341828

Qin, J., Jiang, S., Wang, Z., Cheng, X., Li, B., Shi, Y., et al. (2022). Metasurface micro/mano-optical sensors: principles and applications. *ACS Nano* 16, 11598–11618. doi: 10.1021/acsnano.2c03310

Qiu, Y. L., and Li, Y. (2018). A theoretical method for the high-sensitivity fluorescence detection of PAEs through double-substitution modification. *Environ. Sci. Pollut. Res.* 25, 34684–34692. doi: 10.1007/s11356-018-3432-x

Reyes, J. M., and Price, P. S. (2018). Temporal trends in exposures to six phthalates from biomonitoring data: implications for cumulative risk. *Environ. Sci. Technol.* 52, 12475–12483. doi: 10.1021/acs.est.8b03338

Rong, Y., Ali, S., Ouyang, Q., Wang, L., Li, H., Chen, Q., et al. (2021). Development of a bimodal sensor based on upconversion nanoparticles and surface-enhanced Raman for the sensitive determination of dibutyl phthalate in food. *J. Food Compos. Anal.* 100:103929. doi: 10.1016/j.jfca.2021.103929

Sate Administration for Market Regulation. (2019). The Guidance of the General Administration of Market Supervision on the Prevention and Control of 'plasticizer' Pollution Risk in Food[S/OL]. Available at: https://www.samr.gov.cn/zw/zfxxgk/fdzdgknr/spscs/art/2023/art_904e69afd8ea41c69e55509556db15f0.html (Accessed November 3, 2019).

Savicheva, E. A., Mitronova, G. Y., Thomas, L., Böhm, M. J., Seikowski, J., Belov, V. N., et al. (2020). Negatively charged yellow-emitting 1-aminopyrene dyes for reductive

amination and fluorescence detection of glycans. *Angew. Chem. Int. Ed.* 59, 5505–5509. doi: 10.1002/anie.201908063

Selva Sharma, A., Marimuthu, M., Varghese, A. W., Wu, J., Xu, J., Xiaofeng, L., et al. (2024). A review of biomolecules conjugated lanthanide up-conversion nanoparticles-based fluorescence probes in food safety and quality monitoring applications. *Crit. Rev. Food Sci. Nutr.* 64, 6129–6159. doi: 10.1080/10408398.2022.2163975

Seol, D., Jang, D., Oh, J. W., Cha, K., and Chung, H. (2019). Discrimination of phthalate species using a simple phage-based colorimetric sensor in conjunction with hierarchical support vector machine. *Environ. Res.* 170, 238–242. doi: 10.1016/j.envres.2018.12.030

Soon, J. M., Brazier, A. K. M., and Wallace, C. A. (2020). Determining common contributory factors in food safety incidents - a review of global outbreaks and recalls 2008-2018. *Trends Food Sci. Technol.* 97, 76–87. doi: 10.1016/j.tifs.2019.12.030

Sun, Q., Zhang, X., Liu, C., Nier, A., Ying, S., Zhang, J., et al. (2023). The content of PAEs in field soils caused by the residual film has a periodical peak. *Sci. Total Environ.* 864:161078. doi: 10.1016/j.scitotenv.2022.161078

Tan, W., Yu, H., Huang, C., Li, D., Zhang, H., Zhao, X., et al. (2018). Intercropping wheat and maize increases the uptake of phthalic acid esters by plant roots from soils. *J. Hazard. Mater.* 359, 9–18. doi: 10.1016/j.jhazmat.2018.07.026

Tu, D., Garza, J. T., and Coté, G. L. (2019). A SERS aptasensor for sensitive and selective detection of bis (2-ethylhexyl) phthalate. *RSC Adv.* 9, 2618–2625. doi: 10.1039/C8RA09230C

Wang, M., Chang, M., Chen, Q., Wang, D., Li, C., and Hou, Z. (2020). Au₂Pt-PEG-Ce₆ nanoformulation with dual nanozyme activities for synergistic chemodynamic therapy/phototherapy. *Biomaterials* 252:120093. doi: 10.1016/j.biomaterials.2020.120093

Wang, X., Chen, C., Chen, Y., Kong, F., Xu, Z., et al. (2020). Detection of dibutyl phthalate in food samples by fluorescence ratio immunosensor based on dual-emission carbon quantum dot labelled dual aptamers. *Food Agric. Immunol.* 31, 813–826. doi: 10.1080/09540105.2020.1774746

Wang, W., Leung, A. O. W., Chu, L. H., and Wong, M. H. (2018). Phthalates contamination in China: status, trends and human exposure-with an emphasis on oral intake. *Environ. Pollut.* 238, 771–782. doi: 10.1016/j.envpol.2018.02.088

Wang, Y., Li, W., Hu, X., Zhang, X., Huang, X., Li, Z., et al. (2021). Efficient preparation of dual-emission ratiometric fluorescence sensor system based on aptamer-composite and detection of bis(2-ethylhexyl) phthalate in pork. *Food Chem.* 352:129352. doi: 10.1016/j.foodchem.2021.129352

Wang, M., Shi, F., Li, J., Min, L., Yang, Z., Li, J., et al. (2024). An au bipyramids@CuZn MOF core-shell nanozyme enables universal SERS and a colorimetric dual-model bioassay. *Chem. Commun.* 60, 6019–6022. doi: 10.1039/D4CC01602E

Wang, H., Wang, C., Huang, J., Liu, Y., Wu, Y., You, R., et al. (2023). Preparation of SERS substrate with 2D silver plate and nano silver sol for plasticizer detection in edible oil. *Food Chem.* 409:135363. doi: 10.1016/j.foodchem.2022.135363

Wang, Q., Wang, J., Li, M., Ge, Z., Zhang, X., Luan, L., et al. (2021). Size-dependent surface enhanced Raman scattering activity of plasmonic AuNS@AgNCs for rapid and sensitive detection of butyl benzyl phthalate. *Spectrochim. Acta A Mol. Biomol. Spectrosc.* 248:119131. doi: 10.1016/j.saa.2020.119131

Wang, F., Wang, Y., Xiang, L., Redmile-Gordon, M., Gu, C., Yang, X., et al. (2022). Perspectives on ecological risks of microplastics and phthalate acid esters in crop production systems. *Soil Ecol. Lett.* 4, 97–108. doi: 10.1007/s42832-021-0092-4

Wang, H., Wu, F., Wu, L., Guan, J., and Niu, X. (2023). Nanozyme colorimetric sensor array based on monatomic cobalt for the discrimination of sulfur-containing metal salts. *J. Hazard. Mater.* 456:131643. doi: 10.1016/j.jhazmat.2023.131643

Wang, Y., Zhang, K. W., and Du, Y. K. (2022). Recent progress of carbon dot fluorescent probes for tetracycline detection. *New J. Chem.* 46, 20554–20560. doi: 10.1039/D2NJ04064F

Wang, D. N., Zhang, Y. Z., Zhao, X. Y., and Xu, Z. (2019). Plasmonic colorimetric biosensor for visual detection of telomerase activity based on horseradish peroxidase-encapsulated liposomes and etching of au nanobipyramids. *Sensors Actuators B Chem.* 296:126646. doi: 10.1016/j.snb.2019.126646

Wang, Y., Zhou, Z., Xu, W., Luan, Y., Lu, Y., Yang, Y., et al. (2018). Surface molecularly imprinted polymers based ZnO quantum dots as fluorescence sensors for detection of diethylhexyl phthalate with high sensitivity and selectivity. *Polym. Int.* 67, 1003–1010. doi: 10.1002/pi.5596

Wang, Y., Zhu, H. K., and Kannan, K. (2019). A review of biomonitoring of phthalate exposures. *Toxics* 7:21. doi: 10.3390/toxics7020021

World Health Organization. (2021). Available at: https://www.who.int/news-room/fact-sheets/detail/food-safety (Accessed March 15, 2021).

Wu, M. C., Lin, M. P., Lin, T. H., and Su, W. F. (2018). Ag/SiO₂ surface-enhanced Raman scattering substrate for plasticizer detection. *Jpn. J. Appl. Phys.* 57:04FM07. doi: 10.7567/JJAP.57.04FM07

Wu, J., Lv, W., Yang, Q., Li, H., and Li, F. (2021). Label-free homogeneous electrochemical detection of MicroRNA based on target-induced anti-shielding against the catalytic activity of two-dimension nanozyme. *Biosens. Bioelectron.* 171:112707. doi: 10.1016/j.bios.2020.112707

Xu, S., Li, H., Guo, M., Wang, L., Li, X., Xue, Q., et al. (2021). Liquid–liquid interfacial self-assembled triangular ag nanoplate-based high-density and ordered SERS-active arrays for the sensitive detection of dibutyl phthalate (DBP) in edible oils. *Analyst* 146, 4858–4864. doi: 10.1039/D1AN00713K

Xu, H., Zhu, J. H., and Cheng, Y. X. (2021). Functionalized UIO-66@ag nanoparticles substrate for rapid and ultrasensitive SERS detection of di-(2-ethylhexyl) phthalate in plastics. *Sensors Actuators B Chem.* 349:130793. doi: 10.1016/j.snb.2021.130793

Xu, H., Zhu, J., Wu, X., Cheng, Y., Wang, D., Cai, D., et al. (2023). Recognition and quantitative analysis for six phthalate esters (PAEs) through functionalized ZIF-67@ag nanowires as surface-enhanced Raman scattering substrate. *Spectrochim. Acta A Mol. Biomol. Spectrosc.* 284:121735. doi: 10.1016/j.saa.2022.121735

Xue, Y. C., and Jiang, H. (2023). Monitoring of chlorpyrifos residues in corn oil based on Raman spectral deep-learning model. *Foods* 12:2402. doi: 10.3390/foods12122402

Yan, Y., Qu, Y., Du, R., Zhou, W., Gao, H., Lu, R., et al. (2021). Colorimetric assay based on argininefunctionalized gold nanoparticles for the detection of dibutyl phthalate in baijiu samples. *Anal. Methods* 13, 5179–5186. doi: 10.1039/D1AY01464A

Yanagisawa, H., and Fujimaki, S. (2019). Simple colorimetric determination of phthalates in polymers by dye formation. *Anal. Sci.* 35, 1215–1219. doi: 10.2116/analsci.19P165

Yang, Y. Y., Li, Y. T., Li, X. J., Zhang, L., Kouadio Fodjo, E., and Han, S. (2020). Controllable in situ fabrication of portable AuNP/mussel-inspired polydopamine molecularly imprinted SERS substrate for selective enrichment and recognition of phthalate plasticizers. *Chem. Eng. J.* 402:125179. doi: 10.1016/j.cej.2020.125179

Yang, H., Li, J., Rao, Y., Yang, L., Xue, Y., Zhang, Y., et al. (2023). Ultrasensitive multiplex SERS immunoassay based on porous au-ag alloy nanoparticle–amplified Raman signal probe and encoded photonic crystal beads. *Microchim. Acta* 190:13. doi: 10.1007/s00604-022-05539-4

You, J. J., Liu, H., Zhang, R. R., Pan, Q. F., Sun, A. L., Zhang, Z. M., et al. (2022). Development and application of tricolor ratiometric fluorescence sensor based on molecularly imprinted nanoparticles for visual detection of dibutyl phthalate in seawater and fish samples. *Sci. Total Environ.* 848:157675. doi: 10.1016/j.scitotenv.2022.157675

Yu, L. L., Song, Z. R., Peng, J., Yang, M., Zhi, H., He, H., et al. (2020). Progress of gold nanomaterials for colorimetric sensing based on different strategies. *Trends Anal. Chem.* 127:115880. doi: 10.1016/j.trac.2020.115880

Zeng, H. H., Li, X. Q., Hao, W. L., Zhang, L. Z., Wei, T., Zhao, X. F., et al. (2017). Determination of phthalate esters in airborne particulates by heterogeneous photo-Fenton catalyzed aromatic hydroxylation fluorimetry. *J. Hazard. Mater.* 324, 250–257. doi: 10.1016/j.jhazmat.2016.10.055

Zhang, T., Guan, A., Wang, G., Huang, X., Li, W., Liu, C., et al. (2023). Magnetic molecularly imprinted nanoparticles for rapid and selective detection of dimethyl phthalate in water using SERS. *ACS Sustain. Chem. Eng.* 11, 11149–11160. doi: 10.1021/acssuschemeng.3c01847

Zhang, Y. J., Guo, J. L., Xue, J. C., Bai, C. L., and Guo, Y. (2021). Phthalate metabolites: characterization, toxicities, global distribution, and exposure assessment. *Environ. Pollut.* 291:118106. doi: 10.1016/j.envpol.2021.118106

Zhang, Y., Han, Y., Liu, Z., Fan, L., Guo, Y., et al. (2023). Colorimetric and electrochemical assay for dual-mode detection of di-2-ethylhexyl phthalate based on hemin-graphene nanocomposites. *Microchem. J.* 191:108788. doi: 10.1016/j.microc.2023.108788

Zhang, W., Liu, J., Niu, W., Yan, H., Lu, X., Liu, B., et al. (2018). Tip-selective growth of silver on gold nanostars for surface-enhanced Raman scattering. *ACS Appl. Mater. Interfaces* 10, 14850–14856. doi: 10.1021/acsami.7b19328

Zhang, T., Liu, Y., Pi, J., Lu, N., Zhang, R., Chen, W., et al. (2022). A novel artificial peroxisome candidate based on nanozyme with excellent catalytic performance for biosensing. *Biosens. Bioelectron.* 196:113686. doi: 10.1016/j.bios.2021.113686

Zhang, J. F., Zhang, Y., and Shi, G. Y. (2022). Interface engineering with self-assembling au@ag@β-cyclodextrin bimetal nanoparticles to fabricate a ring-like arrayed SERS substrate for sensitive recognition of phthalate esters based on a host–guest interaction and the coffee ring effect. *Anal. Methods* 14, 259–268. doi: 10.1039/D1AY01636A

Zhang, H., Zhang, M., Zhou, Y., Qiao, Z., Gao, L., Cao, L., et al. (2024). Organic photoelectrochemical transistor aptasensor for dual-mode detection of DEHP with CRISPR-Cas13a assisted signal amplification. *J. Hazard. Mater.* 470:134175. doi: 10.1016/j.jhazmat.2024.134175

Zhang, D., Zhou, K., Liu, C., Li, X., Pan, S., Zhong, L., et al. (2023). Dissipation, uptake, translocation and accumulation of five phthalic acid esters in sediment-*Zizania latifolia* system. *Chemosphere* 315:137651. doi: 10.1016/j.chemosphere.2022.137651

Zhang, C., Zhou, J., Ma, T., Guo, W., Wei, D., Tan, Y., et al. (2023). Advances in application of sensors for determination of phthalate esters. *Chin. Chem. Lett.* 34:107670. doi: 10.1016/j.cclet.2022.07.013

Zhao, T., Chen, Q., Wen, Y., Bian, X., Tao, Q., Liu, G., et al. (2022). A competitive colorimetric aptasensor for simple and sensitive detection of kanamycin based on terminal deoxynucleotidyl transferase-mediated signal amplification strategy. *Food Chem.* 377:132072. doi: 10.1016/j.foodchem.2022.132072

Zhao, Y., Sun, Y., Zhu, C., Zhang, Y., Hou, J., Zhang, Q., et al. (2022). Phthalate metabolites in urine of Chinese children and their association with asthma and allergic symptoms. *Int. J. Environ. Res. Public Health* 19:14083. doi: 10.3390/ijerph192114083

Zhou, Z., Li, T., Xu, W., Huang, W., Wang, N., Yang, W., et al. (2017). Synthesis and characterization of fluorescence molecularly imprinted polymers as sensor for highly sensitive detection of dibutyl phthalate from tap water samples. *Sensors Actuators B Chem.* 240, 1114–1122. doi: 10.1016/j.snb.2016.09.092

Zhou, Y., Li, J., Zhang, L., Ge, Z., Wang, X., Hu, X., et al. (2019). HS-β-cyclodextrin-functionalized ag@Fe$_3$O$_4$@ag nanoparticles as a surface-enhanced Raman spectroscopy substrate for the sensitive detection of butyl benzyl phthalate. *Anal. Bioanal. Chem.* 411, 5691–5701. doi: 10.1007/s00216-019-01947-3

Zhu, N., Li, X., Liu, Y., Liu, J., Wang, Y., Wu, X., et al. (2021). Dual amplified ratiometric fluorescence ELISA based on G-quadruplex/hemin DNAzyme using tetrahedral DNA nanostructure as scaffold for ultrasensitive detection of dibutyl phthalate in aquatic system. *Sci. Total Environ.* 784:147212. doi: 10.1016/j.scitotenv.2021.147212

Zhu, F., Zhang, H., Qiu, M., Wu, N., Zeng, K., Du, D., et al. (2019). Dual-label time-resolved fluoroimmunoassay as an advantageous approach for investigation of diethyl phthalate & dibutyl phthalate in surface water. *Sci. Total Environ.* 695:133793. doi: 10.1016/j.scitotenv.2019.133793

Zhu, N. F., Zou, Y. M., Huang, M. L., Dong, S., Wu, X., Liang, G., et al. (2018). A sensitive, colorimetric immunosensor based on cu-MOFs and HRP for detection of dibutyl phthalate in environmental and food samples. *Talanta* 186, 104–109. doi: 10.1016/j.talanta.2018.04.023

Glossary

Full name	Abbreviation	Full name	Abbreviation
Fluorescence	FL	Nanocubes	NCs
Colorimetric	CL	Nanospheres	NS
Surface-enhanced Raman scattering	SERS	Nanorod	NR
Gas chromatography	GC	Nanowires	NWs
Mass spectrometry	MS	Ag–Au bimetallic nanocomposite	SGBMNC
High-performance liquid chromatography	HPLC	Triangular Ag NP	T Ag NP
Molecularly imprinted polymer	MIP	Upconversion	UC
Enzyme-linked immunosorbent assay	ELISA	Metal–organic frameworks	MOFs
Non-equilibrium rapid replacement aptamer	NERRA	Quantum dots	QDs
Arginine functionalized	ARG	Graphene qds	GQDs
Galvanic replacement reaction	GRR	Carbon dots	CDs
Limit of detection	LOD	Red carbon dots	R-CDs
Bis(2-ethylhexyl) phthalate	DEHP	Blue carbon dots	B-CDs
Dibutyl phthalate	DBP	Antibody	Ab
Dimethyl phthalate	DMP	Tetrahedral DNA nanostructure	TDN
Diethyl phthalate	DEP	Hemin-graphene	H-Gr
Benzyl butyl phthalate	BBP	Horseradish peroxidase	HRP
Diisobutyl phthalate	DIBP	Sulfotransferases	SULTs
Potassium hydrogen phthalate	PHP	3,3′, 5,5′- tetramethylbenzidine	TMB
Two-dimensional	2D	Oxidized TMB	oxTMB
Three-dimensional	3D	Cyclodextrin	CD
Nanoparticles	NPs	Polydopamine	PDA

Frontiers in
Sustainable Food Systems

Exploring sustainable solutions to global food security

Aligned with the UN Sustainable Development Goals, this journal explores the intersection of food systems, science and practice of sustainability including its environmental, economic and social justice dimensions.

Discover the latest Research Topics

See more →

Frontiers in
Sustainable Food Systems

frontiers | Research Topics